INSTITUTE OF SOUND AND VIBRATION RESEARCH.

FACULTY OF ENGINEERING AND APPLIED SCIENCE.

UNIVERSITY OF SOUTHAMPTON.

# The measurement of vibrational power transmission using laser technology.

By J. R. Baker

A thesis submitted for the degree of Doctor of Philosophy.

August 1992.

UNIVERSITY OF SOUTHAMPTON.

ABSTRACT.

FACULTY OF ENGINEERING.

INSTITUTE OF SOUND AND VIBRATION RESEARCH.

Doctor of Philosophy.

# The measurement of vibrational power transmission using laser technology.

by Jonathan Richard Baker.

Control of noise and vibration in complex, built-up structures is a common problem for the vibration engineer. Reduction of vibration levels through extensive application of damping materials and vibration isolation techniques is time-consuming and can involve expensive 'down time'. The power flow measurement technique overcomes this problem by allowing quantitative comparison of the net, vibration energy transmission amplitude through different elements of a structure, and thus identification of the primary vibration transmission pathways. Vibration control techniques can then be applied in the most efficient and least costly manner.

To date, implementation of the power flow measurement technique has concentrated on the use of accelerometers. Accelerometers, however, as a contacting transducer, mass-load the structure and cause the measured vibration signal to be reduced in amplitude and shifted in phase. This leads to power flow measurement errors, whose magnitude increases with transducer mass. In contrast, laser Doppler vibrometers offer a remote, non-contacting means of vibration measurement. Practical power flow measurement results obtained using two I.S.V.R. laser vibrometers compare favourably with those acquired simultaneously employing the two accelerometer method. This laser vibrometer is not sufficiently sensitive for many practical structural vibration problems, however, and a new, high-sensitivity, PZT laser vibrometer has been developed to overcome this problem. Two PZT laser vibrometers are employed to take low velocity amplitude, (10 μm/s), power flow measurements over the frequency range 0 to 2.5 kHz. Measured amplitudes are found to differ by only a small percent from those obtained using the two accelerometer method.

Dynamic speckle noise is a feature of all laser vibrometer measurements taken on diffuse, target surfaces. Its effect has been investigated and it is shown how spurious, optical noise, caused by speckle motion, can reduce the vibrometer sensitivity to normal-to-surface vibration. Further to this, it is shown how these effects can introduce pseudo-vibration signals into the laser vibrometer output. Typical noise signal amplitudes are determined.

To minimise the effect of inter-transducer response errors, an optical configuration consisting of a new, laser velocity gradient transducer and a PZT laser vibrometer is utilised to make practical power flow measurements. This is shown to be a viable alternative to the use of accelerometers since it not only has comparable accuracy, but also, in enabling remote, non-contact measurements, increases the rate at which measurements can be made, and extends use of the technique to surfaces where accelerometers cannot be employed, e.g. hot, lightweight and inaccessible surfaces.

ACKNOWLEDGEMENTS.

I must first acknowledge my joint supervisors, Professors Neil Halliwell and Bob White for all their help and guidance throughout the course of my studies. I am especially grateful to Professor Halliwell for not only attempting to teach me something about optics, lasers and their practical use, but also for his patience when proving to me that it is possible to write comprehensible technical reports, papers etc.

I would like to thank both Steve Rothberg and Dr Jeremy Coupland for all their help, both in discussion and with practical matters. Drs Trevor Wilmshurst and Richard Laming similarly spent many hours explaining some of the intricacies of the black art that is practical electronics, and it would have been impossible to complete this work without their help.

Without the support of many, often unrecognised people within the I.S.V.R., this thesis would have been more difficult and taken significantly longer to complete: these include Mr Denis Howell, Mr Mike Bartlett, Mr Steve Mooney and Miss Sally Abrams.

Finally I must thank my parents for their support and encouragement, and my wife Sarah for saying the right things at the right time, and for being there.

CONTENTS.

## NOMENCLATURE.

| | |
|---|---|
| a | Normal-to-surface acceleration, Light intensity modulation amplitude (Chapter 4). |
| A | Travelling wave displacement amplitude. |
| $A_P$ | Displacement amplitude. |
| $A_T$ | Displacement amplitude. |
| b | Beam width. |
| B | Standing wave displacement amplitude. |
| c | Speed of light. |
| C | Exponential near-field displacement amplitude. |
| $C_1$ | Constant. |
| $C_2$ | Constant. |
| $C_G$ | Constant. |
| d | Thickness. |
| D | Lens diameter (4,5), flexural stiffness (6). |
| e | Gain control signal. |
| E | Young's modulus, Light amplitude (5). |
| f | Temporal frequency, Lens focal length (4), |
| F | Force. |
| FT | Fourier Transform. |
| g | Grating frequency. |
| G | Cross spectrum. |
| 2h | Transducer separation. |
| H | Transfer function. |
| i | Current. |
| I | Second moment of area, Light intensity. |
| Im | Imaginary component. |
| In | Inertance. |
| j | $(-1)^{1/2}$. |
| $J_n$ | Bessel function of $n^{th}$ order. |
| k | Flexural wavenumber. |
| l | Optical pathlength imbalance, cantilever beam length (5). |
| L | Optical pathlength. |
| M | Bending moment. |
| $M_B$ | Mass per unit length. |

$M_T$ Transducer mass.

n Integer.

p Image shear.

P Power.

<P> Time-average power.

$P_{SF}$ Shear force component of flexural wave, power flow.

$P_{BM}$ Bending moment component of flexural wave, power flow.

(q) Quadrature or $90^0$ phase shift.

Q Shear force.

Re Real component.

S Cross-sectional area.

t Time.

T Integration time, transmission function (4).

u In-plane or longitudinal displacement.

U In-plane displacement amplitude.

v Velocity.

V Velocity amplitude.

w Normal-to-surface displacement.

x Spatial dimension.

$x_1$ Target to lens distance.

$x_2$ Lens to image plane distance.

y Spatial dimension.

z Vibrometer output.

Z Point impedance.

$\alpha$ Viewing angle.

$\mathfrak{A}$ Constant.

$\beta$ Viewing angle, focus angle (4).

$\gamma$ Photodetector response term.

$\Gamma$ Fringe visibility.

$\Delta$ Optical phase change.

$\varepsilon$ Phase error.

$\eta$ Amplitude error.

$\theta$ Phase.

$\boldsymbol{\theta}$ Inter-transducer phase error.

$\lambda$ Wavelength.

$\mu$ Refractive index.

$\nu$ Poisson's ratio.

$\xi$ Phase error.

$\Xi$ Resultant speckle phase.

$\Pi$ Pi, 3.142.

$\rho$ Material density.

$\langle \sigma_D \rangle$ Average speckle diameter.

$\langle \sigma_L \rangle$ Average speckle length.

$\tau$ Time delay.

$\chi$ Intensity ratio.

$\psi$ Amplitude error.

$\omega$ Radian frequency.

"True wit is nature to advantage dressed,
What oft were thought but ne'er so well expressed".

*Alexander Pope.*

## 1. INTRODUCTION.

For the vibration engineer in a 'high-noise' environment, the identification of the primary noise source is generally straightforward, e.g. an engine, compressor, press etc. What is more problematic is reduction of the noise radiation without adversely affecting either the performance of the machine, or requiring that the system undergo expensive 'down-time' or re-design. Remedial action is therefore usually aimed at reducing acoustic and structural vibration transmission, rather than redesign of the noise source itself.

As shown in figure 1.1, in most practical situations there exist a range of pathways in which vibration can travel away from the source to some point of interest. These include direct acoustic radiation, transmission through inlet, supply and exhaust piping and the machine mounts. For such a structure, complete eradication of this transmission problem would require the application of damping materials and vibration control techniques on a large scale. A practical measurement technique that enables the most significant pathways to be identified will therefore offer great savings in both time and money. A number of practical vibration transmission measurement schemes currently in use are described below.

The most simple method of transmission path identification is to generate a waveform, e.g. a pulse, in the system under test and then monitor the response at different points in the system. The presence of multiple transmission paths and frequency dependent transmission characteristics modify the waveform shape, however, and hence preclude use of this method for most practical structures. Cross-correlation[1-3] techniques can be used to overcome this problem. With broadband force excitation, the response at a point in the structure will exhibit peaks corresponding to various time delays in the transmission paths, with peak amplitudes related to the attenuation factors associated with each path. The problem arises, however, that flexural wave motion is dispersive and with a broad band excitation, the peaks in the correlation become smeared out over time. Combined with the multiple

signals associated with the many vibration transmission paths, the individual correlation signals merge and become indistinguisable. In addition, for highly reverberant structures, techniques such as cross-correlation give results representing good wave propagation in all directions. Therefore a technique that indicates the small, *net* power flow is required, since only then can vibration control techniques be applied efficiently.

Approximate mobility methods[4] are based on the measurement of the input point and cross transfer function, (velocity/force), of a structure, as a function of frequency. The measured point mobility of a structure can be shown[4], a) at high frequencies to be approximately equal to that of the equivalent, infinite structure, and b) at lower frequencies, to have a mean value equal to the point mobility of the equivalent, infinite structure. This enables structures to be characterised in terms of an approximate, 'infinite', mobility and thus allow an estimate to be made of the power flow between coupled systems, e.g. through isolators. Although measurement of the transfer function allows the components of the structure to be characterised, e.g. pure waveguide, resonant system or the number of transmission paths, it is not suitable for assessement of multipath vibration transmission since it does not give enough information for individual paths to be identified.

The finite element method[5] is an analysis technique employed to determine the dynamic response of complex structures. The structure is modelled as consisting of many elements, each of which is described in terms of its deformation pattern. Employing a computer, the energy expressions for each element are evaluated and the contributions are combined to give the total structural response. The accuracy of the finite element model increases with the number of elements employed to represent the structure, but at the expense of time and cost. At high frequencies, as the fine geometric and material detail becomes more important, and fabrication tolerances for nominally identical structures start to differ, the technique becomes unreliable. Therefore for most practical structures, finite element modelling is restricted to less than a few hundred Hertz.

For Statistical Energy Analysis (SEA)[6], the structure is modelled as consisting of coupled subsystems, each of which is then characterised in terms of its time-average, vibration energy. The power flow between subsystems is then defined as being equal to the time-average rate of energy transmission between coupled susbsystems, which is, in turn, proportional to the difference in their time-average vibration energy. The SEA technique models the dynamic behaviour of a subsystem as an average of many vibration modes. The analysis of vibration interaction between components is therefore greatly simplified but the results are therefore only approximate. Similarly, although the reliability of SEA predictions increase with the number of modes contributing to the response, e.g. at higher frequencies where the number of resonant modes per unit bandwidth is high, the uncertainty of the estimation is still not quantifiable. An additional, practical disadvantage of SEA is that it does not provide information about the vibration energy distribution within each subsystem, or the associated displacements, velocities, stresses or strains which are often required for analysing damage, or failure performance, of a structure.

The power flow measurement technique[7], based on the point measurement of vibration and spatial vibration derivatives, allows the amplitude, frequency and direction of the net, vibration energy transmitted through a system to be measured directly. The technique models a complex, built-up structure as a series of inter-connected beam and plate-like sub-structures. Power flow measurements on each sub-structure then allow the transmitted vibration energy distribution throughout the entire structure to be ascertained. Noiseux[8] was the first to note the practical advantages of this technique, and practical measurements have since shown the scheme to be straighforward to use, accurate and allow direct comparison of measured data. Measurements at many points clearly indicate the position of vibration sources and sinks, and enable the effect of introducing any structural change to be easily evaluated.

## 1.1 DEVELOPMENT OF THE POWER FLOW MEASUREMENT TECHNIQUE.

For a majority of practical measurement situations, the three wavetypes of most importance are flexural, longitudinal and shear waves[9]. Of these, flexural wave motion is the most significant source of acoustic radiation and historically has received the most attention. Consideration of other wavetypes has mainly been concerned with the reduction of cross-sensitivity effects. For this reason, a significant majority of structural vibration research has been concerned with flexural wave motion, and flexural wave power flow will be predominantly considered here.

A practical technique for the measurement of flexural wave, structural intensity, (power flow per unit thickness), in plates was first proposed by Noiseux[8]. This scheme employed three linear accelerometers mounted on a lightweight block to form a triaxial accelerometer, giving outputs proportional to the transverse acceleration and two orthogonal rotational accelerations. In the far-field, i.e. far from vibration sources, sinks and discontinuities, the time-averaged bending moment and shear force components of the structural intensity (S.I.) are equal[9]. Employing the triaxial accelerometer scheme to measure the bending moment, power flow component, Noiseux was thus able to simultaneously measure the S.I. in two orthogonal directions. Measurements in a reverberant vibration field showed how the travelling and standing wave S.I. components could be distinguised and the power flow, or net vibration energy transmission pattern through the structure, generated. This illustrated the practical use of the power flow technique. Redman-White[10] noted however, that the accuracy of an approximation in Noiseux's theory is doubtful and a more accurate measurement scheme proposed by Pavic[11] was required to fully validate the technique.

Pavic[11] proposed a scheme that simultaneously measured the shear force and bending moment S.I. components, employing linear accelerometers and the finite difference approximation to calculate spatial vibration gradients. This scheme utilised eight and four accelerometers for plate and beam measurements respectively, and hence required significant

signal processing for each S.I. calculation. It did, however, enable measurements to be made in the 'near-field', i.e. close to discontinuities such as vibration sources, sinks, boundaries etc. Pavic also analysed and quantified the three main sources of measurement error as,

(i) instrumentation phase error,

(ii) the effect of decaying near-field waves on travelling wave components,

(iii) the compromise between the accuracy of the finite difference technique and the signal-to-noise ratio, as the transducer spacing is varied.

Of greater practical interest was the one-dimensional, far-field S.I. measurement system proposed by Pavic[11], employing only two linear transducers. Although, in practice, this scheme is limited to measurement positions at least one fifth of a wavelength from a discontinuity[10], it offers many advantages over the previous scheme including savings in computation time, increased simplicity in signal processing and greater ease of use. To date, this system is the basic form of the majority of all practical, flexural wave, S.I. measurement schemes.

Redman-White[10] extended the S.I. measurement technique through a thorough investigation of a range of transducer configurations for both one and two dimensional measurements. For one-dimensional, beam-like structures, three transducer configurations were investigated:

(i) a biaxial accelerometer employing two linear accelerometers mounted on a lightweight block attached to the vibrating surface; this configuration was found to be too sensitive to cross-sensitivity effects,

(ii) a differencing accelerometer scheme where two linear accelerometers were symmetrically mounted onto a 'T' piece, that was in turn positioned on the vibrating structure; this system was found to be too sensitive to resonances in the mount,

(iii) the scheme originally proposed by Pavic employing two linear accelerometers, mounted directly onto the structure, with the

structural intensity at the mid-point being calculated.

Of these sytems, the two linear transducer system was found to be the most practical and accurate measurement configuration. A portable, real-time, analogue electronic structural intensity meter was designed to realise this scheme[10].

Most practical S.I. measurement schemes employ accelerometers since their use is widespread and well understood. Accelerometers are contacting transducers however, and their attachment to a structure is not only time consuming, but adds mass. On lightweight and lightly damped structures, accelerometers can therefore adversely affect the vibration characteristics[12] and thus the accuracy of any S.I. measurement. Further to this, spurious contact resonance effects can occur. Carroll has also shown[13] how cable strain effects, caused by differential vibration of the accelerometer and its cable, can give large phase response and hence S.I. measurement errors.

To overcome or minimise some of these problems, a range of non-contact, vibration measurement schemes and transducers have been employed for S.I. measurements. These fall into two broad categories; extrapolation of vibration information from acoustic pressure measurements[14-16], and optical vibration measurement techniques[17-21].

One example of an acoustic, S.I. measurement technique is 'SIMAP', proposed by Williams[14], where acoustic pressure measurements made close to a radiating plate are employed, using near-field acoustic holography, to calculate the normal-to-surface velocity of the plate. From these data, the two-dimensional, structural intensity distribution through the plate can be determined. Practical measurements show the ability of the scheme to accurately determine both where, and how vibration power is injected into the plate. In addition, the acoustic intensity can be calculated from the same set of data, enabling the location of acoustic sources to be revealed. Williams was able to show that vibration and acoustic sources do not necessarily overlap. The principal disadvantage of this scheme is the "heavy computer processing"[14] required to make

each set of measurements, which in conjunction with the microphone scanning system employed, makes the scheme impractical for many engineering environments.

A whole-field, optical measurement scheme proposed by Clark[17] employed double exposure holography to visualise the deformation of a force-excited plate. The first exposure was obtained of the plate undeformed. Interference of light from the deformed plate with the undeformed plate image then produced a fringe pattern, which when viewed gave information on the plate displacement distribution. With a pulsed laser illumination, triggered to be in quadrature with the point driving force, the plate vibration due to travelling wave motion can be viewed, independent of standing waves. Although an excellent power flow visualisation technique, this scheme is primarily laboratory-based since the optics require isolation from wind currents, temperature effects and vibration.

Utilisation of point, laser transducer systems for S.I. measurements has also become widespread[18-21]. Hayek[21] employed a commercial, scanning laser vibrometer system to measure the normal-to-surface velocity of a structure over a predetermined area. Employing a finite difference approximation, both the near and farfield S.I. can then be calculated from these data. The main disadvantage of this scheme is that since the scanning optics and the data acquisition and storage are computer controlled, the scheme is both time-consuming and expensive relative to other laser transducer systems.

Using two laser vibrometers, and allowing for alteration of the transducer optical configuration, McDevitt[20] proposed a scheme which can be employed to make either flexural, or longitudinal wave, power flow measurements. Due to the complex optical configuration of the reported system however, this scheme is at present, restricted to laboratory use.

It can be concluded that the theory of both one, (beam-like structures), and two, (plate-like structures), dimensional, flexural wave, power flow is well-known and understood. Present work in this area is therefore

confined to improvements in measurement and calculation accuracy, and refinement of existing schemes into practical measurement techniques. These will be 'user-friendly' so that they can be employed by vibration engineers in a simple and straightforward manner for a wide range of typical vibration measurements. Future theoretical work will therefore be directed to consideration of other wavetypes and their interaction[22], the effect of discontinuities on incident travelling waves[23], and curved structures and cylinders[24]. The use of active vibration control as a means of minimising power flow thorugh a structure[25] is also likely to receive further investigation.

## 1.2 OBJECTIVES.

The primary objective of this work was to investigate the use of laser vibrometry for power flow measurements, as a means of overcoming the problems associated with utilisation of contacting transducers, and thus improve both the measurement accuracy and ease of use of the technique.

The prime interest of vibration engineers in most practical measurement situations is flexural wave vibration energy transmission. Therefore any laser-based technique will be concerned with the measurement of the normal-to-surface, structural vibration. The beam-like structure is the simpliest system encountered in structural vibration and so the laser transducer schemes proposed in this work will be employed primarily to make one-dimensional, power flow measurements.

In Chapter 2, the theoretical basis and limitations of the power flow measurement scheme is described and a brief history of the development of the technique is given. The governing equations and simplifying assumptions for the practical, power flow measurement scheme are then derived. The major sources of measurement error of the two accelerometer scheme are discussed and suggestions for improvement made. Practical S.I. measurements are then made on a theoretically 'infinite' beam.

There are presently a wide range of reported and commercial laser vibrometer systems[26-30,38,49]. These sytems can be included as a direct substitute for accelerometers, in the two transducer, far-field, S.I. measurement technique. In Chapter 3, two I.S.V.R. laser vibrometers[29], the prototype Bruel and Kjaer 3544 laser vibrometer, are employed to make practical S.I. measurements. To enable low velocity amplitude measurements to be made, a new, piezo-electric element based, high-sensitivity laser vibrometer has been developed[30]. Practical S.I. measurements are then made with two of these transducers.

As first noted by Pavic[11] and shown empirocally in chapters 2 and 3, the major source of practical measurement error in the two-transducer, far-field S.I. scheme is the relative phase response of the two

transducers. Therefore any reduction in the technique sensitivity to this effect will improve the measurement accuracy. In Chapter 4, a new velocity gradient measurement scheme is described which, used in conjunction with a laser vibrometer, offers this improvement. Practical S.I. measurements are then made with this scheme.

When laser light is scattered from an optically rough or diffuse target surface, i.e. most surfaces of engineering interest, a granular light intensity pattern, termed laser speckle, may be seen[31]. In Chapter 5, it is shown how these random intensity patterns are able to introduce spurious, random noise into laser vibrometer output signals. This is shown not only to reduce the vibrometer sensitivity but also, for velocity amplitudes near to the device optical noise floor, to introduce large amplitude, inter-transducer response errors. For practical S.I. measurements, the inter-laser transducer response is critical and so the likely effect of speckle noise must be taken into account. In addition, periodically repeating speckle patterns, associated with periodic, non-normal target motion, e.g. rotation, tilt or in-plane vibration, can introduce pseudo, normal-to-surface vibration signals into the vibrometer output[32,33]. These signals are shown to be easily mistaken for genuine normal-to-surface vibration information and if they occur at the same frequency as the normal-to-surface vibration of interest, large S.I. measurement errors can result.

In Chapter 6, conclusions are given on,
(i) the accuracy of the existing, two accelerometer technique,
(ii) the laser power flow meter configurations proposed in Chapters 3 and 4, and their ability to make practical vibration measurements compared with the existing, two accelerometer techique,
(iii) the relative accuracy and ease of use of the various methods and their ability to quickly make a large number of measurements,
(iv) the significance of random and pseudo-random laser speckle noise effects on laser vibrometer measurements, with particular reference to S.I. measurements.

## 2. POWER FLOW.

Power flow, as a vector quantity representing the net transmitted vibration energy through a structure, is an invaluable measurement tool for the vibration engineer. The power flow measurement technique offers a direct means for obtaining both quantitative and direction information about vibration energy transmission and so enables the noise control engineer to quickly and easily identify the position of vibration sources and the major transmission paths. Vibration control and reduction techniques can then be applied in the most efficient manner.

The most simple form of structure considered in vibration engineering is the uniform, beam-like structure, where wave motion is confined to one direction and can be described in terms of time and a single spatial variable. Of all wave types present in typical structures, flexural wave motion, with its relatively large normal-to-surface displacements, is the most important source of sound radiation into the surronding fluid. Therefore in this chapter, the governing equations for one-dimensional, flexural wave power flow are reviewed and practical measurement implementations and signal processing schemes are discussed. Measurement error sources are described, typical levels calculated and means by which they may be minimised suggested. The results of practical power flow measurements on an infinite beam structure are compared with input power measurements and the accuracy of the two-accelerometer technique discussed.

## 2.1. POWER FLOW THEORY.

The following analysis is limited to pure flexural waves for which rotary inertia and shear deformation can be neglected. For greater than 90% accuracy, this restricts the theory to wavelengths greater than six times the beam thickness[9], e.g. for a 6mm thick bar of mild steel the theory is limited to frequencies of less than 43kHz.

Vibration power is defined as the product of force F(t) and velocity v(t), and its time-average, <P>, is given by,

$$\langle P \rangle = \frac{1}{T} \int_0^T F(t)v(t)dt \qquad (2.1)$$

where T is the integration time. The time-averaged, rather than the instantaneous power flow is calculated since the objective is to measure the average, or net vibration energy transmission.

Cremer[9] showed that for flexural wave motion, there exists power transmission mechanisms due to both the shear force and bending moment in a structure. The shear force Q, and bending momemt M in a beam are given by,

$$M(x,t) = -EI \frac{\delta^2 w}{\delta x^2} \qquad (2.2)$$

$$Q(x,t) = -\frac{\delta M}{\delta x} = EI \frac{\delta^3 w}{\delta x^3} \qquad (2.3)$$

where EI is the flexural rigidity of the beam, w is the normal-to-surface displacement and x is the axis parallel to the beam surface. The instantaneous power at a point P(x,t), consists of two components,

(i) the product of the bending moment and angular velocity,

(ii) the product of the shear force and linear velocity, i.e.,

$$P(x,t) = M \frac{\delta^2 w}{\delta x \delta t} + Q \frac{\delta w}{\delta t} \qquad (2.4)$$

From equations (2.2) to (2.4), the vibration power transmitted through a one-dimensional structure is given by,

$$P(x,t) = EI \left[ - \frac{\delta^2 w}{\delta x^2} \frac{\delta^2 w}{\delta x \delta t} + \frac{\delta^3 w}{\delta x^3} \frac{\delta w}{\delta t} \right] \qquad (2.5)$$

In contrast to the second order expressions for longitudinal and torsional wave power flow[9], equation (2.5) illustrates that flexural wave power flow has a fourth order differential equation and is potentially more difficult to accurately measure. As will be shown however, employing a number of assumptions and for specific measurement conditions, this expression can be greatly simplified and a practical, two-transducer scheme employed to make flexural-wave, power flow measurements.

## 2.2 SINGLE POINT DISPLACEMENT MEASUREMENTS OF POWER FLOW.

In the far-field of a structure, i.e. far from vibration sources, sinks and discontinuities such as changes in material or cross-section, the normal-to-surface beam displacement $w(x,t)$ is given by,

$$w(x,t) = A\sin(\omega t - kx) + B\sin\omega t\sin kx \qquad (2.6)$$

where A and B are the peak travelling and standing wave displacement amplitudes respectively, $\omega$ is the radian frequency and k is the flexural wavenumber. Substituting equation (2.6) into (2.5), the shear force $P_{SF}$ and bending moment $P_{BM}$ power flow components can be considered separately,

$$P_{BM}(x,t) = \omega k^3\Big[ A^2\sin^2(\omega t-kx) + AB\sin^2(\omega t-kx) - \frac{B^2}{8}\{\cos 2(\omega t-kx) - \cos 2(\omega t+kx)\}\Big] \qquad (2.7)$$

$$P_{SF}(x,t) = \omega k^3\Big[ A^2\cos^2(\omega t-kx) + AB\cos^2(\omega t-kx) + \frac{B^2}{8}\{\cos 2(\omega t-kx) - \cos 2(\omega t+kx)\}\Big] \qquad (2.8)$$

These expressions show that in the absence of standing waves, i.e. B = 0, $P_{SF}$ and $P_{BM}$ are 180 degrees out of phase and have a sum equal to the constant $\omega k^3A^2$. Hence in contrast to other wave forms, the average power flow can be measured without the time-averaging operation given in equation (2.1) being required, i.e. in this particular condition, a single displacement measurement can be employed to calculate the average power transmission.

In most practical situations, structural discontinuities reflect a proportion of the incident travelling wave, producing a standing wave pattern and the relative amplitudes of each wavetype will be unknown. The one transducer scheme will therefore no longer be sufficient to measure the net vibration energy transmission and the time-averaging operation must be employed.

As first noted by Noiseux[8], the time-averaged shear force, $\langle P_{S.F.} \rangle$, and bending moment, $\langle P_{B.M.} \rangle$, power flow components are equal, i.e.

$$\langle P_{SF}(x,t) \rangle = \langle P_{BM}(x.t) \rangle = \frac{1}{2} \langle P(x,t) \rangle \qquad (2.9)$$

In the vibration far-field therefore, (see section 2.3.3), only one power flow component need be measured, significantly reducing both the number of transducers and the signal processing required. A majority of researchers[8,10,34] employ accelerometers, with their wide dynamic range and vibration frequency range, to measure the shear force component of power flow. The following analysis will therefore consider this implementation.

## 2.3 PRACTICAL POWER FLOW MEASUREMENT SCHEMES.

Employing acceleration signals, substitution of equations (2.5) and (2.6) into (2.9) results in a time-averaged power flow given by,

$$\langle P(x_0) \rangle = 2EI \frac{k^2}{\omega^2} \left\langle \frac{\delta a}{\delta x} \int a \, dt \right\rangle \qquad (2.10)$$

where $\omega$ is the frequency of interest and a is the normal-to-surface acceleration, equal to $-\omega^2 w$. The spatial acceleration derivative $\delta a/\delta x$, in equation (2.10) can be measured with a range of contacting transducers, including a biaxial accelerometer[8], a differencing accelerometer[10] or two linear accelerometers[11]. These transducer configurations are shown in figure 2.1.

Redman-White[10] showed that for practical measurements biaxial accelerometers were too sensitive to other wave motion in the structure while differencing accelerometers were too sensitive to resonances in the mount. He concluded that for most practical measurement situations, the two linear accelerometer scheme first proposed by Pavic[11] was the most accurate. This scheme is the most widely employed configuration and the one that will be considered further.

The two linear accelerometer scheme employs the finite difference approximation to measure the spatial gradient. The two accelerometer signals $a_1$ and $a_2$, of normal-to-surface vibration, are obtained from positions a distance 2h apart, where 2h is less than the flexural wavelength. The spatial derivative at the mid-point position $x_0$, is then given by,

$$\frac{\delta a}{\delta x} \approx \frac{1}{2h} ( a_2 - a_1 ) \qquad (2.11)$$

Similarly,

$$a \approx \frac{1}{2} ( a_1 + a_2 ) \qquad (2.12)$$

From simple bending theory,

$$k^4 = \frac{\omega^2 M_B}{EI} \tag{2.13}$$

where $M_B$ is the mass per unit length of the beam. The time-averaged power flow may now be written in terms of linear acceleration signals as,

$$\langle P(x_0) \rangle \approx \frac{(M_B EI)^{1/2}}{2h\omega} \left\langle \left[ (a_2 - a_1) \int (a_2 + a_1)\, dt \right] \right\rangle \tag{2.14}$$

Assuming negligible damping, then from equation (2.6) the acceleration signals may be represented by,

$$a_1 = -\omega^2 [A\sin(\omega t - k(x-h)) + B\sin\omega t \sin k(x-h)] \tag{2.15}$$

$$a_2 = -\omega^2 [A\sin(\omega t - k(x+h)) + B\sin\omega t \sin k(x+h)] \tag{2.16}$$

Substitution into equation (2.14) gives a measured power flow expression of,

$$\langle P(x_0) \rangle \approx \frac{A^2 \omega \Pi}{h} (M_B EI)^{1/2} \sin 2kh \tag{2.17}$$

Ideal acceleration and acceleration spatial gradient measurements given by,

$$a = -\omega^2 [A\sin(\omega t - kx_0) + B\sin\omega t \sin kx_0] \tag{2.18}$$

and,

$$\frac{\delta a}{\delta x} = \omega^2 k \left[ A\cos(\omega t - kx_0) - B\sin\omega t \sin kx_0 \right] \tag{2.19}$$

can be substituted into equation (2.10) to give a structural intensity $\langle P(x_0) \rangle_E$ of,

$$\langle P(x_0)\rangle_E = 2A^2\omega k\pi(M_B EI)^{1/2} \qquad (2.20)$$

This expression does not include any finite difference approximations and the measurement accuracy will therefore be limited only by the transducer accuracy. Comparison of equations (2.17) and (2.20) shows that the finite difference approximation method underestimates the spatial derivative, but that an exact correction can be applied,

$$\langle P(x_0)\rangle_E = P_{MEASURED}\,\frac{2kh}{\sin 2kh} \qquad (2.21)$$

Hence provided both the flexural wavenumber and transducer separation are accurately known, the exact power flow can be calculated from the approximate, measured power flow.

The two sets of acceleration signals in equation (2.14) can be processed in either the time or the frequency domain. The relative merits of each scheme are discussed in the following sections.

As can be seen from equation (2.14), employing this measurement scheme the power flow at a point is measured, which must then by weighted by the beam dimensions to calculate the total vibration energy transmission. Hence the term structural intensity, (power flow per unit area), rather than power flow, is commonly used to describe the technique.

## 2.3.1 TIME DOMAIN REALISATION.

In the time domain, the time integral of the acceleration signal is calculated employing the relationship,

$$\int a\,dt = \frac{1}{j\omega}\,a = \frac{1}{\omega}\,a_{(q)} \qquad (2.22)$$

where (q) denotes the quadrature operation equivalent to a $90^0$ phase shift. For analogue-electronic structural intensity measurements, Redman-White showed that obtaining an exact $90^0$ phase shift was one of

the major measurement error sources[10]. However most modern, digital signal processing based schemes employ an exact $-j/\omega$ multiplication and signal integration is no longer an error source. Substituting equation (2.22) into equation (2.14),

$$\langle P(x_0) \rangle = \frac{(M_B EI)^{1/2}}{2h\omega^2} \left\langle \left[ (a_2 - a_1)(a_{2(q)} + a_{1(q)}) \right] \right\rangle \qquad (2.23)$$

For an exact quadrature phase shift, this expression may be further simplified to,

$$\langle P(x_0) \rangle = \frac{(M_B EI)^{1/2}}{h\omega^2} \left\langle \left[ (a_2 a_{1(q)}) \right] \right\rangle \qquad (2.24)$$

since $\langle a_2 a_{2(q)} \rangle = \langle a_1 a_{1(q)} \rangle = 0$, $\langle a_2 a_{1(q)} \rangle = -\langle a_1 a_{2(q)} \rangle$. Comparison of equations (2.24) and (2.5) illustrates how provided (i) there is accurate signal integration, and (ii) measurements are made in the far-field, a simple, practical, two linear transducer measurement scheme exists for calculating the one-dimensional, flexural wave, power flow.

Equation (2.24) is the single frequency power flow expression and hence for digital systems, requires that the time signal be Fourier transformed into the frquency domain to be filtered. This signal is then inverse Fourier transformed back into the time domain to produce a single frequency signal. Although for most digital systems these operations are both simple and accurate, it is more straightforward to calculate the frequency domain implementation discussed in section 2.3.2, for which a single Fourier transform operation for measurements over the entire frequency range is required.

### 2.3.2 FREQUENCY DOMAIN REALISATION.

Cross spectral analysis provides an alternative, frequency domain means of obtaining the acceleration signal integral given in equation (2.24). The broadband cross spectrum of the time-average product of two signals can be written[34],

$$\langle a_1(t) \int a_2(\tau)d\tau \rangle = \int_0^{\infty} \frac{\text{Im } G(a_1,a_2,f)}{2\pi f} \, df \qquad (2.25)$$

where Im G is the imaginary component of the one-sided cross spectral density and $\tau$ is time. The structural intensity at frequency $\omega$ can therefore be written,

$$\langle P(x_0,\omega) \rangle = \frac{(M_B EI)^{1/2}}{2h\omega^2} \text{ Im } G(a_1,a_2,\omega) \qquad (2.26)$$

The main advantage of the frequency domain scheme is that it requires no special development of signal processing, the cross-spectrum of two signals being a standard feature of most signal processing software. Also, as will be shown in section 2.4, inter-transducer response errors can be minimised by employing frequency domain signal analysis.

The main disadvantages of the cross-spectrum method include it being unable to deal with transients once their duration exceeds the single FFT capability of the processor, and as the processor only receives time-limited, sampled data, even for stationary signals the readings will always be an estimate of the true results.

### 2.3.3 VIBRATION NEAR-FIELDS.

The near-field of a vibrating structure is defined as the region in which non-propagating, exponentially decaying displacements $w_{NF}(x,t)$ occur[9], about a discontinuity situated at x=0, where,

$$w_{NF}(x,t) = Ce^{\pm kx}e^{j\omega t} \qquad (2.27)$$

where C is the near-field displacement amplitude. For kx = 4.6, i.e. x = 0.732$\lambda$ where $\lambda$ is the flexural wavelength, the amplitude of the near-field wave has decayed to 0.01 times its inital maximum value at x = 0, e.g. a vibration source, sink or structural discontiuity. Hence the preceding, far-field analysis can be applied for measurements made more than $3\lambda/4$ from a discontinuity.

## 2.4 TRANSDUCER ERRORS.

As noted in the previous sections, provided care is taken in the choice of measurement position and accurate signal processing schemes are employed, accurate structural intensity measurements are possible. The next major cause of practical, structural intensity measurement errors are the transducers employed to measure the normal-to-suface, or flexural wave vibration. The following transducer errors are common to most transducers and so accelerometers, currently the most commonly employed means of measurement, will be used as an example.

### 2.4.1 TRANSDUCER INTERNAL RESONANCE EFFECTS.

Accelerometers are a typical form of seismic transducer, incorporating a piezo-electric crystal that is loaded by a mass-spring system. Structural vibration causes the mass-spring system to vibrate which in turn induces an electric charge from the crystal. Inherent in this form of transducer, however, is the presence of the mass-spring resonance frequency. A typical accelerometer frequency response function is shown in figure 2.2, for varing internal, mass-spring damping coefficients. As this figure shows, as the vibration frequency of interest appoaches this resonance frequency, both the accelerometer amplitude and phase response change, i.e. the accelerometer frequency response becomes non-linear at higher frequencies.

From figure 2.2, the amplitude response can be considered constant, i.e. ±1 dB, up to approximately one third of the accelerometer natural frequency. This limits use of a general purpose accelerometer, with damping coefficient of less than 0.05[35], to 10 kHz. As will be shown in section 2.4.4 however, the accelerometer phase response is the principal limitation on the S.I. measurement technique accuracy. As figure 2.2 shows, the transducer phase response varies significantly close to the resonance frequency. Therefore using a general purpose accelerometer, accurate S.I. measurements requiring a variation in transducer phase response of less than $1^{o}$, are limited to below approximately 0.06 times the resonance frequency, i.e. 1.8 kHz.

For practical measurements, these response characteristics will not only vary between nominally identical transducers, but also, close to the resonance frequency, will become sensitive to temperature and vibration amplitude, and vary with time. Therefore the transducer resonance effect severly limits the frequency range for which accelerometers may be used for accurate S.I. measurements.

It should be noted that acceleroemters also have a transverse resonance frequency, which is usually lower in frequency than the normal-to-surface resonance. Although the accelerometer transverse sensitivity is typically less than 3%[35], the increase in transducer transverse sensitivty close to the transverse resonance may still introduce erroneous measurement errors.

## 2.4.2 EFFECT OF CONTACTING TRANSDUCERS.

The addition of a contacting transducer, such as an accelerometer or strain gauge, will adversely affect the accuracy of the measurement through modification of the vibration characteristics. This effect can be modelled as the addition to the structure of a mass discontinuity with impedance $Z_M$ of,

$$Z_M = j\omega M \tag{2.28}$$

where M is the transducer mass. An infinite beam excited by a point force, (the subject of practical measurements in section 2.5), has a theoretical impedance $Z_{IB}$ of[4],

$$Z_{IB} = 2S\rho\omega^{1/2}\left[\frac{EI}{\rho S}\right]^{1/4}(1 + j) \tag{2.29}$$

The ratio of the beam velocity response with and without the attached transducer $H(\omega)$, can be measured from the ratio of the impedances, i.e.

$$H(\omega) = \frac{v'}{v} = \frac{Z_{IB}}{Z_{IB} + Z_M} = \left[1 + \frac{Z_M}{Z_{IB}}\right]^{-1} \tag{2.30}$$

where v' and v are the input point beam velocity with and without the transducer attached respectively. Figure 2.3 shows the variation of $H(\omega)$ with $\omega$ for a range of transducer masses and the beam employed in section 2.5. This figure shows that for a given transducer, both the amplitude and phase measurement errors increase with increasing vibration frequency, and that larger measurement errors result from the use of heavier transducers. The main disadvantage of utilising very light accelerometers however is that larger transducers have higher sensitivity. For accurate structural intensity measurements, the mass-loading effect of a contacting transducer must therefore be considered to be a significant source of measurement error. The scale of this measurement error on the structural intensity is investigated in section 2.4.4.

### 2.4.3 CROSS-SENSITIVITY TO OTHER WAVETYPES.

When making flexural-wave, structural intensity measurements, it is important to take into account any sensitivity of the technique to other wavetypes. This cross-sensitivity has two principal causes:
(i) the accelerometer has an inherent sensitivity to in-plane or longitudinal wave motion, although typically only 2 to 5%,
(ii) the Poisson ratio effect, which, for example, for an unconstrained mild steel bar with a peak, in-plane displacement amplitude of 1 unit, will produce a peak, normal-to-surface displacement of 0.3 units.

In most practical situations the relative flexural and longitudinal wave amplitudes will be unknown and so accurate, independent flexural wave, structural intensity measurements are not possible with the two-transducer scheme. Employing the four accelerometer configuration shown in figure 2.4, this problem may be overcome. Based on acceleration signals from the two sides of the beam being 180 degrees out of phase, and in-phase, for flexural and longitudinal wave motion respectively, from equation (2.24) the flexural wave structural intensity is given by,

$$\langle P(x_0,\omega)\rangle \approx \frac{(M_B EI)^{1/2}}{2h\omega^2}\langle (a_1 - a_3)(a_{2(q)} - a_{4(q)})\rangle \qquad (2.31)$$

while the longitudinal wave structural intensity given by[9],

$$\langle P(x_0,\omega)\rangle = -ES \left\langle \frac{\delta u}{\delta x} \frac{\delta u}{\delta t} \right\rangle \qquad (2.32)$$

where u is the longitudinal displacement. Employing the four accelerometer scheme, this expression may be rewritten as,

$$\langle P(x_0,\omega)\rangle \approx \frac{ES}{8\upsilon^2\omega^3 h} \langle (a_1 + a_3)(a_{2(q)} + a_{4(q)})\rangle \qquad (2.33)$$

where $\upsilon$ is Poisson's ratio. With this scheme, the flexural and longitudinal wave, structural intensities can be measured simultaneously, over the frequency range of interest. However, to maximise the signal-to-noise ratio of the two sets of acceleration signals, the maximum difference in acceleration signal and hence value of the ratio transducer separation/wavelength must be employed. The upper limit on the transducer separation is determined by the finite difference approximation error however, and for the preceding theory to be applicable, the transducers must be less than a flexural wavelength apart. The transducer separation is therefore a compromise between these two sets of constraints.

The longitudinal wavelength $\lambda_L$, equal to $(E/\rho)^{1/2}$, can be related to the flexural wavelength $\lambda_F$ given in equation (2.13), by the expression,

$$\lambda_L = \lambda_F \frac{0.551}{d} \qquad (2.34)$$

where d is the beam thickness. Since d is typically only a few centimetres, $\lambda_L >> \lambda_F$, the optimum accelerometer separation for longitudinal wave measurements will be much larger than for flexural wave measurements. Therefore in practice, accurate, simultaneous longitudinal and flexural wave power flow measurements are not possible.

In many situations, this measurement scheme will be impractical, due to either access limitations or the inability to accurately position the

accelerometer pairs either side of the beam. Therefore the implications of the cross-sensitivity effect on the two transducer scheme must be considered instead. As noted in section 2, flexural wave vibration amplitudes are usually greater than for other wavetypes and so the effect of longitudinal wave motion can often be neglected. However when the in-plane displacement amplitude is significant, although not producing genuine flexural wave motion, it will contribute to the normal-to-surface vibration of interest. Hence when evaluating the major 'flexural'-wave vibration transmission paths in a complex, built-up structure, the Poisson ratio effect should be included in the measurement.

## 2.4.4 INTER-TRANSDUCER FREQUENCY RESPONSE ERRORS.

Introducing transducer amplitude and phase measurement errors of $\psi$ and $\varepsilon$ respectively into equations (2.15) and (2.16) gives,

$$a_1 = -\omega^2(1+\psi_1)\left[A\sin(\omega t-k(x_0-h)+\varepsilon_1) + B\sin(\omega t+\varepsilon_1)\sin k(x_0-h)\right] \qquad (2.35)$$

$$a_2 = -\omega^2(1+\psi_2)\left[A\sin(\omega t-k(x_0+h)+\varepsilon_2) + B\sin(\omega t+\varepsilon_2)\sin k(x_0+h)\right] \qquad (2.36)$$

This produces an expression for the structural intensity including error terms $\langle P(x_0)\rangle_{ME}$ of,

$$\langle P(x_0)\rangle_{ME} \approx (M_B EI)^{1/2}\frac{\pi\omega}{h}(1+\psi_1)(1+\psi_2)\left[A^2\sin(2kh+\varepsilon_1-\varepsilon_2)\right.$$
$$\left. + AB\sin 2kx_0\sin(\varepsilon_1-\varepsilon_2) + B^2\sin k(x_0+h)\sin k(x_0-h)\sin(\varepsilon_1-\varepsilon_2)\right] \qquad (2.37)$$

Equation (2.37) shows that a 1% error in the transducer amplitude response will produce a 1% error in the measured structural intensity. Of greater significance however is that the inter-transducer phase error term $(\varepsilon_1-\varepsilon_2)$, introduces standing wave effects into the measured structural intensity. The scale of the phase error can be considered by taking the ratio of the 'error' power flow $\langle P(x_0)\rangle_{ME}$ and the zero error

structural intensity of equation (2.17), $\langle P(x_0)\rangle$,

$$\frac{\langle P(x_0)\rangle_{ME}}{\langle P(x_0)\rangle} = \frac{1}{\sin(2kh)}\left[\sin(2kh+\varepsilon_1-\varepsilon_2) + \sin(\varepsilon_1-\varepsilon_2)\left[\frac{B}{A}\right]\sin 2kx_0 + \sin(\varepsilon_1-\varepsilon_2)\left[\frac{B}{A}\right]^2 \sin k(x_0+h)\sin k(x_0-h)\right] \quad (2.38)$$

Figures 2.5 and 2.6 show how this ratio varies with 2kh, (the non-dimensional ratio of the transducer separation and the flexural wavelength), for different values of the phase error term $(\varepsilon_1-\varepsilon_2)$. In figure 2.5, measurement errors for a theoretically infinite beam are quantified and show how,

(i) positive and negative values of the phase error term produce over- and underestimates of the structural intensity respectively,

(ii) for large phase errors, *negative* under and over estimates of the structural intensity are possible, a negative ratio implying that the wrong sign and hence direction of structural intensity will be measured,

(iii) structural intensity measurement errors can be minimised by employing as large a value of 2kh as possible. For example, for the infinite beam described in section 2.5, 2kh = 1.57 equates to a transducer separation of 4.3 cm at 500 Hz and 8.62 cm at 2 kHz.

Figures 2.6a and 2.6b illustrate the effect of standing waves on the structural intensity measurement error, i.e. measurements on a non-infinite structure. These figures clearly show that even with a relatively small inter-transducer phase response error, e.g. $2^0$, extremely large measurement errors can arise in reverberant vibration environments. However as with figure 2.5, the measurement error can be minimised by employing a large transducer separation.

From equation (2.38) it can be seen that it is the relative transducer phase response $(\varepsilon_1-\varepsilon_2)$, and not the absolute phase values relative to a calibration signal that are significant. Hence if both transducers have an absolute $+5^0$ phase response error, there is no error in the measured structural intensity. For accurate structural intensity measurements therefore, the two transducers must be closely phase-matched. Should

this not be possible, frequency domain compensation methods do exist.

Chung[36] showed that in the frequency domain, any difference in inter-transducer response characteristics can be cancelled out by employing the inter-transducer frequency response function $H_{12}$, measured by exposing the transducers to the same vibration field. The corrected, cross-spectrum term $G_{12}'$ can then be substituted into equation (2.26),

$$G_{12}' = \frac{G_{12}}{H_{12}|H_1|^2} \qquad (2.39)$$

where $H_1$ is the first transducer gain factor. The main disadvantage of this scheme is that it assumes that the inter-transducer response does not change with time, amplitude or temperature, see, for example, section 2.4.1. To overcome any such variation problem, $H_{12}$ and $H_1$ must be measured at regular intervals.

An alternative method is to take two sets of measurements, the second set with the transducer positions reversed with respect to the first, as is done in the sound intensity technique[36]. The corrected cross-spectrum term then becomes,

$$G_{12}' = \frac{(G_{12}G_{12}^S)^{1/2}}{|H_1||H_2|} \qquad (2.40)$$

where $G_{12}^S$ is the second measurement cross-spectrum. The main disadvantage of this scheme is that calculation of the square root of a complex variable is difficult and time-consuming. However this scheme has the advantage that it is straight forward to measure both $H_1$ and $H_2$ over a wide frequency range.

Taking all these factors into account, the most simple and accurate measurement scheme is to employ two transducers that are closely matched in both amplitude and phase response, and for practical structural intensity measurements are positioned with separation of at least $\lambda/8$. Should this not be possible, only then are inter-transducer response compensation methods required.

## 2.5 PRACTICAL, TWO-ACCELEROMETER STRUCTURAL INTENSITY MEASURMENTS.

Practical structural intensity measurements were made employing the structure shown in figure 2.7. The 6.21 m long mild steel beam, of average cross-section 6.38 mm by 50.5 mm, was supported by vertically hanging steel wires, with a spacing of approximately 1 m. Both ends were terminated in foam wedges, placed in turn in sand boxes to provide anechoic end-conditions. The beam was driven by a coil-and-magnet shaker at its mid-point, on the beam vertical neutral axis to ensure that no longitudinal or torsional wave motion was produced. Approximately 4.3m of the beam length was outside the sandboxes. A force transducer positioned between the shaker and the beam was used to measure force excitation levels. An accelerometer mounted on the opposite side of the beam from the shaker attachment was employed to measure the beam response at the force input point.

Figure 2.8 shows the magnitude and phase of the beam accelerance $In(\omega)$, (acceleration response divided by the input force), measured employing a 'chirp' or swept-sine excitation of 1 $Watt_{RMS}$ (shaker power). The acceleration of an infinite beam at the force, F, input point is given by[4],

$$a(x_0,t) = \frac{\omega^2 F}{4EIk^3} e^{j\omega t(1+j)} \qquad (2.41)$$

The beam therefore has an input point accelerance of,

$$In(\omega) = \frac{\omega^2}{4EIk^3} (1+j) \qquad (2.42)$$

The theoretical accelerance is shown as a straight line superimposed on figure 2.8. As this figure shows, at low frequencies the beam has many resonance frequencies. However at higher frequencies, i.e. above 250 Hz, both the magnitude and phase of the measured beam accelerance tends towards that of the theoretical infinite beam.

Figure 2.9 shows the real and imaginary components of the measured beam

accelerance. From this figure it can be seen that above approximately 2.3 kHz, the measured data deviates from infinite beam characteristics. This is due to two effects;

(i) the dimensions of the force transducer in contact with the beam begin to become comparable with the flexural wavelength, so that the excitation source can no longer be considered as a point force,

(ii) the combined mass of the force transducer and accelerometer of approximately 18 grams was sufficient to affect the response of the beam.

The difference in beam accelerance characteristics between figures 2.8 and 2.9 is due to the difference in scale, i.e. variations in the beam accelerance from "infinite" beam characteristics are greater if due to resonance effects, than if due to the use of contacting transducers. However, as noted in section 2.3, unlike contacting transducer use (section 2.4.2), beam resonance effects do not affect the structural intensity amplitude.

Combining equations (2.42) and (2.30), at 3.7 kHz the true beam accelerance for a total force transducer and accelerometer mass of 18 grams is given by,

$$In'(\omega) = \frac{\omega^2}{4EIk^3} (0.987 + j0.839)) \qquad (2.42a)$$

Comparison of equations (2.42) and (2.42a) shows that for the combined transducer mass of 18 gram, the real part of the accelerance will not be significantly affected, but that the imaginary component will be reduced by a factor of 0.839. These predicted reductions compare favourably with the measured accelerance data shown in figure 2.9. Rather than have to compensate for the transducer mass effect at higher frequencies, it was decided that the infinite beam experiments would be restricted to frequencies of less than 2.3 kHz.

Point accelerance measurements were repeated for shaker electrical excitation levels of 10 Watts (1 Amp r.m.s.) and 0.1 Watts (0.1 Amp r.m.s.). The beam accelerance did not vary from that shown in figure 2.8 and it was concluded that for the range of excitation levels

employed in the following measurements, the beam response was linear and independent of excitation level.

## 2.5.1 INPUT POWER MEASUREMENTS.

The vibration power into a beam $P_{IN}$, is calculated from equation (2.1), which for a sinusoidal input force $F(t)=F\sin\omega t$, and resulting velocity $v(t)=V\sin(\omega t+\theta)$ gives,

$$P_{IN} = F(t)v(t) = FV\cos\theta \qquad (2.43)$$

or in the frequency domain,

$$P_{IN}(\omega) = \frac{1}{2}\,\mathrm{Re}[G(F,v,\omega)] \qquad (2.43a)$$

For ease of implementation and a minimum of signal analysis, the expression given in equation (2.43a) is usually employed.

## 2.5.2 MEASUREMENT OF INTER-TRANSDUCER RESPONSE CHARACTERISTICS.

The relative response characteristics of three accelerometers were measured by mounting each of them on a shaker, excited by a random excitation of 10 volts, 1 Amp r.m.s., over the frequency range 0 to 3.2 kHz. The frequency response function of each accelerometer pair was measured and averaged over ten samples. The best match is shown in figure 2.10. The resonance type effect between 320 and 700 Hz was found to be due to a 'rocking' resonance mode of the shaker and was minimised by placing the accelerometers on the shaker centreline. Charge amplifiers, as analogue electronic devices, offer an additional source of inter-transducer response error and for these measurements, each accelerometer-charge amplifier pair was maintained.

From figure 2.10, the amplitude and phase response erors over the measured frequency range vary between +0%, -2.5% and $+0.8^0$, $-0.6^0$ respectively. These measurements were repeated for shaker electrical excitation levels of 0.1 and 1.75 Amps r.m.s., but the inter-transducer

amplitude and phase response characteristics were found not to vary significantly.

### 2.5.3 BEAM EXCITATION SIGNAL.

For practical measurements, it was found necessary to employ a 'chirp', or swept sine excitation of the form shown in figure 2.11. The chirp signal was employed because,

(i) employing broadband random noise a maximum input power level of typically only 10 nW at a given frequency was possible without exceeding the shaker current drive limit,

(ii) the analysis of narrow band excitation signals over a wide frequency range would be time-consuming.

Hence the chirp excitation offered the best compromise between measurement speed and input power amplitude.

The chirp excitation was digitally produced with the variables of frequency range, number of data blocks and hence duration, and signal amplitude. Although this signal contained approximately equal excitation levels per 1 Hz bandwith, the shaker frequency response function weighted the input to give the typical force excitation shown in figure 2.12. Also as shown in this figure, the input point acceleration response was frequency dependent and so structural intensity measurements are required at a number of frequencies to properly validate this technique.

### 2.5.4 COMPARISON OF INPUT AND TRANSMITTED POWER MEASUREMENTS.

Three sets of stuctural intensity data were obtained employing an electrical input power of 1.8 $Watt_{rms}$ chirp excitation over the frequency ranges 450-550 Hz, 950-1050 Hz and 1450-1550 Hz. From section 2.3.3, for these frequencies the far-field was calculated as existing at distances greater than 24.4 cm from the vibration source. A transducer separation of 5 cm, equivalent to between $0.3\lambda$ and $0.15\lambda$ over the measured frequency range, was employed. For this separation, the inter-transducer response errors measured in section 2.5.2 correspond to

worst case (simultaneous maximum amplitude and phase error), structural intensity measurement errors of approximately ±3.5%. The transducer positions were as shown in figure 2.7. The input power and structural intensity measurements were calculated employing the maths functions software available on the computer acquisition system. These functions, based on implementing equations (2.43a) and (2.26) respectively, are shown in appendix 8.1. The power measurements are shown in figures 2.13 to 2.18 respectively.

These figures show that the spectra of input power were affected by,
(i) as previously discussed, the shaker frequency response function weighting the excitation such that the input force amplitude was not constant with frequency,
(ii) the uniform, rectangular time window inherent in the excitation signal which resulted in a 'sinc' function weighting of the excitation spectrum.
As can be seen from the transmitted power measurements in figures 2.14, 2.16 and 2.18 however, the structural intensity has similar frequency content to the excitation and hence these factors did not adversely affect the beam response characteristics.

Under ideal, infinite conditions the structural intensity to the left and right of the excitation point would be equal to half the input power. However as shown in figures 2.14, 2.16 and 2.18, the distribution of vibration energy transmitted to the left and right sides of the beam is not equal. This is due to physical differences between the two beam halves and end conditions producing different beam characteristics in each direction.

Due to the variation over the excitation frequency range of the input and transmitted power, it is unrealistic to compare frequency-averaged power levels. Instead powers at discrete frequencies are compared in figure 2.19. This figure clearly shows that after the finite difference approximation correction has been applied, the total, transmitted power amplitudes compare very well with the input power amplitudes, with a maximum difference of 6.4%. The most likely causes of measurement error

include the accelerometer amplitude and phase response at frequencies approaching the transducer resonance frequency, (section 2.4.1), mass-loading of the structure (section 2.4.2), inter-transducer response errors (section 2.4.4) and resonance behaviour of the beam.

## 2.6 CONCLUSIONS ON THE STRUCTRAL INTENSITY MEASUREMENT TECHNIQUE.

The one-dimensional, flexural-wave structural intensity measurement technique has been reviewed and expressions for far-field measurements developed. For infinite beam conditions, it has been shown theoretically how a single transducer measurement is sufficient to measure the average vibration energy transmission. However for practical structures, the presence of standing waves make this scheme inaccurate. Instead a two transducer scheme employing, for example, acceleration signals, must be utilised. The structural intensity is then proportional to the time-averaged product of the time integral of average acceleration and the acceleration difference.

Signal processing schemes in the time and frequency domains have been discussed. In the frequency domain implementation, it has been shown how the structural intensity is proportional to the imaginary component of the cross-spectrum of the two accelerometer signals. Since modern, commercially available digital signal acquisition and processing systems offer the cross-spectrum between two signals as a standard operation, this implementation is recommended.

Transducer response errors have been investigated and typical structural intensity errors resulting from these errors calculated. These results show that significant measurement errors can arise for typical inter-transducer response errors, both for infinite structures and structures in which standing waves are present. Theoretical results show that inter-transducer phase response errors are more significant than amplitude errors, with errors of more than a few degrees leading not only to under or over estimates of the structural intensity, but in the worst case, giving the wrong direction of energy transmission. Phase response error effects can be minimised however;

(i) for small inter-transducer errors, an error of less than ±5% results from using a transducer separation of at least $0.05\lambda$,

(ii) for larger inter-transducer errors by employing a frequency domain correction, based on inclusion of the predetermined response error correction in the structural intensity calculation.

It has been shown how a beam structural response may be modified in both amplitude and phase when utilising contacting transducers, such as accelerometers, and that this effect increases with increasing frequency. In addition, accelerometer amplitude and phase response errors can result at vibration frequencies approaching the transducer resonance frequency. These errors vary with temperature, vibration amplitude and time and therefore can introduce large measurement errors.

Employment of non-contacting, non-seismic transducers, such as Laser Vibrometers, offers a simple solution to both these problems, as well as reducing the measurement time and increasing the range of structures upon which measurements may be made.

Practical, two-accelerometer structural intensity measurements have been made on a point force excited, mild steel beam. Point accelerance measurements showed the beam to have infinite structure characteristics over the frequency range 250 Hz to 2.3 kHz. Practical measurements were made over the frequency ranges 450-550 Hz, 950-1050 Hz and 1450-1550 Hz, employing a 100 Hz bandwidth 'chirp', or swept-sine excitation. For all three sets of measurements, good agreement was obtained between the input power and the total power transmitted through the beam. This proves the accuracy and value of this technique as a means for measuring both the magnitude and direction of transmitted, flexural wave, vibration energy.

## 3. LASER VIBROMETER MEASUREMENTS OF STRUCTURAL INTENSITY.

In recent years, employment of Laser Technology, and in particular Laser Doppler Velocimetry (LDV)[37], as a measurement tool for the vibration engineer has become widespread. Allied with their ability to make remote, non-contact measurements of vibrating surfaces, laser vibrometers can be employed in a range of vibration measurement environments for which contacting transducers, such as accelerometers, cannot. Typical examples include light structures where contacting transducers mass-load the structure, hot surfaces where contacting transducers are likely to be destroyed should they be attached, and rotating surfaces where transfer of the vibration signal from a structure to the analysis/recording system is complex.

Application of LDV to this problem has produced a range of laser vibrometers[27,28,29,38] a number of which are now commercially available. Laser vibrometer operation relies on detection of the Doppler frequency shift in laser light scattered from a target surface. When mixed with a reference beam on the vibrometer photodetector surface, a time-resolved output, proportional to the modulus of the target surface velocity vector, then results. Both the velocity amplitude and phase are required and thus the direction ambiguity problem, inherent in this form of Doppler detection, must be overcome. This is achieved by frequency shifting the reference beam, thus providing a carrier frequency which is subsequently modulated by any target surface motion[37]. Commercial systems differ primarily in the frequency shifting mechanism they employ, e.g. Bragg cells[28], rotating diffraction gratings[27], rotating scattering discs[29] and rotating retroreflectors[38], leading to a range of laser vibrometers varying in expense, robustness, bulk, ease of use and portability.

This chapter reviews the employment of an existing laser Doppler vibrometer[29] to measure one-dimensional, flexural-wave structural intensity (S.I.). The results of these measurements are analysed, and it is shown how the device sensitivity is not sufficient for S.I. measurements where vibration velocity amplitudes of less than

approximately 0.1 mm/s are produced. For many practical structures, normal-to-surface velocity amplitudes of less than $10^{-4}$ m/s at one point in a structure can still result in large amplitude noise radiation elsewhere. To overcome this problem, a new design of laser transducer, the PZT laser vibrometer, has been developed[30], allowing high-sensitivity, non-contact measurement of normal-to-surface target motion. Comparative vibration measurements with an accelerometer mounted on a shaker are described and the results discussed. Practical structural intensity measurements are then made using two PZT vibrometers and the results compared with the two-accelerometer technique of Chapter 2. The practical advantages and disadvantages of the two schemes are then reviewed and typical measurement environments suggested for each scheme.

## 3.1 LASER VIBROMETRY.

Although laser vibrometer systems differ both in their optical configuration and signal processing electronics, they are all based on the measurement of the Doppler frequency shift in light scattered from the vibrating surface of interest. The physics of operation of LDV measurement is reviewed below.

As shown in figure 3.1, when laser light of frequency f is incident on an optically rough surface, any surface motion causes the scattered light to undergo a Doppler frequency shift[37]. For light incident at an angle $\alpha$ and viewed at an angle $\beta$ to the normal-to-surface velocity vector v, the Doppler frequency shift $f_D$ is given by,

$$f_D = \frac{|\underline{v}|}{\lambda} \mu(\cos\beta + \cos\alpha) \text{ Hz} \qquad (3.1)$$

where $\mu$ is the refractive index of the medium (1 for air), and $\lambda$ is the optical wavelength. The frequency of the scattered light $f+f_D$, is not directly measurable as the response time of commercially available photodetectors is not sufficiently fast. Instead the scattered light is mixed, as shown in figure 3.2, with a reference beam of frequency f taken from the same light source, and heterodyned on the photodetector surface. The output of the detector then becomes modulated by the Doppler frequency component of the incident light $f_D$, which from equation (3.1) is proportional to the surface velocity.

Using this optical configuration, it is still not possible to resolve the sign of the surface velocity. To remove this ambiguity, the reference beam is frequency shifted by a known amount $f_R$, to produce an optical beat on the detector surface of $f_D+f_R$. The detector output is then demodulated using an appropriate signal processor to produce a time resolved voltage output, proportional to the surface velocity. A practical laser vibrometer system is described below.

## 3.2 THE I.S.V.R. LASER VIBROMETER.

The I.S.V.R. laser vibrometer[29] shown in figure 3.3 employs a Michelson Interferometer optical configuration with a rotating scattering disc to produce the reference beam frequency shift. This configuration has the advantage that a single beamsplitter both divides and recombines the laser beam and scattered light respectively. As the system utilises backscattered light from both the target surface and scattering disc reference surface, it is self aligning and results in a robust design. Using this optical geometry, the vibrometer measures the target velocity vector parallel to the incident laser beam. The mirror shown in figure 3.3 is included to make the geometry more compact. The I.S.V.R. laser vibrometer has a dynamic range of 70dB, permitting velocity measurements of amplitude -10 dB to -80 dB reference 1 m/s, over the vibration frequency range 0 to 20 kHz.

From section 2.3, the one-dimensional, far-field, flexural wave structural intensity $\langle P(x_0) \rangle$, measured using acceleration signals is given by,

$$\langle P(x_0) \rangle = 2EI\frac{k^2}{\omega^2} \left\langle \frac{\delta a}{\delta x} \int a \, dt \right\rangle \qquad (2.10)$$

which can be rewritten in terms of the normal-to-surface velocity v as,

$$\langle P(x_0) \rangle = 2EIk^2 \left\langle v \int \frac{\delta v}{\delta x} dt \right\rangle \qquad (2.10a)$$

Employing the two transducer, finite difference approximation and equation (2.13),

$$\langle P(x_0) \rangle \approx \frac{\omega(M_B EI)^{1/2}}{2h} \left\langle (v_2+v_1) \int (v_2-v_1)dt \right\rangle \qquad (3.2)$$

$$= \left[ \frac{\rho E}{12} \right]^{1/2} \frac{bd^2\omega}{2h} \left\langle (v_2+v_1) \int (v_2-v_1)dt \right\rangle \qquad (3.2a)$$

where the exact structural intensity $\langle P(x_0) \rangle_E$ can be calculated using

the finite difference approximation correction as,

$$\langle P(x_0)\rangle_E = P_{MEASURED} \frac{2kh}{\sin 2kh} \qquad (2.21)$$

Hence two I.S.V.R. laser vibrometers can be substituted for two accelerometers in the two transducer scheme discussed in Chapter 2. As discussed in section 2.4.3, before any S.I. measurements are made however, the relative response characteristics of the two transducers must be measured so that any significant response differences, e.g. an amplitude difference of more than ±20% and a phase difference of more than $\pm 5^{o}$, may be compensated for using the methods discussed in section 2.4.4.

### 3.2.1 INTER-VIBROMETER RESPONSE CHARACTERISTICS.

The inter-vibrometer response characteristics were measured using the system shown in figure 3.4. A step-sine excitation was employed to drive the shaker since,
(i) the shaker velocity amplitudes employing broadband random excitation were not sufficiently large to be measured with this device,
(ii) narrowband frequency, shaker excitation was too time-consuming for response measurements over a broad frequency range.

Measurements were made with a constant power amplifier current driving the shaker, producing an approximately constant acceleration amplitude excitation of 16 dB reference 1 $m/s^2$, equivalent to velocity amplitudes of -40 dB reference 1 m/s at 100 Hz, and -65 dB at 2 kHz. Employing a 5 Hz step increment, the inter-vibrometer frequency response function (FRF) was measured over the frequency ranges 100 Hz to 1 kHz, and 1 kHz to 2 kHz. These are shown in figures 3.5 and 3.6. With reference to figure 3.5, these spectra show the two vibrometers to have a difference in amplitude response of up to ±10% (0.8 dB), and a phase response of better than $\pm 3^{o}$. This amplitude error will result in a S.I. measurement error of ±10%, well within the ±20% practical measurement error limit. For an infinite beam, a $\pm 3^{o}$ phase response error will result in S.I. measurement errors of 0.5 dB at 500 Hz and 0.4 dB at 2250 Hz. Hence

accurate S.I. measurements can be made using two I.S.V.R. laser vibrometers, with a worst case measurement error on an infinite beam of 1.4 dB.

With reference to figure 3.6, it can be seen that at higher frequencies, e.g. above 1600 Hz, and hence at lower velocity amplitudes, both the inter-transducer amplitude and phase response errors increase beyond the previously described, acceptable measurement limits. This is due to two effects,

(i) The vibrometer 'sample-and-hold' circuit, employed to compensate for any loss in Doppler signal amplitude due to insufficient light being incident on the photodetector, reduces the vibrometer signal-to-noise ratio. Since the 'hold' circuit has a constant time duration, it will have a greater, adverse effect at higher frequencies where the vibration signal period is shorter. Hence when the inter-vibrometer phase response of two low velocity amplitude, high frequency signals is measured, the difference of two noisy signals is obtained and large phase errors, of the magnitude shown in figure 3.6, will occur.

(ii) As the target velocity amplitude falls towards the noise floor level, dynamic speckle effects become more significant and the signal-to-noise ratio of the vibrometer output is reduced. As with (i), the difference of two increasing noisy signals is then obtained with large inter-transducer phase errors resulting.

To further investigate these effects, additional inter-transducer FRF measurements were made with velocity amplitudes of -60 dB reference 1 m/s at 100 Hz, and -85 dB at 2.25 kHz, close to the vibrometer high-sensitivity limit. As figures 3.7 and 3.8 clearly illustrate, as the device noise floor is approached, the inter-vibrometer phase response errors increase by an order of magnitude, to a level where unacceptably large S.I. measurement errors will result. Due to the magnitude of this phase error, a reduction in S.I. measurement error will result from the use of a large transducer separation to flexural wavelength ratio.

Measurements also showed that a small change in the target laser beam

position, e.g. due to non-normal target surface motion, resulted in a large change in the phase error frequency distribution. This is due to any change in the backscattered target speckle pattern randomly modulating the spatial characteristics of the resultant speckle pattern incident on the photodetector, with an associated random modulation of the noise characteristics of the vibrometer output. Hence for low velocity amplitude S.I. measurements, the inter-vibrometer phase response will vary randomly with any change in position of either laser vibrometer target laser beam. Therefore for many practical measurements, the inter-transducer phase response compensation methods discussed in section 2.4.4 cannot be applied. Since these response errors become problematic only as the vibrometer noise floor is approached, it is interesting to consider what determines this physical, velocity measurement limit.

### 3.2.2 DISCUSSION OF LASER VIBROMETER NOISE FLOORS.

The I.S.V.R. laser vibrometer noise floor shown in figure 3.9 was measured using a stationary target surface. The vibration spectrum was measured over the frequency range 0 to 800 Hz, with a 1 Hz frequency resolution and 10 averages. The noise floor consists of an infinite series of spikes at the reference surface, disc rotation frequency and its harmonics. The mean spike amplitudes are approximately constant with frequency but with individual spike amplitudes varying randomly about the mean level with each new measurement position. As discussed in Chapter 3, these spikes are caused by pseudo-random intensity modulation of the light incident on the vibrometer photodetector, resulting in a pseudo-random detector noise output. The frequency spectrum of this form of noise signal is as shown in figure 3.9. It is apparent therefore that the vibrometer *stationary-surface* noise floor level is determined optically and not by the electronic signal processing.

It can be concluded from figure 3.9 that for measurements where the inter-transducer phase relationship is not important, the I.S.V.R. laser vibrometer can be used to accurately measure velocities of down to -80 dB reference 1 m/s. Rothberg et al[39] have also shown that the spike

amplitudes do not increase in the presence of large amplitude, non-normal motion, i.e. the noise floor spike amplitudes for a stationary and a vibrating target surface are equal.

As can also be seen from figure 3.9, for vibration at frequencies not coincident with the disc rotation speed or its harmonics, measurements are possible between the spikes, down to a lower level of approximately -115 dB. However any non-normal motion will cause the broadband noise amplitude to increase, raising the noise floor amplitude between the spikes to a level dependent, as with other laser vibrometer systems, upon the target motion. Therefore when the phase response between two I.S.V.R. laser vibrometers is critical, i.e. for S.I. measurements, the vibrometer dynamic range is limited to velocity amplitudes above the 'optical' noise floor level.

### 3.2.3 STRUCTURAL INTENSITY MEASUREMENTS.

S.I. measurements employing two I.S.V.R. laser vibrometers were made using the system shown in figure 2.5. The vibration amplitudes produced using a swept-sine excitation were found to be at, or below the vibrometer detection limit. Any practical measurements would therefore have resulted in large S.I. measurement errors. Hence narrow band excitation, producing larger velocity amplitudes, was employed over the frequency range 500 Hz to 2.25 kHz, in 250 Hz increments. The vibrometer S.I. measurement results are compared with those obtained using two accelerometers in figure 3.10. These results were calculated using the signal processing scheme described in section 2.5. A transducer separation of down to 1 mm can be obtained using a mirror to direct one of the laser vibrometer target laser beams. However for the measurements recorded in this chapter, a separation of 10cm was employed to minimise the effect of inter-transducer phase errors.

As the results in figure 3.10 show, good agreement was obtained between the vibrometer and accelerometer S.I. measurements. The maximum difference of 1.2 dB (14.8%) is less than the worst case error of 1.4 dB predicted in section 3.2.1. Therefore provided the target velocity

amplitude falls within the range -10 to -80 dB reference 1 m/s, accurate S.I. measurements can be made using two I.S.V.R. laser vibrometers.

In many structural vibration environments, small velocity amplitudes can still represent large amplitude, vibration energy transmission through the structure. For example, from equation (3.2a), a beam of thickness d, vibrating with velocity v, will have the same S.I. magnitude as a beam of thickness 5d and velocity v/5. Hence there is a requirement for a laser vibrometer system that includes the practical, optical advantages of the I.S.V.R. laser vibrometer, i.e. robust, portable and offering simple 'point-and-shoot' operation, but that has a higher sensitivity. This system is described in section 3.3.

## 3.3 THE PZT LASER VIBROMETER,

With reference to figure 3.11, the PZT laser vibrometer is a new, high-sensitivity transducer, employing a Michelson Interferometer optical configuration. It utilises a piezo-electric ceramic element of lead zirconate (PZT) as a reference surface, frequency shifting device and a signal processing scheme suggested by Dandridge et al[40] to demodulate the detector output signal. This results in a vibrometer with a voltage output proportional to the normal-to-surface target velocity. This scheme differs from the Dandridge system by including,
(i) a diffuse rather than a specular reference surface, resulting in a self-aligning and significantly more robust optical geometry,
(ii) a reference surface oscillating at 750 kHz compared with the 50 kHz of the Dandridge system, permitting larger amplitude velocities to be measured, with an associated increase in the vibrometer dynamic range,
(iii) an optical geometry and opto-electronics that have been optimised for use with the diffusely reflecting target surfaces that are usually encountered in engineering components.

In section 3.3.1, the physics of operation of this device are described. PZT vibrometer measurements on a sinusoidally oscillating shaker are compared with an accelerometer in 3.3.2 and its suitability for S.I. measurements reviewed. In section 3.3.3, S.I. measurements on an infinite beam structure are made simultaneously with two PZT vibrometers and two accelerometers and the results compared. Conclusions on the use of the PZT vibrometer for S.I. measurements are then made in 3.3.4.

### 3.3.1 PHYSICS OF OPERATION.

The optical configuration employed by the PZT vibrometer is shown in figure 3.11. The laser beam is amplitude divided into two beams which are incident on the target and reference surface respectively. Light is back-scattered from each surface onto the photodetector. Neglecting polarisation effects, the output current $i_d$ from the photodetector can be written as,

$$i_d = \gamma\left[I_P + I_T + 2(I_P I_T)^{1/2}\cos\theta\right] \quad (3.3)$$

where $I_P$ and $I_T$ are the reference and target beam scattered light intensities, $\gamma$ is the photodetector response term and $\theta$ the phase difference term due to a pathlength imbalance. With reference to figure 3.11, this phase term is directly proportional to any relative change $(L_1-L_2)$, in position of either surface, such that,

$$\theta = 2kl + \theta_0 \text{ radians} \quad (3.4)$$

where $l = (L_1-L_2)$, $k$ is the wavenumber of laser light and $\theta_0$ is the initial phase difference. As noted in section 3.1, using this optical geometry it is not possible to determine the target surface velocity direction. The reference beam is thus frequency pre-shifted to provide a carrier frequency in the photodetector output, which movement of the target frequency modulates[37]. Tracking the carrier frequency then provides a time-resolved analogue output of the target surface velocity.

In the proposed system, the reference light is frequency shifted by driving the reference surface, i.e. a PZT element, sinusoidally such that,

$$L_1 = A_P\sin\omega_P t \quad (3.5)$$

where $A_P$ and $\omega_P$ are the PZT element peak displacement amplitude and oscillation frequency respectively. For sinusoidal target motion, the time-varying detector current $i_d(t)$ will then be,

$$i_d(t) = \gamma\left[I_P + I_T + 2(I_P I_T)^{1/2}\cos(2k[A_P\sin\omega_P t - A_T\sin\omega_T t] + \theta_0)\right] \quad (3.6)$$

where $A_T$ and $\omega_T$ are the target displacement amplitude and frequency respectively. This equation reduces to,

$$i_d(t) = C_1[\,1 + C_2\cos(\theta_P\sin\omega_P t - \theta_T)\,] \quad (3.7)$$

where,

$$\theta_P = 2kA_P;\ \theta_T = 2kA_T\sin\omega_T t - \theta_0\ ;\ C_1 = \gamma(I_P + I_T)\ ;\ C_2 = \frac{2(I_P I_T)^{1/2}}{I_P + I_T}$$

Expanding (3.7) in terms of Bessel functions,

$$i_d(t) = C_1\Big[\,1 + C_2\cos\theta_T\Big\{J_0(\theta_P) + 2\sum_{n=1}^{\infty}J_{2n}(\theta_P)\cos(2n\omega_P t)\Big\} + C_2\sin\theta_T\Big\{2\sum_{n=0}^{\infty}J_{2n+1}(\theta_P)\sin((2n+1)\omega_P t)\Big\}\Big] \qquad (3.8)$$

Therefore in contrast with the majority of LDV systems, the photodetector output contains PZT element-generated carrier frequency terms at $\omega_P$ and higher order harmonics, each of which the target surface will frequency modulate. It will now be shown how the target surface velocity information can be retrieved from this form of signal by selecting specific carrier frequencies at $\omega_P$ and $2\omega_P$.

With reference to figure 3.12, the photodetector output is initially bandpass filtered to produce signals $i_{\omega P}(t)$ and $i_{2\omega P}(t)$ given by,

$$i_{\omega P}(t) = 2C_1C_2J_1(\theta_P)\sin(\omega_P t)\sin(\theta_T) \qquad (3.9a)$$

$$i_{2\omega P}(t) = 2C_1C_2J_2(\theta_P)\cos(2\omega_P t)\cos(\theta_T) \qquad (3.9b)$$

For a maximum signal-to-noise ratio in the succeeding signal processing, the amplitude of these two signals should be matched, i.e. $J_1(\theta_P) \approx J_2(\theta_P)$. To prevent the PZT element overheating and vibrating in a non-linear manner, a maximum value of $\theta_P$ is required. Figure 3.13 is a comparison of Bessel functions of the first and second order and shows that for a value of $\theta_P = 2.65$ radians, they are equal in magnitude.

As shown in figure 3.12, phase sensitive detectors[41] with reference inputs at frequency $\omega_P$ and $2\omega_P$ respectively then produce outputs of,

$$x = C_G C_1 C_2 \sin\theta_T \quad ; \quad y = C_G C_1 C_2 \cos\theta_T \tag{3.10}$$

where $C_G$ is the effective channel gain which incorporates $J_1(\theta_P)$ and $J_2(\theta_P)$. A system of analogue multipliers and differentiators[42] then gives the outputs,

$$z = x \frac{dy}{dt} - y \frac{dx}{dt} \quad ; \quad e^2 = x^2 + y^2 \tag{3.11}$$

where,

$$z = (C_G C_1 C_2)^2 \frac{d\theta_T}{dt} \tag{3.12}$$

$$e^2 = (C_G C_1 C_2)^2 \tag{3.13}$$

Here z is proportional to $d\theta_T/dt$ and hence represents the target velocity. However the term $C_1C_2$ is dependent on the intensity of light scattered from the target and this will vary with measurement position. As shown in figure 3.12, this effect is overcome by employing an automatic gain control system, whereby $C_G$ is adjusted to keep $e^2$ constant for varying $C_1C_2$ and thus maintain the term $(C_GC_1C_2)^2$ in equation (3.13) constant also.

From equation (3.7), it can be seen that the term $\theta_T$ in the vibrometer output also includes a contribution from the initial phase difference $\theta_0$. Employing a rotating disc, reference surface, the I.S.V.R. laser vibrometer suffers from dynamic speckle effects which produce a pseudo-random modulation of $\theta_0$ and hence a non-zero value of $d\theta_0/dt$. As noted in section 3.2.2, spurious speckle noise effects are therefore always evident in the vibrometer output and determine the device sensitivity. In contrast, the PZT vibrometer reference surface oscillates normally to the incident laser beam and produces negligible dynamic speckle effects. Hence for normal-to-surface target vibration, $\theta_0$ is a constant and $d\theta_0/dt$ is zero. Under these conditions, the maximum vibrometer sensitivity will be dictated by the electronic noise floor amplitude. Under these conditions, the PZT vibrometer is able to

measure velocity amplitudes of three orders of magnitude (60 dB) less than the I.S.V.R. laser vibrometer.

### 3.3.2 COMPARISON WITH AN ACCELEROMETER.

The prototype vibrometer has two vibration frequency ranges; 0 to 1 kHz and 0 to 10 kHz, with measured dynamic ranges of 100 dB and 90 dB respectively. The difference in dynamic range is due to the wider filter bandwidth increasing the electronic noise in the vibrometer output signal. A range of sensitivity settings in the demodulator circuit are employed to improve the signal-to-noise ratio for varying velocity amplitudes. A stationary target surface, noise floor amplitude of -140 dB reference 1 m/s was measured at 500 Hz. The maximum velocity amplitude of -40 dB reference 1 m/s is determined by the input bandpass filters at $\omega_R$ and $2\omega_R$. This level can be increased through broadening of the filter bandwidth but at the expense of increased electronic noise and hence reduced sensitivity, i.e. there is a 'trade-off' between the vibrometer high-sensitivity limit and its maximum velocity amplitude.

Figure 3.14 compares a spectrum of the vibrometer output with that of an accelerometer for the same measurement situation. A 2 mW He-Ne laser was used, producing an incident intensity target beam of 1 mW. The beam was directed onto the top of the accelerometer, which was being driven by an electrodynamic shaker at 123 Hz. A small piece of retro-reflective tape was placed on the accelerometer to ensure sufficient intensity in the backscattered light collected by the photodetector.

The spectra shown in figure 3.14 contain 100 averages with a frequency resolution of 1 Hz. Excellent agreement is obtained and for this measurement, the minimum detectable level for the vibrometer is shown to be better than -120 dB, or 1 μm/s. This velocity amplitude corresponds to the vibrometer 'optical' noise floor discussed in section 3.2.2. and the increase in the noise floor amplitude is due to dynamic speckle effects. Employing the most sensitive setting of the charge amplifier, a minimum detectable accelerometer velocity amplitude of -140 dB is obtained. This compares with a stationary surface noise floor level of

-160 dB reference 1 m/s at 500 Hz. The difference in accelerometer sensitivities is due to broadband, random, electronic noise from the signal generator driving the shaker.

These results clearly show the ability of the PZT vibrometer to make low amplitude, normal-to-surface velocity measurements. Its dynamic range complements that of the I.S.V.R. laser vibrometer, while sharing the practical advantages of the same optical configuration, i.e. it is robust, self-aligning and offers simple, straightforward 'point-and-shoot' operation. Low velocity amplitude, structural intensity meaaurements using two of these devices are described in the next section.

### 3.3.3 STRUCTURAL INTENSITY MEASUREMENTS.

The two PZT laser vibrometers were calibrated by pointing the target laser beams onto a pre-calibrated accelerometer mounted on a shaker, and adjusting the vibrometer calibration constants until the signal magnitudes were equal. A range of vibration frequencies and amplitudes were employed to check the vibrometer calibration and linearity over its dynamic range.

The inter-vibrometer amplitude response at low levels of velocity amplitude was measured as typically ±0.5 dB, (6%), while the relative phase response is tabulated in figure 3.15. As these results show, phase response errors of up $\pm 3^{o}$ were obtained, similar to those measured for the I.S.V.R. laser vibrometer. These phase errors are due to two effects,

(i) small differences in the nominally identical setup and electronic component values of the two vibrometers,

(ii) as with the I.S.V.R. laser vibrometer in section 3.2, dynamic speckle effects introduce noise into the vibrometer output.

As shown in chapter 2, for structures where the travelling wave amplitude is comparable with, or greater than the standing wave amplitude, a large value ratio of transducer separation to flexural

wavelength can be employed to minimise the effect of any inter-transducer phase errors. However when the standing wave amplitude is greater than the travelling wave amplitude of interest, the accuracy of the S.I. measurement technique is critically dependent upon the inter-transducer phase response errors. Hence these phase response errors must be minimised.

The first of these error sources can be minimised through careful selection or matching of the signal processing electronic components. Alternatively, as with the two accelerometer system, a pair of response-matched laser vibrometers could be employed. As discussed in section 3.2, for most practical measurements the second phase error source is a random function of both frequency and time, and therefore cannot be cancelled out using phase response compensation methods. Hence, as with a majority of laser vibrometer systems, accurate S.I. measurements can only be made with the PZT laser vibrometer if the velocity amplitudes are above the 'optical' noise floor level.

As in section 3.2.3, a transducer separation of down to 1 mm can be obtained using a mirror to direct one of the target laser beams. However measurements were instead made with a separation of 15 cm, determined by the prototype vibrometer physical dimensions, to ensure that any S.I. measurement errors due to inter-transducer phase errors were minimised. The vibrometer laser beams were directed onto the top surface of two accelerometers mounted on an infinite beam. The two sets of S.I. measurements are compared in figure 3.16. Constant amplitude velocity excitations of approximately -85 dB and -105 dB reference 1m/s, were employed over the frequency range 500 to 2250 Hz. The agreement between the S.I. measurements shown in figure 3.16 is good with an average difference of -0.525 dB. The maximum difference of 1.4 dB is consistent with the 1.4 dB worst case measurement error, for inter-transducer phase and amplitude response errors of $\pm 3^{o}$ and 6% respectively.

As noted in section 2.4.2, the mass-loading effect of the accelerometers reduces the point acceleration amplitude by -1.79% at 500 Hz and -3.75% at 2250 Hz. Phase errors due to accelerometer mass-loading of the

structure will be the same for each transducer. Hence both the inter-transducer phase response and the S.I. measurement errors due to this effect will be zero. These errors are equivalent to S.I. measurement errors of -3.5%, (0.2 dB), at 500 Hz and -7.4%, (0.4 dB), at 2250 Hz. Therefore at higher frequencies, or for structures with smaller point impedances, the accuracy of the PZT vibrometer and accelerometer S.I. measurement schemes are comparable.

## 3.4 CONCLUSIONS ON THE LASER VIBROMETER, STRUCTURAL INTENSITY METER.

In this chapter, the direct substitution of laser vibrometers for accelerometers in the two-transducer scheme has been reviewed. Measurements utilising the I.S.V.R. laser vibrometer showed that providing vibration velocity amplitudes are above the device noise floor, spurious optical noise-induced phase errors could be neglected and accurate S.I. measurements could therefore be made. Although S.I. measurements were therefore restricted to velocity amplitudes greater than 0.1 mm/s, this maximum sensitivity level is a constant. This is in contrast with other vibrometer systems where the noise floor level, and thus the minimum velocity amplitude that accurate S.I. measurements could be made at, is dependent upon the target motion itself, i.e. it will be effected by the pseudo-random optical effects discussed in Chapter 5.

In many practical structures, low amplitude velocities can still result in significant vibration and noise radiation. A new, high-sensitivity PZT vibrometer, incorporating many of the optical advantages of the I.S.V.R. laser vibrometer, i.e. portable, robust and offering simple 'point-and-shoot' operation, has therefore been developed to overcome this sensitivity limitation. This device, with stationary surface noise floor levels of 0.1 μm/s and 0.32 μm/s over the frequency ranges 0 to 1 kHz and 0 to 10 kHz respectively, has a sensitivity approaching that of an accelerometer. Structural intensity measurements using two PZT vibrometers on an infinite beam were, on average, within 6% of those measured simultaneously using the two-accelerometer scheme. As noted in Chapter 2, over the measurement frequency range of 500 to 2250 Hz, the accelerometer scheme suffers from S.I. measurement errors of 3.5% to 7.4% respectively due to mass-loading of the structure. Hence for light structures, and at high frequencies, the accuracy of two, PZT laser vibrometer, S.I. measurement technique will be more accurate than the two-accelerometer technique.

In conclusion, employment of the two laser vibrometer, S.I. measurement scheme is complementary to, rather than a direct replacement for the

two accelerometer technique. The relative merits of the two schemes may be summarised as,

(i) accelerometers have greater sensitivity than either of the laser vibrometers described in this chapter and so will allow lower amplitude S.I. measurements to be made,

(ii) the matched-response, accelerometer pair used in chapter 2 have smaller inter-transducer phase response errors than either of the two laser vibrometer systems used in this chapter; hence more accurate S.I. measurements will be obtained when the relative phase response becomes critical, i.e. in structures where the standing wave amplitude is greater than the travelling wave amplitude of interest,

(iii) for structures where the travelling wave amplitude is greater than, or comparable with, the standing wave amplitude, the accuracies of the two-accelerometer and two-vibrometer techniques are similar,

(iv) the frequency range over which accelerometers may be employed for accurate S.I. measurements is limited by its inherent, internal resonance frequency, e.g. using general purpose accelerometers, measurements are restricted to less than 1.8 kHz for better than $1^{o}$ phase error,

(v) accelerometers mass-load a structure at a rate proportional to the accelerometer mass and the vibration frequency, hence the laser vibrometer scheme will measure the structural intensity more accurately than accelerometers on light structures and at high frequencies,

(vi) the two laser vibrometer scheme allows remote, non-contact structural intensity measurements to be made, and thus not only offers the possibility of quickly making a large number of measurements, but also extends application of the technique to situations where accelerometers cannot be used, e.g. hot and inaccesible surfaces.

## 4. THE LASER VELOCITY GRADIENT TRANSDUCER.

In Chapters 2 and 3, it was shown how when using the finite difference approximation, the major error source in the two transducer, structural intensity (S.I.) measurement scheme, is the difference in transducer response characteristics. Prior to measurements being made, the transducer amplitude responses can be matched using a transducer calibrator. The relative, transducer phase responses cannot be matched in this way, however, and resulting S.I. measurement errors can only be minimised by correction with the predetermined, inter-transducer phase response function. This option is time consuming and for some transducers, such as laser vibrometers, it is not valid since any non-normal target surface motion will cause the phase response error to vary. In this situation, large S.I. measurement errors may result. Therefore, if through use of a specially developed laser transducer system, the technique measurement accuracy can be improved, the resultant, laser technology-based structural intensity measurement scheme will supercede the two-accelerometer technique, presently in widespread employment.

In this chapter, improvements in S.I. measurement accuracy through use of a velocity difference transducer are described and a range of optical techniques for measuring normal-to-surface displacement, or velocity spatial derivatives are then reviewed[43-48]. A final transducer scheme is then proposed, based on the optimum optical configuration of these measurement systems, and employing a signal processing scheme originally developed for a fibre-optic vibrometer[49]. The prototype system is then employed to make velocity and velocity gradient measurements and the results are compared with accelerometer measurements and theoretical predictions. Finally, used in conjunction with a laser vibrometer, practical, one-dimensional, structural intensity measurements are made with the velocity gradient transducer and the results compared with the traditional, two-accelerometer technique described in Chapter 2.

## 4.1 ADVANTAGES OF THE VELOCITY GRADIENT MEASUREMENT SCHEME.

In Chapter 3 it was shown how the structural intensity expression derived in Chapter 2 could be written in terms of the normal-to-surface velocity v as,

$$\langle P(x_0) \rangle = 2\omega(M_B EI)^{1/2} \langle v \int \frac{dv}{dx} dt \rangle \qquad (2.10a)$$

where $\langle ... \rangle$ represents a time average. Using two, point velocity laser vibrometers, this expression can be realised from the time-average product of the integrated sum, and difference of the two transducer outputs. It is readily apparent from the above equation that the structural intensity can be directly, and hence more easily measured, from the product of the point velocity v, and the integrated velocity gradient dv/dx. In what follows, it is shown that this not only simplifies the S.I. calculation procedure but also, in reducing the technique sensitivity to inter-transducer phase errors, improves the technique measurement accuracy.

The velocity gradient measurement methods discussed in the following sections directly measure the difference in normal-to-surface velocity between two points, A and B, on a vibrating target surface. The velocity gradient dv/dx is then calculated using a finite difference approximation,

$$\frac{dv}{dx} \approx \frac{v_B - v_A}{2h} \qquad (4.1)$$

where 2h is the point separation and $v_A$ and $v_B$ are the normal-to-surface velocities at points A and B respectively. Measuring the S.I. at a point $x_0$, and employing a laser vibrometer in conjunction with the velocity gradient measurement scheme, the velocity v and velocity gradient dv/dx terms are given by,

$$v = \omega A \cos(\omega t - kx_0) + \omega B \cos\omega t \sin kx_0 \qquad (4.2)$$

and,

$$\frac{dv}{dx} \approx \frac{\omega}{h}\left[A\sin(\omega t - kx_0)\sinh kh + B\cos\omega t\cos kx_0\sinh kh\right] \qquad (4.3)$$

where A and B are the travelling and standing wave amplitudes respectively and $\omega$ is the vibration frequency. The S.I. measured using the velocity gradient scheme $\langle P(x_0)\rangle_{VGT}$, is thus given by,

$$\langle P(x_0)\rangle_{VGT} \approx \frac{2A^2\pi\omega}{h}(M_B EI)^{1/2}\sinh kh \qquad (4.4)$$

Comparison of this equation with the exact S.I. expression given in equation (2.20) for ideal velocity and velocity gradient signals, shows this expression to underestimate the S.I.. However, as with the two vibrometer scheme in Chapter 3, a finite difference approximation correction factor can be employed. For the proposed scheme this is given by,

$$\text{Correction factor} = \frac{kh}{\sin(kh)} \qquad (4.5)$$

Employing the frequency domain implementation described in section 2.3.2, for practical measurements the S.I. can be calculated from,

$$\langle P(x_0)\rangle_{VGT} \approx \frac{(M_B EI)^{1/2}}{2h}\,\mathrm{Im}\,G(dv/dx, v, f) \qquad (4.6)$$

Since the imaginary component of the cross-spectrum of the two transducer signals is directly proportional to the structural intensity, i.e. there are no frequency terms in the expression, S.I. measurements can be obtained more easily and quickly than with the two-accelerometer scheme.

Introducing inter-transducer amplitude $\eta_1$, $\eta_2$, and phase $\xi_1$, $\xi_2$, error terms into the velocity gradient and velocity signals in equations (4.2) and (4.3) respectively, results in an S.I. expression of,

$$\langle P(x_0)\rangle_{VGT} = \frac{2A^2\pi\omega}{h}(M_B EI)^{1/2}(1+\eta_1)(1+\eta_2)\sinh kh \ *$$

$$\left[\cos(\xi_1-\xi_2) + \left[\frac{B}{A}\right]\cos 2kx_0\sin(\xi_1-\xi_2) + \frac{1}{2}\left[\frac{B}{A}\right]^2\sin 2kx_0\sin(\xi_1-\xi_2)\right] \quad (4.7)$$

After correction for the finite difference approximation, calculation of R, the ratio of equations (4.7) and (2.37), (the two accelerometer scheme), enables the relative effect of the inter-transducer phase errors on the S.I. measurement error to be evaluated,

$$R = \frac{\sin 2kh\left[\cos\theta_1 + \left[\frac{B}{A}\right]\cos 2kx_0\sin\theta_1 + \frac{1}{2}\left[\frac{B}{A}\right]^2\sin 2kx_0\sin\theta_1\right]}{\sin(2kh+\theta_2) + \left[\frac{B}{A}\right]\sin 2kx_0\sin\theta_2 + \left[\frac{B}{A}\right]^2\sinh(x_0+h)\sinh(x_0-h)\sin\theta_2} \quad (4.8)$$

where $\theta_1$ and $\theta_2$ are the inter-transducer phase errors of the laser and accelerometer measurements respectively, i.e.

$$\theta_1 = (\xi_1 - \xi_2) \quad ; \quad \theta_2 = (\varepsilon_1 - \varepsilon_2)$$

This ratio is shown in figure 4.1 as a function of the ratio of the transducer separation and flexural wavelength, 2kh. Equal value inter-transducer phase response errors are employed, i.e. $\theta_1 = \theta_2 = \theta$, and,

a) $2kx_0 = (\pi/4)$ so that equal weighting is given to both sin and cos terms in equation (4.8),

b) $(B/A) = 1$, i.e. equal amplitude travelling and standing wave displacements.

With reference to figure 4.1, for equal inter-transducer phase response errors, the S.I. error measured using the proposed scheme will be less than that for the two accelerometer scheme. For example, with a transducer separation to wavelength ratio (2kh) of 0.628, an inter-transducer phase response error of $3^0$ will produce a measurement error in the new scheme that is 0.93 times that obtained using the two accelerometer scheme.

With reference to figure 4.2, the variation of R with 2kh also shows that for small values of 2kh, i.e. small transducer separations, the accuracy of the new laser measurement method is comparable with, if not better than the two accelerometer scheme, even if it suffers from larger inter-transducer response errors. This improvement in accuracy is due to the reduction in the number of steps necessary to calculate the S.I., which in turn reduces the sensitivity to inter-transducer phase errors. Realised in practice, this improvement in measurement accuracy will result in a practical alternative to the currently widely employed, two accelerometer technique.

In sections 4.2 to 4.5, optical velocity gradient transducer schemes are discussed, their relative merits compared, and a new laser velocity difference transducer described. Practical S.I. measurements made using this system are described in section 4.6.

## 4.2 SHEAROGRAPHY.

Shearography is an optical measurement method permitting the full field evaluation of surface displacement derivatives[43]. A typical optical configuration is shown in figure 4.3[44]. The target surface is illuminated by a collimated, coherent laser source at an angle $\alpha$ to the optical axis. The image shearing system consists of two inclined, glass blocks and a convex, imaging lens. Provided the imaging criterion, $(1/z_1) + (1/z_2) = (1/f)$, where f is the lens focal length, is met, two images of the target surface are formed in the image plane. Each image will have the same orientation but will be shifted laterally with respect to the other.

As shown in figure 4.4, the image shear is a function of the glass block material and inclination relative to the optical axis. Hence a ray of light passing through a glass block with parallel faces, will be laterally shifted by an amount p equal to,

$$p = d\sin\alpha_B\left[1 - \frac{\cos\alpha_B}{(\mu^2-\sin^2\alpha_B)^{1/2}}\right] \qquad (4.9)$$

where $\mu$ is the refractive index of the block, d is the block thickness and $\alpha_B$ is the block angle of inclination with respect to the optical axis. The amount of shift can therefore be altered through variation of $\alpha_B$. Provided the dimensions of the illuminated area are much smaller than the imaging lens to target surface distance, then $\alpha_B$, and hence the image shear p, can be considered constant for all illuminated points.

Since most surfaces are rough on the scale of an optical wavelength, the two superimposed, coherent speckle images will produce a resultant speckle pattern intensity distribution. Each speckle within this pattern will be modulated by a high frequency fringe pattern of period g, given approximately by[44],

$$g \approx \frac{\lambda f}{D} \qquad (4.10)$$

where D is the separation of the two aperture centres. This fringe pattern is aligned perpendicularly to the line joining A and B and any change in the relative phase of light from either point will cause it to translate across the speckle, in the x-axis direction. When photographic film is placed in the image plane and exposed twice, the object being deformed between exposures, the processed film yields a fringe pattern depicting the difference in undeformed and deformed gratings, and hence any relative phase change in light from points A and B.

Employing the optical configuration shown in figure 4.3, the relative phase change, $\Delta$, is given by[43],

$$\Delta = \frac{2\pi}{\lambda}\left[(1+\cos\alpha)\frac{\delta w}{\delta x} + (\sin\alpha)\frac{\delta u}{\delta x}\right] \qquad (4.11)$$

where w and u are the normal-to-surface and in-plane displacements respectively. Thus a fringe pattern will only be obtained when bending of the surface takes place, since a uniform displacement in the z-direction will produce no relative phase change, while a uniform tilt of the surface will produce a uniform phase change and hence a uniform brightness change over the image.

The fringe pattern produced by double exposure photography is not easily visible due to low spatial frequency noise. This noise is associated with areas of the target that are undeformed and the fringe quality is hence improved using high-pass, Fourier, (spatial) filtering[44].

The main limitations of the shearography technique are;
(i) for large amplitude deformation, decorrelation of the two resultant speckle pattern images occurs, the fringe contrast decreases and the recorded data become saturated by random speckle noise,
(ii) the measurement sensitivity is determined by the fringe pattern period and is therefore predetermined,
(iii) the fringe quality, relative to holographic techniques, is poor,
(iv) there is no directional information recorded with the fringes.

In the following section, a real-time velocity difference measurement

method based on the shearography technique is proposed and its use for practical measurements evaluated.

## 4.2.1 VELOCITY DIFFERENCE MEASUREMENT.

For structural intensity measurements, the difference in normal-to-surface velocity between two points on the surface is required. With reference to figure 4.5, replacement of the photographic film by a pinhole aperture and a photodetector, results in a real-time, velocity difference measurement system. With a) the pinhole and photodetector located on the optical axis, b) the glass blocks inclined such that $\alpha_{B1} = \alpha_{B2}$ and c) the apertures positioned so that the point separation is 2h, only light from points A and B, positioned equi-distant from the optical axis, will be incident on the detector. Vibration of either point will cause a Doppler frequency shift in the scattered light, and set up an optical beat frequency on the detector surface. With $\alpha = 0$ and the shearing scheme aligned normally to the target surface, the photodetector output will be modulated at a frequency proportional to the difference in normal-to-surface velocity of points A and B.

The major disadvantages of this scheme include,

(i) since only light from points A and B, with a typical separation of 5cm, is utilised to measure the velocity difference, much of the illuminating laser light is wasted: hence to ensure sufficient light intensity is incident on the detector for accurate signal demodulation to occur, either, a) a high power laser with a high safety class must be used in conjunction with a PIN diode photodetector, or b) a low power laser can be employed in conjunction with a photomultiplier or avalanche photodiode,

(ii) if a smaller point separation or illuminated area is employed, the speckle grating period will be large and the resulting beat frequency of light incident on the detector will be too low to be accurately determined,

(iii) there is no direction information in the detector output signal, e.g. a bending wave travelling from A to B will produce the same

velocity difference signal as one going from B to A,

(iv) using an imaging lens to focus light from A and B onto the detector makes the scheme alignment critical and the transducer optics will be sensitive to vibration.

## 4.3 THE VELOCITY GRADIENT ANEMOMETER.

Velocity gradient anemometry (VGA) is an optical method for measuring spatial velocity gradients in fluid flows[45,46]. It is similar in operation to Laser Doppler Anemometry in that the frequency shift of laser light scattered from moving particles is measured. However, by measuring light scattered by two different particles, with a separation defined by the collection optics, a velocity difference, rather than a single velocity is measured.

Hansen[45,46] has derived an exact mathematical description of this technique and so only a brief review will be given here. As shown in figure 4.6, for fluid flow measurements the measurement volume is illuminated by a collimated, coherent laser light source. The resultant light amplitude distribution is then imaged onto a photodetector surface, which is positioned on the optical axis. Employing a spatial filter immediately behind the imaging lens, e.g. a cosinusoidal diffraction grating filter of period g, and with a transmission function T(x) given by,

$$T(x) = 1 + \cos 2\pi g x \qquad (4.12)$$

only light from particles with separation (1/g) and positioned equi-distant about the optical axis will interfere on the detector surface. The resultant beat frequency will modulate the detector output, at a rate proportional to the difference in Doppler frequency in light scattered from points A and B. With the alignment shown in figure 4.6, frequency tracking this signal will then produce an output proportional to the difference in velocity in the z-direction.

Light from particle pairs with separation not equal to (1/g) will pass the spatial filter but will not interfere in the image plane. Similarly, light from particle pairs with separation (1/g) but not positioned symmetrically about the optical axis, will interfere in the image plane, but off the optical axis. Therefore as shown in figure 4.6, to ensure that only interference of light from particle pairs positioned at A and

B takes place on the photodetector surface, a pinhole aperture is employed.

As noted by Hanson[45], although a large aperture positioned in front of the imaging lens will increase the beat signal amplitude, it will also reduce the depth of focus of the lens and hence the occurence of Doppler frequency signals. Therefore as shown in figure 4.6, for fluid flow measurements an additional aperture is utilised in front of the imaging lens.

For a structural vibration, velocity difference measurement scheme, the measurement volume will be replaced by a target surface and the aperture positioned in front of the lens will no longer be required. With normal-to-surface illumination, the photodetector will measure the rate of change of phase difference in light scattered from points A and B, and hence will be insensitive to velocity differences in both the x and y directions, i.e. it will only measure tilt.

However this scheme suffers from the following disadvantages,
(i) as with the shearography technique, a large proportion of the illuminating laser light is not employed to make a measurement,
(ii) there is no direction information in the detector output,
(iii) employing an imaging lens not only makes the target surface to lens distance important but also any transducer based on this scheme would not be robust.
(iv) the separation of points A and B is predetermined by the grating period.

## 4.4 THE LASER TORSIONAL VIBROMETER.

The laser torsional vibrometer[47,48] is an optical transducer developed for measuring fluctuations in the mean rotation speed, and hence the torsional oscillations of rotating objects, e.g. drive shafts. With reference to figure 4.7, consider a shaft of arbitrary cross-sectional area, rotating at N revolutions per second about an axis defined by the unit vector $\underset{\sim}{\hat{z}}$, which is assumed to be perpendicular to the cross-section. When the shaft rotates, it oscillates as a rigid body with instantaneous velocity vector $\underset{\sim}{V}$.

The essentially single frequency laser beam from the He-Ne laser is divided into two equal intensity beams, which are incident on points A and B of the shaft surface. Laser light scattered from any point on the moving surface undergoes a Doppler frequency shift $f_d$, which for direct backscatter is given by,

$$f_d = \frac{2\mu U}{\lambda} \qquad (4.13)$$

where U is the instantaneous velocity in the direction of the incident laser beam, $\lambda$ is the optical wavelength and $\mu$ is the refractive index of the medium (1 for air). At points A and B, the instantaneous velocities with respect to the axis of rotation, $\underset{\sim}{V}_A$ and $\underset{\sim}{V}_B$ respectively, together with the solid body oscillation $\underset{\sim}{V}$, will produce Doppler frequency shifts in direct backscatter of,

$$f_A = \frac{2\mu}{\lambda}\,\underset{\sim}{\hat{i}}.(\underset{\sim}{V} + \underset{\sim}{V}_A)$$

$$f_B = \frac{2\mu}{\lambda}\,\underset{\sim}{\hat{i}}.(\underset{\sim}{V} + \underset{\sim}{V}_B) \qquad (4.14)$$

where $\underset{\sim}{\hat{i}}$ is the unit vector in the direction of the incident laser beam. Light incident on the photodetector will therefore produce an optical beat frequency, $f_D$, given by,

$$f_D = f_A - f_B = \frac{2\mu}{\lambda} \hat{\underline{i}} . (\underline{V}_A - \underline{V}_B) \qquad (4.15)$$

From figure 4.7, it can be seen that,

$$\underline{V}_A = 2\Pi N \, (\underline{R}_A \times \hat{\underline{z}})$$

$$\underline{V}_B = 2\Pi N \, (\underline{R}_B \times \hat{\underline{z}}) \qquad (4.16)$$

Hence,

$$f_D = \frac{4\Pi\mu N}{\lambda} \hat{\underline{i}} . (\overline{BA} \times \hat{\underline{z}})$$

$$= \frac{4\Pi\mu N}{\lambda} \hat{\underline{z}} . (\hat{\underline{i}} \times \overline{BA})$$

$$= \frac{4\Pi\mu N}{\lambda} \hat{\underline{z}} . \hat{\underline{t}} \, |BA| \sin\theta \qquad (4.17)$$

where $\theta$ is the included angle between $\hat{\underline{i}}$ and $\overline{BA}$, and $\hat{\underline{t}}$ is perpendicular to $\hat{\underline{i}}$ and $\overline{BA}$. However $|\overline{BA}|\sin\theta = 2h$, where $2h$ is the laser beam separation and therefore,

$$f_D = \frac{4\mu\Pi N}{\lambda} 2h \, \hat{\underline{z}} . \hat{\underline{t}}$$

$$= \frac{4\mu\Pi N}{\lambda} 2h \sin\alpha \qquad (4.18)$$

where $\alpha$ is the angle between the plane of the incident beams and the rotational axis. If the instrument is held so that the plane of the incident laser beams is parallel to the shaft cross-section, then $\alpha = \Pi/2$ and,

$$f_D = \frac{4\mu\Pi N}{\lambda} 2h \qquad (4.19)$$

With this optical geometry, the beat frequency is insensitive to radial

and axial shaft (or operator) movement and for constant values of $\alpha$ and $\theta$ will only respond to variations in shaft speed, i.e. torsional oscillations.

For point velocity difference measurements, the torsional vibrometer has a number of practical advantages:
(i) it has a very simple optical geometry requiring only a single beamsplitter and mirror, i.e. no imaging lens,
(ii) it can be employed for measurements on any shape of surface,
(iii) employing the optical geometry shown in figure 4.7 and described above, the transducer is insensitive to solid body motion and the device can therefore be hand-held during measurements.

For the reasons described above, the torsional vibrometer optical configuration offers the most practical solution for a point velocity difference transducer. This transducer is however unable to distinguish the sign of the velocity gradient, the mean rotation speed N, of the target surface providing the required reference frequency shift, (equation 4.19), when making torsional vibration measurements. Therefore additional development of this system is required for velocity gradient measurements on non-rotating surfaces. This work is described in section 4.5.

## 4.5 VELOCITY GRADIENT TRANSDUCER.

With reference to figure 4.8, the velocity gradient transducer has an optical configuration based on the torsional vibrometer[47,48] and utilises a signal processing scheme employed in a laser, fibre vibrometer[49].

This fibre vibrometer, shown in figure 4.9, is a non-contact, laser transducer, for normal-to-surface velocity measurements. Light from a laser diode is launched into one port of a single mode, fibre coupler, and is then directed, via the coupler and a "selfoc" collimating lens onto the target surface. The other output port is finished in index-matching solution to provide an anechoic termination. The "selfoc" lens directs the laser light onto the target surface, and returns backscattered light into the fibre, where it heterodynes on the detector with reference light reflected from the fibre - collimating lens interface. Target and reference light travel the same optical fibre path and hence refractive index variations caused by a hostile noise and vibration environment affect both identically, and are therefore ignored with the heterodyne process.

The fibre vibrometer optical carrier frequency, employed to enable direction information to be obtained, is generated using current modulation of the laser diode. Thus reference and target light incident on the detector differ in phase by an amount proportional to the difference in optical pathlength l, shown in figure 4.9. The detector output contains discrete frequency terms at the diode modulation frequency and higher order harmonics. Control of the diode current modulation amplitude however, allows demodulation of the detector output, and permits a time-resolved, transducer output voltage to be produced, that is an analogue of the target surface vibration velocity.

The fibre vibrometer frequency modulation system was employed in the velocity gradient transducer since it allows the difference in normal-to-surface vibration velocity of two, simultaneously vibrating, target surfaces to be measured, i.e. a reference surface is not

required. This is in contrast to other laser vibrometers, e.g. the I.S.V.R. and PZT laser vibrometers, where one of the two illuminated surfaces is required to generate a carrier frequency. The proposed velocity gradient transducer is described in more detail in the following section.

### 4.5.1 OPTICAL CONFIGURATION.

With reference to figure 4.8, the velocity gradient vibrometer (VGV) employs a laser diode light source, rather than a He-Ne laser. The laser diode physical characteristics are given in Appendix 8.3. At a constant temperature and with a constant potential difference across its terminals, a constant amplitude, or d.c. current through the laser will produce a constant frequency output $f_0$, at a constant power $I_0$. To ensure that these conditions are maintained and for maximum temporal coherence, a stabilised power supply is employed.

The laser diode optical output is both assymmetric and divergent. Hence a commercial two lens, collimating system was employed in the VGV to produce a collimated laser beam. This scheme rigidly maintains the diode-lens positions and is therefore robust and insensitive to vibration.

A major practical consideration when utilising laser diodes for interferometric measurements is prevention of scattered, or reflected light, re-entering the laser diode cavity. This causes "mode-hopping", a non-linear effect that induces the laser to instantaneously jump in optical output frequency, i.e. the temporal coherence of the diode output will decrease. For the VGV system, employment of a polarising filter and quarter wave plate were found to be sufficient to overcome this problem.

With reference to figure 4.8, the VGV system employed a beamsplitter and mirror to produce the two target beams, and then recombine the backscattered light and direct it onto the photodetector surface. This resulted in a system with several practical advantages:

(i) the system was self-aligning and hence robust,
(ii) there was sufficient backscattered light for a PIN diode photodetector to be used, simplifying the electronic circuit design.

## 4.5.2 SIGNAL PROCESSING.

As Dandridge et al[50] have shown, modulation of the laser diode current within the diode linear operation range (Appendix 8.3), will produce a proportional modulation of the diode optical frequency. This variation in emission frequency is mainly due to alteration of the optical pathlength of the laser cavity. For a sinusoidal current modulation, the time-varying laser optical frequency f(t), can therefore be written as,

$$f(t) = f_0 + \delta f \sin\omega_M t \qquad (4.20)$$

where $f_0$ is the optical frequency associated with the d.c. current amplitude, $\delta f$ is the frequency modulation amplitude and $\omega$ is the modulation frequency. The variation of $\delta f$ with drive current modulation amplitude is, as shown by Dandridge, dependent upon the laser diode structure. For the laser employed in the VGV system, $\delta f$ is typically 3 to 6 MHz/mAmp.

A current modulation of this form also produces an intensity modulation, at the modulation frequency, i.e. the diode light intensity is given by,

$$I(t) = I_0(1 + a\sin\omega_M t) \qquad (4.21)$$

where a is the modulation amplitude and $I_0$ is the mean intensity level. This intensity modulation is due to the change in the operating point of the laser. The modulation amplitude a can be predicted from the diode, optical power - current characteristic shown in Appendix 8.3, since measurements show a to be independent of the modulation frequency up to at least 100 MHz[51].

For the interferometer scheme shown in figure 4.8, the optical frequency will be a function of both time and space, e.g. at a distance x from

the diode, the optical frequency f(x,t) will be given by,

$$f(x,t) = f_0 + \delta f \sin\omega_m\left(t - \frac{x}{c}\right) \qquad (4.22)$$

where c is the speed of light. For an optical pathlength imbalance l, where $l=(L+l_1-l_2)$, there will be a phase difference $\theta$, in light scattered onto the photodetector from points A and B. This phase difference will be equal to,

$$\theta = \frac{2\pi}{c}\int_0^{2l}\left[f_0 + \delta f \sin\omega_M\left(t - \frac{x}{c}\right)\right]dx \qquad (4.23)$$

i.e. the phase difference is equal to the summation of the frequency change over the pathlength imbalance. Integrating equation (4.23),

$$\theta = \frac{4\pi f_0 l}{c} + \frac{2\pi\delta f}{\omega_M}\left[-2\sin(-2l\omega_M/c)\sin(\omega_M t - l\omega_M/c)\right]$$

Since $c \approx 10^8$ and $\omega_M l \approx 10^5$, $(\omega_M l/c) \ll 1$ and the phase difference can be written,

$$\theta \approx \frac{4\pi f_0 l}{c} + \frac{4\pi\delta f l}{c}\sin\omega_M t \qquad (4.24)$$

$$= \theta_T + \theta_M \sin\omega_M t \qquad (4.24a)$$

The phase difference term $\theta$ thus consists of two terms,

(i) $\theta_T$, the phase change due to the difference in optical pathlength,

(ii) $\theta_M$, the phase difference in light from the two surfaces due to the change in optical frequency.

Of these two terms, $\theta_T$, equal to 2kl, and hence consistent with classical interferometer systems, is dominant, as $f_0$ is approximately $10^9$ times greater than $\delta f$.

Neglecting polarisation effects, the detector output current i(t) will be of the form,

$$i(t) = \gamma[I_A + I_B + 2(I_A I_B)^{1/2}\cos\theta] \quad (4.25)$$

where $\gamma$ is the detector sensitivity. Rewriting equation (4.25) with $I_A = \chi I_B$,

$$i(t) = \gamma\bar{A}I_B(1 + \Gamma\cos(\theta_T + \theta_M\sin\omega_M t) \quad (4.26)$$

where $\bar{A} = (1+\chi)$, $\Gamma = 2\chi/\bar{A}$. Modulation of the diode current induces an associated modulation of the laser intensity amplitude. Therefore substituting equation (4.21) for $I_B$ in (4.26),

$$i(t) = \gamma\bar{A}I_{BO}(1 + a\sin\omega_M t)[1 + \Gamma\cos(\theta_T + \theta_M\sin\omega_M t) \quad (4.27)$$

where $I_{BO}$ is the mean, backscattered, intensity amplitude from point B. $\Gamma$ is a measure of the modulation depth of the signal or 'fringe visibility' and as will be shown, for accurate signal processing must be maximised. The detector output thus consists of two terms, i.e.

$$i(t) = i_S(t) + i_E(t) \quad (4.28)$$

where $i_S(t)$ is the signal term of interest given by,

$$i_S(t) = \chi\bar{A}I_{BO}[1 + \Gamma\cos(\theta_T + \theta_M\sin\omega_M t] \quad (4.29)$$

and $i_E(t)$ is the error current term given by,

$$i_E(t) = \chi\bar{A}I_{BO}[a\sin\omega_M t + \Gamma a\sin\omega_M t\cos(\theta_T + \theta_M\sin\omega_M t)] \quad (4.30)$$

For accurate signal demodulation, $i_E(t)$ must be minimised. Assuming this term is negligible, $i_S(t)$ may be expanded in terms of Bessel functions as,

$$i_S(t) = \chi\bar{A}I_{BO}\left[1 + \Gamma\cos\theta_T\left\{J_0(\theta_M) + 2\sum_{k=1}^{\infty}J_{2k}(\theta_M)\cos 2k\omega_M t\right\} - \Gamma\sin\theta_T\left\{2\sum_{k=1}^{\infty}J_{2k-1}(\theta_M)\sin(2k-1)\omega_M t\right\}\right] \quad (4.31)$$

The detector signal thus consists of a series of carrier frequency terms at the diode modulation frequency $\omega_M$ and its higher order harmonics, each of which is frequency modulated by the difference in target surface motion. With reference to figure 4.10, mixing this signal with a square wave signal s(t), of Fourier series,

$$s(t) = \frac{1}{2} - \frac{2}{\pi}\sum_{n=0}^{\infty}(-1)^n\frac{\cos(2n+1)\omega_M t}{2n+1} \qquad (4.32)$$

and bandpass filtering at $2\omega_M$ results in the signal,

$$i_{2\omega_M}(t) = K_1\cos 2\omega_M t\cos\theta_T + K_2\sin 2\omega_M t\sin\theta_T \qquad (4.33)$$

where,

$$K_1 = \chi\pi\Gamma I_{BO}J_2(\theta_M) \; ; \; K_2 = \chi\pi\Gamma I_{BO}\frac{8}{\pi}\left[\sum_{n=0}^{\infty}\frac{(-1)^n J_{2n+1}(\theta_M)}{(2n+3)(2n-1)}\right] \qquad (4.34)$$

When $\theta_M = 2.82$ radians, $K_1 = K_2 = K$, and equation (4.33) can be further simplified to,

$$i_{2\omega_M} = K\cos(2\omega_M t - \theta_T) \qquad (4.35)$$

A signal of this form can be demodulated using a phase locked loop (PLL), set to track phase excursions of the 'carrier' frequency $2\omega_M$. The output of the PLL is then proportional to $d\theta_T/dt$ where,

$$\frac{d\theta_T}{dt} = \frac{4\pi f_0}{c}\frac{\delta l}{\delta t}$$

$$\propto v_A - v_B \qquad (4.36)$$

where $v_A$ and $v_B$ are the target surface velocities at A and B, in the direction parallel to the incident laser beams.

Multiplication of the error signal of equation (4.30) by the reference square wave and bandpass filtering at $2\omega_M$ results in an error signal

$i_{2\omega M}(t)'$ of,

$$i_{2\omega_M}(t)' = \chi\Re I_{BO}[E_O \sin\theta_T \cos 2\omega_M t + (E_1 + E_2\cos\theta_T)\sin 2\omega_M t)] \quad (4.37)$$

where $E_O$, $E_1$ and $E_2$ are the error signal terms given by,

$$E_O = \frac{\Gamma a}{2}\left[J_1(\theta_M) - J_3(\theta_M)\right] \quad , \quad E_1 = \frac{-4a}{3\pi}$$

$$E_2 = \frac{-4a\Gamma}{3\pi} J_O(\theta_M) + \frac{a\Gamma}{\pi}\sum_{n=1}^{\infty}(-1)^n J_{2n}(\theta_M)\left[\frac{1}{2n-3} - \frac{1}{2n+1} - \frac{1}{2n+3} - \frac{1}{2n-1}\right] \quad (4.38)$$

For accurate signal demodulation, these error terms must be minimised. This can be achieved[51] by maximising the ratio ($\Gamma$/a). In figure 4.11, the variation of the absolute phase error $E_{PH}$, where $E_{PH} = |E_1 + E_2 + E_3|$, with $\theta_M$, is shown for different value ratios of ($\Gamma$/a). From this figure, with $\theta_M = 2.82 \pm 0.04$ radians, a minimum phase error is obtained with a ($\Gamma$/a) ratio of greater than 50, i.e. $\Gamma$ must be as large as possible and a minimum intensity modulation amplitude must be employed.

From equation (4.24), for a pathlength imbalance of 0.1 m, $\delta f$ is approximately 673 MHz. From Dandridge[50], with a modulation sensitivity of 3 GHz/mAmp, a current modulation amplitude of 0.224 mAmps will be required to produce the necessary frequency shift. From the laser optical power characteristics given in Appendix 8.3, the diode has a sensitivity of approximately 0.125 mW/mA in the diode linear operation range. Therefore for a laser diode optical power of 5 mW, an intensity amplitude modulation a, of approximately 0.0056 is produced. With retroreflective tape applied to both target surfaces, the average backscattered light intensity for points A and B will be approximately equal, i.e. $\Gamma \simeq 1$, and the ratio ($\Gamma$/a) will be much greater than 50. Error terms in $\theta_M$ will therefore be negligible.

For the fibre vibrometer, the condition $\theta_M = 2.82$ radians was maintained using a feedback system. As illustrated in figure 4.10, the detector output signal was bandpass filtered at $2\omega_M$ and $4\omega_M$, using filters with identical amplitude and phase response characteristics, and the ratio

of the two signals taken. This ratio, ideally given by $J_2(2.82)/J_4(2.82)$ = 4.39, was then compared with a reference value and any error signal generated used to vary the laser diode modulation amplitude. For the VGV system however, once $\theta_M$ had been preset, variations in 1 were small and for practical measurements it was not necessary to employ this feedback circuit.

Before practical S.I. measurements were made using the velocity gradient vibrometer, a series of laboratory experiments were carried out to confirm the ability of the transducer to make accurate, consistent vibration measurements. These are described below.

4.5.3 PRACTICAL VIBRATION MEASUREMENTS.

The vibrometer has two vibration frequency measurement ranges, 0-1 kHz and 0-10 kHz, with stationary surface noise floor amplitudes of approximately -110 dB and -100 dB reference 1 m/s respectively. The reduction in sensitivity with increase in vibration frequency bandwidth is due to broadband electronic noise. The upper velocity limit is set by the bandpass filter width in the demodulation circuit at 0.2 m/s, peak-to-peak.

For practical vibration measurements, the scheme shown in figure 4.12 was employed, with the two target laser beams pointed at two accelerometers, each mounted on an electrodynamic shaker which could be excited independently. A small piece of retro-reflective tape was applied to each accelerometer surface to ensure sufficient light was backscattered onto the photodetector. An optical pathlength imbalance of 12 cm was employed for all the following measurements.

Point velocity measurement. Point velocity measurements were made using one stationary and one vibrating shaker. A typical vibrometer velocity spectrum is compared with the integrated accelerometer output in figure 4.13. THe shaker was excited at 141 Hz and the spectra shown contain 100 averages with a 1 Hz frequency resolution. With a maximum difference of 0.3 dB in the peak vibration amplitudes, good agreement is obtained

between the two measurement spectra. The vibrometer has an optical noise floor of approximately -95 dB reference 1 m/s, compared with the accelerometer noise floor of approximately -140 dB reference 1 m/s.

This measurement clearly shows the ability of the vibrometer to make single point, vibration velocity measurements. The system could therefore also be used as a 'free-air' version of the fibre vibrometer system and employed as an alternative to either the PZT, or I.S.V.R. vibrometer structural intensity measurement systems. Since similar levels of inter-transducer phase response error are likely however, there will be no improvement in S.I. measurement accuracy. In addition, unless measurements were restricted to a constant and predefined target-to-detector distance, the feedback system described in section 4.5.2 would have to be employed.

Velocity difference measurement. To measure the velocity difference, $V_A$-$V_B$, between two vibrating points, the system shown in figure 4.12 was employed with both shakers being driven, but at different frequencies and with different amplitudes. The spectra shown in figure 4.14 show the integrated vibration spectra obtained from the two accelerometers, representing the two shaker velocities. Figure 4.15 shows the velocity difference measured by the vibrometer, representing the difference between the two vibration velocity spectra shown in figure 4.14. Both sets of spectra contain 100 averages with a 1 Hz frequency resolution.

The amplitudes of the vibration peaks shown in the velocity difference, frequency spectrum of figure 4.15 are similar to those of the two, accelerometer measured, velocity spectra of figure 4.14. This measurement therefore proves the ability of the VGV system to take velocity difference, and hence using a finite difference approximation, velocity gradient measurements.

## 4.6 STRUCTURAL INTENSITY MEASUREMENTS.

The S.I. measurement scheme employing a velocity gradient vibrometer and the PZT vibrometer is shown in figure 4.16. A point separation of 10 cm was employed, with the velocity measurement at the centre of points A and B.

Comparison of equations (4.5) and (2.21) shows the scheme proposed in figure 4.16 to have a different finite difference approximation error to the two transducer scheme. The ratio of the two correction factors is given by,

$$(kh_V/\sin kh_V) \;/\; (2kh_A/\sin 2kh_A) \qquad (4.39)$$

where $2h_V$ and $2h_A$ are the VGV and accelerometer separations respectively. Therefore for $h_A = (h_V/2)$, the structural intensity measured by the two methods will be the same, without any finite difference approximation correction factor being applied.

Simultaneous, practical S.I. measurements were made using the two measurement methods, with the laser transducers positioned 50 cm along the theoretically infinite beam from the accelerometers. This was to investigate the effect of the use of contacting transducers on the measured S.I.. Mass-loading of the beam was not expected to be significant since 2 gram accelerometers were employed.

Computer generated, narrow band excitation was used to make measurements over the frequency range 500 to 2250 Hz, with 250 Hz frequency increments. Two excitation amplitudes, varied using a power amplifier and measured by the PZT vibrometer, were employed over the specified frequency range:

(i) a 'mid-range' velocity amplitude of approximately -55 dB reference 1 m/s,

(ii) a low velocity amplitude range of approximately -75 dB reference 1 m/s.

The results given in figure 4.17 were obtained with a 3.2 kHz frequency bandwidth and a 1 Hz frequency resolution. Ten averages of each measurememt were made. These results show the agreement between the VGV and two accelerometer measurement methods to be within experimental error, i.e. a maximum difference of -0.9 dB, and an average difference of -0.44 dB. The difference in measurement results is due to a combination of inter-transducer amplitude and phase response errors, and internal damping of the beam reducing the travelling wave amplitudes measured by the two methods. If the mass-loading effects noted in Chapter 2 were significant, the acceleration, and hence the S.I. amplitude would be reduced, relative to their true values. Since the two accelerometer method results are generally larger then those measured by the laser-transducer method, mass-loading effects are not significant.

These results not only show the VGV method to be the most accurate laser, S.I. measurement scheme, but also to have a measurement accuracy comparable with the two accelerometer method. In addition the two accelerometers were chosen for their close amplitude and phase match, while both laser transducers were only prototype devices. Use of a 'matched-pair' of laser transducers will therefore further improve the measurement accuracy.

## 4.7 CONCLUSIONS ON THE LASER, STRUCTURAL INTENSITY METER.

It has been shown theoretically how, employing a laser, structural intensity meter consisting of a velocity gradient transducer and a laser vibrometer, the structural intensity measurement accuracy can be improved. This is acheived through reduction of the technique sensitivity to inter-transducer phase errors and simplification of the signal processing required for calculating the structural intensity.

The velocity gradient may be calculated using a finite difference approximation from the difference in velocity between two points, divided by the point separation. Three laser velocity gradient measurement methods - shearography, (a whole field technique which could be adapted for point measurements), velocity gradient anemometry and the I.S.V.R. torsional vibrometer - have been described and their use in a laser structual intensity measurement scheme discussed. With its simple optical geometry, robustness and insensitivity to solid body motion, the torsional vibrometer was chosen as the most appropriate method. For measurements on non-rotating target surfaces, this transducer provides no vibration direction information. A pseudo-heterodyne frequecy modulation system, based on a frequency modulated laser diode and an unbalanced Michelson Interferometer optical configuration, was utilised to overcome this problem. Signal demodulation, based on a system originally developed for a fibre-optic laser vibrometer, was then employed to give a transducer output proportional to the difference in normal-to-surface velocity between two points on a target.

Velocity and velocity difference measurements using the new, laser velocity gradient transducer show the vibrometer, in common with other laser vibrometer systems, to suffer from dynamic speckle noise effects associated with large amplitude, non-normal target surface motion. Levels of this amplitude are unlikely to be produced in practical situations however, and as discussed in Chapter 5, can be neglected for most practical vibration measurements. Velocity and velocity difference amplitudes of normal-to-surface vibration measured using the velocity gradient transducer have compared favourably with simultaneously

acquired acccelerometer measurements. The transducer has therefore been employed for S.I. measurements.

One-dimensional, flexural wave, structural intensity measurements using the laser velocity gradient transducer, and a laser, point velocity transducer, have been made over the frequency range 500 to 2.25 kHz, at two different excitation amplitudes. Measured results compared well with those obtained simultaneously with the two accelerometer scheme of Chapter 2, with an average measurement difference of -0.44 dB (4.9%), i.e. within practical measurement error limits.

The proposed laser transducer configuration thus allows S.I. measurements to be made with an accuracy comparable with the widely used, two accelerometer method. The laser transducer method has in addition however, all the advantages of non-contact use, i.e. simple, point and shoot measurements are possible, a large number of measurements can be made quickly, and there are no mass-loading effects on low density and lightly damped structures. This transducer scheme therefore offers a superior alternative to the existing two accelerometer S.I. measurement technique.

## 5. LASER VIBROMETRY : PSEUDO-VIBRATIONS.

Speckle patterns are a feature common to all laser vibrometer measurements on diffuse target surfaces. These granular light intensity patterns are produced when coherent light is scattered from a surface that is rough on the scale of an optical wavelength, i.e. most surfaces of engineering interest. In many measurement situations, laser speckle patterns have little effect upon the vibrometer performance and can be neglected. However, when the target surface undergoes some form of non-normal or tilt motion, as well as the normal-to-surface vibration of interest, speckle noise problems can occur. These include reduction of the device sensitivity through the introduction of random speckle phase noise, and insufficient, resultant light intensity incident on the detector for a discernable signal to be produced.

Further to these random effects, it has recently been shown[32,33,39] that when making laser vibrometer measurements on surfaces undergoing *periodic*, non-normal motion, spectra similar to those obtained for normal-to-surface vibration of the same period are recorded. These 'pseudo-vibration' signals have been shown to be caused by the associated, speckle pattern dynamics. For practical laser vibrometer measurements, these signals may be indistinguisable from, and can easily mask, genuine, normal-to-surface vibration. Hence measurements of flexural wave, structural intensity will not be independent of other wave motion in a structure, e.g. longitudinal waves, and the accuracy of any laser power flow meter will be reduced. It is therefore important that when the vibration engineer uses the structural intensity measurement technique, he has an appreciation of when speckle noise problems may occur, and what levels of pseudo-vibration signal might arise.

This chapter reviews the formation of laser speckle and its spatial characteristics; describes how speckle pattern dynamics effect the light intensity backscattered onto the vibrometer photodetector, and what effect this has on the detector output. How the vibrometer signal is interpreted as normal-to-surface vibration is then discussed and from

the results of carefully controlled, practical measurements, qualitative comparisons are made with theoretical predictions. Finally, situations where laser speckle effects are likely to be a problem and typical vibrometer sensitivity levels to in-plane and tilt vibration are identified.

## 5.1 LASER SPECKLE PATTERNS.

With reference to figure 5.1, a speckle pattern is produced when component wavelets of an incident laser beam are dephased on scattering from a surface that is rough on the scale of the optical wavelength, i.e. a diffuse surface. This includes most surfaces of engineering interest. Interference of these dephased but still coherent wavelets, results in a chaotic light intensity distribution referred to as a speckle pattern. Due to their random nature, the properties of laser speckle patterns are described statistically. Speckle intensities have a negative exponential probability distribution, and a random phase distribution of between 0 and $2\pi$ radians[31]. It has been shown[53] that speckles are 'cigar-shaped' volumes of approximately constant intensity and phase. Objective speckle patterns contain speckles with a spatially correlated diameter $\langle\sigma_D\rangle$ and length $\langle\sigma_L\rangle$ given by,

$$\langle\sigma_D\rangle \approx \frac{1.22\lambda L}{D} \quad ; \quad \langle\sigma_L\rangle \approx \frac{\lambda L^2}{D^2} \qquad (5.1)$$

where $\lambda$ is the optical wavelength, L is the scattering surface to viewing plane distance and D is the laser spot size as shown in figure 5.1. For a normally incident laser beam, motion of the target surface in some non-normal direction, e.g. tilt, in-plane or rotation, will cause the speckles to either "boil", translate or perform some combination of these two[54].

Speckle translation is the term used to describe how speckles move as a whole, in a direction parallel to the direction of the target surface motion. In contrast, when individual speckles deform, disappear and new speckles reappear without any appreciable displacement of the speckle position, speckle "boiling" is said to have taken place.

Considering the laser-illuminated area to consist of millions of point scatterers, then, as will be shown, the resultant amplitude and phase of each speckle is equal to the summation of many light amplitude contributions. Therefore as the diffuse surface, for example, tilts, the scattered light that produces the speckle pattern will undergo a phase

change, that is independent of where the light was scattered from. This is seen as a translation of the speckle pattern, with each speckle undergoing the same displacement. Speckle translation will therefore occur when there is a change in the angle the incident laser beam makes with the target surface.

In comparison, speckle "boiling" is caused by a change in illumination area due to, for example, in-plane target motion. The resulting change in the point scatterer population causes the intensity and phase of each speckle in the pattern to vary independently, i.e. some speckles will dramactically change while there will be apparently little variation in others.

Laser vibrometer measurements on surfaces undergoing non-normal as well as normal-to-surface vibration will therefore suffer from the effects of random amplitude and phase modulation of the detector output, due to the random change in the incident speckle pattern. This effect is discussed in greater detail in section 5.2.

## 5.2 THEORY OF PSEUDO-RANDOM VIBRATION.

For convenience, consider the vibrometer configuration shown in figure 5.2[27], where the reference beam incident on the detector has uniform amplitude $E_R$, and phase $\theta_R$, and has undergone a constant frequency shift $\omega_R$. Neglecting polarisation effects, the instantaneous reference light amplitude incident on the photodetector is given by,

$$E_R(t) = E_R\cos[(\omega + \omega_R)t + \theta_R] \qquad (5.2)$$

where $\omega$ is the laser light frequency. The output of the photodetector may be predicted from the phasor addition of the contributions from the target and reference beams in each element of area, and subsequent integration over the entire area. For a stationary target surface, the contribution of the $p^{th}$ speckle on the detector from the target may be written,

$$E_{TP}(t) = E_{TP}\cos[\omega t + \theta_{TP}] \qquad (5.3)$$

where $E_{TP}$ and $\theta_{TP}$ are the amplitude and phase of the $p^{th}$ target speckle respectively. For sinusoidal, normal-to-surface vibration, the effect of the speckle motion on the light amplitude is negligible. In contrast the speckle phase term is modulated by the displacement and equation (5.3) may be rewritten,

$$E_{TP} = E_{TP}\cos(\omega t + \theta_{TP} - 2kA_T\sin\omega_T t) \qquad (5.4)$$

where $A_T$ and $\omega_T$ are the target displacement amplitude and frequency respectively, and k is the light wavenumber. Summing the reference and target beam contributions, the resultant intensity $I_P(t)$ over each speckle area is,

$$I_P(t) = |\, E_{TP}(t) + E_R(t) \,|^2$$

$$= I_{TP} + I_R + 2(I_{TP}I_R)^{1/2}\cos[(\omega_R t + 2kA_T\sin\omega_T t) + (\theta_R - \theta_{TP})] \qquad (5.5)$$

where $I_R$ and $I_{Tp}$ are the intensities of the reference beam and $p^{th}$ target beam speckle respectively. With each speckle assumed to have constant phase and intensity over its extent, the component $i_p(t)$ of the photodetector output current due to interference of the $p^{th}$ target beam speckle and the frequency shifted reference beam, is given by,

$$i_p(t) = \gamma S_p I_p(t) \tag{5.6}$$

where $\gamma$ is the photodetector sensitivity and $S_p$ the $p^{th}$ speckle area. Modelling the continuous speckle distribution as discrete areas of constant amplitude and phase, for P speckles incident on the detector the total photodetector output i(t) may be expressed in the form,

$$\begin{aligned} i(t) &= \sum_{p=1}^{P} i_p(t) \\ &= \gamma\{I_R + I_{res} + 2(I_R I_{res})^{1/2}\cos[(\omega_R t + 2k a_T \sin\omega_T t + (\theta_R - \Xi_{res})]\} \end{aligned} \tag{5.7}$$

where,

$$I_{res} = \left[ \sum_{p=1}^{P} \sum_{q=1}^{P} S_p S_q (I_{Tp} I_{Tq})^{1/2} \cos(\theta_{Tp} - \theta_{Tq}) \right]^{1/2} \tag{5.8}$$

and,

$$\tan(\Xi_{res}) = \frac{\sum_{p=1}^{P} S_p (I_p)^{1/2} \sin(\theta_R - \theta_{Tp})}{\sum_{p=1}^{P} S_p (I_p)^{1/2} \cos(\theta_R - \theta_{Tp})} \tag{5.9}$$

where $I_{res}$ and $\Xi_{res}$ are the resultant speckle pattern intensity and phase. These expressions are derived in Appendix 8.5. It can be seen from equation (5.8) that when $(\theta_{Tp} - \theta_{TQ}) = (2n + 1)\pi/2$, where $n=0,\pm1,\pm2..\infty$, low signal amplitudes will occur, resulting in problems

for the signal demodulation electronics.

If the P target beam speckles on the detector do not change in either phase, amplitude or position relative to the detector, then both $I_{res}$ and $\Xi_{res}$ are constant in time and the measured beat frequency $\omega_D$, given by the time derivative of the argument of the cosine term in equation (5.7), i.e.

$$\omega_D = \omega_R + 2kA_T\omega_T\cos\omega_T t - \frac{d\Xi_{res}}{dt} \qquad (5.10)$$

is equal to the required value of,

$$\omega_D = \omega_R + 2kA_T\omega_T\cos\omega_T t \qquad (5.11)$$

since $d\Xi_{res}/dt = 0$. Neglecting electronic noise, the vibrometer output spectrum will consist of a single peak at $(\omega_T/2\pi)$ Hz. However if the spatial characteristics of the speckle pattern incident on the detector change, both the summed speckle intensity and phase terms of equations (5.8) and (5.9) become time dependent, leading to a non-zero and time-dependent value of $d\Xi_{res}/dt$. The output spectrum will now consist of a peak at $(\omega_T/2\pi)$ Hz and spurious noise corresponding to the frequency content of $d\Xi_{res}/dt$. In addition, should the non-normal motion be periodic, the associated speckle pattern changes will repeat at the same fundamental frequency and introduce pseudo-random fluctuations in $d\Xi_{res}/dt$. A typical pseudo-random vibrometer output signal is shown in figure 5.3. The characteristic spectrum of this pseudo-random signal consists of approximately equal amplitude peaks at the fundamental frequency and subsequent harmonics. Hence for a non-normal motion of frequency $\omega_V$, the output spectrum of the instrument will consist of peaks at frequencies given by,

$$f = n\omega_V/2\pi, \qquad n = 1,2,\ldots,\infty \qquad (5.12)$$

Should the non-normal and normal-to-surface vibrations be at the same frequencies, i.e. $\omega_T = \omega_V$, then the spurious, 'pseudo-vibration' will be indistinguisable from the genuine vibration information. The magnitude

of each harmonic noise peak will depend on the amplitude and rate of fluctuation in $d\Xi_{res}/dt$, which in turn, depends upon the dynamic characteristics of the non-normal motion and the detector and speckle size involved.

### 5.2.1 DYNAMIC SPECKLE NOISE SPECTRA.

Typical dynamic speckle noise spectra were measured using the scheme shown in figure 5.4. The retro-reflective tape-coated edge face of a rotating disc was illuminated by a monochromatic laser beam. Light backscattered from the disc was incident on a photodetector, the output of which was high-pass filtered to remove the d.c. bias voltage, and then digitally acquired. The auto-power spectrum of each noise signal was then calculated. No reference surface was employed since any Doppler frequency shift from the rotating disc made comparison of the speckle noise spectra difficult. The disc rotation speed was controlled via its d.c. power supply and measured using a stroboscope.

The range of speckle sizes employed was based on typical vibrometer measurement conditions, i.e. target-detector distances of between 26 cm and 56 cm. The disc rotation speeds were based on the disc motor range, i.e. up to 50 Hz. Speckle noise spectra were measured with,
(i) the speckle size $\langle\sigma_D\rangle$ constant and the disc rotation speed varied over the frequency range 6 to 30 Hz, in 6 Hz increments,
(ii) the disc speed constant and the speckle size varied, as tabulated in figure 5.5.

For all speckle noise spectra the detector output was digitally sampled at 750 kHz to allow direct frequency comparisons to be made. Sample durations were set equal to the rotation period, ensuring that a) no pseudo-random data was acquired and b) there was equal noise energy in each sample. The acquisition system frequency response function was measured using a broadband 'white noise' signal from 0 to 1.5 MHz, and was found to be linear over the measured frequency range. For comparison, the stationary speckle, 'noise' signal was acquired with each set of speckle noise spectra.

The dynamic speckle noise auto-spectra shown in figure 5.6 were obtained with a target-detector distance of 26 cm and a range of disc rotation speeds. These spectra show that the noise amplitude at higher frequencies increases with increasing disc speed while at lower frequencies it decreases with increasing disc speed. This can be attributed to the fact that at higher disc rotation speeds the residence time of a speckle incident on the detector is reduced, and an increase in the rate of change of speckle phase occurs. Hence over one disc rotation period, the dynamic speckle noise modulation of the detector output occurs in an increasingly shorter time, or at greater frequencies. The noise content at higher frequencies thus increases at the expense of lower frequencies.

In comparison, figure 5.7 shows the effect of varying the speckle size $\langle\sigma_D\rangle$, by varying the target-detector distance L, at a constant disc rotation frequency f, of 12 Hz. For the range of speckle sizes shown, there is little difference in noise spectrum characteristics. This effect is as expected however since both $\langle\sigma_D\rangle$ and the speckle speed across the detector $2\pi fL$, increase linearly with L, i.e. the resultant phase of light incident on the photodetector will change at a constant rate, independent of L. It can therefore be concluded that for a constant disc rotation speed, the noise amplitude frequency distribution is independent of the target-detector distance. This result is common to all laser vibrometer systems which use an unfocused, target laser beam, and hence have more than one speckle incident on the photodetector, i.e. all four laser vibrometer schemes described in this thesis.

### 5.2.2 INTENSITY VARIATION DUE TO DYNAMIC SPECKLE EFFECTS.

Equation (5.8) shows that the nominally time invariant, target beam intensity term, $I_{res}$, becomes time dependent when the target surface undergoes non-normal motion. Considering the two $I_{res}$ terms in equation (5.7) separately,

(i) the interference $I_{RES}$ term will be simultaneously, randomly modulated by both the intensity and phase of the backscattered target laser beam, and so these two effects are considered together in the

experimental results described in section 5.4,

(ii) the non-interference $I_{res}$ term will become time dependent and could introduce spurious, optical noise signals into the vibrometer demodulation scheme. However as shown in the previous section, a 30 Hz disc rotation speed results in a noise spectrum with energy only up to approximately 250 kHz, and can thus be removed by high-pass filtering of the detector output signal.

## 5.3 SOURCES OF PSEUDO-VIBRATION.

In practical engineering situations, there exist three types of non-normal motion that can induce the speckle pattern changes discussed above: in-plane, tilt and rotation. If the target-detector distance is sufficiently large to satisfy the Fraunhofer assumption[55], light in the far-field observation plane is proportional to the two-dimensional spatial Fourier transform (FT) of the target plane. The effect these non-normal motions have on the detector-plane speckle pattern may therefore be explained in terms of Fourier optics.

For a typical target-detector distance of 30 cm, the amplitude distribution can be described using the Fourier transform theory but the phase distribution cannot[55]. However since a photodetector measures the light intensity, or the amplitude squared, the Fourier optics theory can still be applied.

If, with no target motion, the complex light amplitude distribution in the target and detector planes is given by $\underline{E}(x_t,y_t)$ and $\underline{E}(x_d,y_d)$ respectively, then the two are related by the expression,

$$\underline{E}(x_d,y_d) \propto FT\{\underline{E}(x_t,y_t)\} \qquad (5.13)$$

evaluated at spatial frequencies $(x_d/\lambda L)$, $(y_d/\lambda L)$, where $\lambda$ is the laser wavelength and L is the target-detector distance. The effects of tilt and in-plane motion may now be predicted using the shift theorem of Fourier transforms. To model a small, two-dimensional tilt of amplitude $(\theta_X,\theta_Y)$ radians, the target plane light amplitude is pre-multiplied by a phase factor, which may be written as,

$$FT\{\exp[-j2k(\theta_X x_t + \theta_Y y_t)].\underline{E}(x_t,y_t) \propto \underline{E}(x_d + 2\theta_X L,\ y_d + 2\theta_Y L) \qquad (5.14)$$

Therefore tilt of the target produces an in-plane displacement of the detector plane speckle pattern, equivalent to $2\theta_X L$ and $2\theta_Y L$ in the $x_d$ and $y_d$ directions respectively. The speckle pattern translates across the detector surface and the changing population of speckles produces

amplitude and phase modulation of the detector output. Conversely, a two dimensional, in-plane translation of the target of amplitude $(u_X, u_Y)$ meters, will impose a linear phase ramp through the detector plane speckle pattern, given by,

$$FT\{\underline{E}(x_t - u_X,\ y_t - u_Y)\} \propto \exp[-j(2\pi/\lambda L)(u_X x_d - u_Y y_d)].\underline{E}(x_d, y_d) \quad (5.15)$$

In practice, for small in-plane translations, amplitude and phase modulation of the detector output occurs through phase changes of the target speckles on its active area. Larger in-plane translations involving significant changes in the illuminated population of scatterers, will begin to cause decorrelation of the speckle pattern, i.e. speckle 'boiling', will take place. In this case, amplitude and phase modulation of the detector output again occurs through the continuous change in the population of speckles on the detector.

The more complex case of rotation may be considered as a combination of the above two effects, where amplitude and phase modulation of the detector output again occurs through the continuous change in the speckle pattern incident on the detector.

## 5.4 EXPERIMENTAL RESULTS.

The laser vibrometer shown in figure 5.2 was used to measure the normal-to-surface velocity of a target excited by an electrodynamic shaker at 50 Hz. The spectrum shown in figure 5.8 is typical of laser vibrometer measurements on a periodically excited structure, where the vibrational energy is concentrated at the fundamental frequency and higher order harmonics.

Figures 5.9a and 5.9b show a comparison of vibrometer and integrated accelerometer measurements taken from a target surface translating in-plane. These measurements were obtained using the configuration shown in figure 5.10, from a cylindrical bar running in a high tolerance bearing and driven by an electro-dynamic shaker. The target laser beam was incident on the end of the bar, in a direction perpendicular to the in-plane excitation. The bar end was machined flat, coincident with the bar rotational axis. Accelerometers were positioned on the bearing housing to provide comparative, normal-to-surface vibration measurements, and on the bar end to measure the in-plane motion.

As shown in figure 5.9, the vibrometer velocity measurements are typically 30 dB higher than those measured by the accelerometer. The first flexural and longitudinal resonance frequencies of the bar are 823 Hz and 35.1 kHz respectively[52], and are therefore well above the excitation frequency and its harmonics shown in figure 5.9. These frequencies are calculated in Appendix 8.6. It is therefore clear that the vibration energy in the harmonics of the vibrometer spectrum is spurious and due to the effect of in-plane motion on the laser speckle.

The accelerometer-measured, in-plane velocity amplitude of -30 dB reference 1 m/s at 50 Hz, is equivalent to a displacement amplitude of approximately 0.1 mm. Hence over one period of vibration, the laser illuminated area will change by 20% and both speckle boiling and speckle translation will take place.

Figure 5.11 shows the vibrometer output from a bar undergoing a tilt

excitation. This was achieved by connecting the bar to the shaker via a crank arrangement, so that the bar was forced to rotate about its rotational axis. It was therefore possible to obtain pure tilt measurements with negligible in-plane or normal-to-surface motion. As with the in-plane excitation, the spectrum contains energy at the fundamental motion frequency and higher order harmonics.

Figure 5.12 shows the vibrometer output from a target rotating at a constant speed. As with the previous measurements, there are pseudo-vibration peaks at the rotation speed and harmonics although there is nominally no normal-to-surface vibration. However in contrast to the previous measurements, the harmonic amplitude does not 'roll-off' at higher frequencies, remaining approximately constant with some random variation. This is typical of measurements made under conditions where a large number of changes occur in the speckle pattern incident on the detector. However this form of vibration spectrum is easily identifiable as being due to pseudo-random speckle effects, since, for genuine vibration signals, a majority of the vibration energy will be concentrated at the fundamental frequency, with an appreciable roll-off in the amplitude of any harmonics. Therefore compared with the in-plane and tilt motion cases, spectra of this form are less likely to be confused with genuine vibration.

### 5.4.1 LOW AMPLITUDE MEASUREMENTS.

In Chapter 3, a new, high-sensitivity laser vibrometer was used to measure low velocity amplitude, structural intensity. Employing a new design of signal demodulation circuit, the PZT vibrometer is able to make velocity measurements down to -140 dB reference 1 m/s, 30 dB lower than is possible using the rotating diffraction grating vibrometer used in section 5.4. Hence for the low velocity amplitude, quantitative measurement of pseudo-random, speckle effects that follows, it was decided to use the PZT laser vibrometer[30].

The PZT vibrometer employs a piezo-electric element, reference surface which is driven at a resonance frequency of 750 kHz, with an amplitude

of approximately $\lambda/2$. The reference surface speckle pattern therefore sinusoidally oscillates, normally through the detector plane, also with a peak displacement amplitude of $\lambda/2$. From equation (5.1), using a 1 mm diameter He-Ne laser beam with a reference-to-detector distance of 30 cm, the average speckle length is 57 mm. Therefore there will be negligible change in the reference surface speckles incident on the photodetector, and any dynamic speckle modulation of the detector output will be due to target surface motion alone.

The following measurements were limited to low amplitude excitation levels of in-plane and tilt target surface motion because,
(i) at high excitation levels, pseudo-random vibration spectra are easily identifiable as such,
(ii) for rotating surfaces, torsional wave motion will be the dominant energy transmission waveform and flexural wave, structural intensity measurements will not be necessary,
(iii) at low excitation levels it is not easy to discern the relative amplitudes of normal-to-surface and non-normal vibration amplitudes and so misinterpretation of the vibration data could occur.

## 5.4.2 IN-PLANE VIBRATION MEASUREMENTS.

Employing the scheme shown in figure 5.10, in-plane vibration measurements were made using the PZT vibrometer, with acclerometers on the bar end and bearing housing providing comparative, in-plane and normal-to-surface velocity measurements respectively. For a sinusoidal, in-plane displacement of the cylindrical bar of y, given by $u = U\sin\omega t$, there will be an in-plane velocity $du/dt$ of $U\omega\cos\omega t$, where U is the displacement amplitude and $\omega$ the excitation frequency. Figures 5.13 and 5.14 show how the amplitude of the vibrometer velocity signal at the fundamental frequency varies with in-plane velocity, for constant amplitude (U) and frequency ($\omega$) respectively. These results demonstrate that an approximately linear relationship exists and that higher amplitude levels are measured when the in-plane velocity of the target is higher.

The speckle velocity across the detector is synonymous with the in-plane target velocity and hence higher amplitudes produce more rapid rates of change of phase. In this way, the pseudo-vibration signal term in equation (5.11), $d\Xi_{res}/dt$, increases in amplitude, as shown in figure 5.13.

Both figures 5.13 and 5.14 show that for constant in-plane velocity amplitude, i.e. similar speckle speeds across the detector, it is the larger target displacement which produces higher spurious levels of vibration. This is attributed to the effect of speckle boiling mentioned earlier, which is more significant at larger displacement amplitudes. Figure 5.15 illustrates the effect of a constant in-plane excitation velocity amplitude over a range of excitation frequencies. This is an approximately constant relationship, except at higher excitation levels and lower frequencies, where, because there is relatively larger in-plane displacement, speckle boiling tends to dominate the rate of change of phase term, $d\Xi_{res}/dt$.

It should be noted that in-plane velocity amplitudes of -35 and -55 dB reference 1 m/s, produce average normal-to-surface, pseudo-vibration velocity amplitudes of approximately -69 and -79 dB. These figures correspond to transverse sensitivities of approximately 2 and 6% respectively, comparing favourably with an accelerometer[35].

### 5.4.3 TILT VIBRATION MEASUREMENTS.

For tilt motion of the target, the measurement system was as shown in figure 5.10, but with the shaker attached via a crank arrangement to the bar. Measuremnts were taken on the centreline of the flat, end surface of the bar. The tilt velocity was measured by an accelerometer positioned on the shaker. With a 35 mm long moment arm, a measured rms tilt velocity of -45 dB relative to 1 m/s, corresponds to an rms tilt angle rate of 161 milliradians per second. An accelerometer mounted on the bearing housing provided normal-to-surface velocity spectra for comparison with the vibrometer measurements.

Figures 5.16 and 5.17 show the relationship between the fundamental frequency, pseudo-vibration velocity amplitude and the tilt velocity, with constant tilt amplitude and frequency respectively. From these figures it can be seen that there exists an approximately linear relationship and that higher amplitude levels are measured when the tilt velocity is higher.

The tangential speckle velocity across the detector is equal to twice the local target surface tilt velocity. Therefore for a target to detector distance of L, a tilt of $\theta$ degrees will produce a peak speckle velocity across the detector of $2Ld\theta/dt$. For a constant tilt amplitude, an increase in the tilt frequency will increase the speckle velocity across the detector. The same effect will also be produced by increasing the tilt amplitude for a constant frequency. Both these effects will therefore result in an increase in $d\Xi_{res}/dt$, with, as shown in figures 5.16 and 5.17, an associated rise in the pseudo-vibration signal amplitude.

Figures 5.16 and 5.17 also show that for a constant tilt velocity, larger target displacements produce higher spurious levels of vibration. As with the in-plane results, this is directly attributable to speckle boiling effects, which are larger for greater tilt angles.

Figure 5.18 illustrates the effect of constant velocity amplitude, tilt excitation over a range of excitation frequencies. As with the in-plane excitation shown in figure 5.15, there exists an approximately constant relationship between the tilt velocity amplitude and the pseudo, normal-to-surface velocity signal. However, also as shown in the in-plane measurements, for higher tilt excitation levels and lower tilt frequencies, larger pseudo-vibration levels are produced as a result of the greater change in scattering population, which increases the 'boiling' effect.

## 5.5 CONCLUSIONS ON LASER SPECKLE EFFECTS.

Spurious, pseudo-vibration speckle noise effects are inherent in all Laser Doppler Vibrometer measurements on diffuse surfaces, i.e. most surfaces of engineering interest. It has been shown how in-plane, tilt and rotation of the target surface can all introduce pseudo-random speckle noise into the vibrometer photodetector output. When the laser vibrometer output spectrum is examined, pseudo-vibration peaks, which can easily be interpreted as normal-to-surface vibration, can result.

For larger excitation levels and displacements, both speckle boiling and translation occur and produce characteristic pseudo-vibration spectra. Since the magnitude of the fundamental and harmonic frequency signals are comparable, i.e. there is no roll-off in the harmonic signal amplitude relative to the fundamental frequency signal, spectra of this form are easy to distinguish from genuine vibration spectra.

Measurements taken using the PZT vibrometer illustrate that at low vibration levels, speckle translation is the predominant dynamic speckle variation effect. Measurements show that there exists an approximately linear relationship between the non-normal velocity amplitude, and the pseudo, normal-to-surface, vibrometer velocity at the motion frequency. The spectra obtained from these measurements were often indistinguishable from genuine vibration and hence could lead to errors due to misinterpretation of measured data. However it should be noted that these measurements were obtained under 'worst case', laboratory conditions and correspond to cross-sensitivities comparable with typical accelerometers.

For many practical vibration measurements, the non-normal motion is unlikely to produce an exactly repeating speckle pattern variation across the photodetector. The speckle noise in the detector output will therefore quickly decorrelate, reducing both the amplitude of the pseudo-vibration signals and increasing the roll-off in harmonic amplitude at higher frequencies. Hence provided care is taken in interpreting measurement data, pseudo-vibration effects will only be of

concern when both, a) the relative magnitude of normal-to-surface and non-normal velocities is unknown, and b) the non-normal motion results in a consistent, pseudo-random modulation of the detector output.

## 6. CONCLUSIONS.

At present there are a number of structural noise and vibration analysis techniques, e.g. approximate mobility methods, statistical energy analysis, finite element analysis and correlation techniques. These techniques, in conjunction with practical vibration measurements, do not, however, supply sufficient information for individual vibration pathways in a built-up structure to be identified. The power flow measurement technique in contrast, allows the net, vibration energy transmission through each, individual structural component to be evaluated, both in terms of its magnitude and direction. The energy distribution throughout the entire structure can then be assimilated directly from practical vibration measurements.

The power flow measurement technique is of most practical advantage in complex, built-up structures where there are many vibration transmission paths from the primary vibration source, e.g. an engine, to some point of interest. Under these conditions, power flow measurements at many points permits the energy transmission distribution to be evaluated and thus vibrational control techniques to be most efficiently applied.

As the major source of acoustic radiation, flexural wave motion has received the most research interest. Employing the Euler-Bernoulli description of vibration energy propagation in simple beam-like or one-dimensional structures, i.e. ignoring rotational inertia and shear deformation, the flexural wave, power flow has been shown to consist of two components; one due to the shear force and the other to the bending moment set up in the beam. Close to vibration sources, sinks and discontinuities such as changes in cross-section, material density etc, the relationship between these two components is complex, and for accurate power flow measurements to be made, both must be measured simultaneously. A scheme employing four linear accelerometers has been proposed to allow such measurements to be made. This scheme however is difficult to implement and each power flow measurement requires a large amount of signal processing.

Of greater simplicity and hence practical use is the 'far-field' scheme, i.e. at a distance greater than one-fifth of a wavelength from a discontinuity, where since the time-average shear force and bending moment components are equal, only one component needs to be measured. Although a range of transducer configurations can be utilised to realise this scheme, two linear accelerometers are usually employed because of their wide dynamic range and broad vibration frequency bandwidth.

It has been shown that the major source of structural intensity measurement error using the two transducer technique is the inter-transducer phase response error. This is most significant in evaluating the spatial vibration derivative from the difference in transducer outputs. Employing accelerometers to measure the vibration gradient, the S.I. measurement technique becomes susceptible to phase errors due to: (i) transducer phase variation, dependent upon factors such as temperature, vibration amplitude and time, as the vibration frequency of interest approaches the inherent transducer resonance frequency; (ii) accelerometers mass-loading the structure, resulting in a vibration signal output that is reduced in amplitude and shifted in phase; (iii) vibration of the accelerometer cable introducing spurious phase errors into the transducer output. With a direct means of measuring the spatial vibration gradient, e.g. the velocity gradient, these sources of measurement error will no longer be of concern.

In recent years, laser technology, and particularly laser Doppler vibrometry, has come into widespread use for vibration measurements. Laser vibrometers facilitate remote, non-contact vibration measurements and quick, simple, 'point-and-shoot' operation, i.e. a large number of measurements can be made quickly and accurately over large, extended structures. Therefore inclusion of laser transducers in the power flow measurement technique offers the potential to greatly enhance both the technique accuracy and the range of vibration environments in which measurements can be made.

Two I.S.V.R. laser vibrometers have been utilised as a direct substitute for accelerometers in the two-transducer, power flow measurement

technique. Comparison of measurement results with the two accelerometer method show the system to be accurate, (± 1.2 dB reference 1 Watt), provided that the normal-to-surface velocity amplitude is greater than the device optical noise floor level. This maximum sensitivity is determined by the rotating disc, frequency shift mechanism at approximately -80 dB reference 1 m/s. At lower velocity amplitudes, inter-transducer phase response errors become significant and the power flow measurement accuracy deteriorates. There is therefore a requirement for a laser vibrometer system that incorporates the user friendly qualities of the I.S.V.R. laser vibrometer but with an improved sensitivity.

A new, high-sensitivity, PZT laser vibrometer, incorporating a piezo-electric ceramic reference surface, frequency shifting device and the same optical configuration as the I.S.V.R. laser vibrometer, has been developed to fulfill this need. This device has a stationary surface noise floor level of -140 dB reference 1 m/s, over the frequency range 0 to 1 kHz, and -130 dB over 0 to 10 kHz. (The difference in sensitivities is due to the increased bandwidth increasing the amount of broadband electronic noise in the vibrometer output). Normal-to-surface vibration velocity measurements on a sinusoidally excited shaker showed excellent agreement with vibration amplitudes simultaneously acquired with an accelerometer.

Two PZT laser vibrometers have been substituted for accelerometers in the two transducer power flow measurement scheme. Employing this method, the major source of measurement error is the inter-transducer phase response. For ideal, normal-to-surface target motion, this phase error can be minimised by closely matching electronic component values in the two transducers. Under these conditions, for velocity amplitudes of -85 and -105 dB reference 1 m/s, good agreement, (an average difference of -0.525 dB reference 1 Watt), between the PZT vibrometer and accelerometer S.I. measurement results has been obtained.

In common with the I.S.V.R. laser vibrometer, when velocity amplitudes measured by the PZT laser vibrometer approach the transducer optical

noise floor, large amplitude phase errors, associated with dynamic speckle effects, may occur. Since dynamic speckle noise is a characteristic of all practical laser vibrometer measurements, the implications for the vibrometer accuracy and dynamic range have been investigated.

Speckle noise is inherent in all measurements of diffuse target surfaces that are undergoing non-normal motion, as well as the normal-to-surface vibration of interest. A random intensity modulation of the light incident on the vibrometer photodetector results, producing an increase in the amplitude of broadband noise in the vibrometer output. This in turn, raises the device noise floor level, i.e. for practical vibration measurements the maximum transducer sensitivity, - the optical noise floor - is determined by the target surface motion and not by the transducer electronics.

For periodic, non-normal motion, a pseudo-random detector noise output is produced. This results in a series of noise spikes in the spectrum at the non-normal vibration frequency and its harmonics. The spike amplitudes, and hence the device optical noise floor, are dependent upon dynamic speckle induced phase noise. For the most severe dynamic speckle noise source of surface rotation, the spike amplitudes are approximately constant with frequency. This form of pseudo-vibration spectra is therefore easily recognisable. In contrast, for the less severe cases of in-plane or tilt target motion, the number of speckle changes, or rate of change of speckle noise over one period of motion, is reduced, relative to the rotation case, and there is less high frequency noise in the detector output. The spike amplitudes then decrease with increasing frequency. Spectra of this form can easily be mistaken as genuine, normal-to-surface vibration data. Even under 'worst case' laboratory conditions however, a cross-sensitivity to in-plane vibration of only 3 to 7% was produced, i.e. comparable with accelerometers. For a majority of practical measurements, these ideal laboratory conditions will not be reproduced, and the vibrometer sensitivity to non-normal motion will be less than the previously quoted figures. Therefore large amplitude, pseudo-vibration signals will only

result when non-normal vibration amplitudes are large, and hence obvious to the vibration engineer. It may be concluded therefore that for accurate S.I. measurements to be obtained with laser vibrometers, i.e. for random and pseudo-random speckle noise effects to be neglected, normal-to-surface velocity amplitudes must be greater than the device optical noise floor level.

It has been shown theoretically how by using a laser velocity gradient measurement scheme in conjunction with a single laser vibrometer, the power flow measurement technique accuracy may be improved, relative to the two accelerometer method. This is acheived by simplifying the S.I. calculation and hence reducing the technique sensitivity to inter-transducer phase errors.

Three velocity gradient measurement systems have been investigated and a final scheme proposed, based on the optical configuration of the I.S.V.R. torsional vibrometer, which is robust, self-aligning and insensitive to solid body motion. The prototype velocity gradient scheme employs a frequency modulated laser diode in an unbalanced Michelson Interferometer configuration. This results in an optical carrier frequency which is modulated by any differential, normal-to-surface velocity of two illuminated points. The vibrometer output is thus proportional to the velocity difference of the two points. This output is related to the velocity gradient by a finite difference approximation.

The velocity gradient transducer was used to make practical velocity and velocity difference measurements on a sinusoidally excited, electrodynamic shaker. Results showed the velocity gradient transducer, in common with other laser vibrometers, to be sensitive to dynamic speckle effects, associated with large amplitude, non-normal target vibration. Vibration amplitudes of typical, normal-to-surface motion compared favourably however, with simultaneously acquired, integrated accelerometer measurements.

The amplitude of power flow measurements acquired using the velocity

gradient transducer and a PZT laser vibrometer compared favourably with simultaneously acquired, two accelerometer measurements. Over the frequency range 500 to 2250 Hz, an average difference of -0.44 dB or 4.9% was obtained, i.e. within experimental measurement error limits. The accuracy of the two measurement methods is therefore comparable. Practical measurements carried out using the laser transducer configuration will, however, have the following advantages over the accelerometer method,

(i) they can be obtained using remote, non-contact transducers,

(ii) the effect of the internal resonance on the transducer phase response at higher frequencies is no longer of concern,

(iii) mass-loading effects are no longer a problem,

(iv) a large number of measurements can be quickly made,

(v) measurements can be made where accelerometer use is precluded, e.g. hot, inaccesible and lightweight surfaces.

It can be concluded therefore that the most practical, accurate and robust transducer system for measuring one-dimensional, flexural wave structural intensity, consists of the laser velocity gradient transducer and the laser vibrometer described in this thesis. This configuration not only offers a direct replacement for the existing two accelerometer method, but its use will also extend employment of the power flow measurement technique to vibration environments where measurements, to date, have not been possible.

## 6.1 RECOMMENDATIONS FOR FURTHER WORK.

To maximise the practical advantages of the velocity gradient transducer for power flow measurements, a number of improvements in the optical configuration are possible.

(i) The velocity gradient scheme utilised in this work employed a laser diode operating in the near-infrared (840 nm), with an output power of typically 5 mW. The transducer is thus rated as a class 3B laser device and hence is unsuitable for widespread use. It is hoped that in the near future a commercial, visible laser diode, with a long coherence length will become available and can be incorporated into the transducer. Further improvements in the photodetector and pre-amplifier circuits will then reduce the transducer optical power to less than 1 mW, and result in a class 2 device.

(ii) Although the velocity gradient transducer has been optimised with bulk optics, the employment of optical fibre waveguides will allow the laser light to be simply and accurately positioned on the vibrating target surface. For one-dimensional power flow measurements, three fibre waveguides would be employed, two for the velocity gradient measurement and one for the velocity. This could best be realised in terms of a fibre probe, analogous to the two microphone probe utilised for sound intensity measurements. Differential fibre vibration effects would be minimised through use of polarising preserving fibres and encasement of all three fibres in a single cable or protective covering. This scheme would allow the transducer electronics and the laser-fibre launch optics to be positioned remotely from the noise source and hence be insensitive to any spurious vibration effects.

As shown in Appendix 8.7, using two velocity gradient and one point velocity laser transducer, non-contact, power flow measurements can also be made on two dimensional, or plate-like structures. Employment of the laser velocity gradient transducer as part of an all-laser, power flow measurement scheme, and hence with all the benefits of non-contact, vibration measurement, could therefore also be extended to more complex structures and transducer configurations, e.g. cylinders, shells etc.

## 7. REFERENCES.


1. E.F. Winter and D.A. Bies.
Correlation properties of flexural waves in long. thin bars.
J. Acoust. Soc. Am. 34(4), 472-475, 1962.

2. P.H. White.
Cross-correlation in structural systems: Dispersion and non-dispersion waves.
J. Acoust. Soc. Am. 45(5), 1118-1128, 1970.

3. N. Aoshima and J. Igarashi.
The measurement of flexural wave propagation by correlation techniques.
ISAS report 436, University of Tokyo, 1969.

4. R.G. White.
Vibration Control II.
Chapter 26 of 'Noise and Vibration'. (Editors R.G. White and J.G. Walker).
John Wiley and Sons, New York. 685-712. 1982.

5. M. Petyt.
Finite element techniques for structural vibration.
Chapter 16 of 'Noise and Vibration'. (Editors R.G. White and J.G. Walker).
John Wiley and Sons, New York. 337-354. 1982.

6. F.J. Fahy and R.G. White.
Statistical Energy Analysis and Vibrational Power Flow.
Proceedings of the 3rd International Congress on Intensity Techniques.
Senlis, France. 29-34. 1990.

7. R.G. White.
Power flow techniques in the study of machinery installations for the purpose of vibration control.
Proceedings of the 111th International Conference of the Acoustical Society of America. 1986.

8. D. U. Noiseux.
Measurement of power flow in uniform beams and plates.
J. Acoust. Soc. Am. 47(1), 238-247. 1970.

9. L. Cremer, M. Heckl and E.E. Ungar.
Structure borne sound.
Springer-Verlag, Munich. 1973.

10. W. Redman-White.
The measurement of structural wave intensity.
Ph.D. Thesis, University of Southampton. 1983.

11. G. Pavic.
Techniques for the determination of vibration transmission mechanisms in structures.
Ph.D. Thesis, University of Southampton. 1976.

12. R.J. Bernhard and J.D. Mickol.
Probe mass effects on power transmission in lightweight beams and plates.
Proceedings of the 3rd International Congress on Intensity Techniques, Senlis, France. 307-314. 1990

13. G.F. Carroll.
Phase accuracy for implementing intensity measurements in structures.
Proceedings of the 3rd International Congress on Intensity Techniques, Senlis, France. 241-248. 1990.

14. E.G. Williams and H.D. Dardy.
SIMAP, Structural intensity from the measurement of acoustic pressure.
J. Acoust. Soc. Am. 78(6), 2061-2068. 1985.

15. J.B. Piaud and J. Nicolas.
Relationship between vibrational and acoustical intensity for an infinite plate.
J. Acoust. Soc. Am. 80(4), 1114-1121. 1986.

16. J.-C. Pascal, T. Loyau and J.A. Mann.
Structural intensity from spatial Fourier transformation and BAHIM acoustical holography method.
Proceedings of the 3rd International Congress on Intensity Techniques, Senlis, France. 197-204. 1990.

17. J.A. Clark and A.J. Tucker.
Optical measurements of structural intensity distributions.
Proceedings of the 2nd International Congress on Acoustic Intensity, Senlis, France. 171-176. 1985.

18. J.R. Baker, J.L. Horner, N.A. Halliwell and R.G. White.
Laser Technology for measuring vibrational power flow in beam-like structures.
SIRA Conference, "Stress and Vibration: Recent developments in Industrial measurement and analysis. 1989.

19. J.R. Baker, N.A. Halliwell and R.G. White.
The application of laser technology to the measurement of structural intensity.
Proceedings of the 3rd International Congress on Intensity Techniques, Senlis, France. 167-172. 1990.

20. T.E. McDevitt, G.H. Koopman and C.B. Burroughs.
A detailed investigation into cross-spectral laser Doppler techniques for flexural and longitudinal vibrational intensity measurements.
Proceedings of the 3rd International Congress on Intensity Techniques, Senlis, France. 173-180. 1990.

21. S.I. Hayek, M.J. Pechersky and B.C. Sven.
Measurement and analysis of near and far-field structural intensity by scanning laser vibometry.
Proceedings of the 3rd International Congress on Intensity Techniques, Senlis, France. 281-288. 1990.

22. G. Rosenhouse and F.P. Mechel.
Mutual transformation of transversal and longitudinal vibrations in structures of finite size and its influence on the experimental determination of vibrational power.
Proceedings of the International Congress on Recent Developments in Acoustic Intensity measurement. Senlis, France. 225-227. 1981.

23. J.L. Horner and R.G. White.
Vibrational power transmission through discontinuities.
Proceedings of the 3rd International Congress on Intensity Techniques, Senlis, France. 387-397. 1990.

24. G. Pavic.
Vibrational energy flow in thin-walled shells.
Proceedings of the 3rd International Congress on Intensity Techniques, Senlis, France. 91-96. 1990.

25. W. Redman-White, P.A. Nelson and A.R.D. Curtis.
Experiments on the active control of flexural wave power flow.
J. Sound and Vib. 112(1), 187-191. 1987.

26. L.E. Drain and B.C. Moss.
The frequency shifting of laser light by electro-optic techniques.
Opto-electronics 4, 429-439. 1972.

27. J. Oldengarm, A. H. Von Krieken and H. Raterink.
Laser Doppler velocimeter with optical frequency shifting.
Optics and Laser Technology 5, 249-252. 1973.

28. P. Buchave.
Laser Doppler velocimeter with variable frequency (optical) shift.
Optics and Laser Technology 7, 11-16. 1975.

29. N.A. Halliwell.
Laser Doppler measurement of vibrating surfaces: a portable instrument.
J. Sound and Vib. 62, 312-315. 1979.

30. J.R. Baker, R.I. Laming, T.H. Wilmshurst and N.A. Halliwell.
A new, high-sensitivity laser vibrometer.
Journal of Laser Applications 22(4), 241-244. 1990.

31. J.C. Dainty. (Editor).
Laser Speckle and related Phenomena.
Springer-Verlag, Berlin. 1975.

32. S.J. Rothberg, J.R. Baker and N.A. Halliwell.
Laser Vibrometry: Pseudo-vibrations.
J. Sound and Vib. 135(3), 516-522. 1989.

33. J.R. Baker, S.J. Rothberg and N.A. Halliwell.
The effect of non-normal target surface motion on laser vibrometer velocity measurements.
Proceedings of the International Conference on Vibrational Problems in Engineering, Wuhan, China. 1041-1046. 1990.

34. J.W. Verheij.
Cross-spectral density methods for measuring structure borne power flow on beams and pipes.
J. Sound & Vib. 70(1), 133-139. 1980.

35.Bruel and Kjaer Ltd.
Mechanical Vibration and Shock measurements.
1981.

36. J.Y. Chung.
Cross-spectral method of measuring acoustic intensity without error caused by instrument phase mismatch.
J. Acoust. Soc. Am. 64, 1613-1616. 1978.

37. F. Durst, A. Melling and J.H. Whitelaw.
Principles and practice of Laser-Doppler Anemometry.
Academic Press. 1981.

38. V. Tank.
Pathlength alteration in an interferometer by rotation of a retroreflector.
Optical Engineering 28(2), 188-190. 1989.

39. S.J. Rothberg, J.R. Baker and N.A. Halliwell.
Practical laser vibrometry for rotating targets.
Proceedings of the International Conference on Vibration Problems in Engineering. Wuhan\Chongqing, China. 831-837. 1990.

40 A. Dandridge, A.B. Tveten and T.G. Giallorenzi.
Homodyne demodulation scheme for fibre-optic sensors using phase generated carrier.
IEEE J. Quant. Elec. QE-18, 10, 1647-1653. 1982.

41. T.H. Wilmshurst.
Signal recovery from noise in electronic instrumentation.
Adam Hilger Ltd, chapters 3 and 7. 1985.

42. T.H. Wilmshurst and J.E. Rizzo.
An autodyne frequency tracker for laser-Doppler Anemometry.
J. Phys. E: Sci. Instrum. 7, 924-930. 1974.

43. J.A. Leendertz and J.N. Butters.
An image shearing speckle-pattern interferometer for measuring bending moments.
J. Phys. E: Sci. Instrum. 6, 1107-1110. 1973.

44. Y.Y Hung and C.E. Taylor.
Speckle-shearing camera - a tool for measurement of derivatives of surface displacement.
Proceedings of the Society of Photo-Optical Institute of Engineers, 17$^{th}$ Annual Technical Meeting, 41, 169-175. 1973.

45. S.G. Hanson.
Application of the laser gradient anemometer (LGA) for fluid flow measurements.
Second International Symposium on applications of laser anemometry to Fluid Mechanics. Lisbon, Portugal. 1984.

46. S.G. Hanson.
The laser gradient anemometer.
Photon correlation techniques in Fluid Mechnaics, 1-11. Springer-Verlag. Berlin.

47. N.A. Halliwell, C.J.D. Pickering and P.G. Eastwood.
The laser torsional vibrometer: a new instrument.
J. Sound and Vib. 93(4), 588-592. 1984.

48. N.A. Halliwell, P.G. Eastwood.
The laser torsional vibrometer.
J. Sound and Vib. 101(3), 446-448. 1985.

49. R.I. Laming, T.H. Wilmshurst, N.A. Halliwell and J.R. Baker.
A practical, all-fibre laser vibrometer.
Experimental Techniques, March/April, 44-47. 1990.

50. A Dandridge and I. Goldberg.
Current-induced frequency modulation in diode lasers.
Electron. Lett. 18, 302-304. 1982.

51. R.I. Laming.
Optical fibre devices: vibrometer, current monitor and amplifier.
Ph.D. Thesis, University of Southampton. 1990.

52. R.E. Bishop and D.C. Johnson.
Mechanics of Vibration.
Cambridge University Press. 1960.

53. R.K. Erf (Editor).
Speckle metrology.
Academic Press. 1978.

54. N. Takai, T. Iwai and T. Asakura.
Correlation distance of dynamic speckle.
Applied Optics 22(1), 170-177. 1983.

55. J.W. Goodman.
Introduction to Fourier Optics.
McGraw-Hill, London. 1968.

## 8. APPENDICES.

8.1 Maths functions programs for calculating input and transmitted power, and 'chirp' excitation.

8.2 PZT laser vibrometer.

8.3 Laser diode test data.

8.4 Velocity gradient transducer.

8.5 Resultant speckle pattern intensity by phasor addition.

8.6 Resonance frequencies of a cantilever beam.

8.7 Two-dimensional power flow measurement.

## 8.1 MATHS FUNCTIONS PROGRAMS FOR CALCULATING INPUT AND TRANSMITTED POWER, AND 'CHIRP' EXCITATION.

a) Input power:

From equation (2.43a), the input power is given be the expression,

$$P_{IN}(\omega) = \frac{1}{2} \mathrm{Re}[G(F,v,\omega)] \qquad (A1.1)$$

employing an acceleration signal however,

$$P_{IN}(\omega) = \frac{1}{\omega} \mathrm{Im}[G(F,a,\omega)] \qquad (A1.2)$$

Using the cross power signal processing facility on the analyser,

COPY, Cross Power, 0, Buffer A

- transfers the results of the cross power calculation of the acceleration and force signals at the input point to a dummy file.

/Jω, Buffer A, Buffer A, 1

- multiplies the data in the dummy file by jω once, then returns the data to the dummy file again.

IMAG, Buffer A, Buffer A.

- removes the real component from the dummy file.

NAME, Buffer A, IM(Gfa)/ω

- names the data in the dummy file.

b) Transmitted power:

From equation (2.26), the transmitted power is given by,

$$\langle P(x_0,\omega) \rangle = \frac{(M_B EI)^{1/2}\Pi}{h\omega^2} \mathrm{Im}\ G(a_1,a_2,\omega) \qquad (A1.3)$$

Using the results of the cross power faciltiy on the analyser,

COPY, Cross Power, 0, Buffer A

- transfers cross power data to a dummy file.

/Jω, Buffer A, Buffer A, 2

- multiplies data by jω twice and returns data to dummy file.

IMAG, Buffer A, Buffer A

- removes real component from dummy file.

MULT, Buffer A, 46.352164 0.0, Buffer A

- multiplies data by beam constants and returns data to dummy file.

DIV, Buffer, 0.05 0.0, Buffer A

- divides data by transducer separation.

NAME, Buffer, Trans'd Power

- names the data in dummy file.

c) 'Chirp' excitation signal:

To create a uniform amplitude chirp of swept-sine signal over the frequency range 450-550 Hz.

COPY, Freq Response, 0, Buffer A

- transfers the frequency response configuration to a dummy file.

CHIRP, Buffer A, 450.0 550.0

- set up the chirp operation in the dummy file for the frequency range from 450 to 550Hz.

MULT, Buffer A, 1.0e0 0.0, Buffer A

- multiply chirp siganl by 1 to get unit amplitude, (can then be scaled using power amplifier).

DAC, Write, Buffer A, 0

- send the chirp signal to the signal generator output.

DAC, On

- switch on the generator.

## 8.2 PZT LASER VIBROMETER.

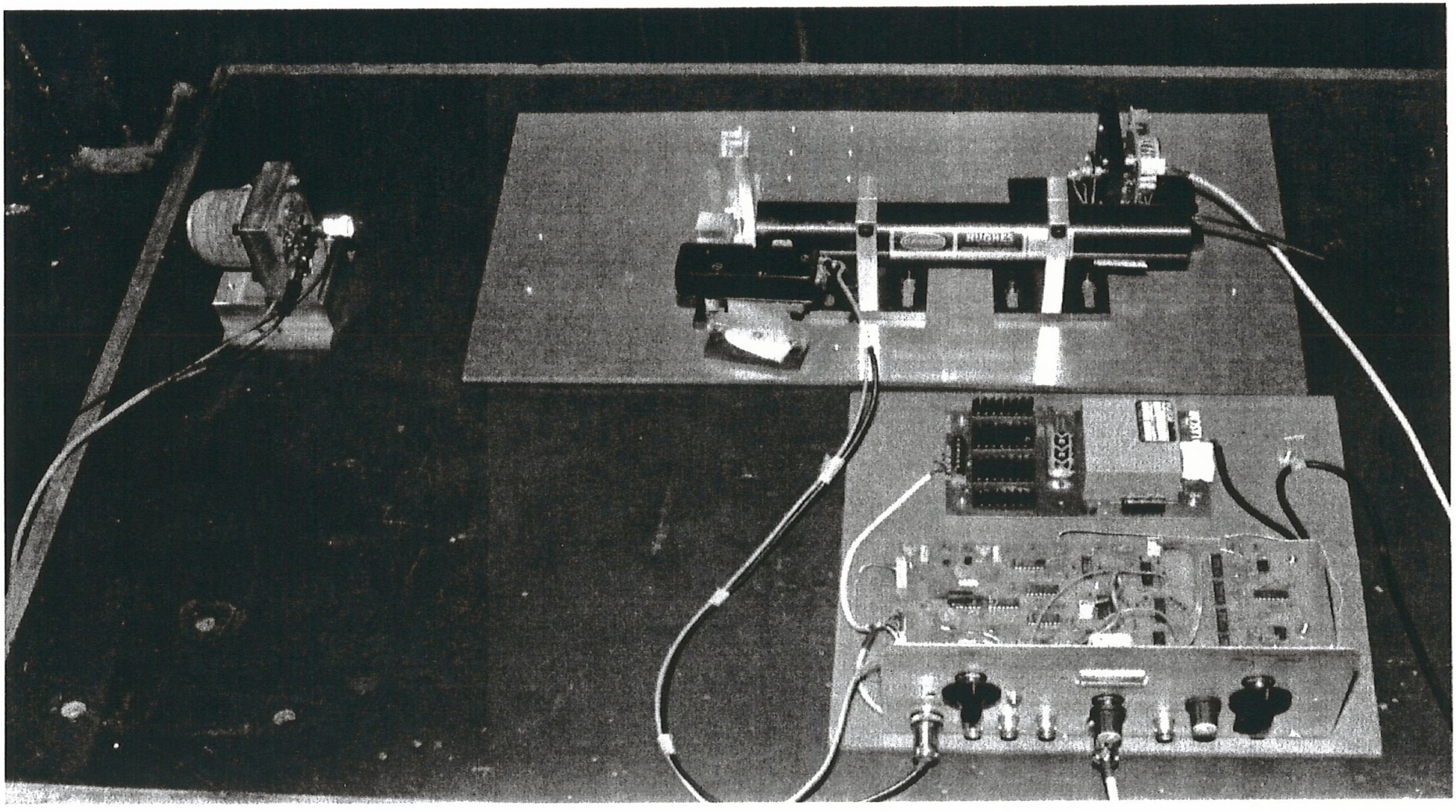
HUGHES

# PZT VIBROMETER: CIRCUIT DIAGRAM

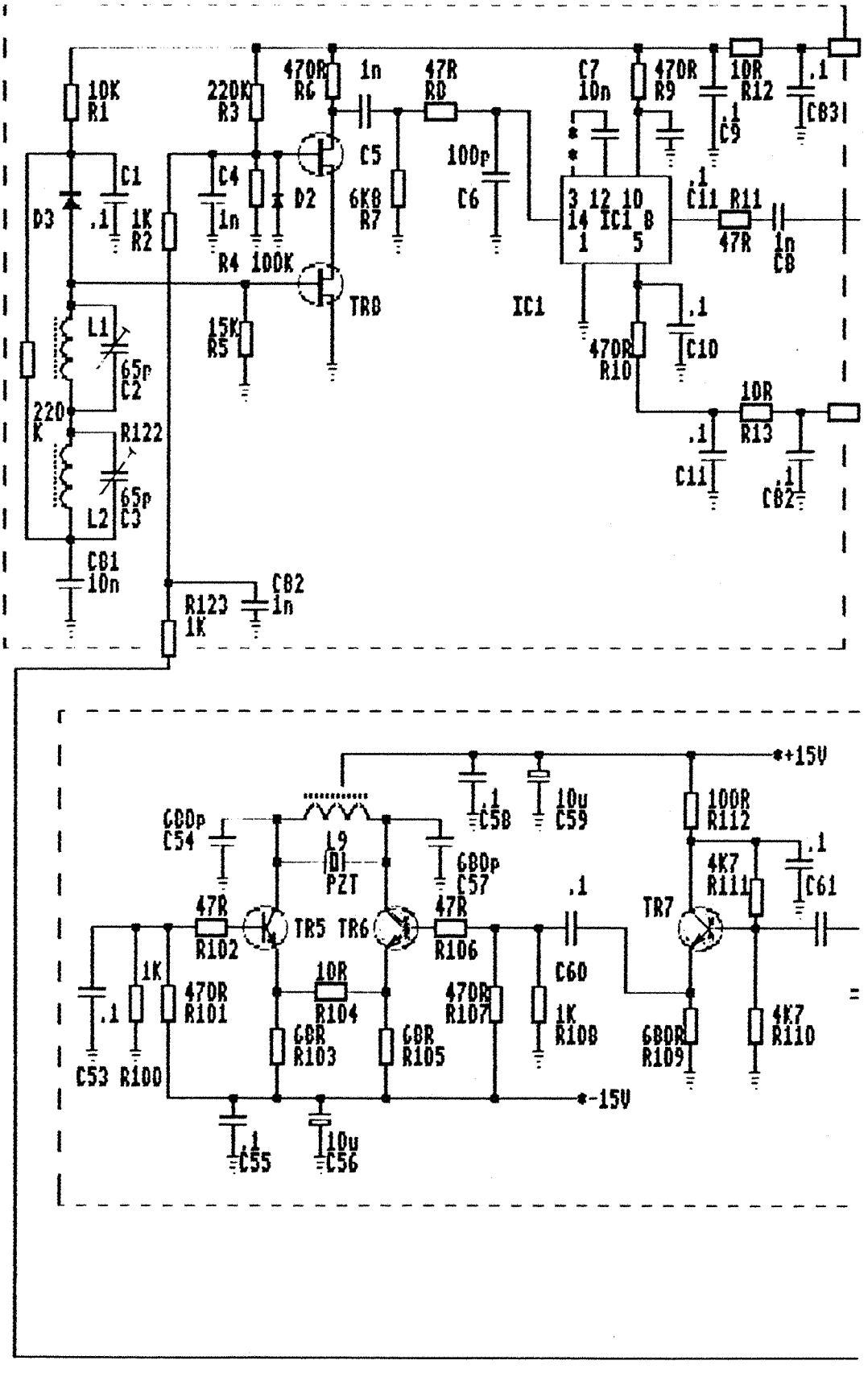

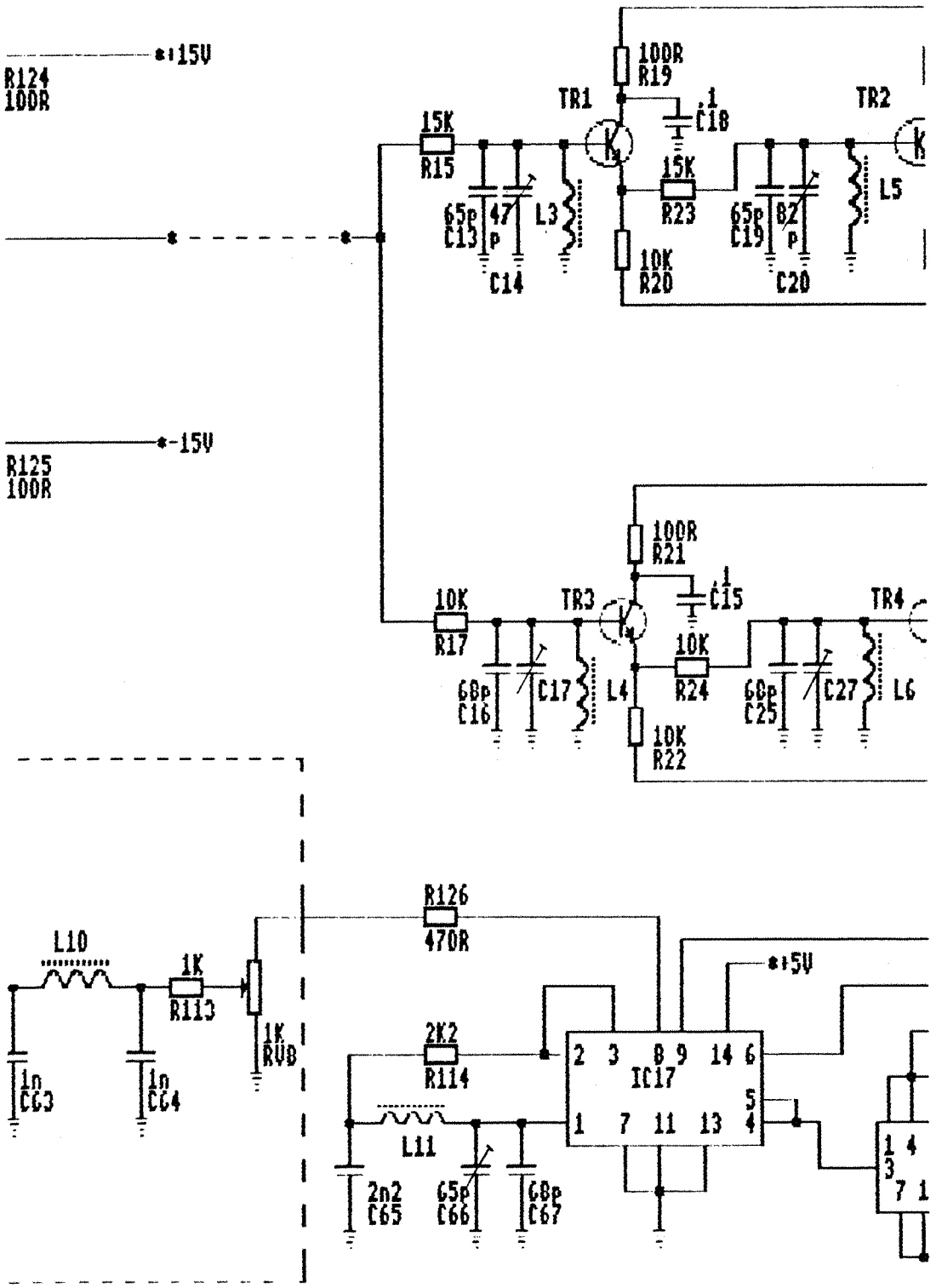
+15V
R124
100R
100R
R19
TR1
C18
TR2
15K
R15
15K
R23
L5
65p
C13
47
p
L3
65p
C19
82
p
C14
10K
R20
C20
-15V
R125
100R
100R
R21
10K
R17
TR3
C15
TR4
10K
R24
68p
C16
C17
L4
68p
C25
C27
L6
10K
R22
R126
470R
L10
1K
R113
1K
RV8
1n
CC3
1n
CC4
+5V
2K2
R114
IC17
2 3 8 9 14 6
1 7 11 13 5 4
L11
2n2
C65
65p
C66
68p
C67
1 4
3
7 1

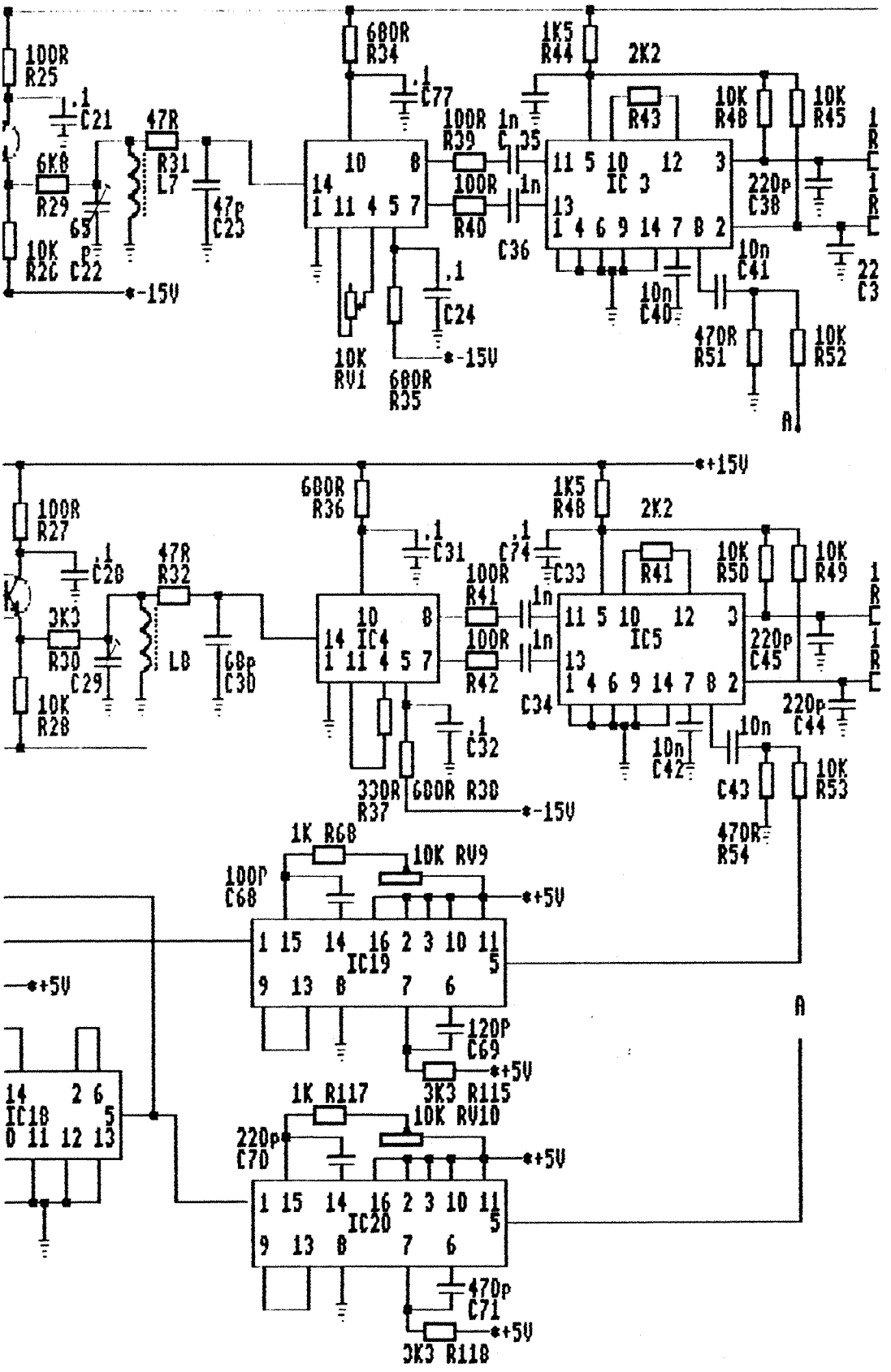
100R R25
.1 C21
47R R31
L7
6K8 R29
65p
47p C23
10K R26
C22
-15V
680R R34
.1 C77
100R R39
1n C35
100R R40
1n C36
.1 C24
10K RV1
680R R35
-15V
1K5 R44
2K2 R43
10K R48
10K R45
IC 3
220p C38
10n C41
10n C40
470R R51
10K R52
22 C3
A
+15V
100R R27
.1 C28
47R R32
3K3 R30
C29
LB
68p C30
10K R28
680R R36
.1 C31
100R R41
100R R42
IC4
.1 C32
330R R37
680R R38
-15V
1K5 R48
2K2 R41
.1 C74
C33
10K R50
10K R49
IC5
220p C45
C34
220p C44
10n C42
10n C43
470R R54
10K R53
1K R68
10K RV9
100P C68
+5V
IC19
120P C69
3K3 R115
1K R117
10K RV10
220p C70
IC20
470p C71
3K3 R118
IC18
A

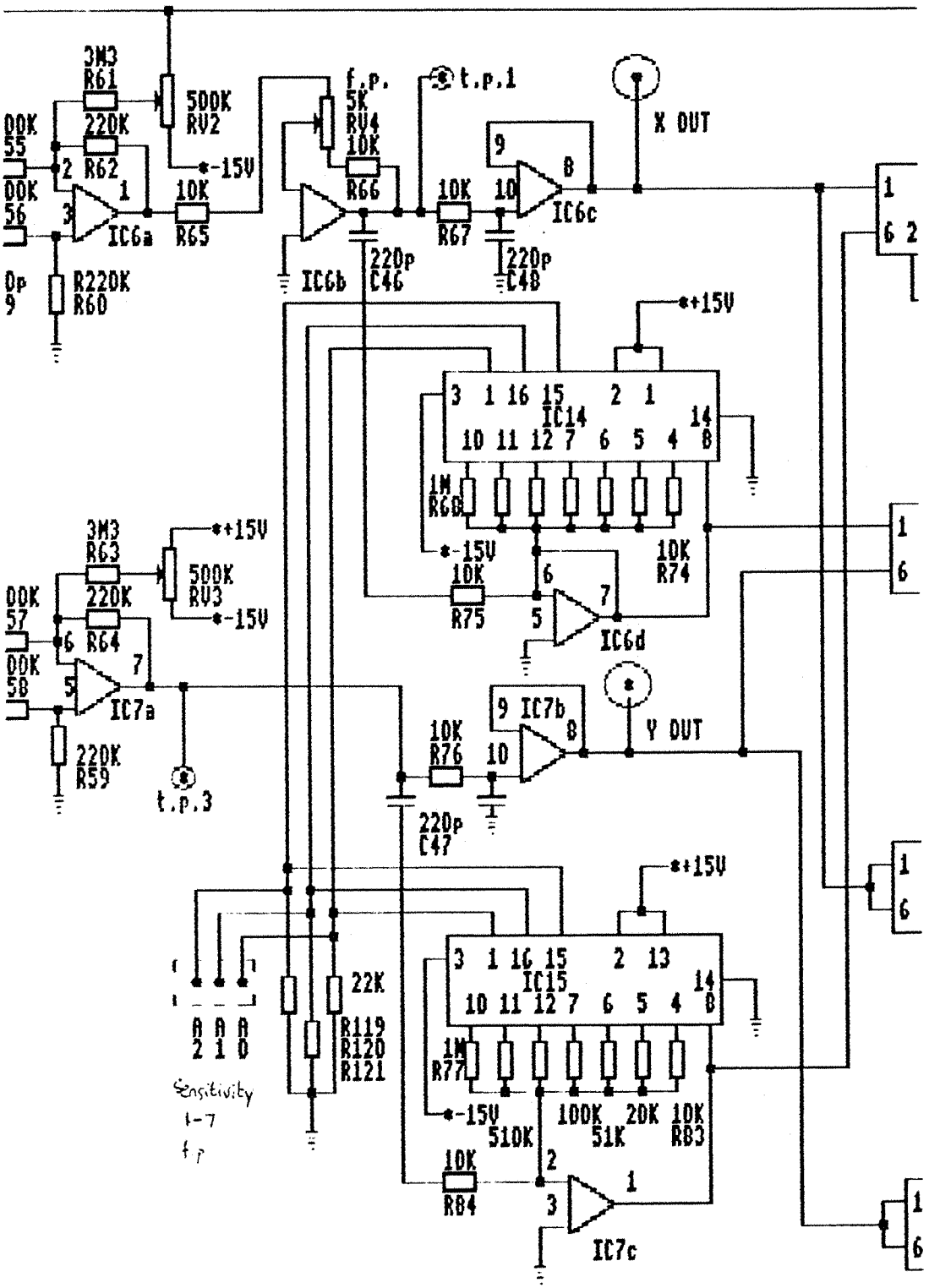
3M3
R61
220K
R62
500K
RV2
-15V
DDK
55
DDK
56
2
3
1
IC6a
10K
R65
0p
9
R220K
R60
f.p.
5K
RV4
10K
R66
t.p.1
IC6b
220p
C46
10K
R67
9
10
8
IC6c
220p
C48
X OUT
1
6 2
+15V
3 1 16 15 2 1
IC14
14
10 11 12 7 6 5 4 8
1M
R68
10K
R74
-15V
10K
R75
6
5
7
IC6d
1
6
3M3
R63
220K
R64
500K
RV3
+15V
-15V
DDK
57
DDK
58
6
5
7
IC7a
220K
R59
t.p.3
9 IC7b
8
10K
R76
10
Y OUT
220p
C47
1
6
+15V
3 1 16 15 2 13
IC15
14
10 11 12 7 6 5 4 8
1M
R77
22K
R119
R120
R121
A A A
2 1 0
Sensitivity
1-7
fp
-15V
510K
100K
51K
20K
10K
RB3
10K
RB4
2
3
1
IC7c
1
6

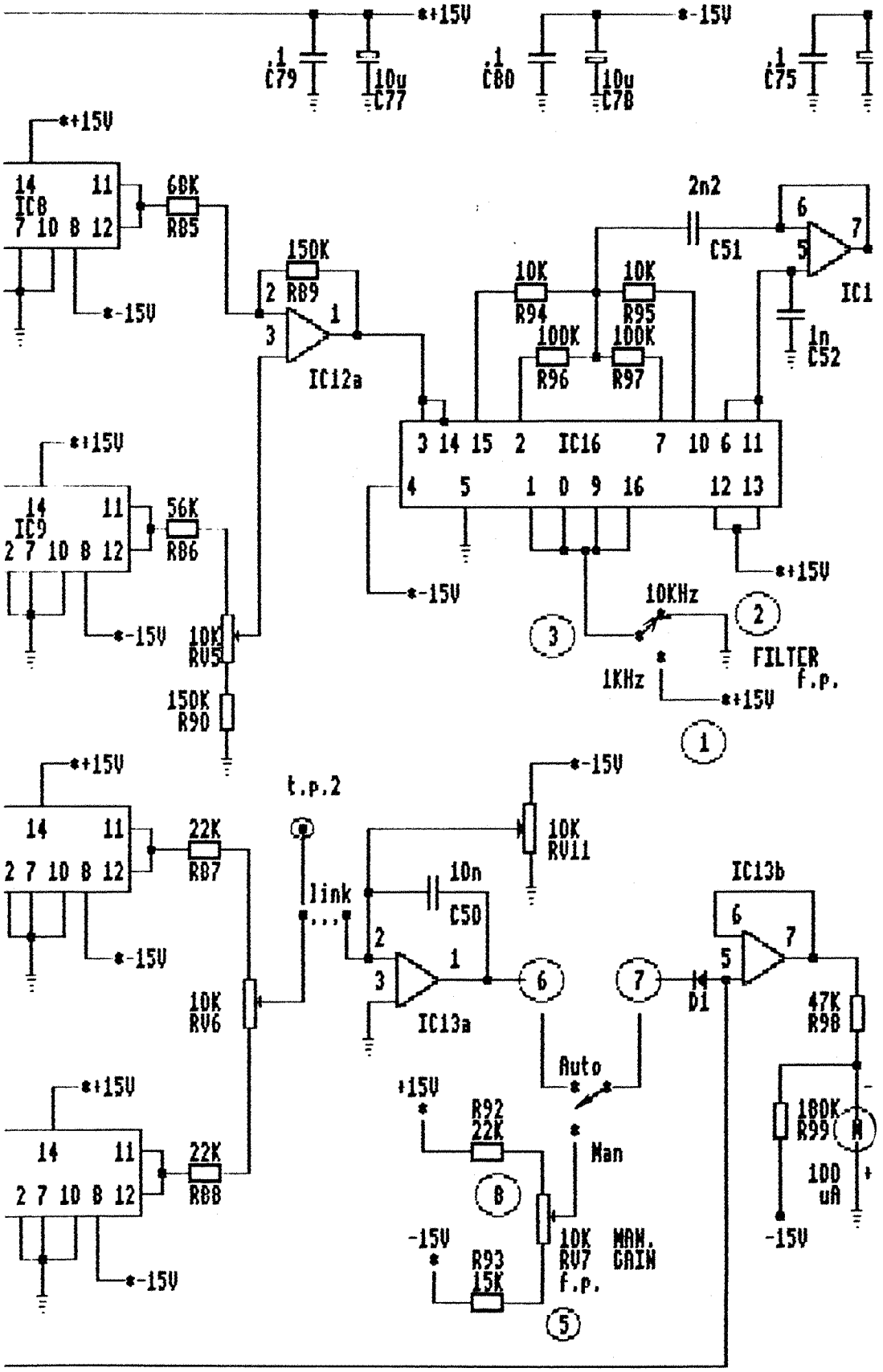
+15V
-15V
C79
10u
C77
C80
10u
C78
C75
IC8
68K
R85
150K
R89
IC12a
2n2
C51
IC1
10K
R94
10K
R95
100K
R96
100K
R97
1n
C52
IC16
IC9
56K
R86
10K
RV5
150K
R90
10KHz
1KHz
FILTER
f.p.
t.p.2
22K
R87
10K
RV6
22K
R88
link
10n
C50
IC13a
10K
RV11
IC13b
D1
47K
R98
180K
R99
100
uA
Auto
Man
R92
22K
R93
15K
10K
RV7
MAN.
GAIN
f.p.


| INTEGRATED CIRCUITS | | | |
|---|---|---|---|
| 1 | 592 | 11 | MPY634 |
| 2 | 592 | 12 | TL082 |
| 3 | SO42P | 13 | TL082 |
| 4 | 592 | 14 | DG508 |
| 5 | SO42P | 15 | DG508 |
| 6 | TL084 | 16 | DG413 |
| 7 | TL084 | 17 | 74HCT04 |
| 8 | MPY634 | 18 | 74HCT74 |
| 9 | MPY634 | 19 | 74HCT123 |
| 10 | MPY634 | 20 | 74HCT123 |

| SEMICONDUCTORS | | | |
|---|---|---|---|
| TR1 | BC182L | TR5 | BUP41 |
| TR2 | BC182L | TR6 | BUP41 |
| TR3 | BC182L | TR7 | BC182L |
| TR4 | BC182L | TR8 | 35KBB |
| D1 | 1N4148 | D2 | 1N4148 |

| INDUCTORS | | | |
|---|---|---|---|
| L1 | 470uH | L7 | 470uH |
| L2 | 1mH | L8 | 100uH |
| L3 | 470uH | L9 | 21t+21t |
| L4 | 100uH | | L114/61 |
| L5 | 470uH | L10 | 100uH |
| L6 | 100uH | L11 | 100uH |

## 8.3 LASER DIODE TEST DATA.

Hitachi Laser Diode Test Data

Type HL8311G Serial No 7M0049

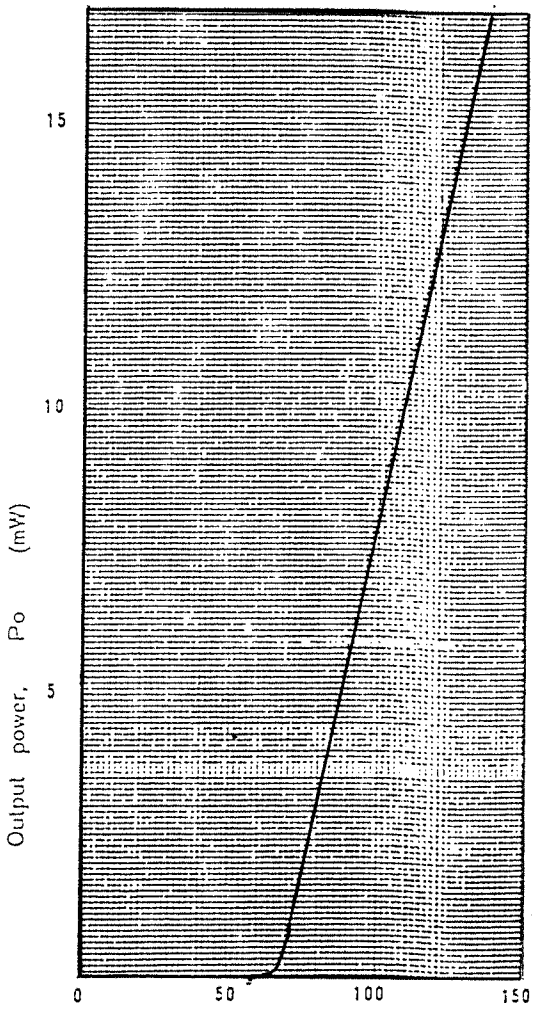


Forward Current, IF (mA,DC)

Light-Current Characteristic

Is: 1.26 mA (Po = 10 mW, VR = 5 V)

Lasing Wavelength

(at 10 mW)

842.1 nm

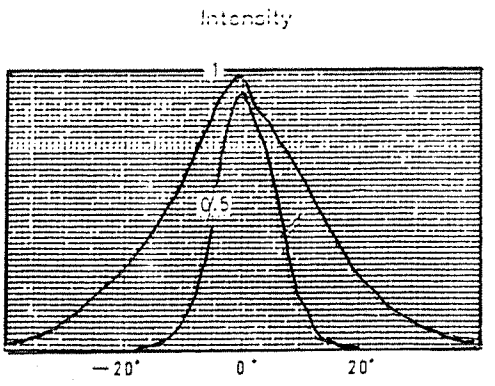


Angle

Far-Field patterns

(at 10 mW)

## 8.4 VELOCITY GRADIENT TRANSDUCER.

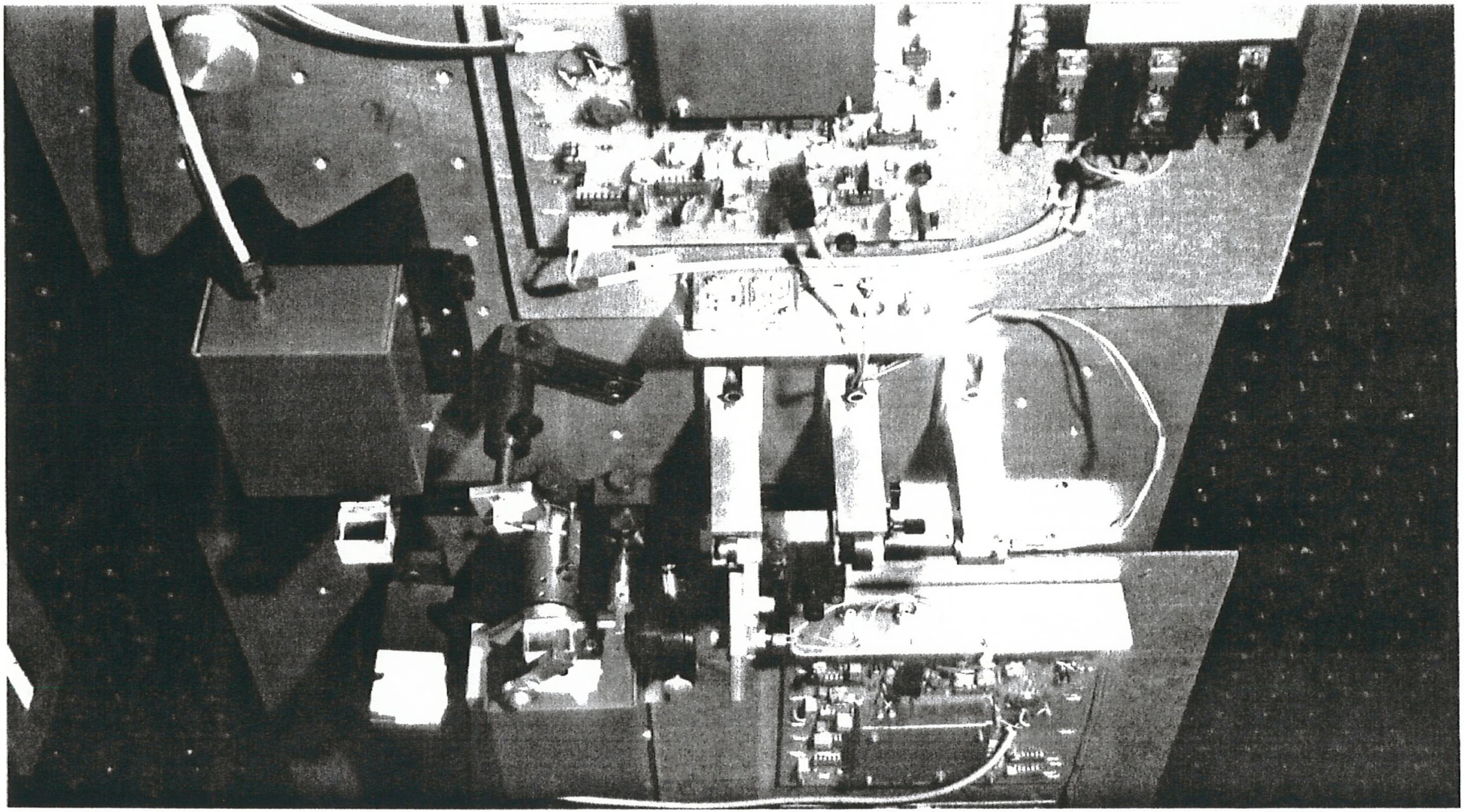

# VELOCITY GRADIENT TRANSDUCER : CIRCUIT DIAGRAMS.

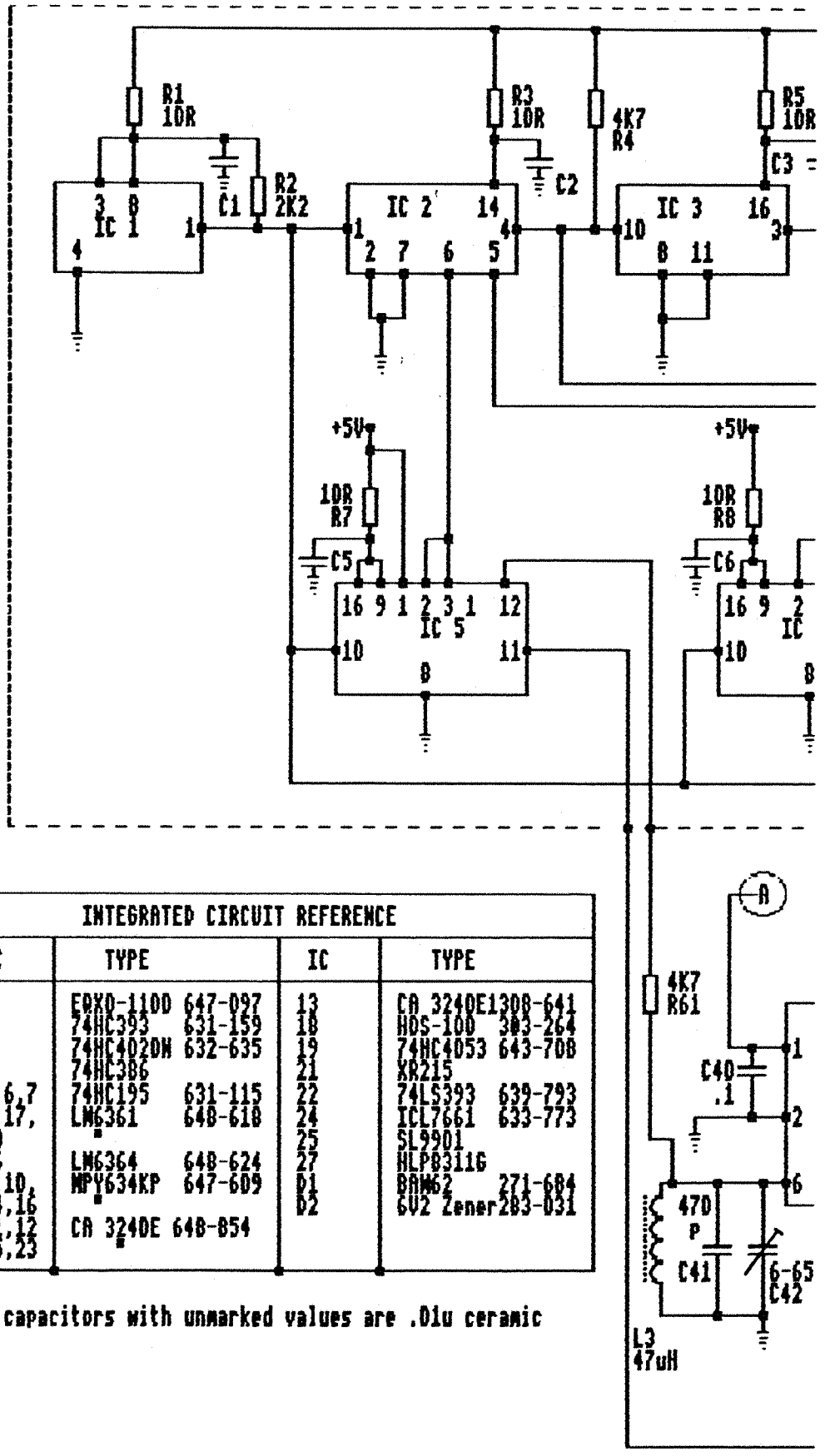


| INTEGRATED CIRCUIT REFERENCE | | | |
|---|---|---|---|
| IC | TYPE | IC | TYPE |
| 1 | EQXO-1100 647-097 | 13 | CA 3240E1308-641 |
| 2 | 74HC393 631-159 | 18 | HDS-100 303-264 |
| 3 | 74HC4020N 632-635 | 19 | 74HC4053 643-708 |
| 4 | 74HC386 | 21 | XR215 |
| 5,6,7 | 74HC195 631-115 | 22 | 74LS393 639-793 |
| 8,17, 20 | LM6361 648-618 | 24 | ICL7661 633-773 |
| 25 | | SL9901 | |
| 26 | LM6364 648-624 | 27 | HLP8311G |
| 9,10, 14,16 | MPY634KP 647-609 | D1 | BRW62 271-684 |
| D2 | 6V2 Zener283-031 | | |
| 11,12 15,23 | CA 3240E 648-854 | | |

All capacitors with unmarked values are .01u ceramic

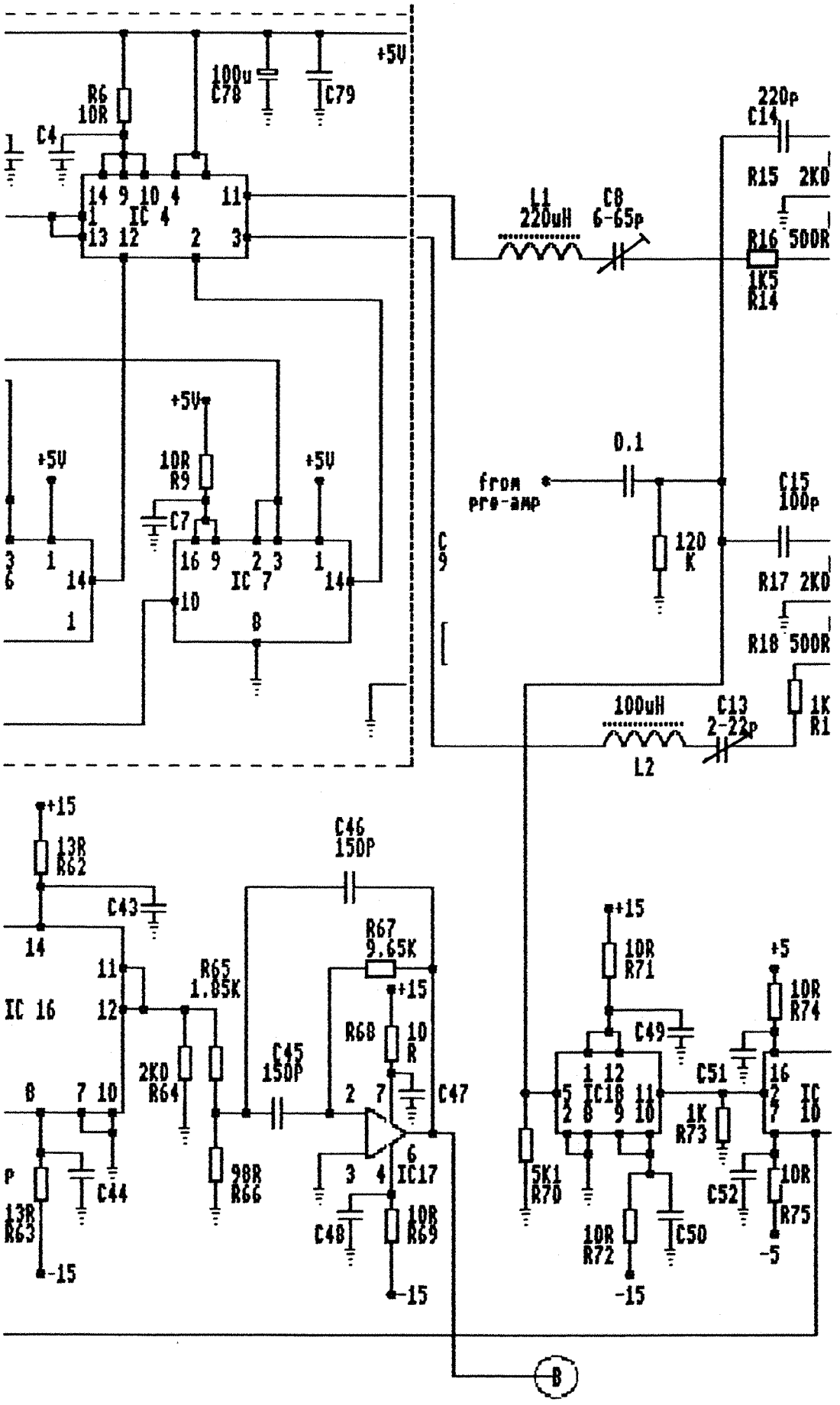
+5V
100u
C78
C79
R6
10R
C4
IC 4
L1
220uH
C8
6-65p
220p
C14
R15 2K0
R16 500R
1K5
R14
+5V
10R
R9
C7
IC 7
0.1
from
pre-amp
120
K
C15
100p
R17 2K0
R18 500R
1K
R1
100uH
L2
C13
2-22p
+15
13R
R62
C43
C46
150P
R67
9.65K
R65
1.05K
IC 16
R68
10
R
C45
150P
2K0
R64
98R
R66
C47
IC17
C48
10R
R69
C44
13R
R63
-15
+15
10R
R71
C49
+5
10R
R74
C51
IC18
1K
R73
5K1
R70
10R
R72
C50
C52
10R
R75
-5
B

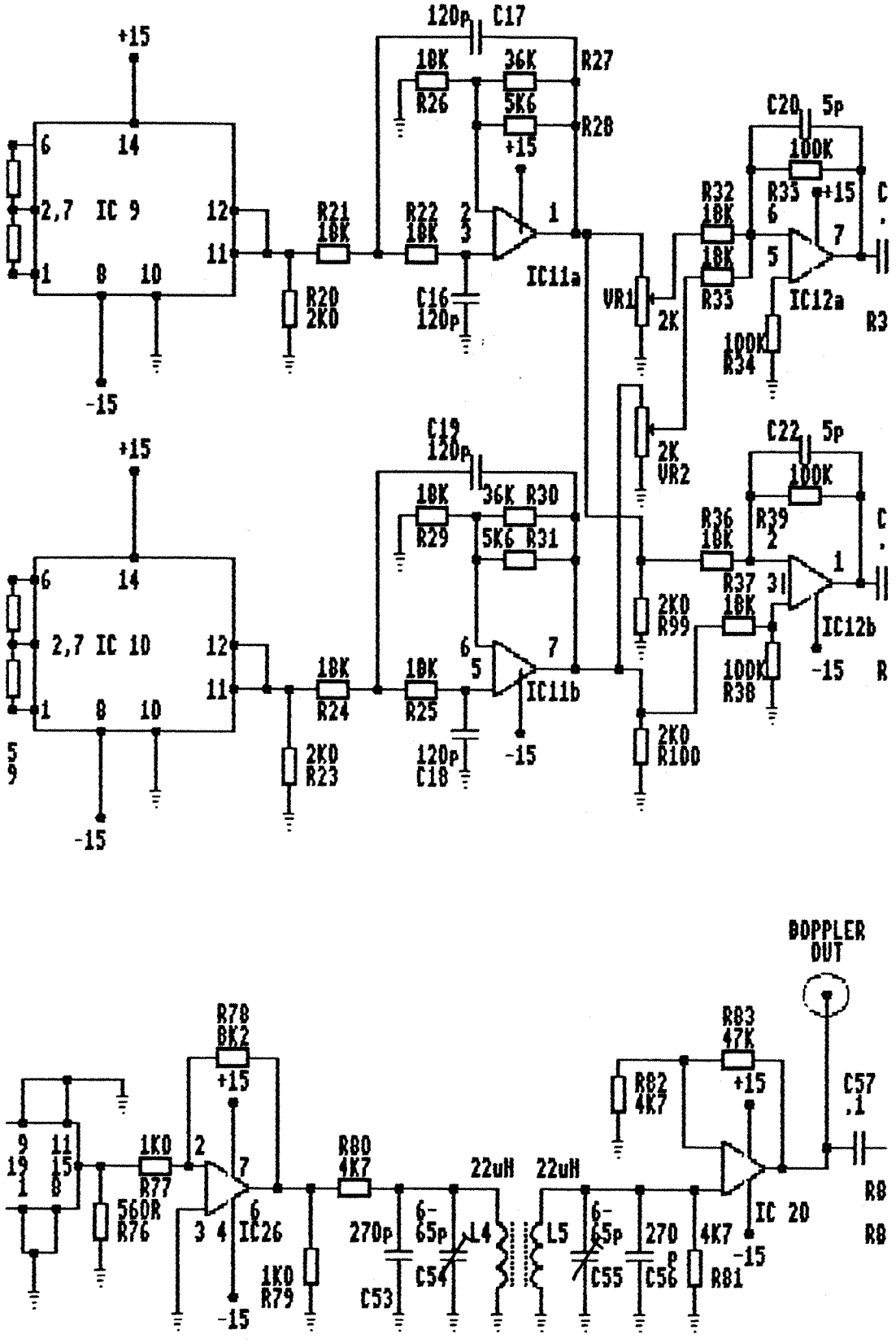
+15
120p C17
18K R26
36K R27
5K6 R28
+15
C20 5p
100K
R32 18K
R33 18K
R33 +15
IC12a
R3
100K R34
6 14
2,7 IC 9
12
11
1 8 10
R21 18K
R22 18K
R20 2K0
C16 120p
IC11a
1
VR1 2K
2K VR2
-15
C19 120p
18K R29
36K R30
5K6 R31
C22 5p
100K
R36 18K
R39
R37 18K
IC12b
2K0 R99
2K0 R100
6 14
2,7 IC 10
12
11
1 8 10
18K R24
18K R25
2K0 R23
120p C18
IC11b
100K R38
-15 R
5
9
-15
BOPPLER OUT
R78 8K2
+15
R83 47K
R82 4K7
C57 .1
9 11
19 15
1 8
1K0 R77
560R R76
2
7
6
3 4 IC26
R80 4K7
22uH
22uH
270p
6-65p
L4
L5
C54
C53
C55
C56
270 p
4K7 R81
IC 20
R8
R8
1K0 R79
-15

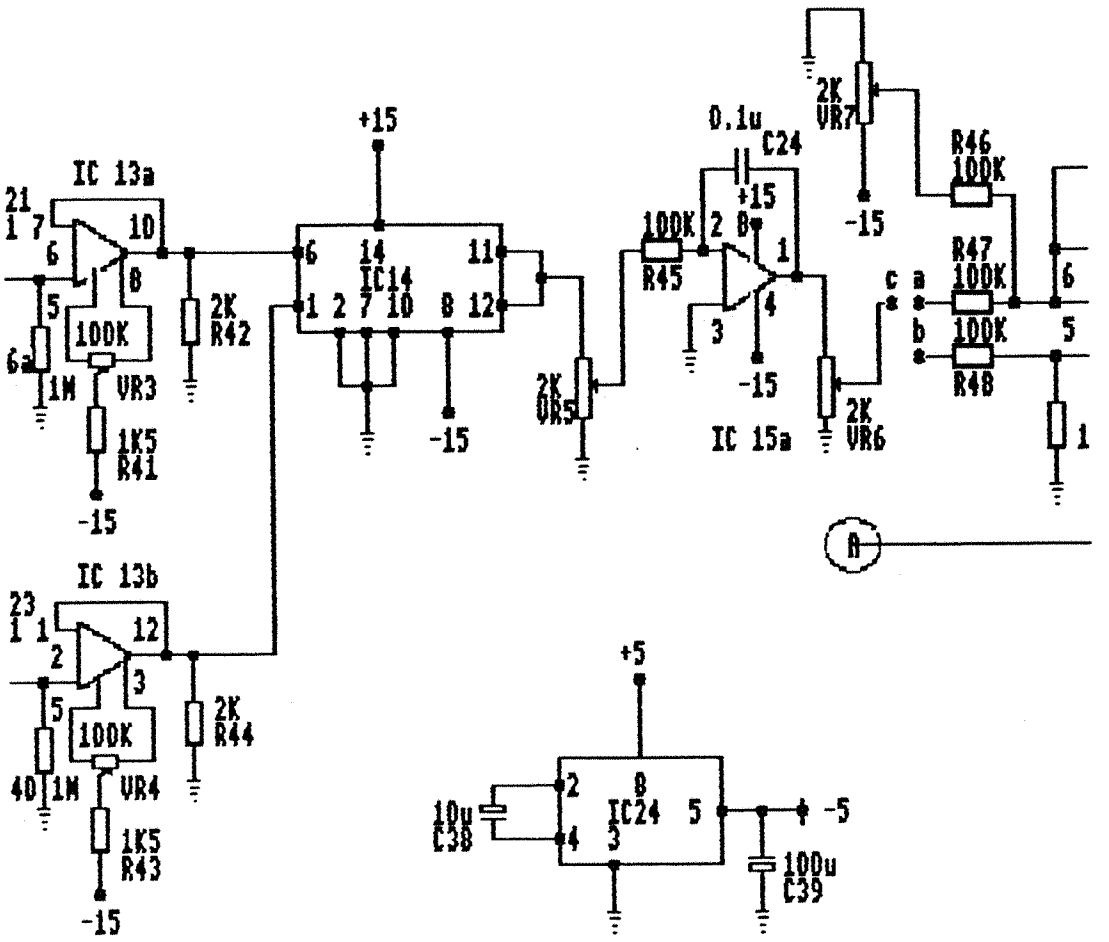
IC 13a
IC 13b
IC14
IC 15a
IC24
+15
-15
+5
-5
100K
2K
1M
1K5
0.1u
100u
10u
R41
R42
R43
R44
R45
R46
R47
R48
VR3
VR4
VR5
VR6
VR7
C24
C38
C39
A

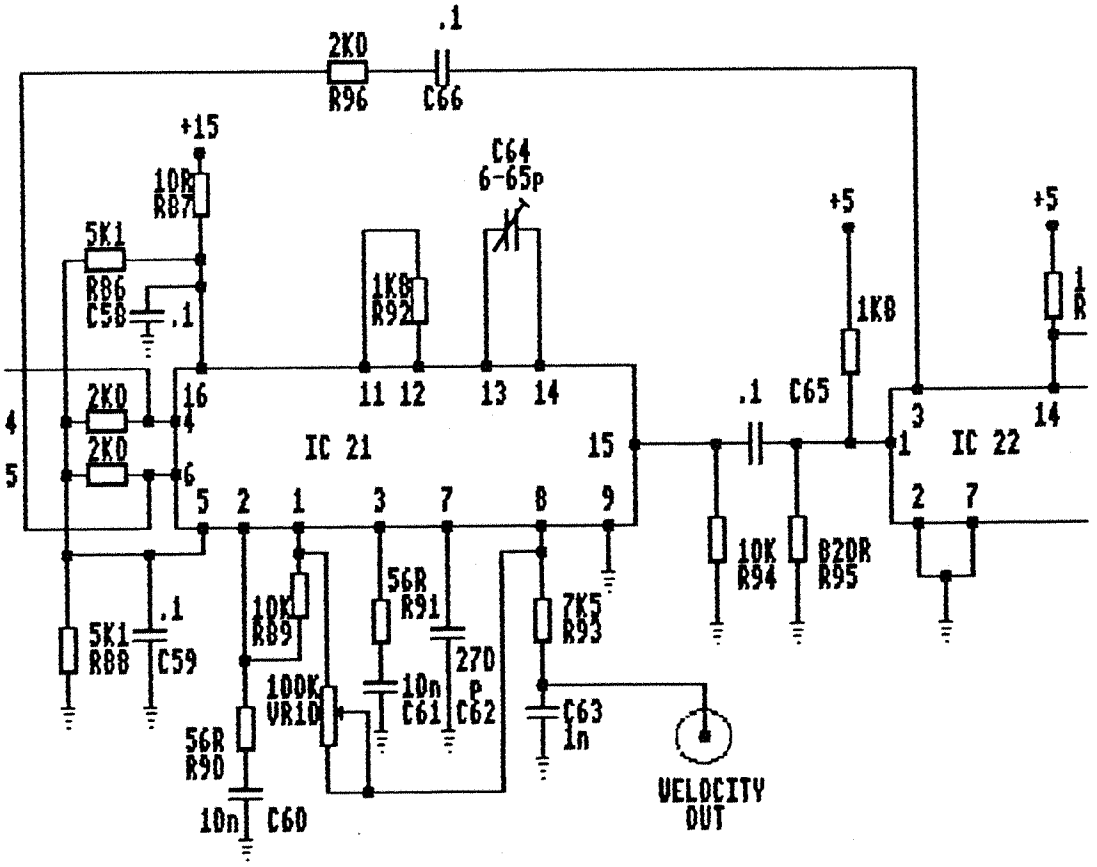
IC 21
IC 22
2K0
5K1
10K
1K8
820R
7K5
56R
270
100K
10n
1n
.1
R86
R87
R88
R89
R90
R91
R92
R93
R94
R95
R96
C58
C59
C60
C61
C62
C63
C64
C65
C66
6-65p
VR10
+15
+5
VELOCITY
OUT

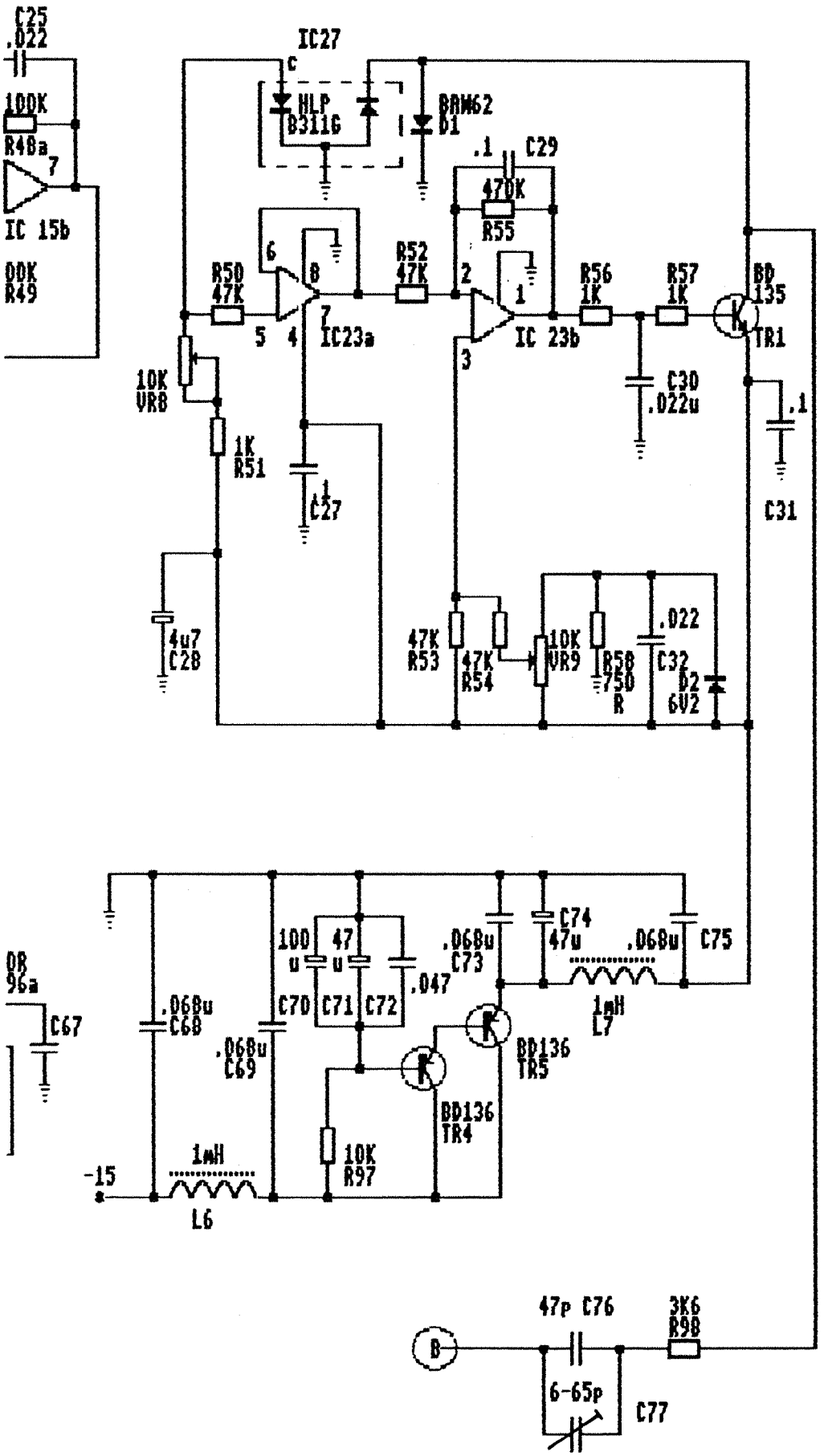
C25
.022
100K
R48a
7
IC 15b
00K
R49
IC27
c
HLP
B311G
BRM62
D1
.1
C29
470K
R55
R50
47K
6
8
7
5
4
IC23a
R52
47K
2
1
3
IC 23b
R56
1K
R57
1K
BD
135
TR1
10K
VR8
1K
R51
C27
C30
.022u
.1
C31
4u7
C28
47K
R53
47K
R54
10K
VR9
R58
750
R
.022
C32
D2
6V2
C74
47u
.068u
C75
100
u
47
u
.047
.068u
C73
1mH
L7
OR
96a
C67
.068u
C68
C70
C71
C72
.068u
C69
BD136
TR5
BD136
TR4
10K
R97
-15
1mH
L6
47p C76
3K6
R98
B
6-65p
C77

## 8.5 RESULTANT SPECKLE PATTERN INTENSITY BY PHASOR ADDITION.

From equation (5.7), it can be seen that the three intensity terms are independent and hence can be treated separately. The time-varying interference term $i_{a.c.}(t)$ is given by,

$$i_{a.c.}(t) = 2\gamma\sum_{p=1}^{P} S_p(I_R I_{Tp})^{1/2}\cos[(\omega_R t + 2kA_T\sin\omega_T t) + (\theta_R - \theta_{Tp})] \quad (A5.1)$$

From this expression, it is evident that each speckle is weighted by the same reference intensity and phase, allowing equation (A5.1) to be rewritten,

$$i_{a.c.}(t) = 2\gamma(I_R)^{1/2}\sum_{p=1}^{P} S_p(I_{Tp})^{1/2}\cos(\theta_C - \theta_{Tp}) \quad (A5.2)$$

where $\theta_C = (\omega_R t + 2kA_T\sin\omega_T t + \theta_R)$ and is the same for each speckle. As shown in figure 5.19, the summation of the individual speckle intensities, each of the form $I_p\cos(\theta_C-\theta_{Tp})$, where $I_p = S_p(I_{Tp})^{1/2}$, produces a resultant intensity vector, also of the form $I_{res}\cos(\theta_C-\Xi_{res})$. This resultant intensity vector can be calculated from the simple geometric relationships;

$$I_{res}^2 = (I_1\sin\theta_1 + I_2\sin\theta_2 + \ldots. I_p\sin\theta_p)^2 + (I_1\cos\theta_2 + I_2\cos\theta_2 + \ldots. I_p\cos\theta_p)^2$$

$$= \sum_{p=1}^{P}\sum_{q=1}^{P} I_p I_q\cos(\theta_p - \theta_q) \quad (A5.3)$$

and,

$$\tan\Xi_{res} = \frac{\sum_{p=1}^{P} I_p\sin\theta_p}{\sum_{p=1}^{P} I_p\cos\theta_p} \quad (A5.4)$$

where $\theta_i = \theta_C - \theta_{Ti}$, $i=1,2...\infty$. The two d.c. terms $i_{d.c.}(t)$ are given by,

$$i_{d.c.}(t) = \gamma(I_R + I_{res}) \qquad (A5.5)$$

where $I_R$ is a constant. As discussed in section 5.2.2, dynamic-speckle induced fluctuations in the $I_{res}$ term in this expression can be neglected.

## 8.6 RESONANCE FREQUENCIES OF A CANTILEVERED BEAM.

From Bishop and Johnson[52], the flexural wavenumbers $k_R$ at resonance for a cantilevered beam are given by the expression,

$$k_R = \left[ \frac{\omega_R^2 \rho S}{EI} \right]^{1/4} \qquad (A6.1)$$

where $\omega_R$ is the radian frequency, $\rho$ is the beam material density, S the cross-sectional area, E the Young's modulus of elasticity, I the second moment of area and R = 1, 2, ...$\infty$. For a fixed-free beam, $k_1 l = 1.875$, where l is the beam length. Hence with a mild steel bar, E = 207 $GNm^{-2}$, $\rho$ = 2850 $Kgm^{-3}$, with radius 0.5 cm and length 12 cm, the first resonance frequency is 823 Hz.

The first longitudinal resonance frequency will occur when $\lambda = 21$. For a linear, homogeneous bar, the wavespeed c is given by the relationship,

$$c = \left[ \frac{E}{\rho} \right]^{1/2} \qquad (A6.2)$$

Hence, employing the relationship $c = f\lambda$, the first resonance frequency can be calculated from,

$$f = \frac{1}{21} \left[ \frac{E}{\rho} \right]^{1/2} \qquad (A6.3)$$

i.e. approximately 35.5 kHz.

## 8.7 TWO-DIMENSIONAL POWER FLOW MEASUREMENT SCHEME.

In the far-field, the time-average, shear force component of power flow in the arbitrarily defined x-direction, $\langle P_x \rangle$, is given by,

$$\langle P_x \rangle = -2D \left\langle \left[ \frac{\delta^3 w}{\delta x^3} + \frac{\delta^3 w}{\delta x \delta y^2} \right] \frac{\delta w}{\delta t} \right\rangle \qquad (A7.1)$$

where D is the flexural stiffness, equal to $(Ed^3/12(1-\gamma))$, where E is Young's Modulus, d is the plate thickness and $\gamma$ Poisson's ratio, and w is the normal-to-surface displacement given by,

$$w(x,y,t) = A\sin(\omega t - k_x x - k_y y) \qquad (A7.2)$$

where $k_x$ and $k_y$ are the flexural wavenumbers in the x and y directions. In the y-direction, the power flow is given by,

$$\langle P_y \rangle = -2D \left\langle \left[ \frac{\delta^3 w}{\delta y^3} + \frac{\delta^3 w}{\delta y \delta x^2} \right] \frac{\delta w}{\delta t} \right\rangle \qquad (A7.3)$$

Assuming simple harmonic motion, these equations can be simplified to,

$$\langle P_x \rangle = -2Dk_T^2 \left\langle \frac{\delta w}{\delta t} \frac{\delta w}{\delta x} \right\rangle \qquad (A7.4)$$

and,

$$\langle P_y \rangle = -2Dk_T^2 \left\langle \frac{\delta w}{\delta t} \frac{\delta w}{\delta y} \right\rangle \qquad (A7.5)$$

where $k_T$ is the true wavenumber, equal to $(\omega^2 M/D)^{1/4}$, and related to $k_x$ and $k_y$ by,

$$k_x = k_T\cos\theta \quad : \quad k_y = k_T\sin\theta \qquad (A7.6)$$

where M is the plate mass per unit thickness and $\theta$ is the angle the resultant power flow vector makes with the x-axis. Since this angle is unknown, $k_x$ and $k_y$ cannot be determined accurately and uni-directional

measurements cannot be considered independently. For accurate power flow measurements, $(\delta w/\delta x)$ and $(\delta w/\delta y)$ must be measured simultaneously with the point velocity $(\delta w/\delta t)$. This scheme will thus require utilisation of two velocity gradient transducers, and a laser velocity transducer. The magnitude of the resultant, time-average, power flow vector, $\langle P_R \rangle$, is then related to the two orthogonal power flow measurements by,

$$\langle P_R \rangle^2 = \langle P_X \rangle^2 + \langle P_Y \rangle^2 \qquad (A7.7)$$

$$= 4D^2 k_Z^6 \left[ \left[ \langle v \frac{\delta w}{\delta x} \rangle \right]^2 + \left[ \langle v \frac{\delta w}{\delta y} \right]^2 \right]$$

As with one-dimensional measurements, in the frequency domain this expression may be written in terms of cross-spectra as,

$$\langle P_R \rangle = 2Dk_Z^3 \left[ \{ \mathrm{Im}\ G(v, dv/dx, f) \}^2 + \{ \mathrm{Im}\ G(v, dv/dy, f) \}^2 \right]^{1/2} \qquad (A7.8)$$

and the angle $\theta$, $\langle P_R \rangle$ makes with the x axis will be given by,

$$\theta = \arctan \left[ \frac{\mathrm{Im}\ G(v, dv/dy, f)}{\mathrm{Im}\ G(v, dv/dx, f)} \right] \qquad (A7.9)$$

The magnitude and direction of the resultant power flow can therefore be measured directly using an optical transducer scheme consisting of two, perpendicularly positioned laser velocity gradient transducers and a laser point velocity transducer positioned at the midpoint.

## 9. LIST OF FIGURES.

FIGURE 1.1 TYPICAL NOISE AND VIBRATION ENVIRONMENT.

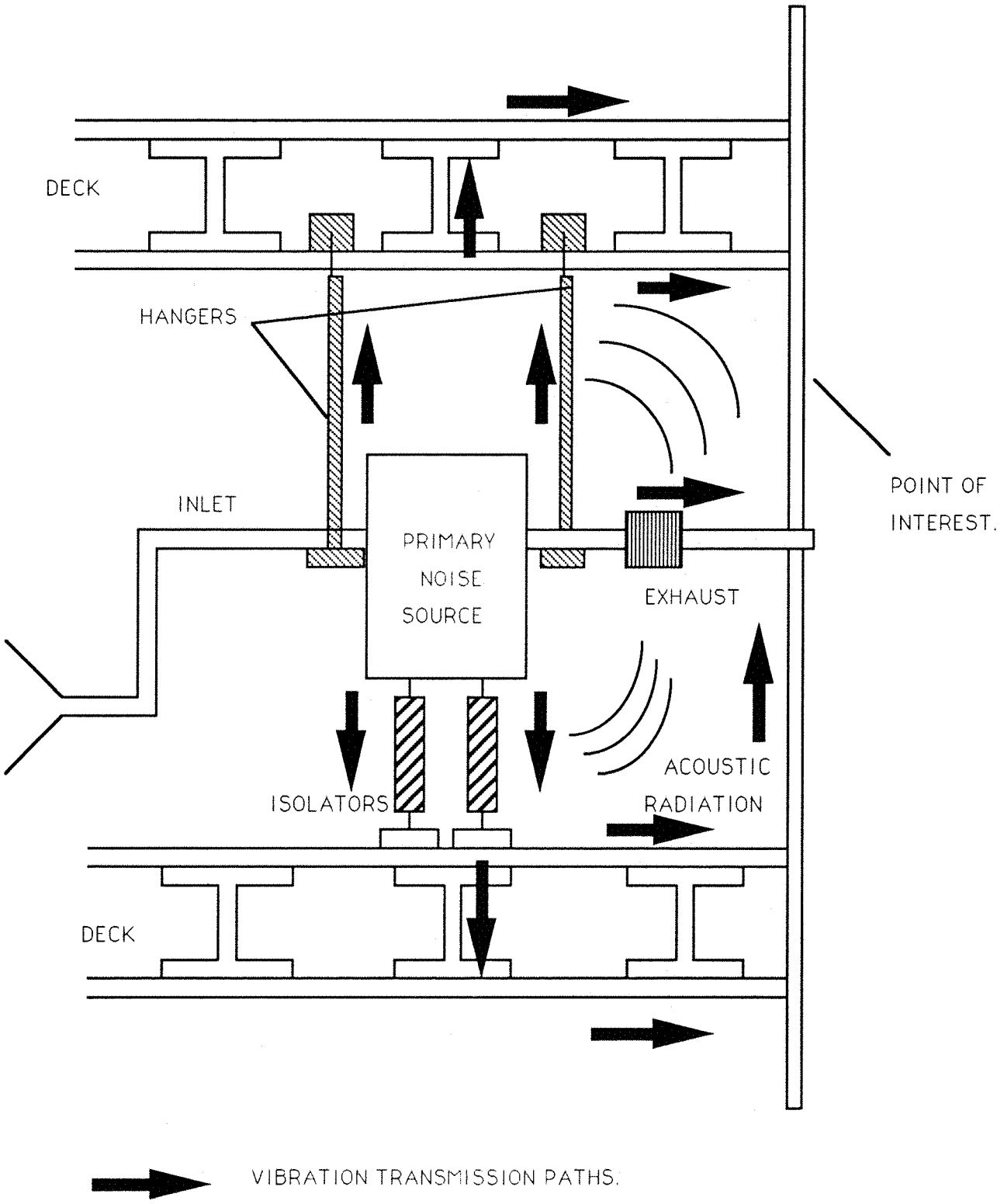

FIGURE 2.1 ACCELEROMETER CONFIGURATIONS FOR MEASURING SPATIAL ACCELERATION GRADIENTS.

A) BIAXIAL ACCELEROMETER.

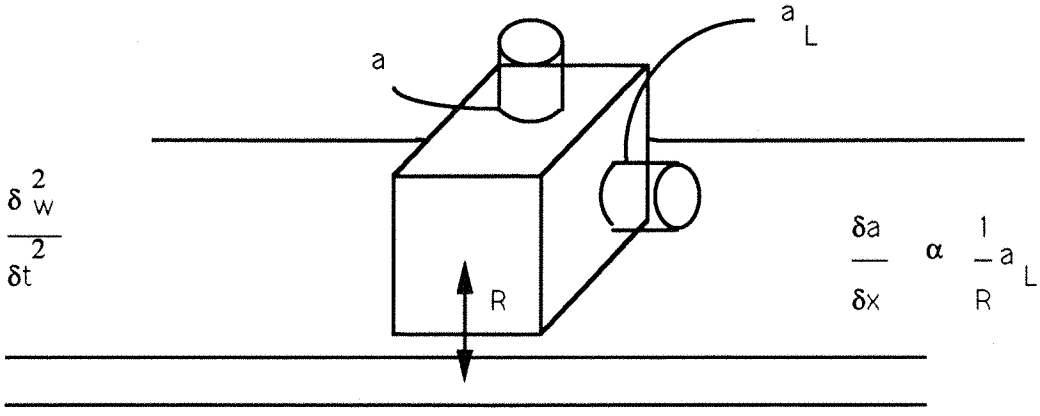


$$a = \frac{\delta^2 w}{\delta t^2}$$

$$\frac{\delta a}{\delta x} \alpha \frac{1}{R} a_L$$

B) DIFFERENCING ACCELEROMETER.

$$\frac{\delta a}{\delta x} \alpha \frac{1}{2h} (a_2 - a_1)$$

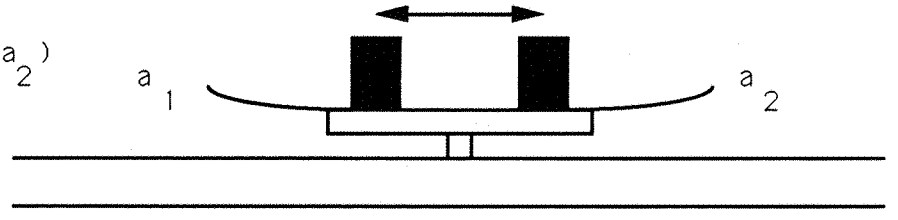


$$a = \frac{1}{2} (a_1 + a_2)$$

C) FINITE DIFFERENCE APPROXIMATION.

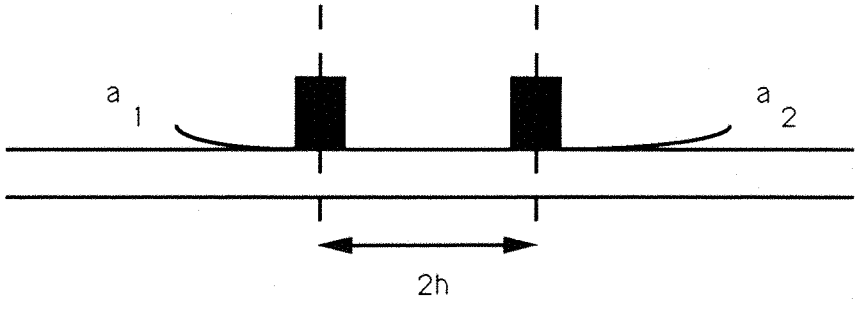


$$a = \frac{1}{2} (a_1 + a_2)$$

$$\frac{\delta a}{\delta x} \alpha \frac{1}{2h} (a_2 - a_1)$$

FIGURE 2.2 TYPICAL ACCELEROMETER AMPLITUDE AND PHASE RESPONSE.

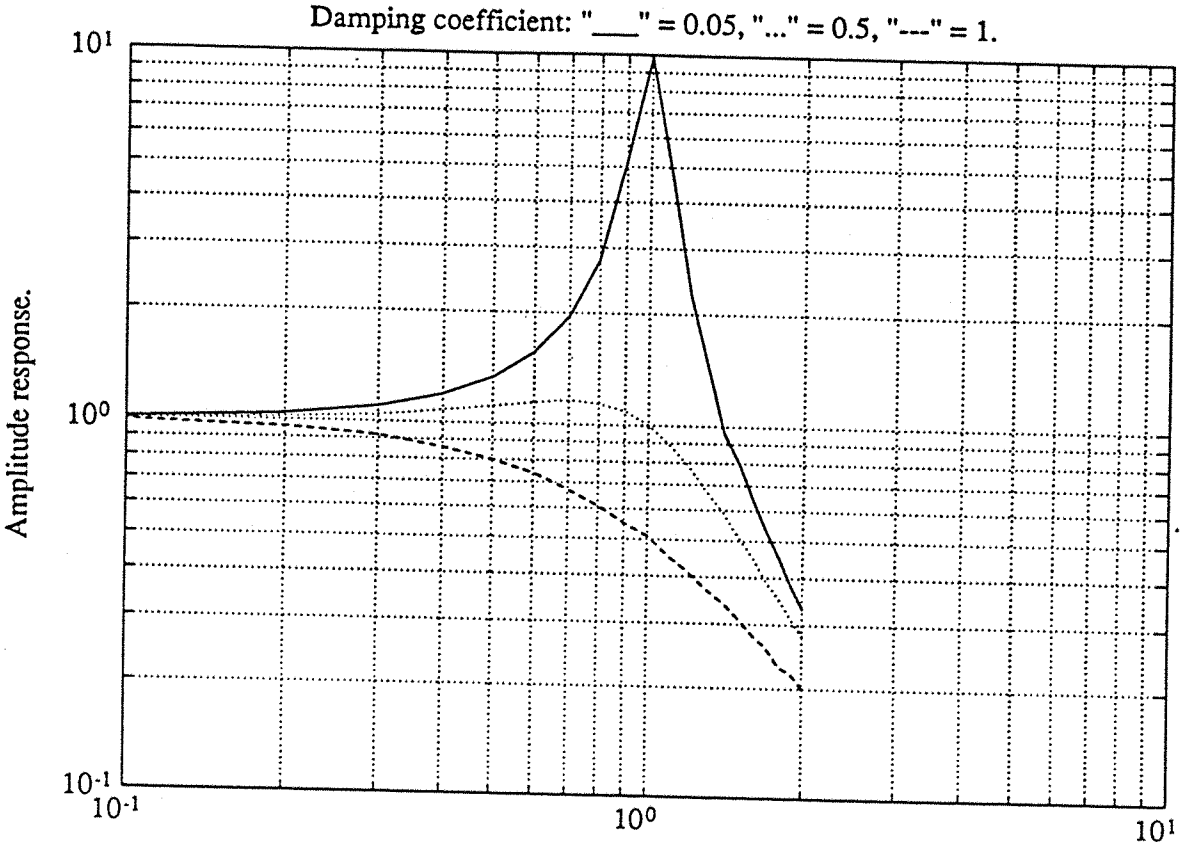


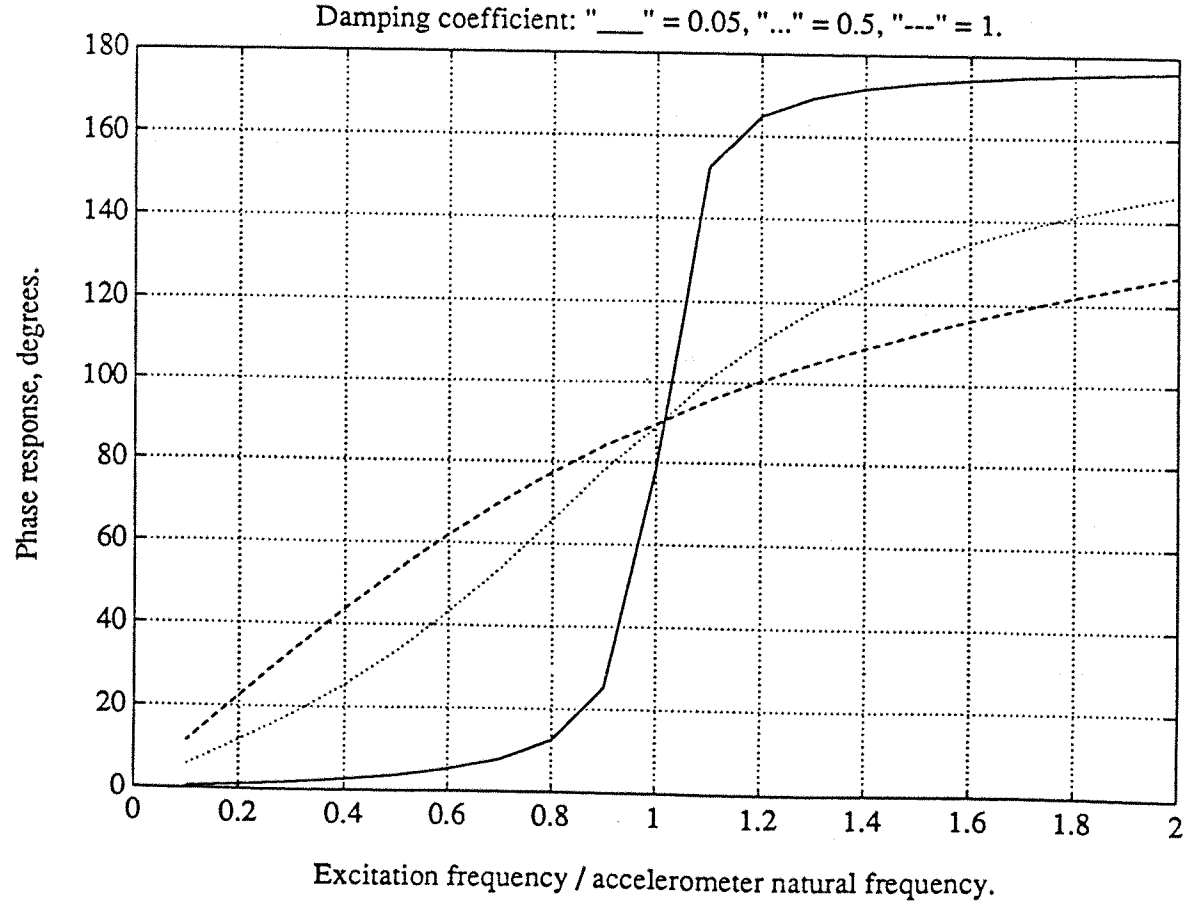

FIGURE 2.3 ACCELEROMETER MASS-LOADING EFFECT ON AN INFINITE BEAM.

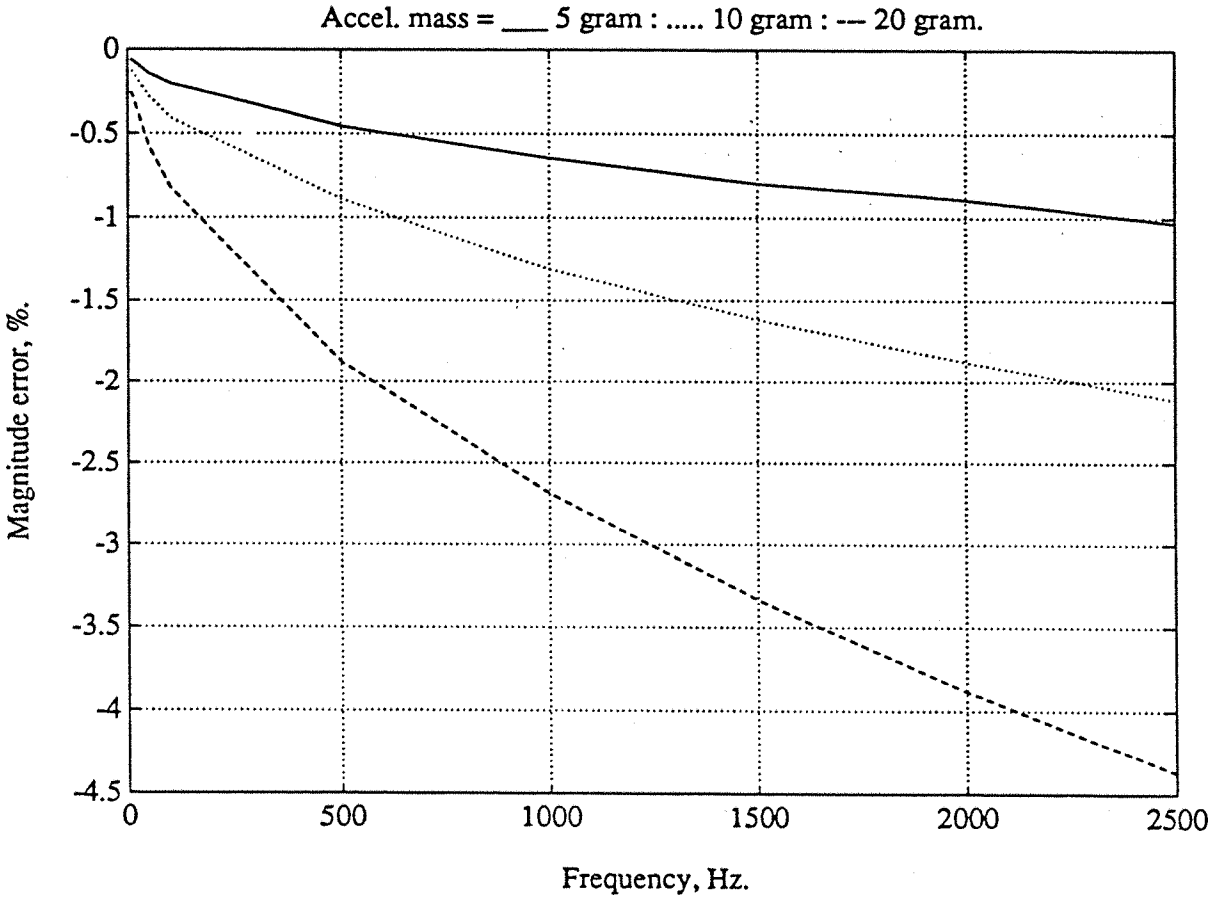


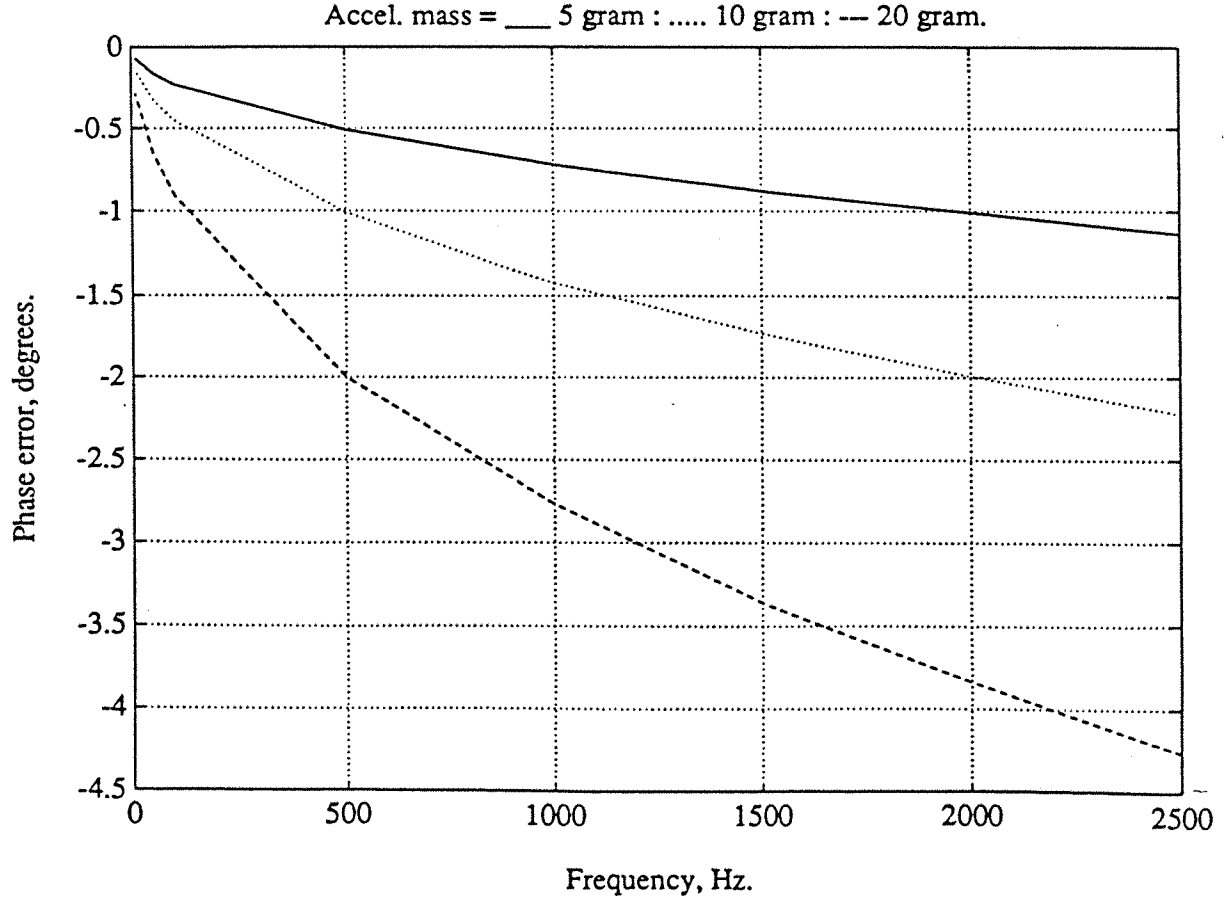

FIGURE 2.4 TRANSDUCER CONFIGURATION FOR SIMULTANEOUS FLEXURAL AND LONGITUDINAL S.I. MEASUREMENT.

a) Measurement scheme.

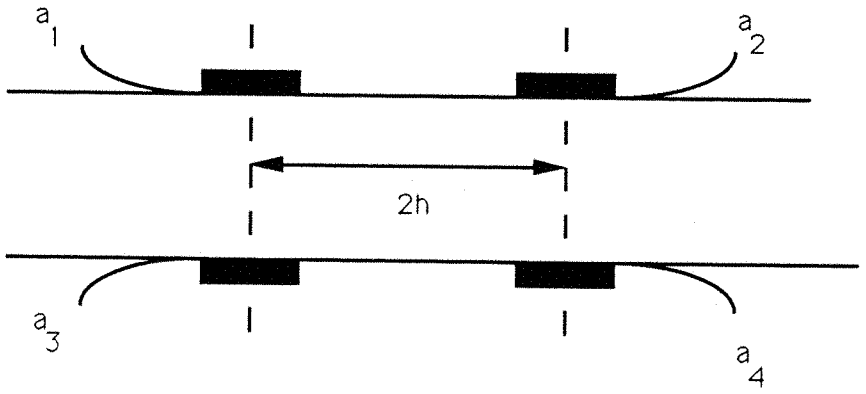


b) Transmission mechanisms.

FLEXURAL WAVE MOTION.

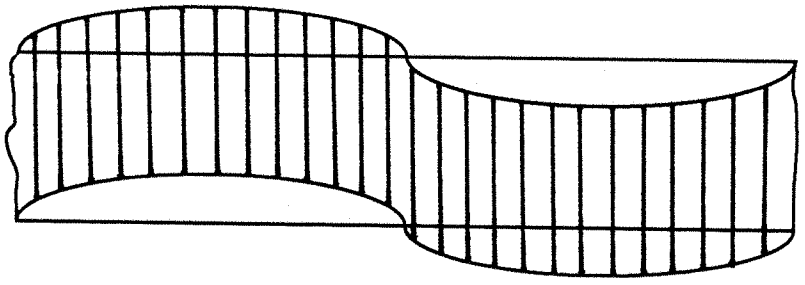

LONGITUDINAL WAVE MOTION.

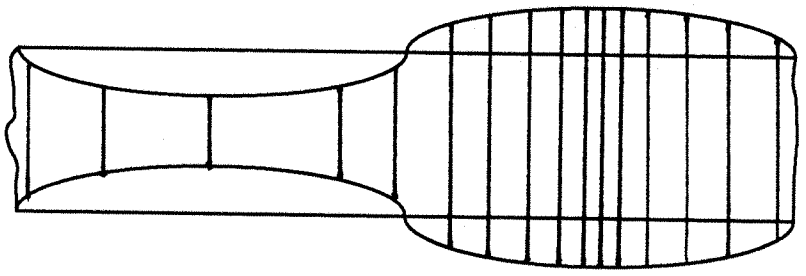

FIGURE 2.5 STRUCTURAL INTENSITY MEASUREMENT ERROR DUE TO INTER-TRANSDUCER PHASE ERRORS: B/A = 0.

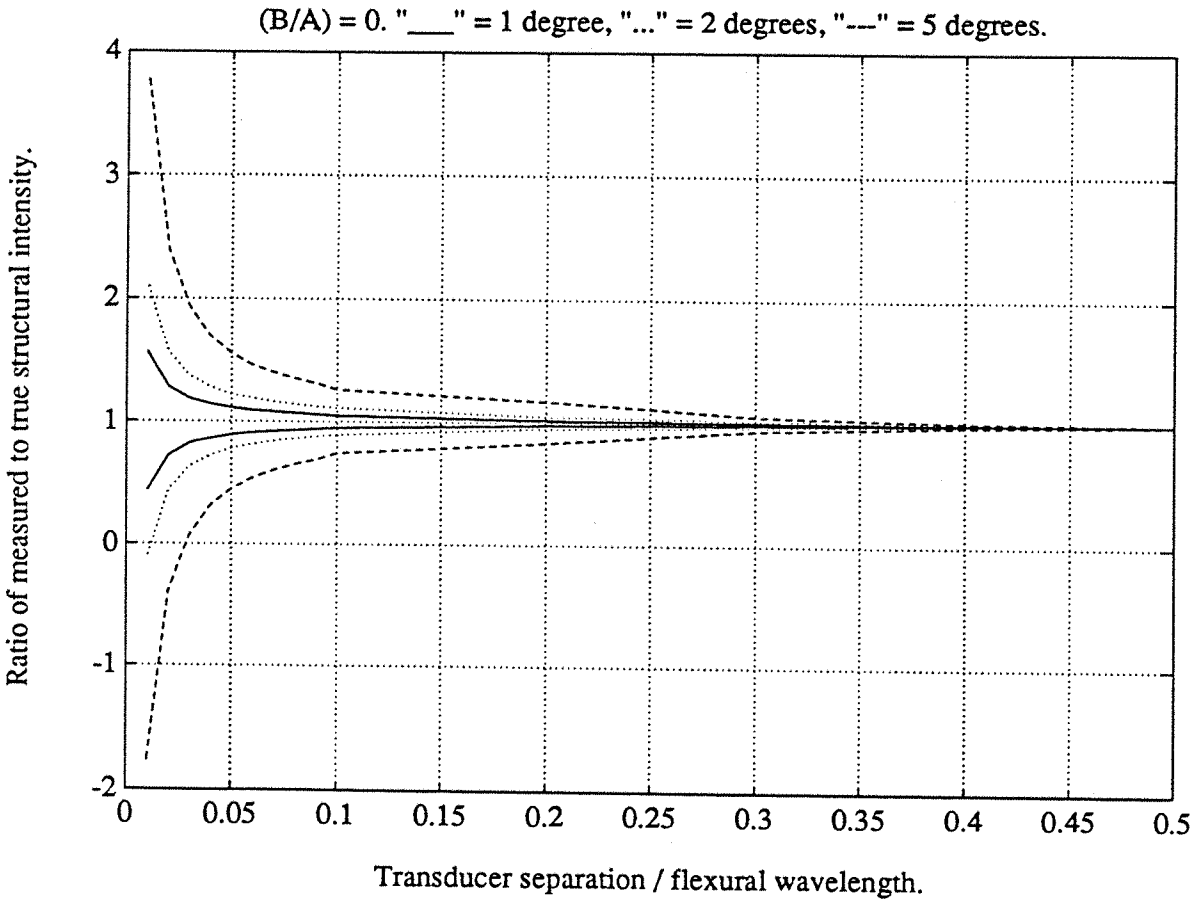

FIGURE 2.6 STRUCTURAL INTENSITY MEASUREMENT ERROR.

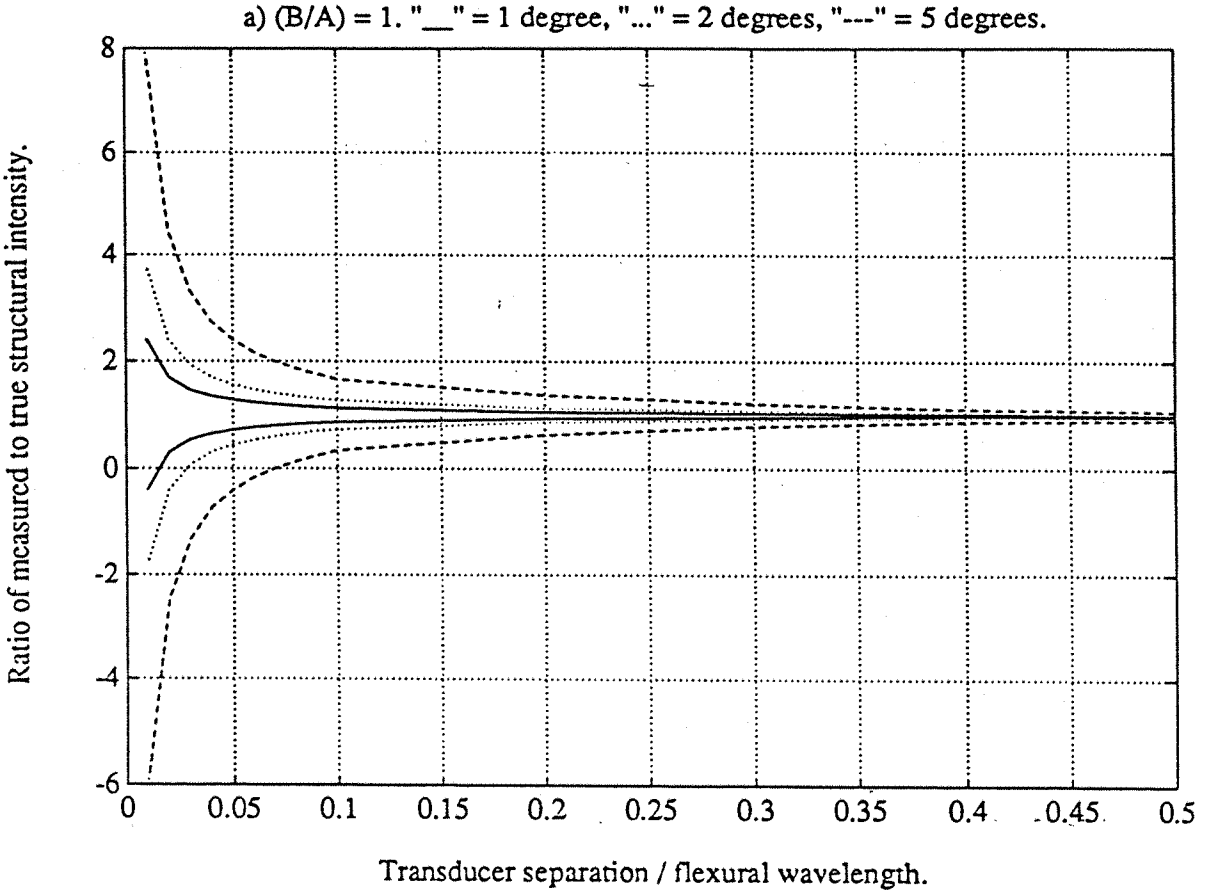


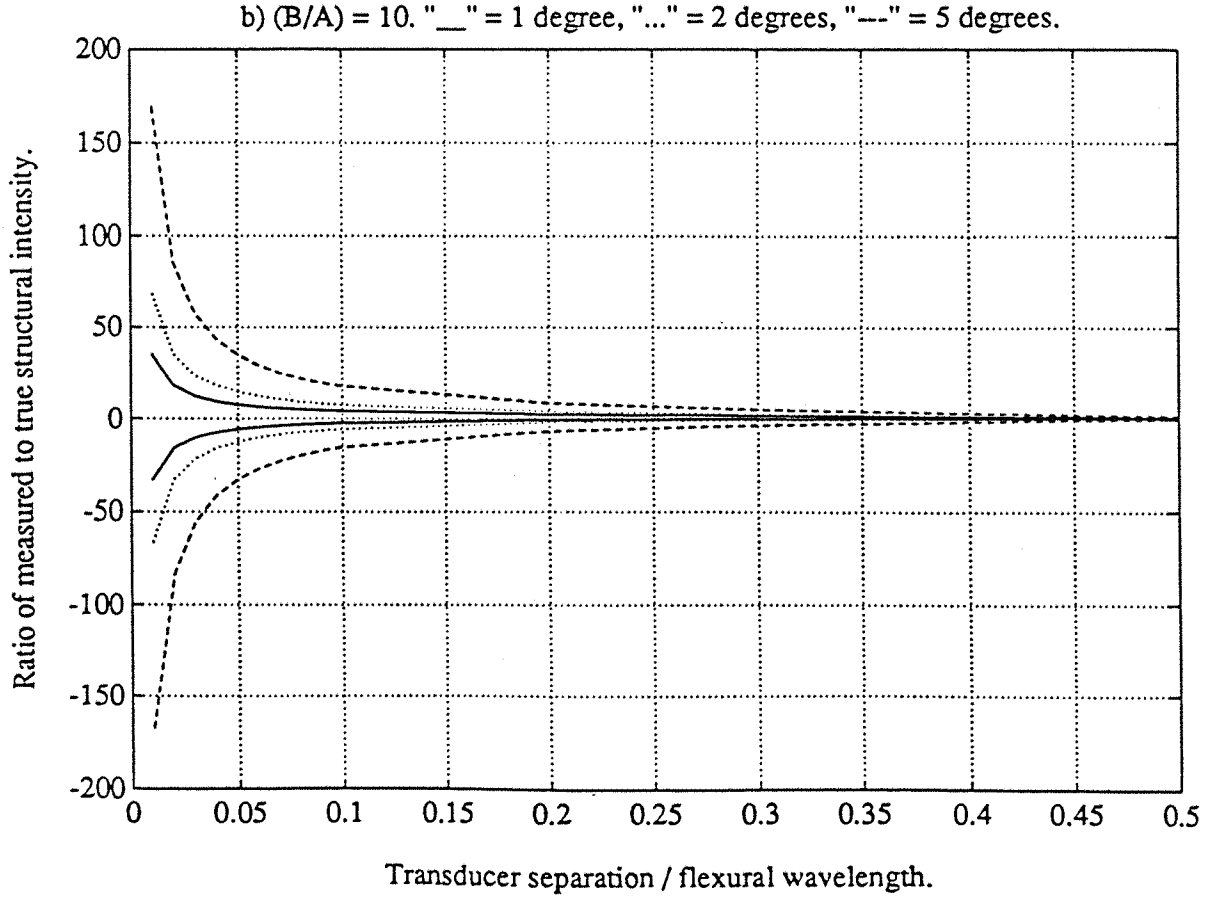

FIGURE 2.7 "INFINITE" BEAM APPARATUS AND MEASUREMENT POSITIONS.

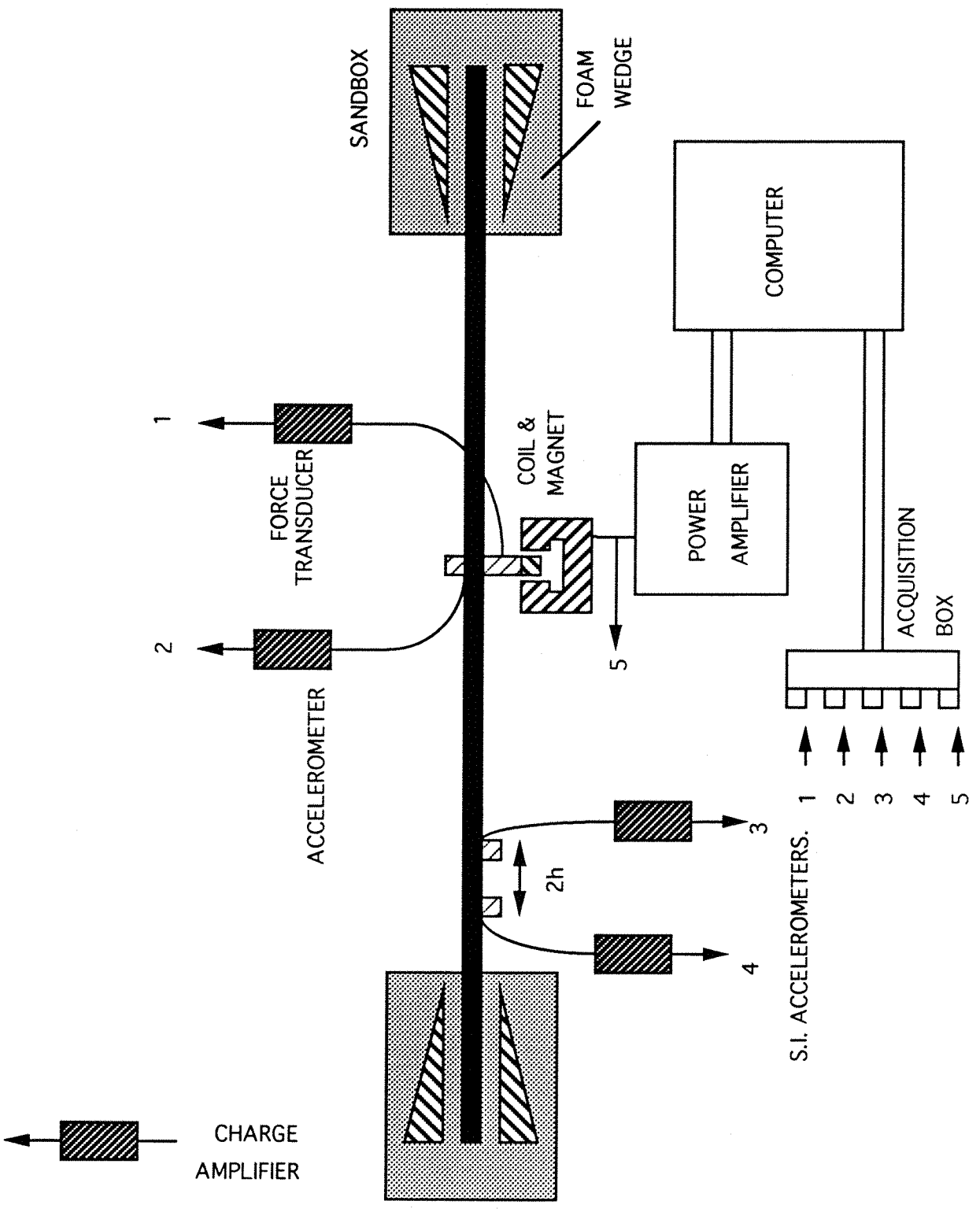

FIGURE 2.8 MEASURED BEAM ACCELERANCE, MAGNITUDE AND PHASE.

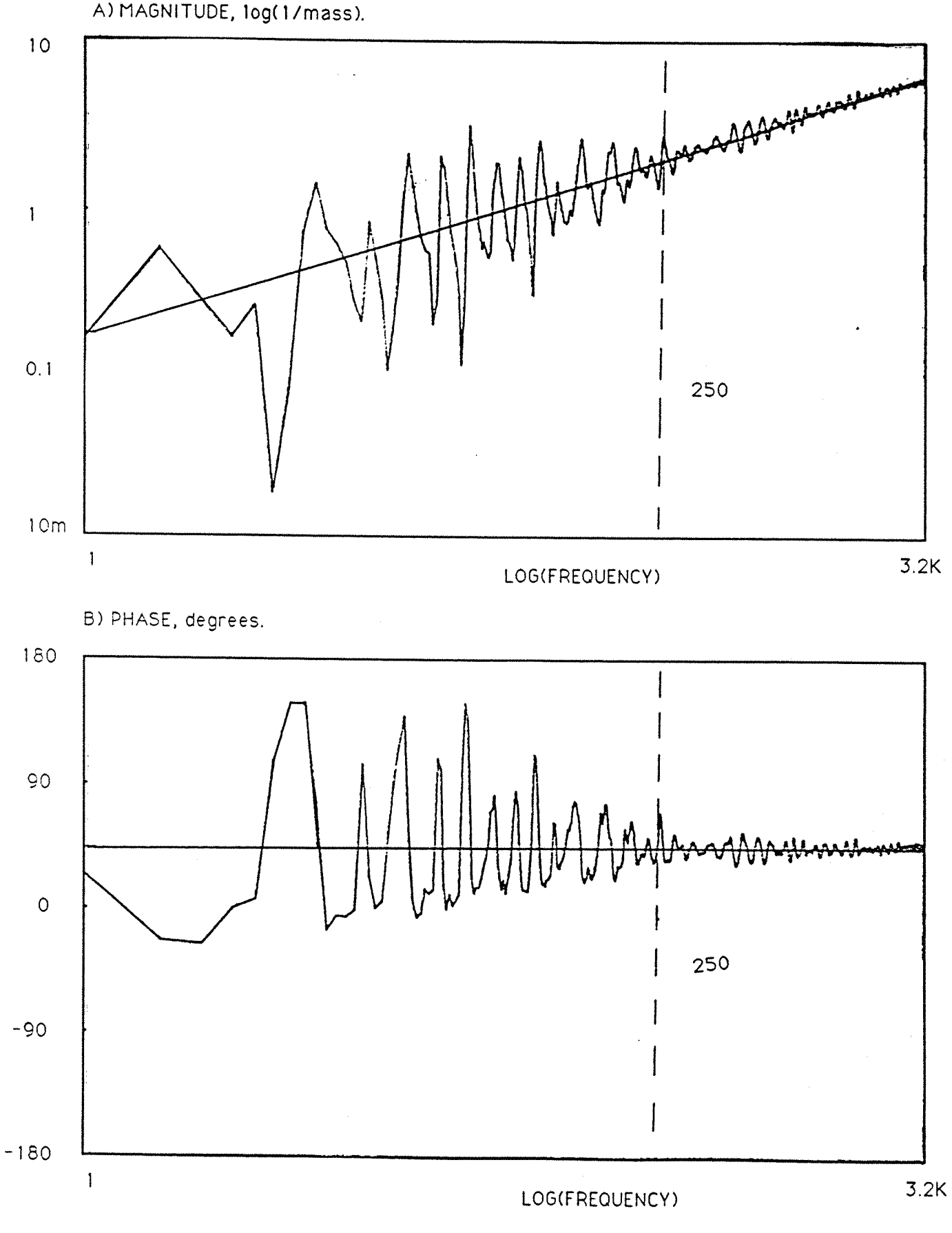

FIGURE 2.9 BEAM ACCELERANCE, REAL AND IMAGINARY COMPONENTS.

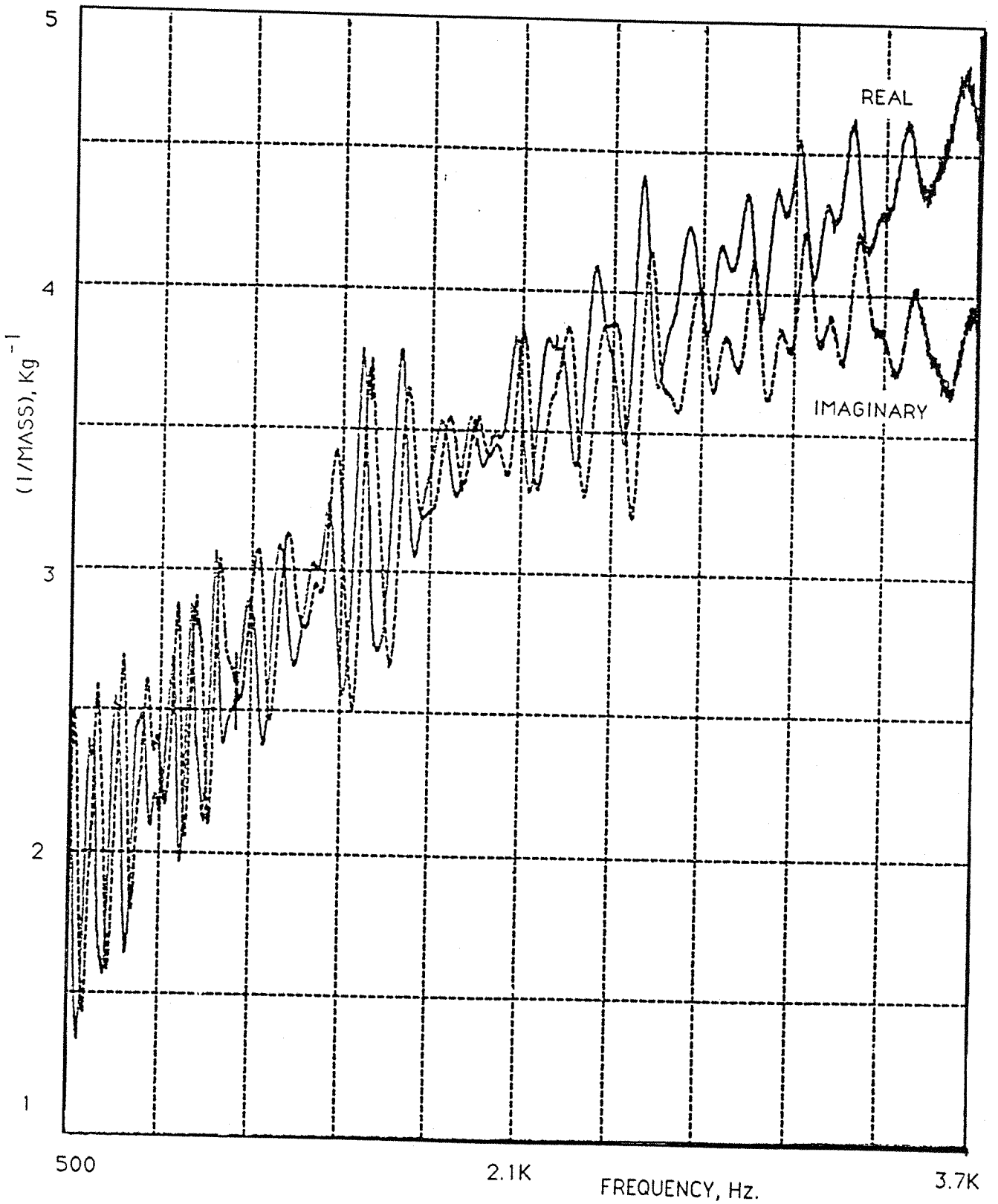

FIGURE 2.10 TYPICAL INTER-ACCELEROMETER RESPONSE CHARACTERISTICS.

A) MAGNITUDE.

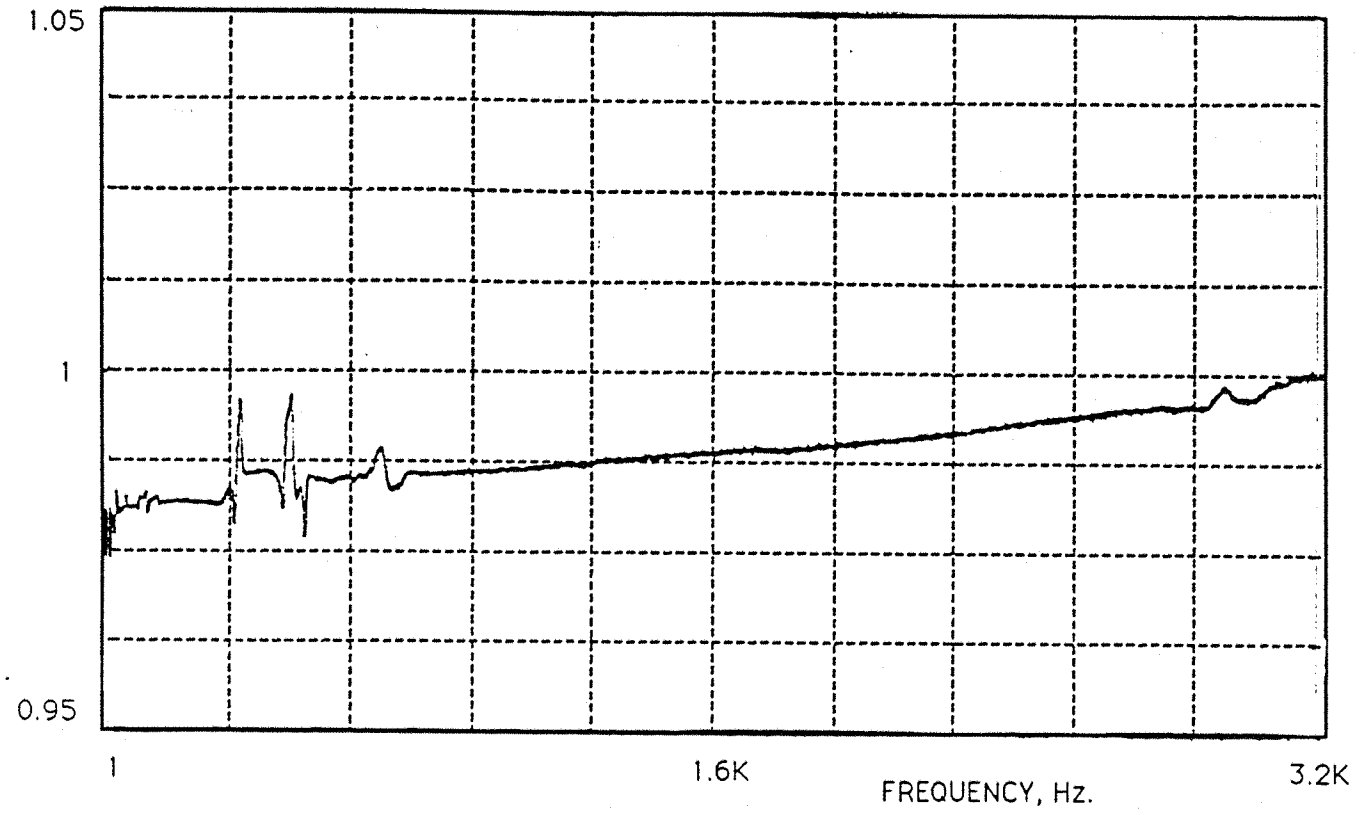


B) PHASE, degrees.

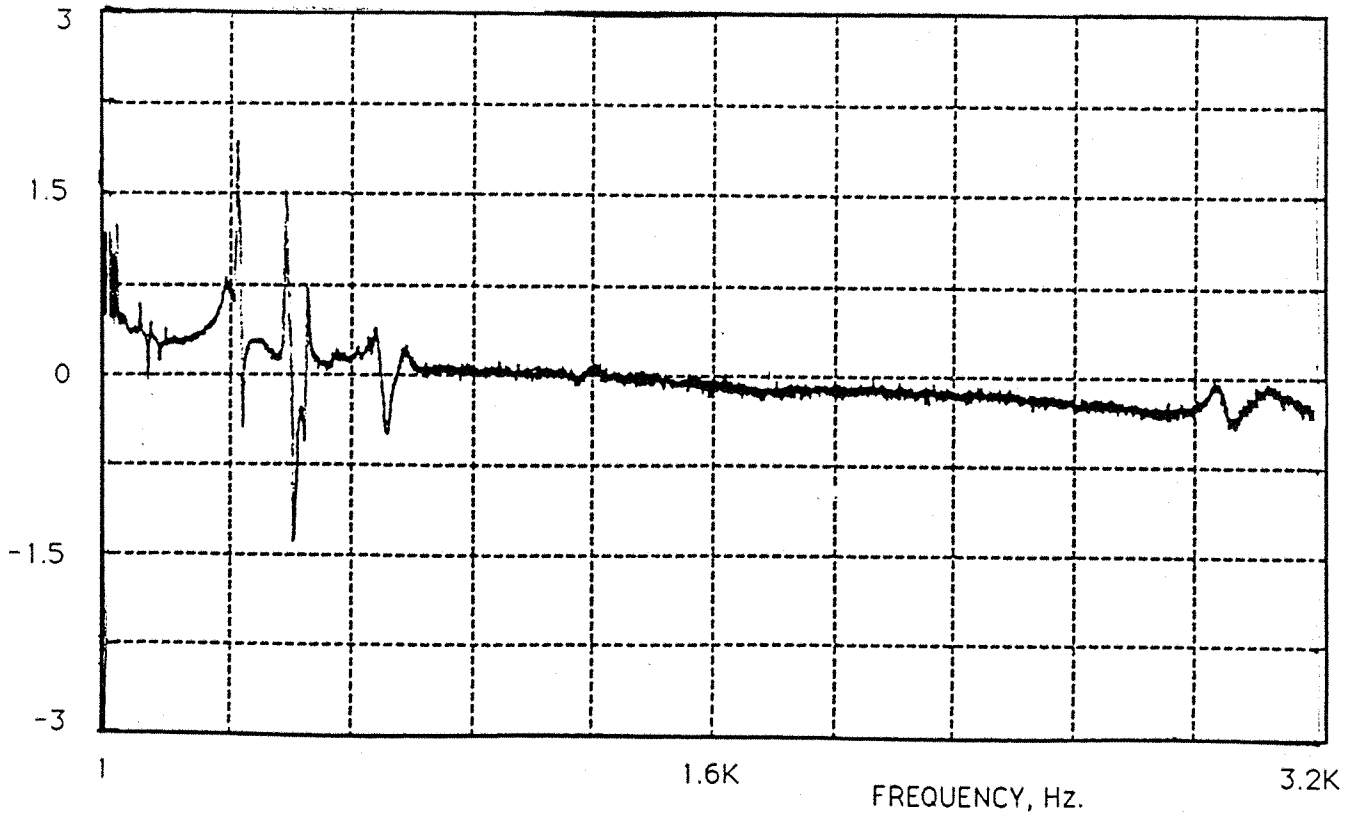

FIGURE 2.11 'CHIRP' EXCITATION SIGNAL.

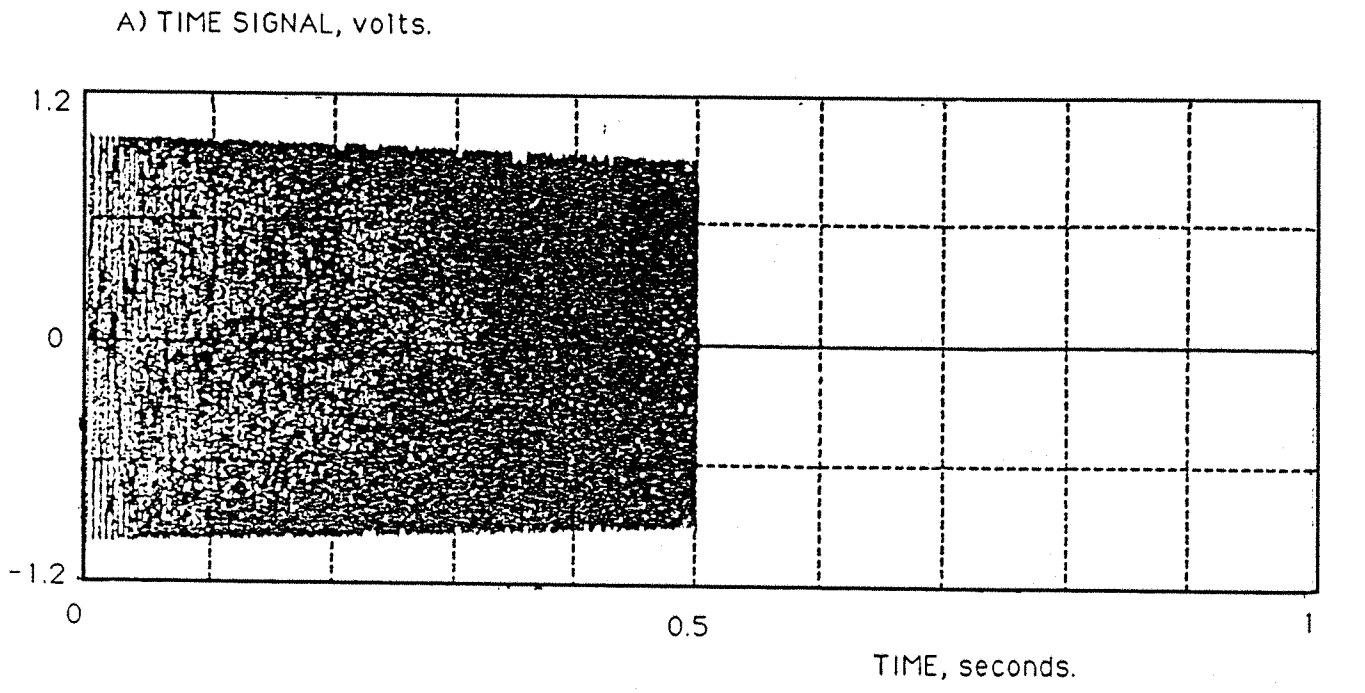


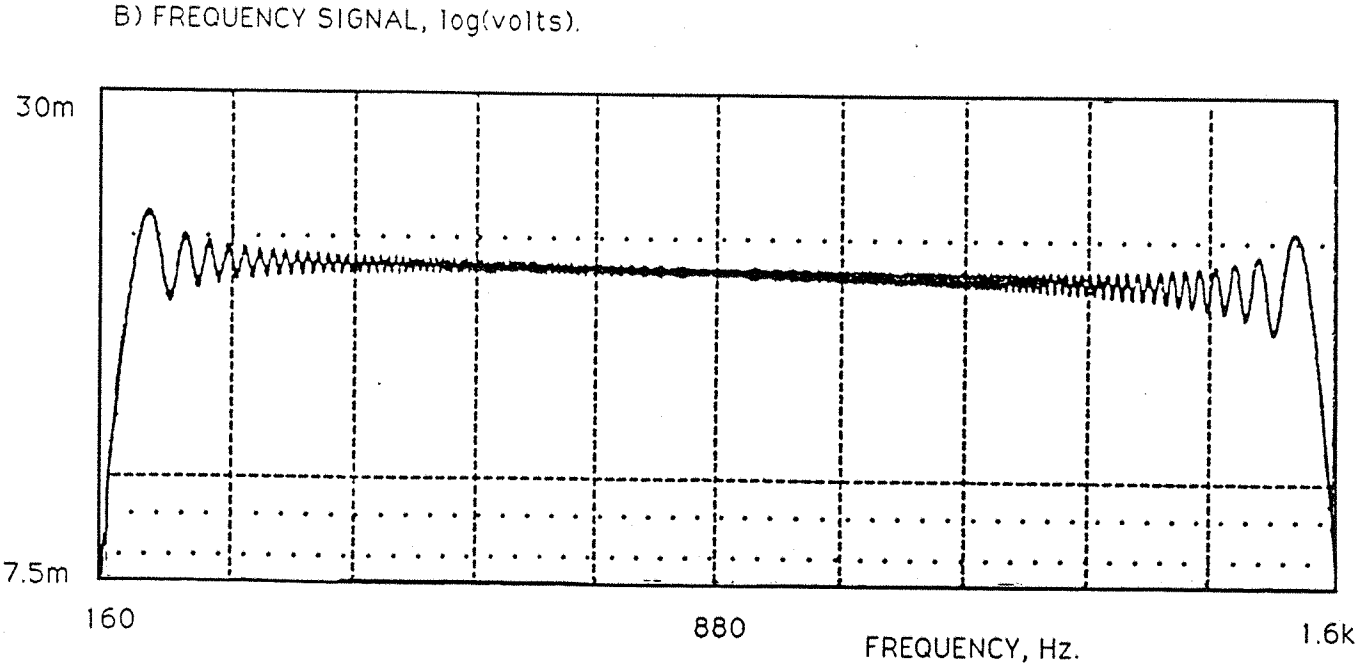

FIGURE 2.12 INPUT FORCE EXCITATION AND ACCELERATION RESPONSE.

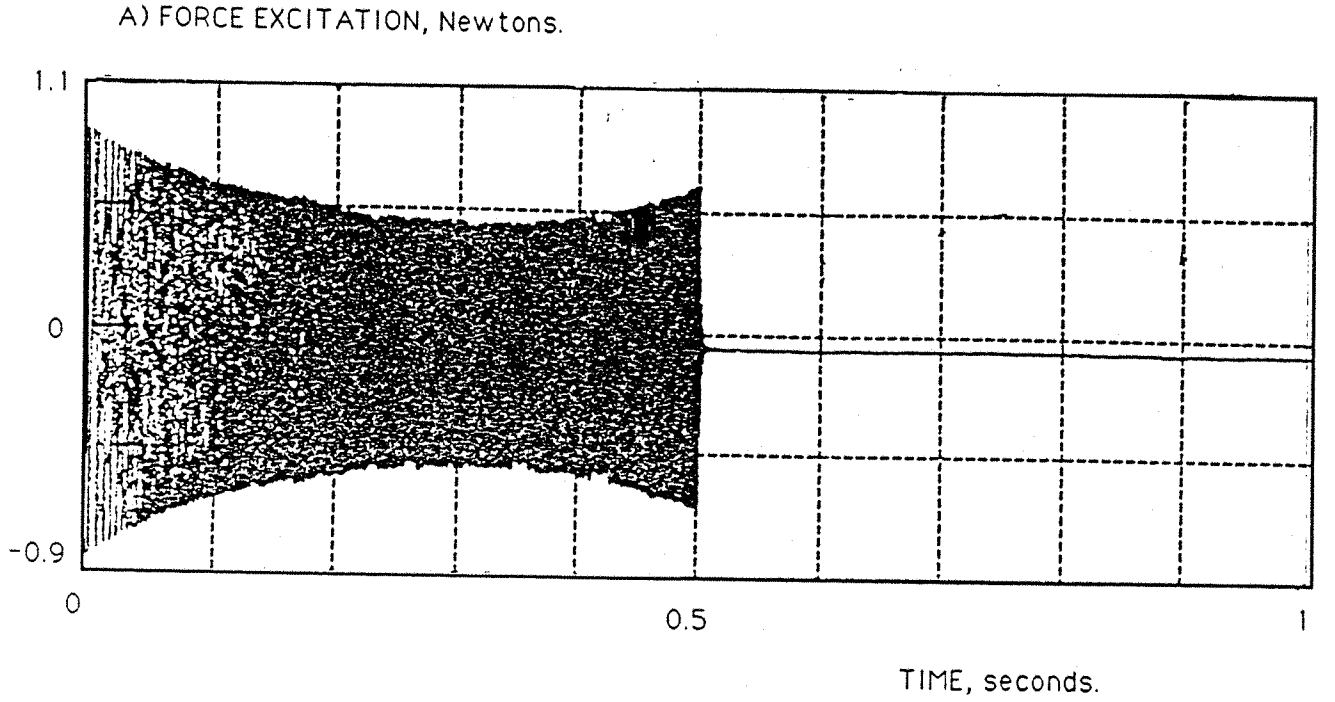


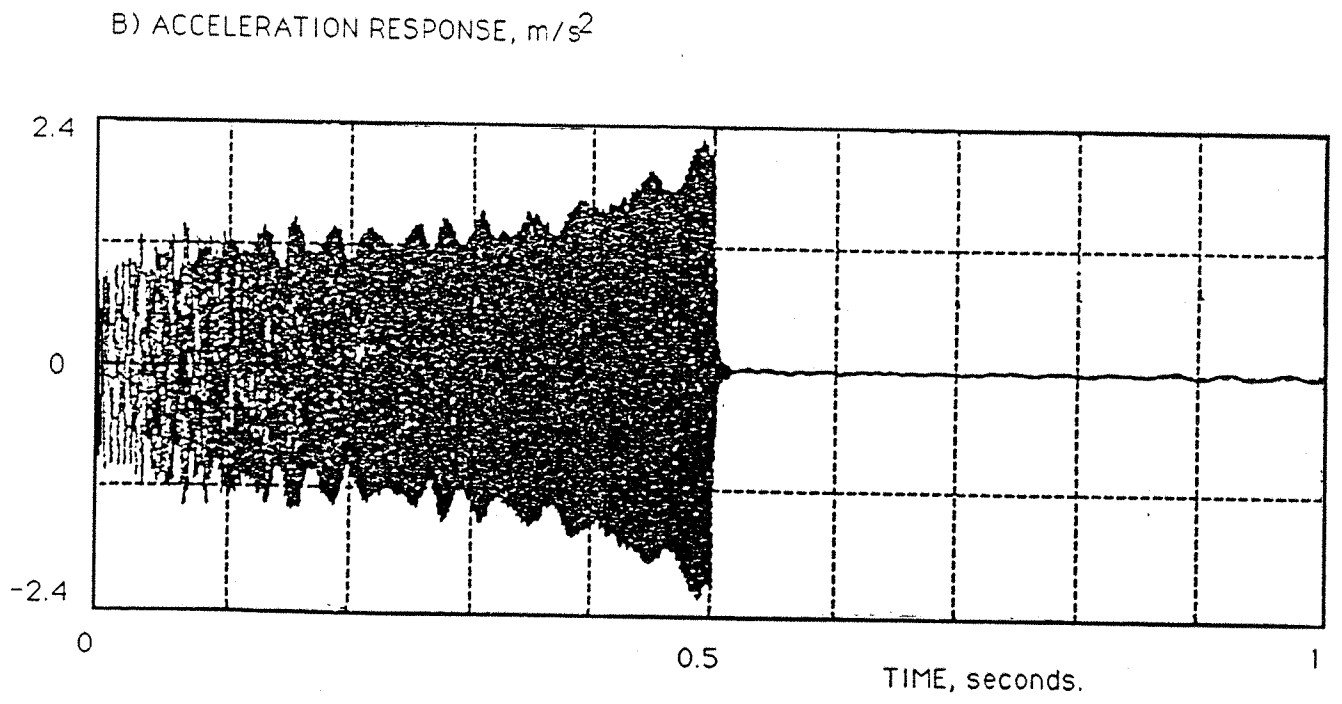

FIGURE 2.13 INPUT POWER, 450-550 Hz.

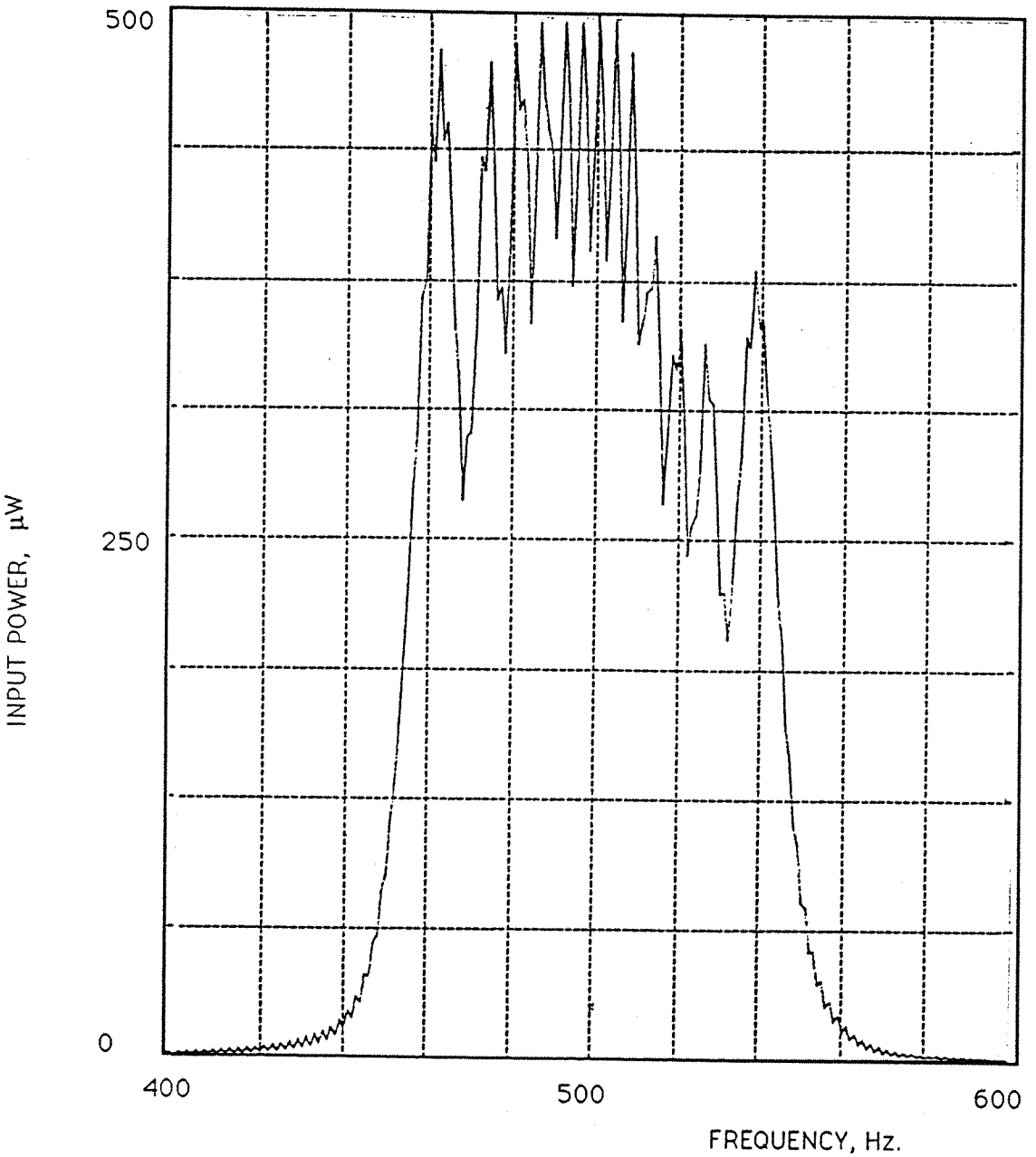

FIGURE 2.14 TRANSMITTED POWER.

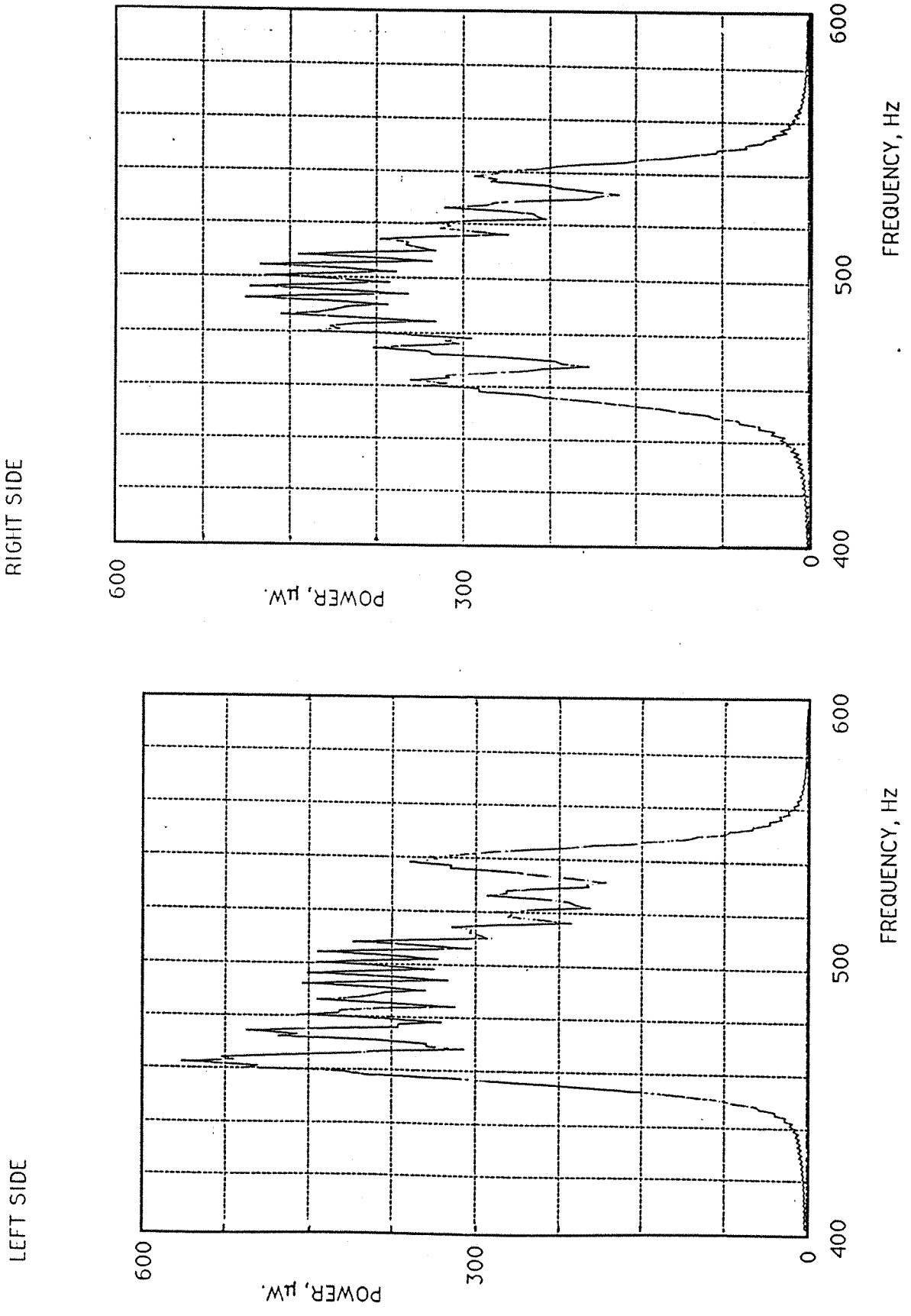

FIGURE 2.15 INPUT POWER, 950-1050 Hz.

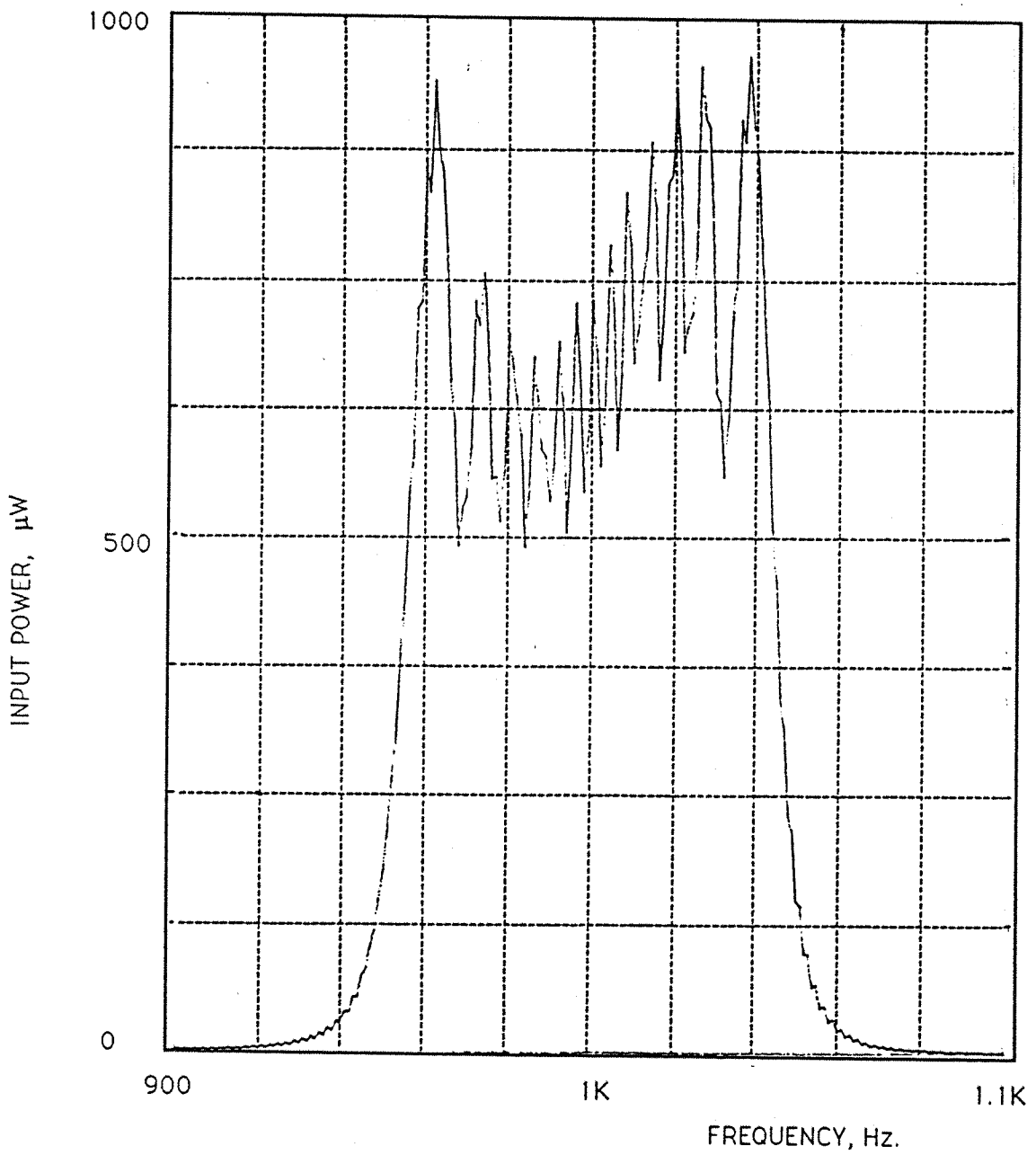

FIGURE 2.16 TRANSMITTED POWER.

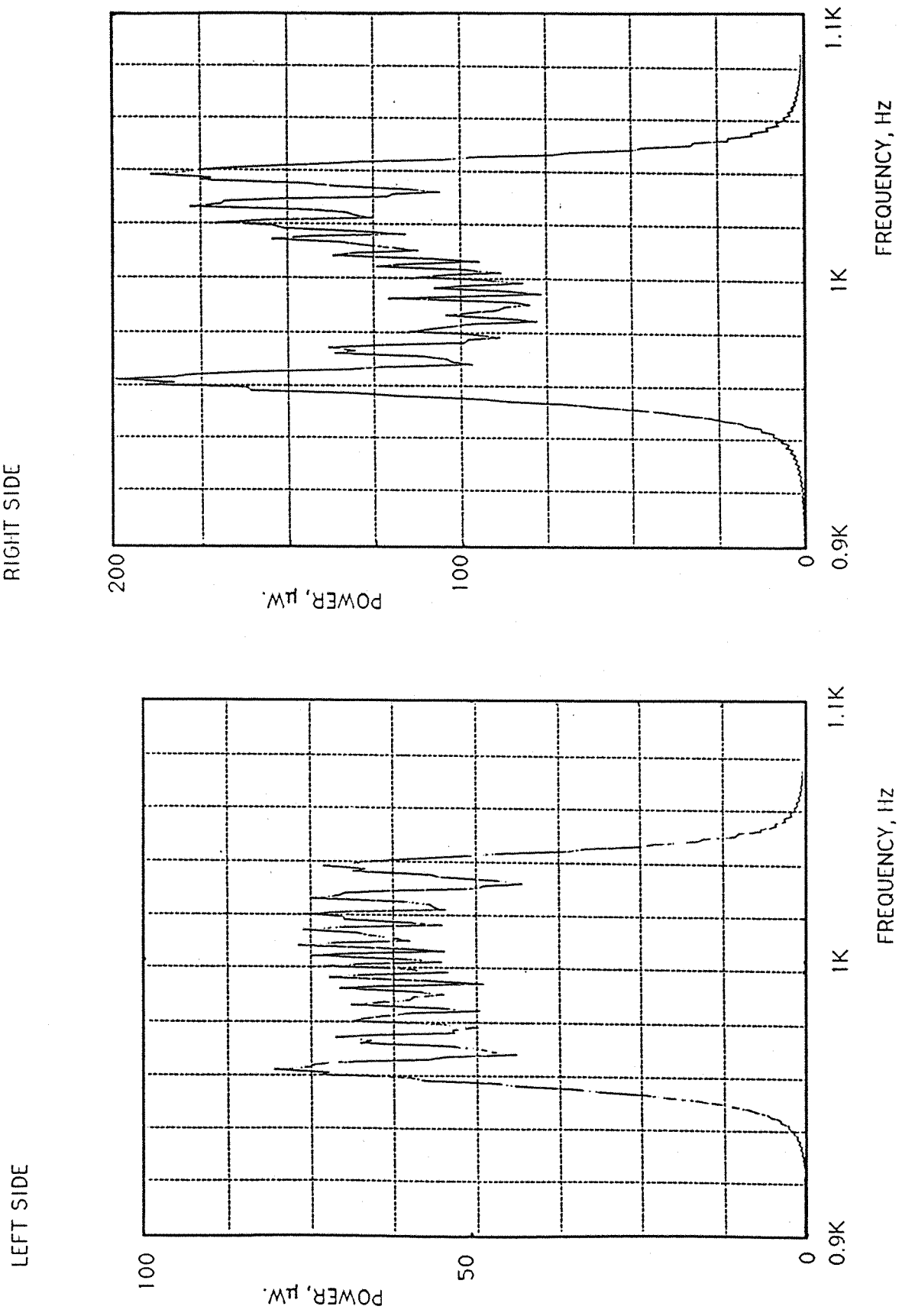

FIGURE 2.17 INPUT POWER 1450-1550 Hz.

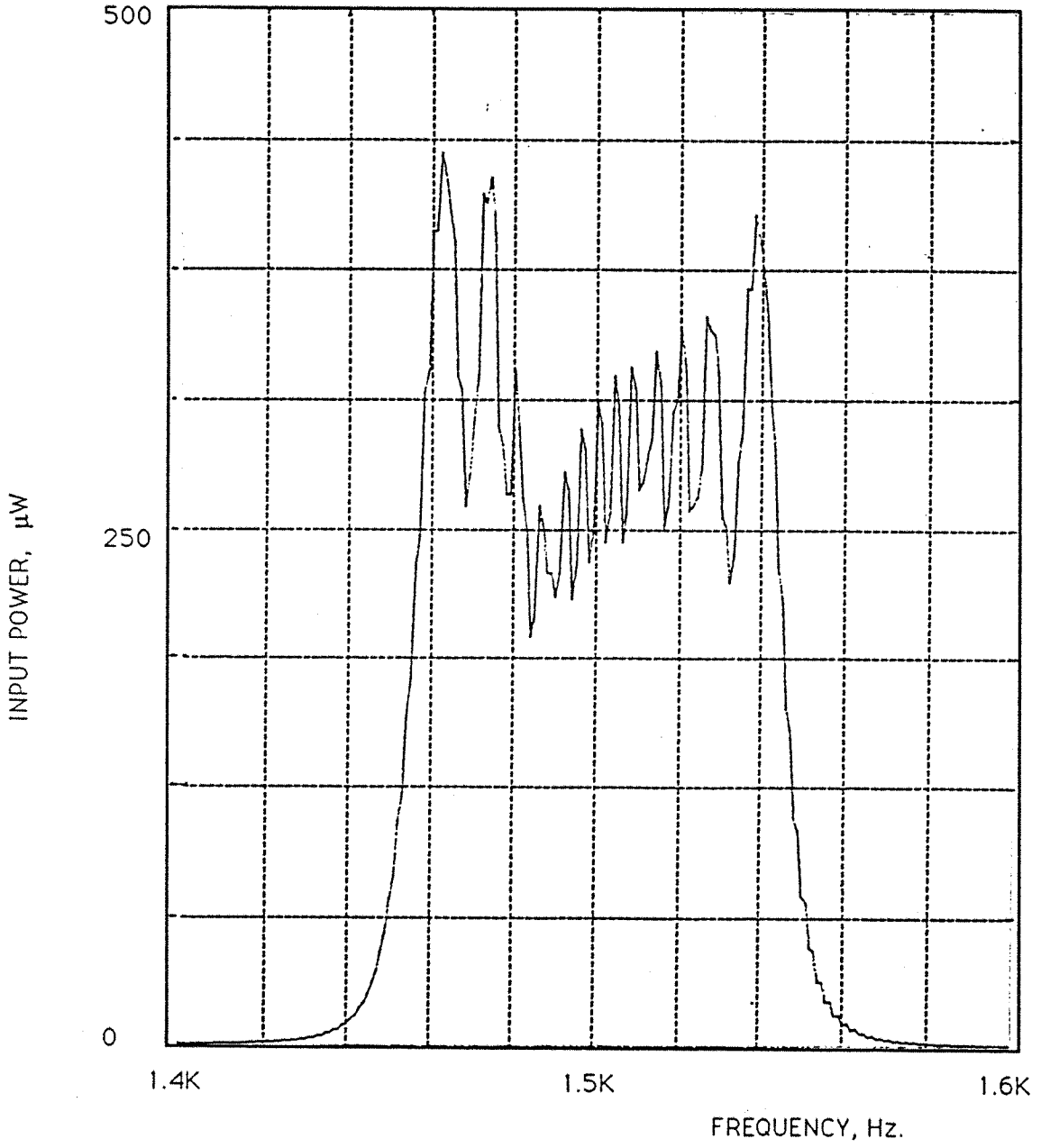

FIGURE 2.18 TRANSMITTED POWER.

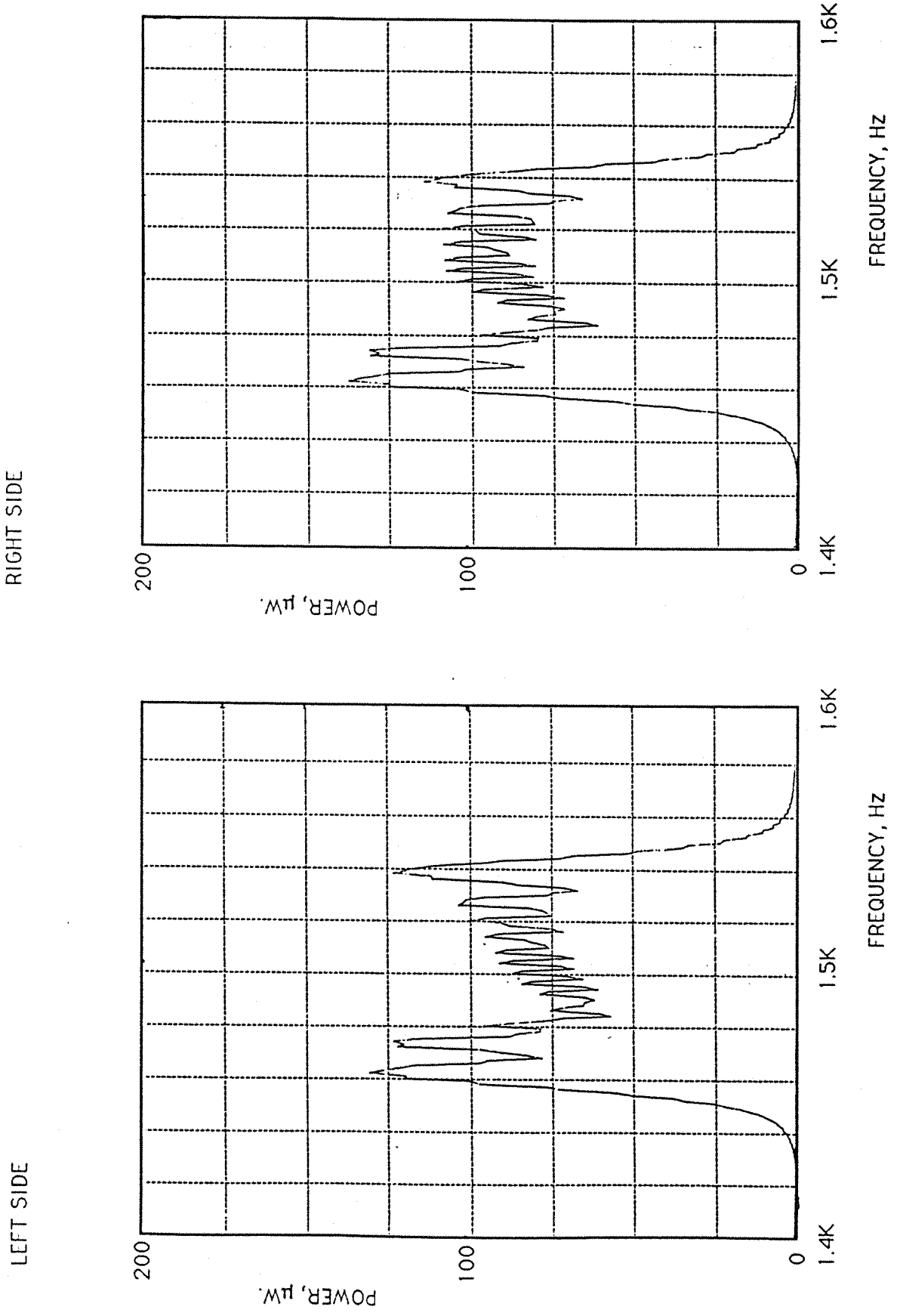

FIGURE 2.19 INPUT AND TRANSMITTED POWER
IN AN INFINITE BEAM

| FREQUENCY, Hz ΔF | f | INPUT POWER, $P_{IN}$ nW. | TRANSMITTED POWER,. $P_T$ nW. LEFT | RIGHT | CORRECTED TRANSMITTED POWER* $P_T$ nW | $\frac{P_T}{P_{IN}}$ |
|---|---|---|---|---|---|---|
| 450 - 550 | 480 | 975 | 432.5 | 447 | 1007.4 | 1.033 |
| | 500 | 1000 | 476 | 425.5 | 1039.4 | 1.039 |
| | 520 | 687.5 | 334.5 | 272.5 | 704.4 | 1.025 |
| 950 - 1050 | 980 | 350.5 | 119.5 | 138.5 | 343.5 | 0.98 |
| | 1000 | 365.5 | 117 | 145.5 | 352.5 | 0.964 |
| | 1020 | 470 | 178 | 153 | 447.3 | 0.951 |
| 1450 - 1550 | 1480 | 326 | 98 | 96.5 | 305 | 0.936 |
| | 1500 | 313.5 | 105.5 | 87 | 303.9 | 0.97 |
| | 1520 | 343.5 | 108.5 | 100.5 | 332.1 | 0.954 |

* Finite difference correction factor is given by,

$$\frac{k\Delta}{\sin k\Delta}$$

where k is the flexural wavenumber and Δ the transducer separation.

FIGURE 3.1 THE DOPPLER EFFECT: SCATTERED LIGHT.

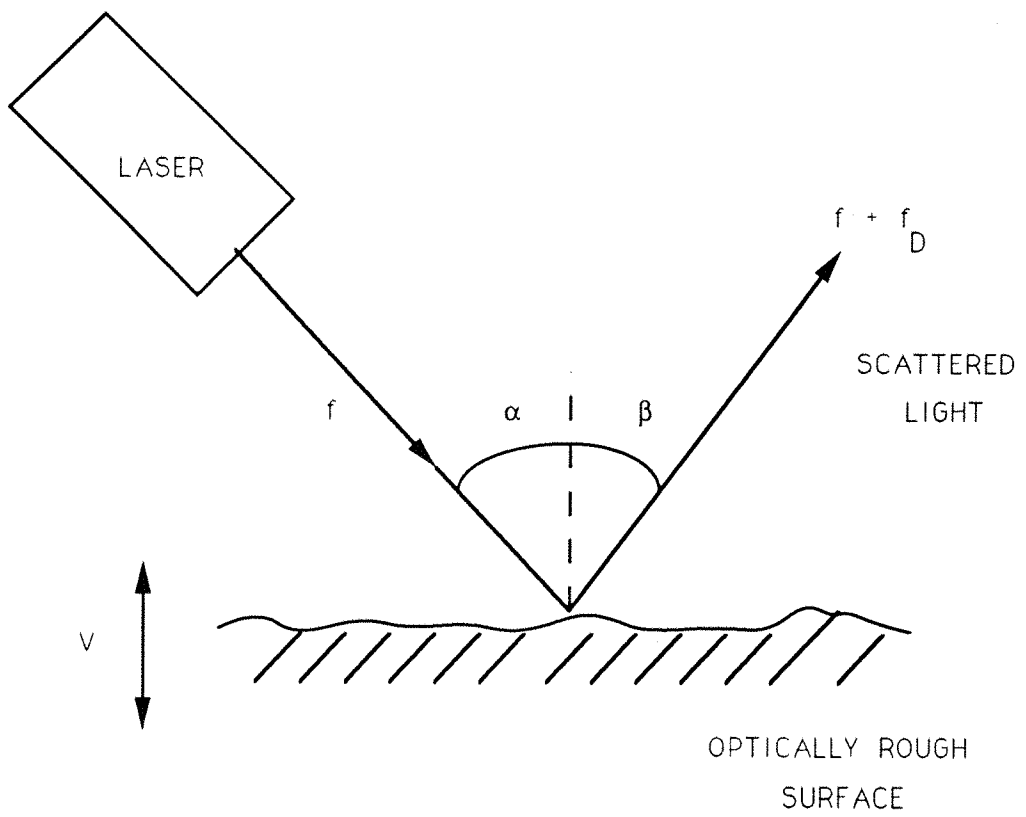

FIGURE 3.2 REFERENCE BEAM HETERODYNE.

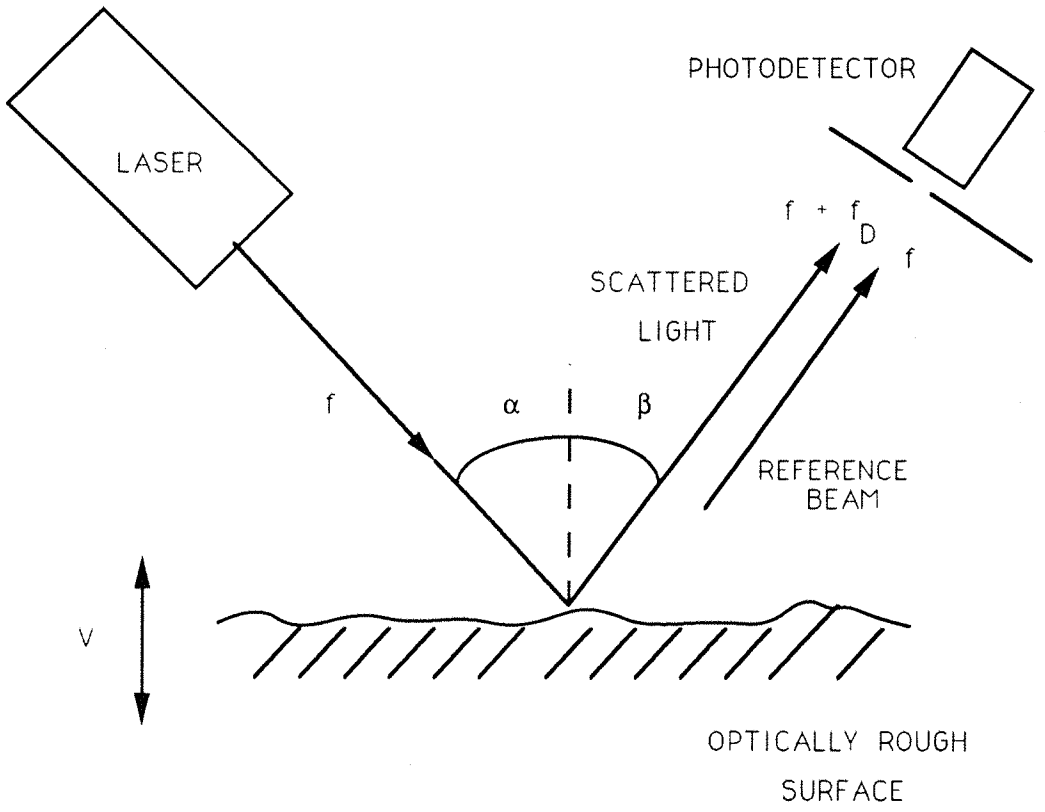

FIGURE 3.3 I.S.V.R. LASER VIBROMETER.

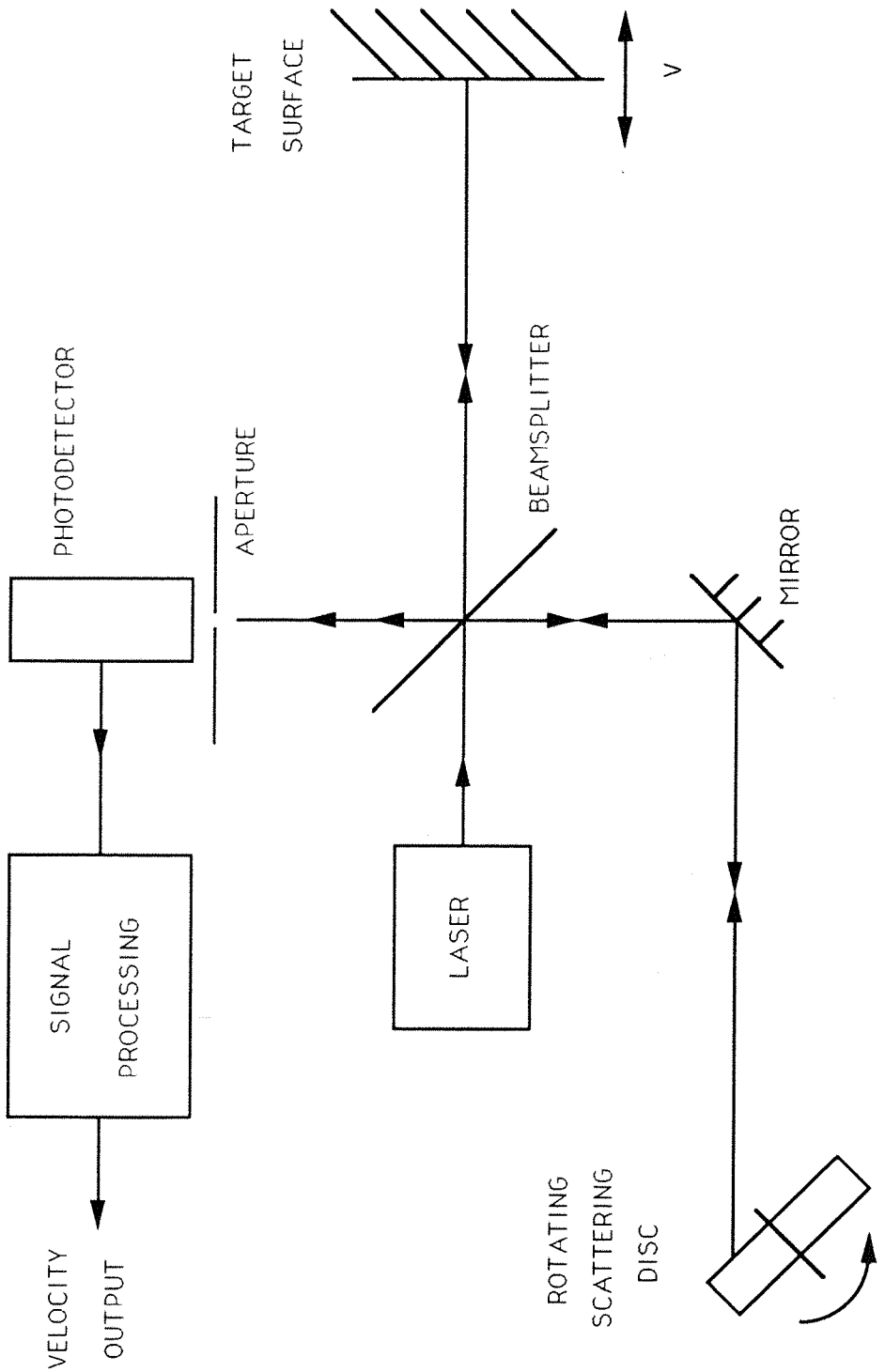

FIGURE 3.4 INTER-TRANSDUCER RESPONSE MEASUREMENT SCHEME.

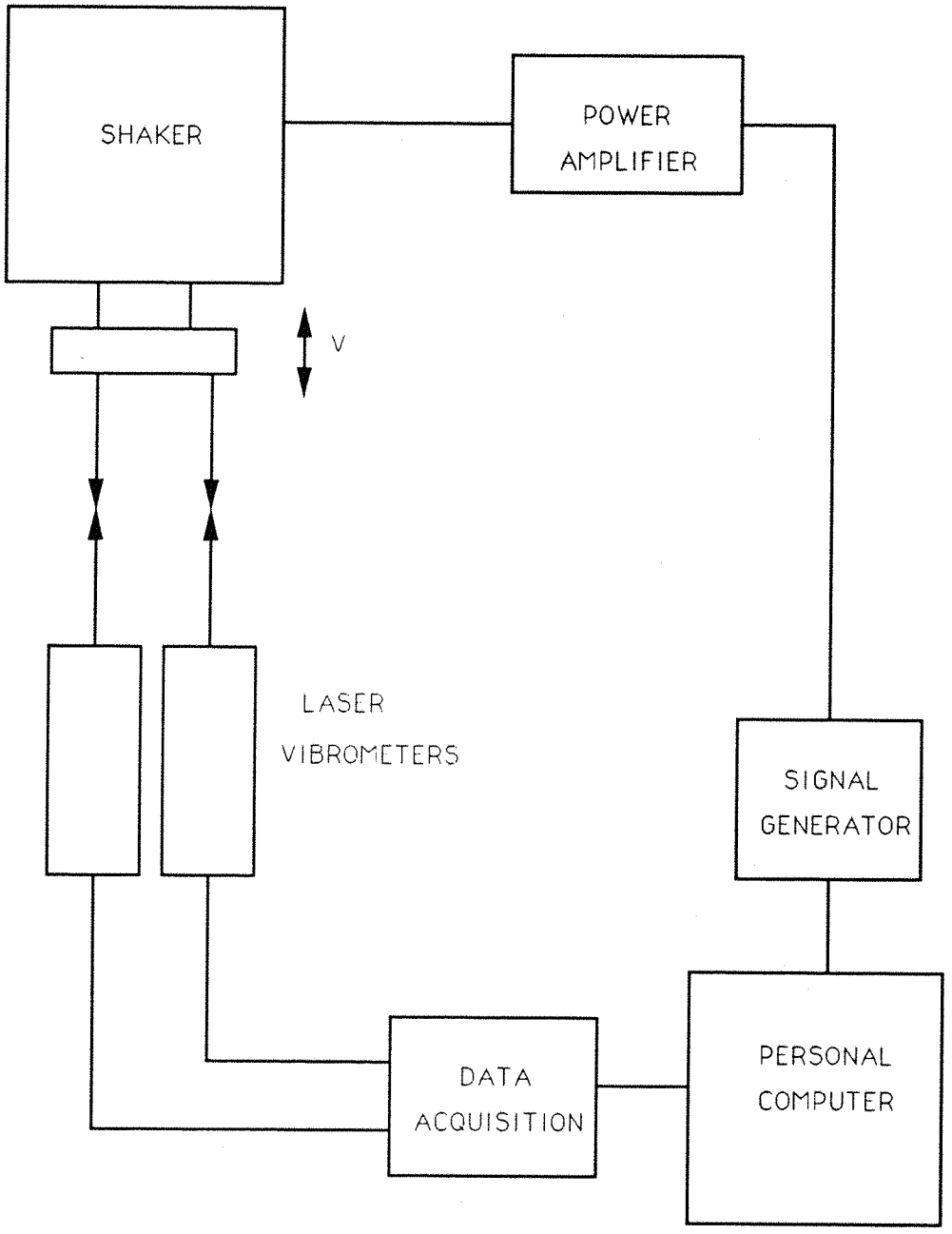

FIGURE 3.5 I.S.V.R. LASER VIBROMETER: INTER-TRANSDUCER F.R.F.
100 - 1000Hz.

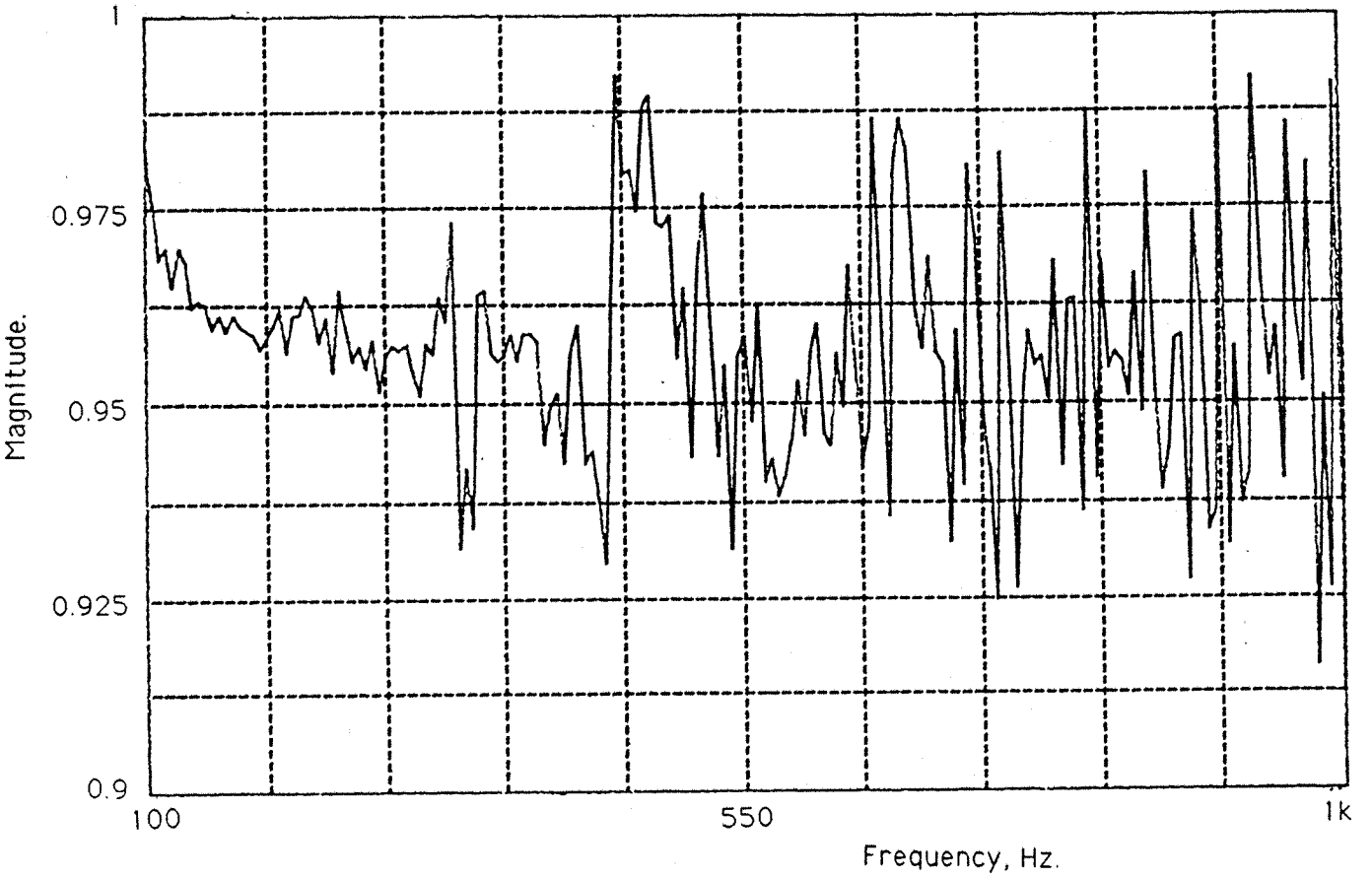


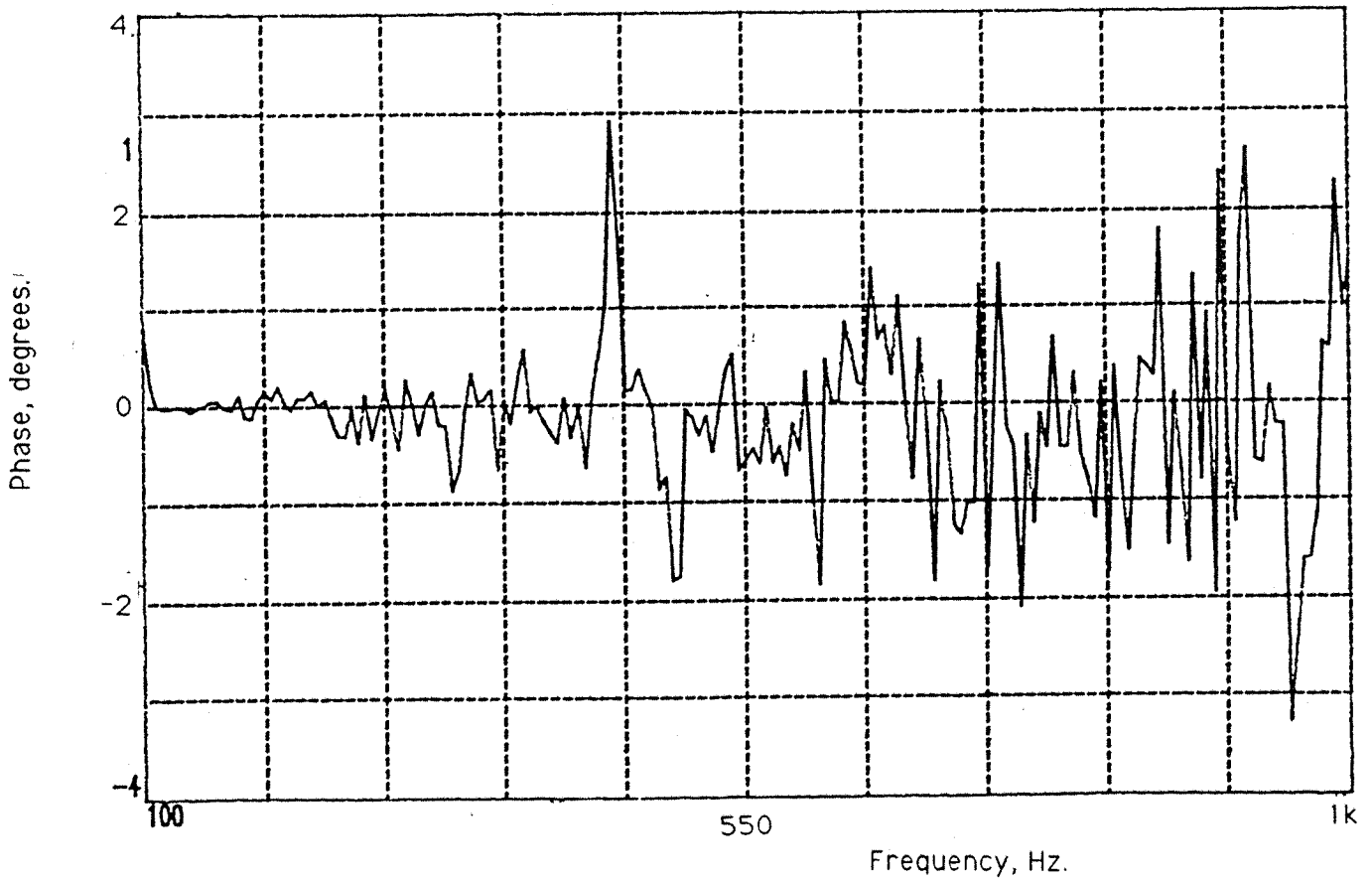

FIGURE 3.6 I.S.V.R. LASER VIBROMETER: INTER-TRANSDUCER F.R.F.
1 - 2KHz.

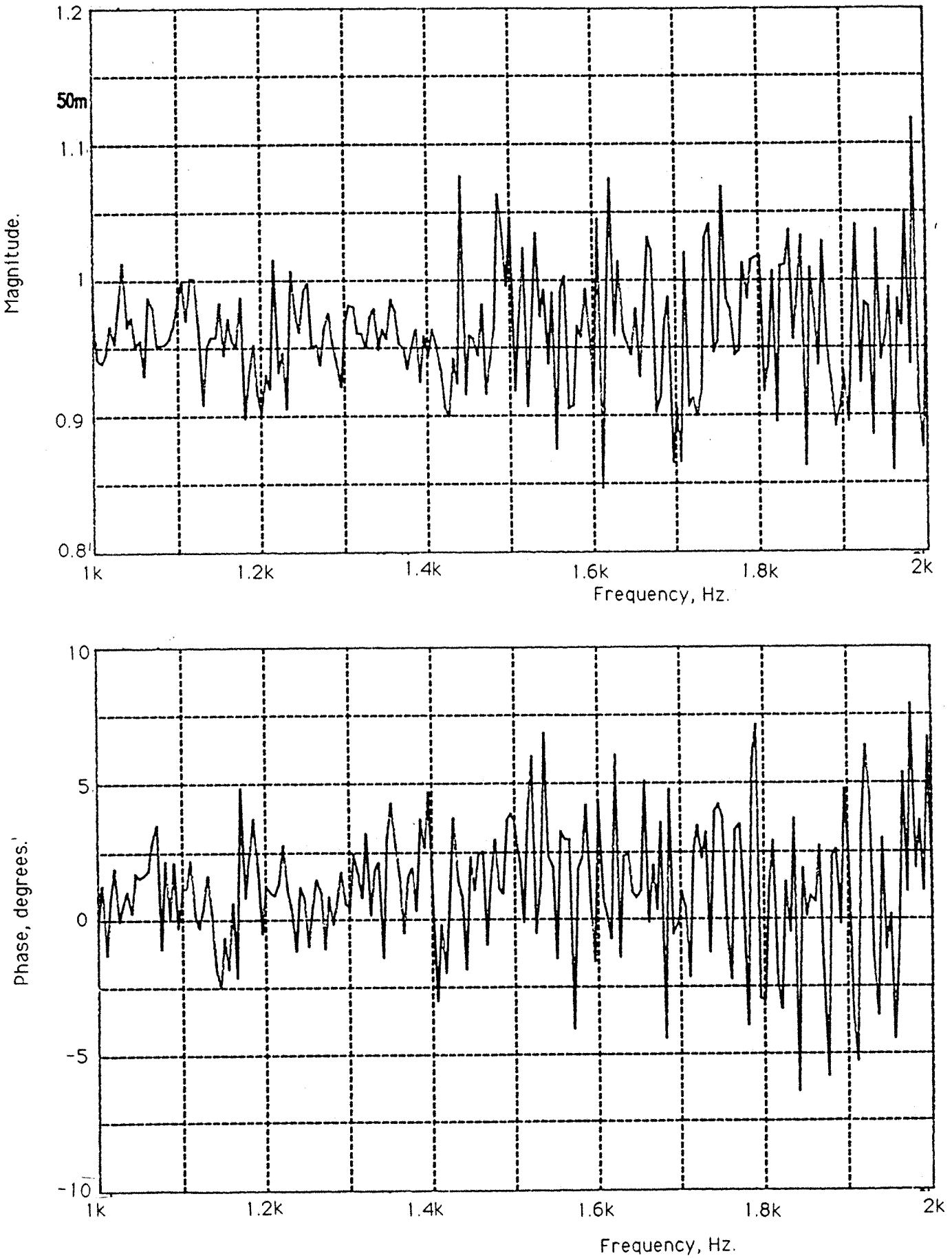

FIGURE 3.7 LOW VELOCITY AMPLITUDE F.R.F.
100 - 1000Hz.

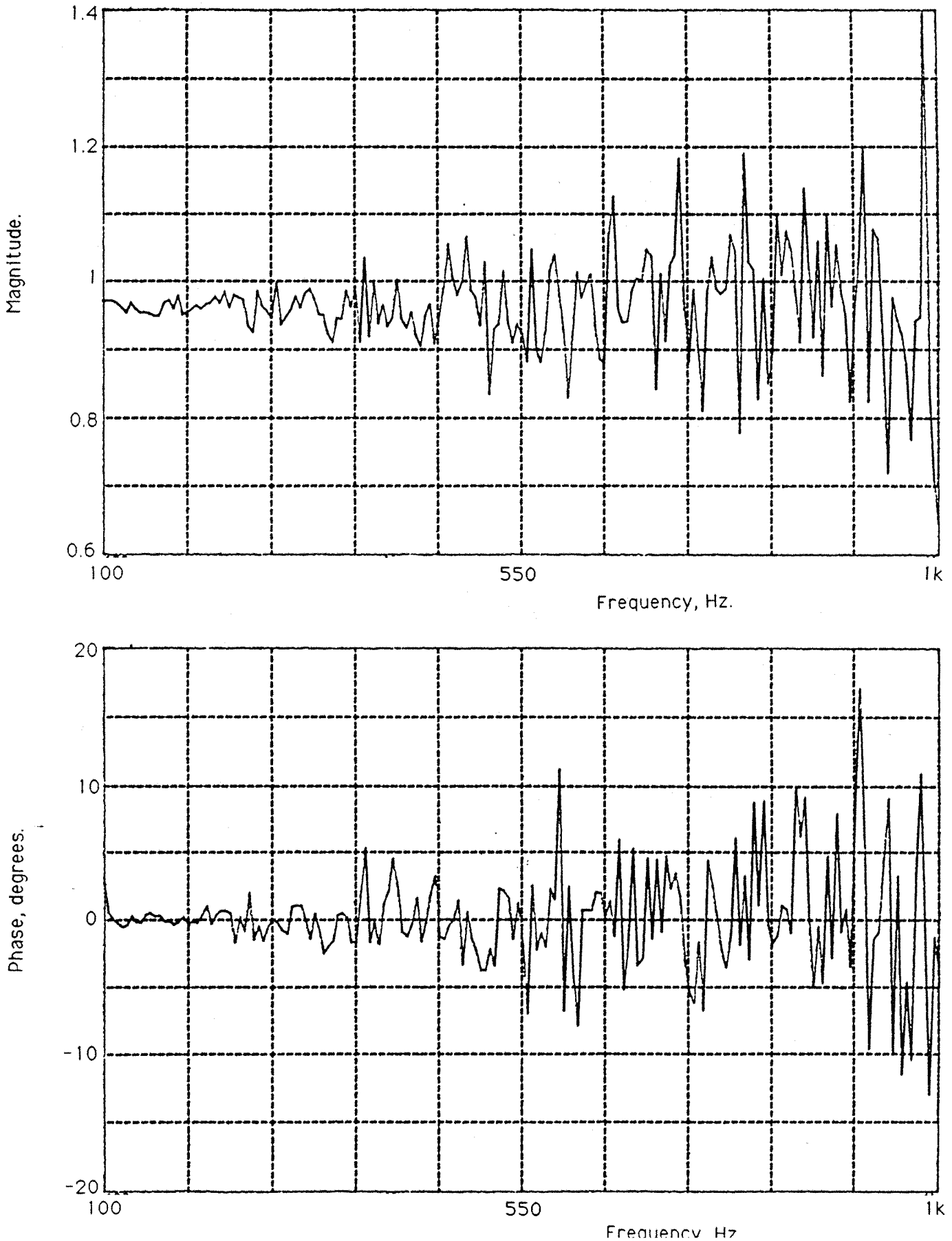

FIGURE 3.8 LOW VELOCITY AMPLITUDE F.R.F.
1 - 2KHz.

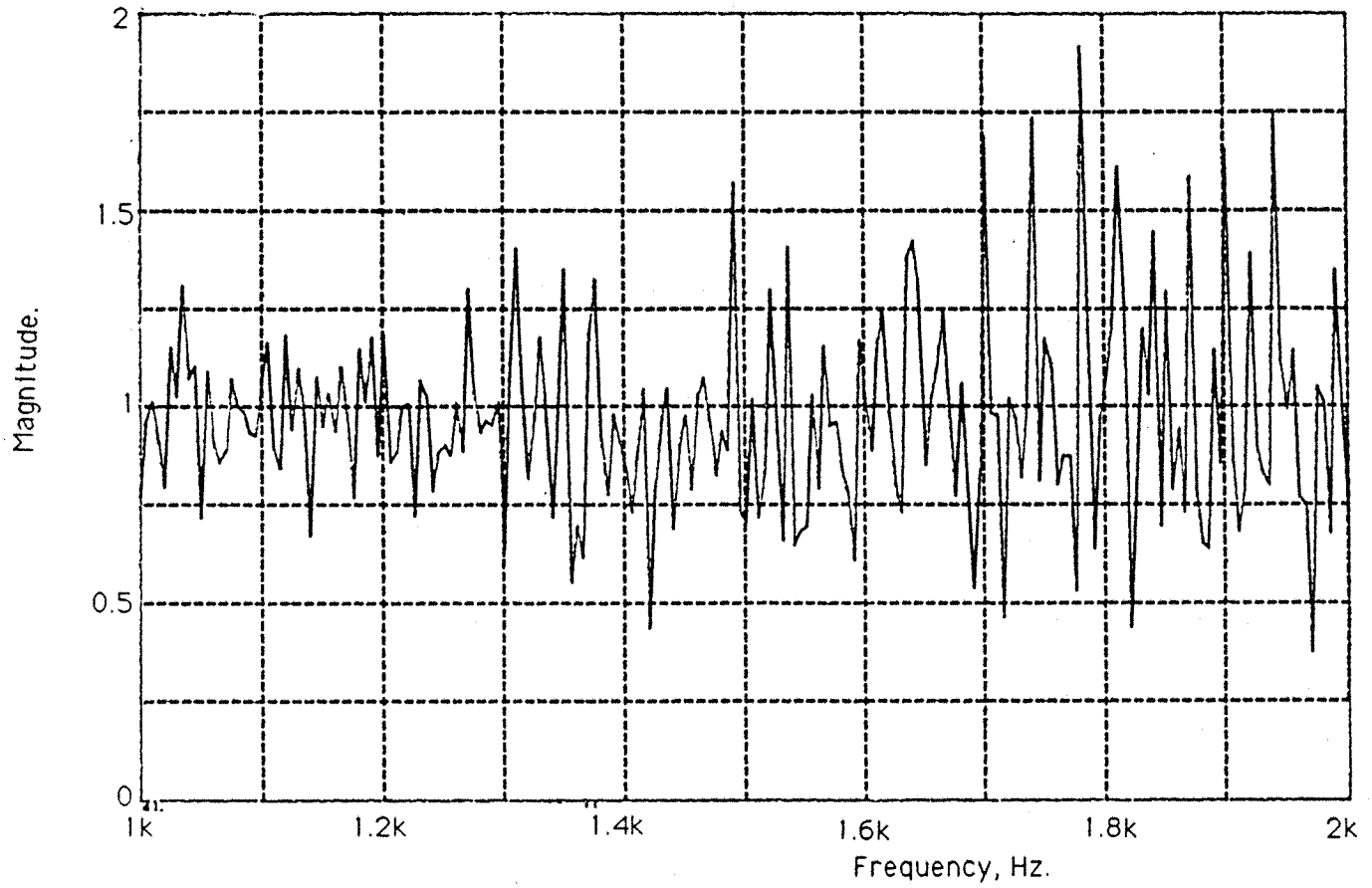


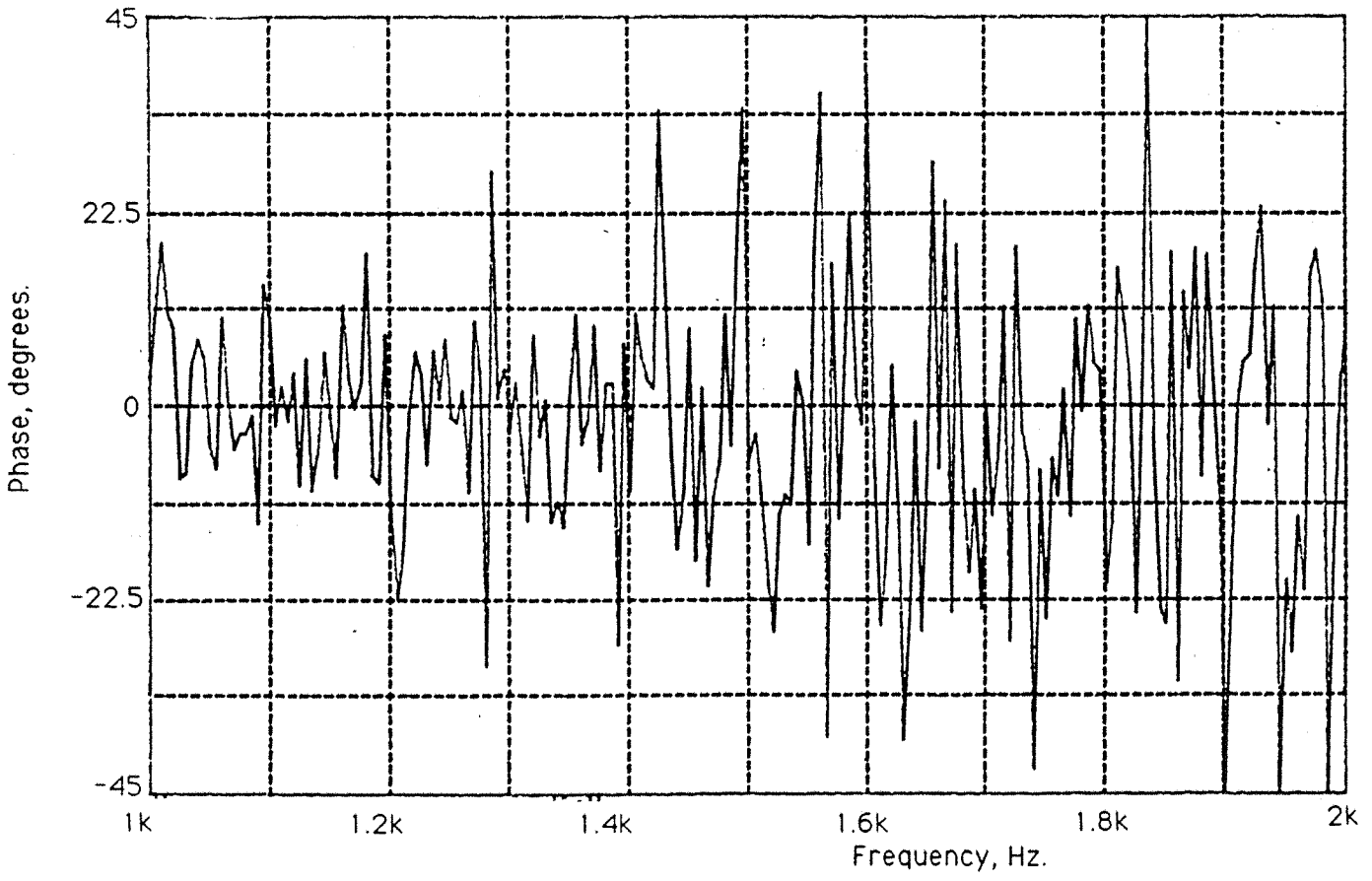

FIGURE 3.9 I.S.V.R. LASER VIBROMETER NOISE FLOOR.

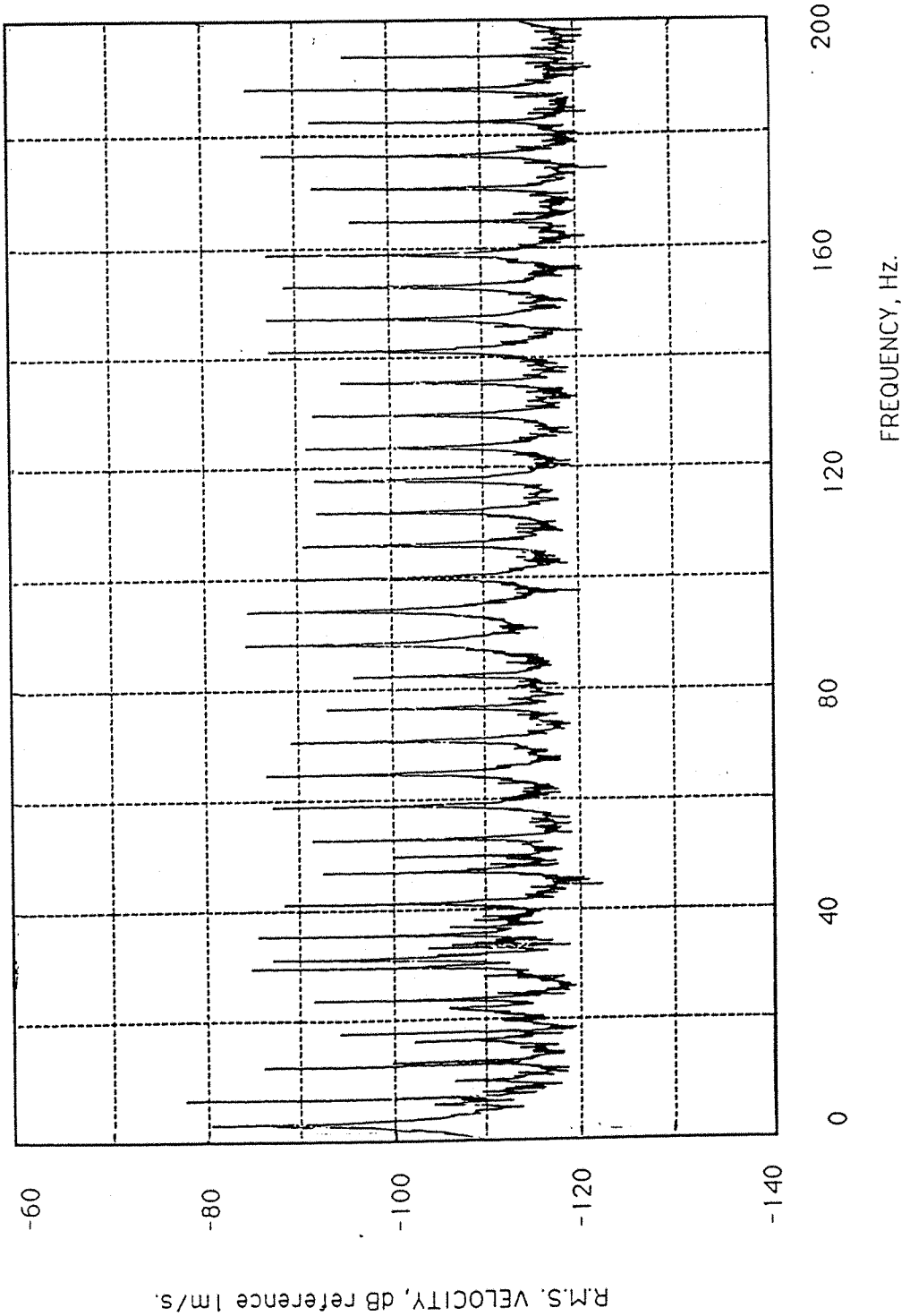

FIGURE 3.10 S.I. MEASUREMENTS USING TWO I.S.V.R. LASER VIBROMETERS.

| EXCITATION FREQUENCY Hz | VELOCITY AMPLITUDE dB reference 1m/s | STRUCTURAL INTENSITY dB reference 1 Watt. | | S.I. DIFFERENCE dB |
|---|---|---|---|---|
| | | ACCELEROMETERS | VIBROMETERS | |
| 500 | -54.8 | -28.8 | -28.4 | 0.4 |
| 750 | -57.6 | -32.6 | -32.5 | 0.1 |
| 1000 | -61.8 | -37.6 | -36.4 | 1.2 |
| 1250 | -62.9 | -42.6 | -41.6 | 1.0 |
| 1500 | -64 | -50.7 | -50.1 | 0.6 |
| 1750 | -65.3 | -44.2 | -44.4 | - 0.2 |
| 2000 | -65.6 | -41.1 | -40.2 | 0.9 |
| 2250 | -64.7 | -41.1 | -42.2 | - 1.1 |

FIGURE 3.11 PZT LASER VIBROMETER..

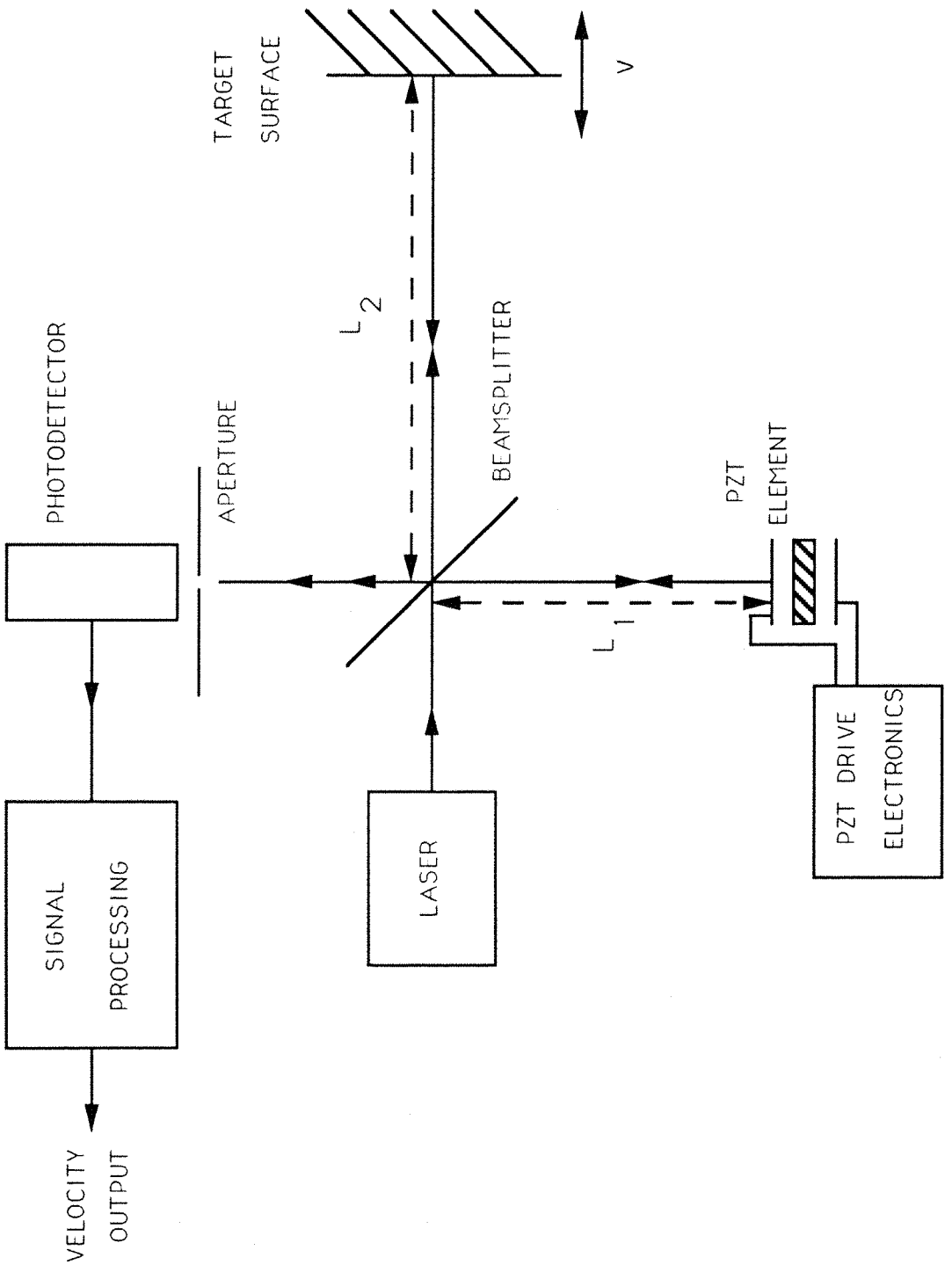

FIGURE 3.12 PZT VIBROMETER SIGNAL PROCESSING.

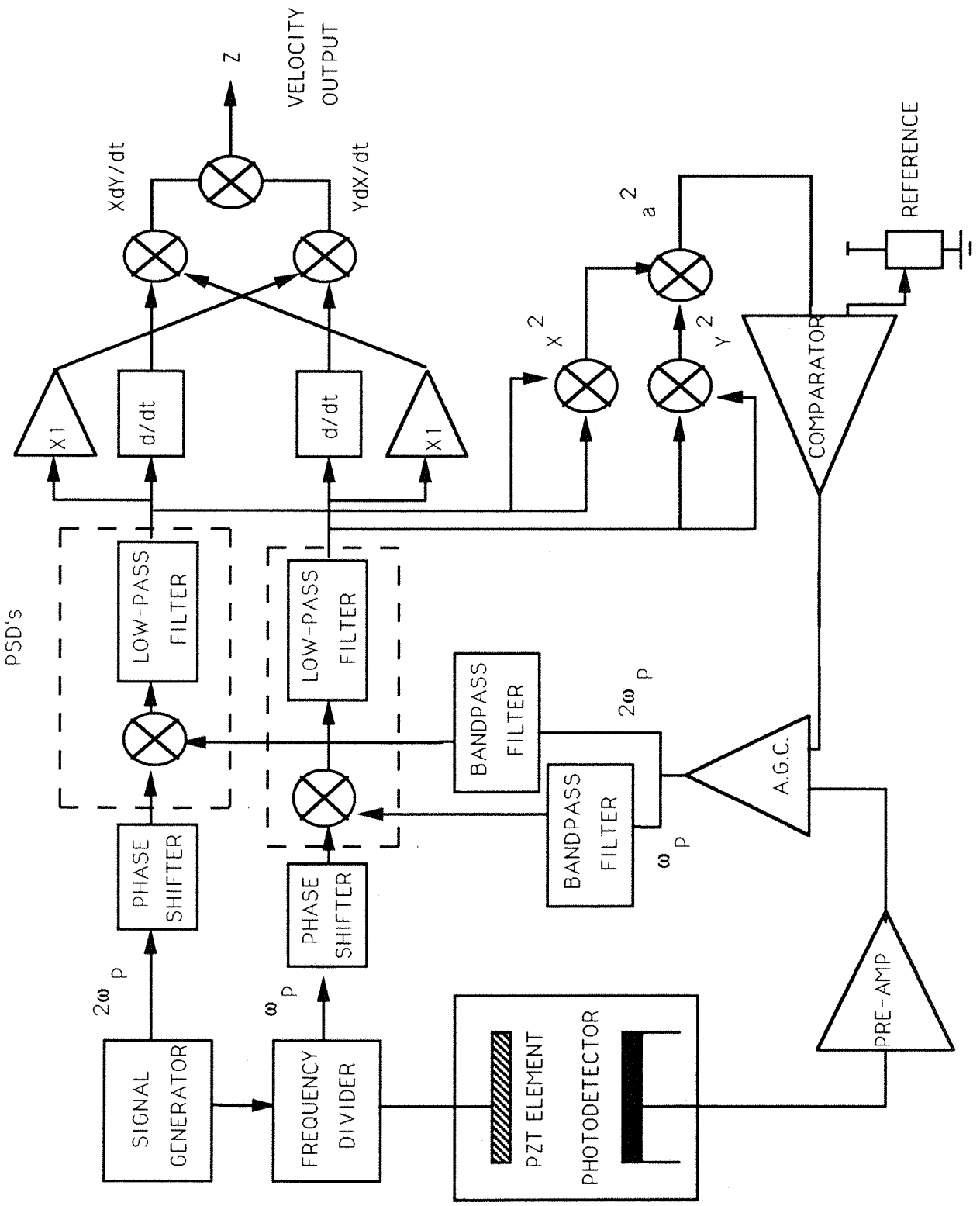

FIGURE 3.13 BESSEL FUNCTIONS OF THE FIRST AND SECOND ORDER.

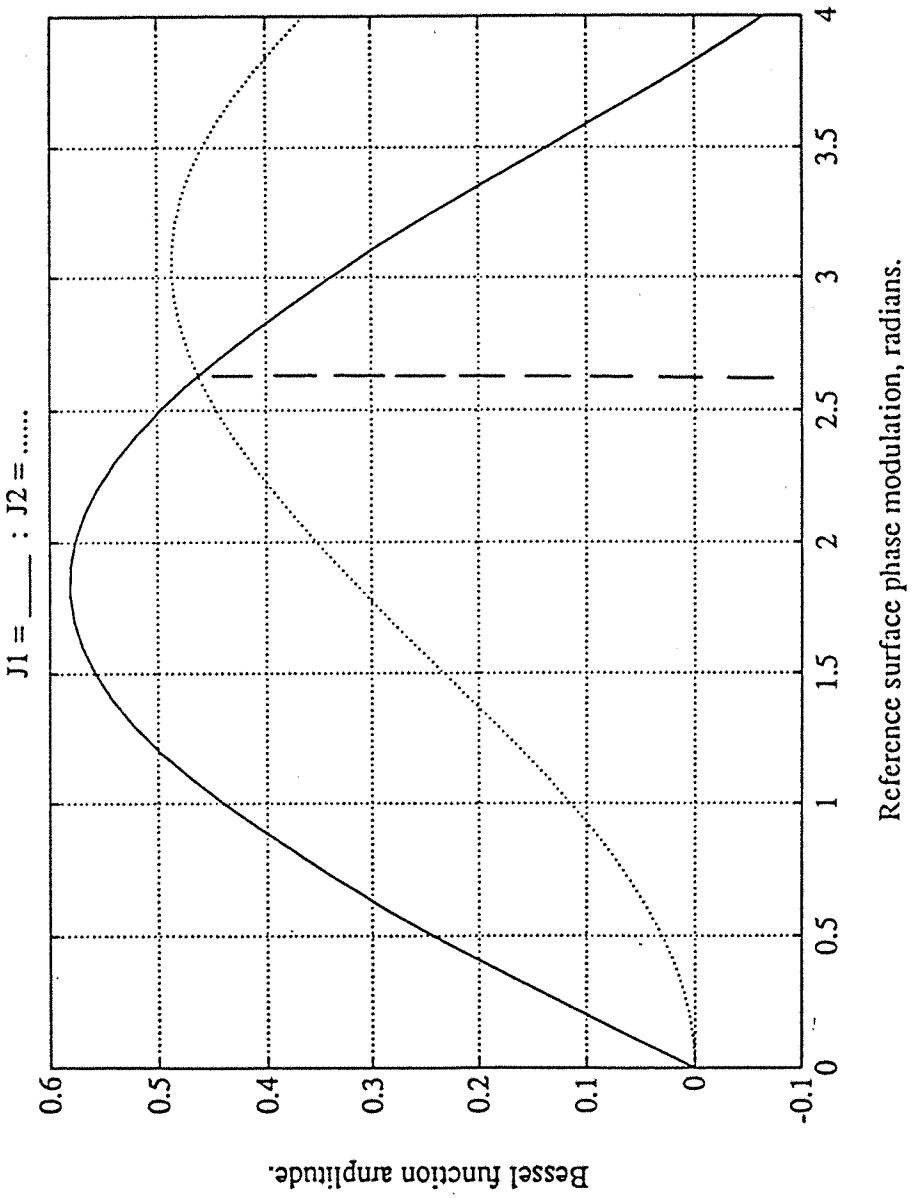

FIGURE 3.14 PZT VIBROMETER VELOCITY MEASUREMENT.

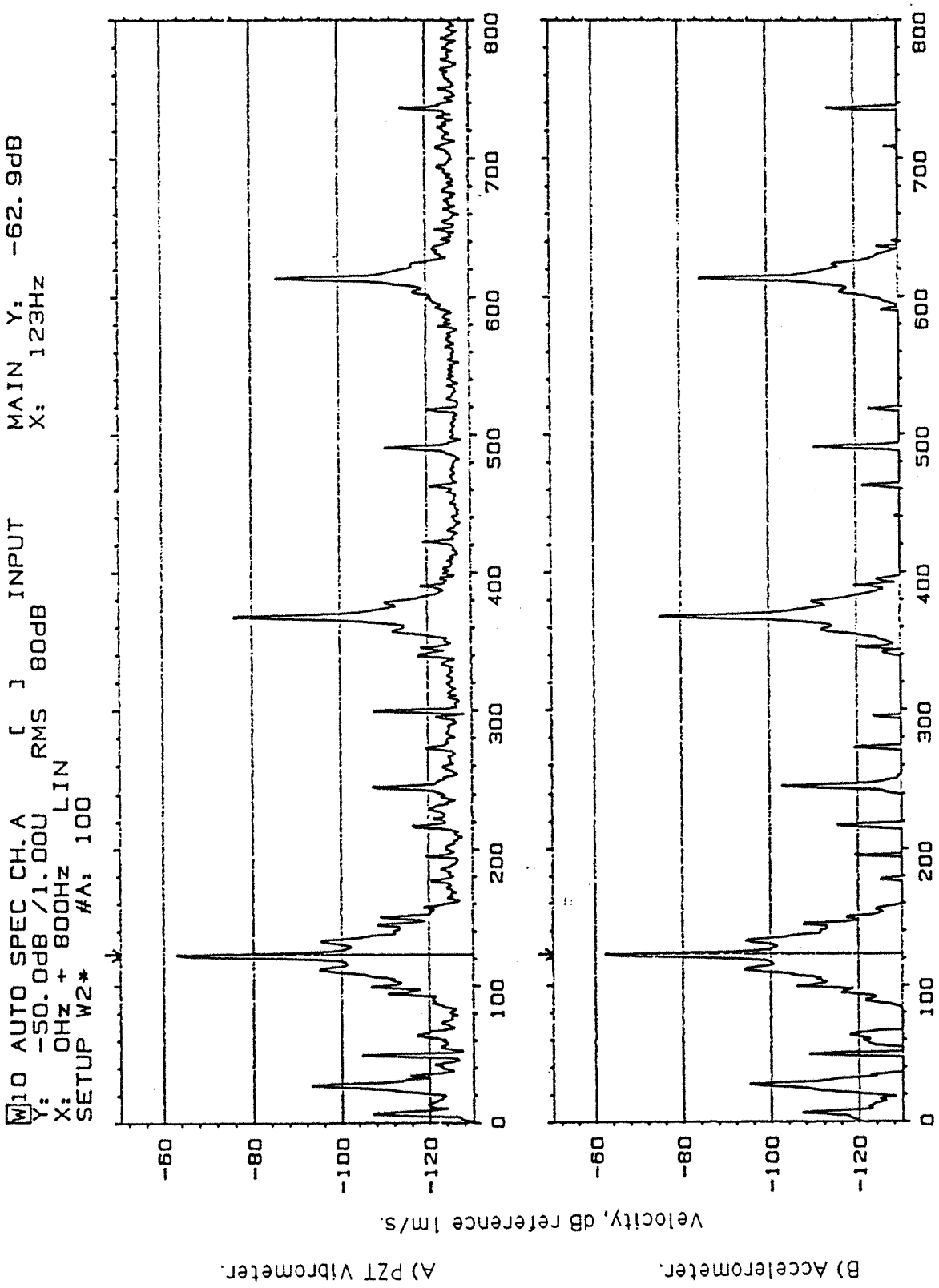

FIGURE 3.15 INTER-VIBROMETER PHASE RESPONSE.

| | Frequency, Hz. | Phase Difference. Degrees. |
|---|---|---|
| A) 0 - 1KHz FILTER. | 100 | -2.8 |
| | 200 | +0.9 |
| | 300 | -0.1 |
| | 400 | -0.8 |
| | 500 | +1.2 |
| | 600 | -1.1 |
| | 700 | +0.1 |
| | 800 | -1.7 |
| B) 0 - 10KHz FILTER | 500 | +1.1 |
| | 750 | -1.5 |
| | 1000 | -2.9 |
| | 1250 | +0.7 |
| | 1500 | 0 |
| | 1750 | +0.5 |
| | 2000 | +1.6 |
| | 2250 | +1.9 |

SHAKER VELOCITY AMPLITUDE OF APPROXIMATELY -85dB REFERENCE 1 m/s

VIBROMETER 'MID-RANGE' SETTING.

FIGURE 3.16 S.I. MEASUREMENTS USING TWO PZT LASER VIBROMETERS.

| EXCITATION FREQUENCY Hz | VELOCITY AMPLITUDE dB reference 1 m/s | STRUCTURAL INTENSITY dB reference 1Watt | | S.I. DIFFERENCE dB |
|---|---|---|---|---|
| | | ACCELEROMETER | VIBROMETER | |
| A) "MID-RANGE" AMPLITUDE EXCITATION LEVELS, -85dB reference 1m/s. | | | | |
| 500 | -83.7 | -63.5 | -63.3 | 0.2 |
| 750 | -85.8 | -67.4 | -68.8 | - 1.4 |
| 1000 | -89 | -67 | -67.4 | - 0.4 |
| 1250 | -89.8 | -65.4 | -65.8 | - 0.4 |
| 1500 | -89.4 | -65 | -65.5 | - 0.5 |
| 1750 | -89.7 | -64.9 | -65.2 | - 0.3 |
| 2000 | -86 | -62.5 | -63.1 | -0.6 |
| 2250 | -80.1 | -58.6 | -59.3 | - 0.7 |
| B) "LOW-AMPLITUDE" EXCITATION LEVELS, -105 dB reference 1m/s. | | | | |
| 500 | -103.6 | -82.8 | -83.7 | - 0.9 |
| 750 | -105.4 | -87.1 | -87.8 | - 0.7 |
| 1000 | -111.6 | -88.3 | -88.6 | - 0.3 |
| 1250 | -109.9 | -85.9 | -86.6 | - 0.7 |
| 1500 | -109.6 | -85.4 | -85.8 | - 0.4 |
| 1750 | -109.8 | -85.3 | -85.7 | - 0.4 |
| 2000 | -106.7 | -83.4 | -84 | - 0.6 |
| 2250 | -99.2 | -79.4 | -79.7 | - 0.3 |

FIGURE 4.1 VARIATION OF ERROR RATIO R, WITH 2kh.

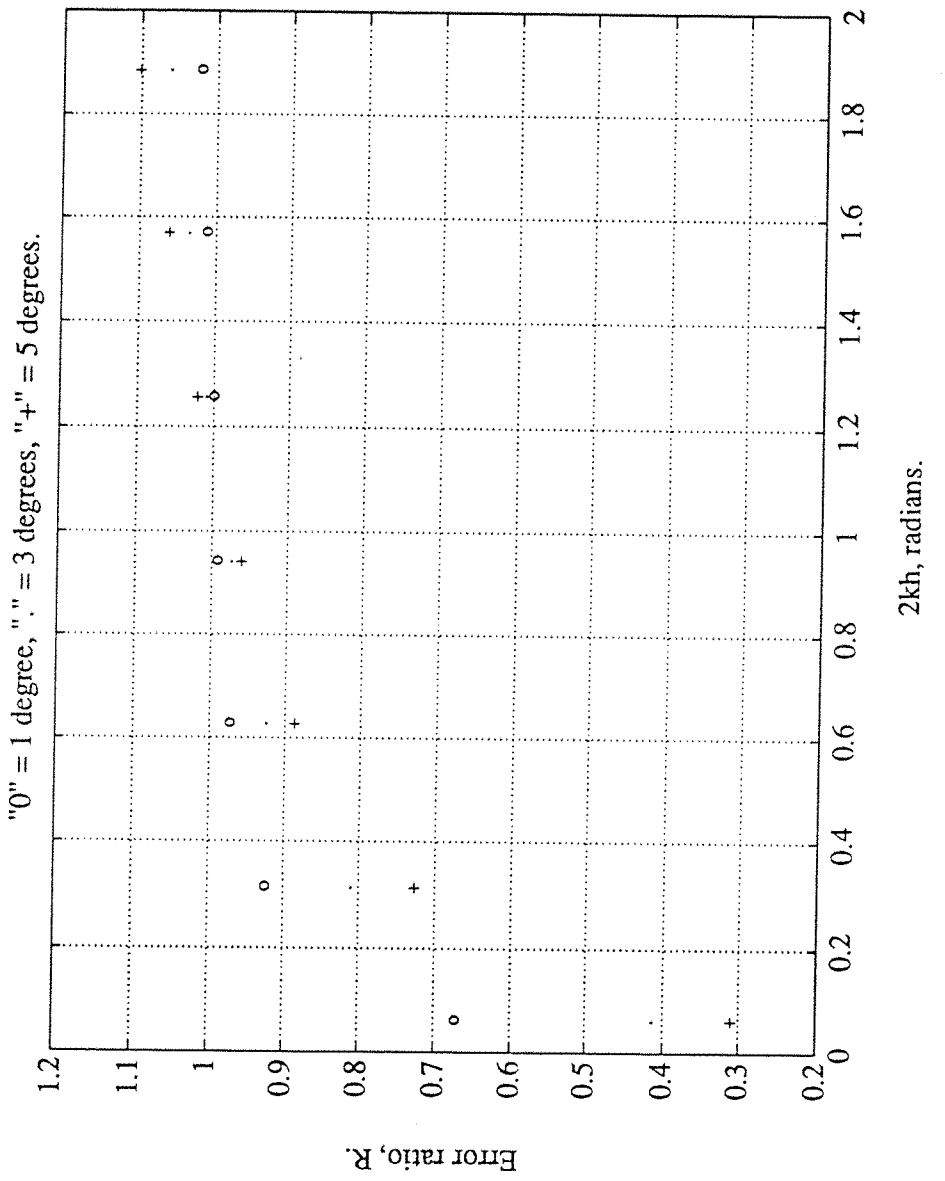

FIGURE 4.2 VARIATION OF R WITH 2kh, FOR TYPICAL INTER-TRANSDUCER PHASE ERRORS.

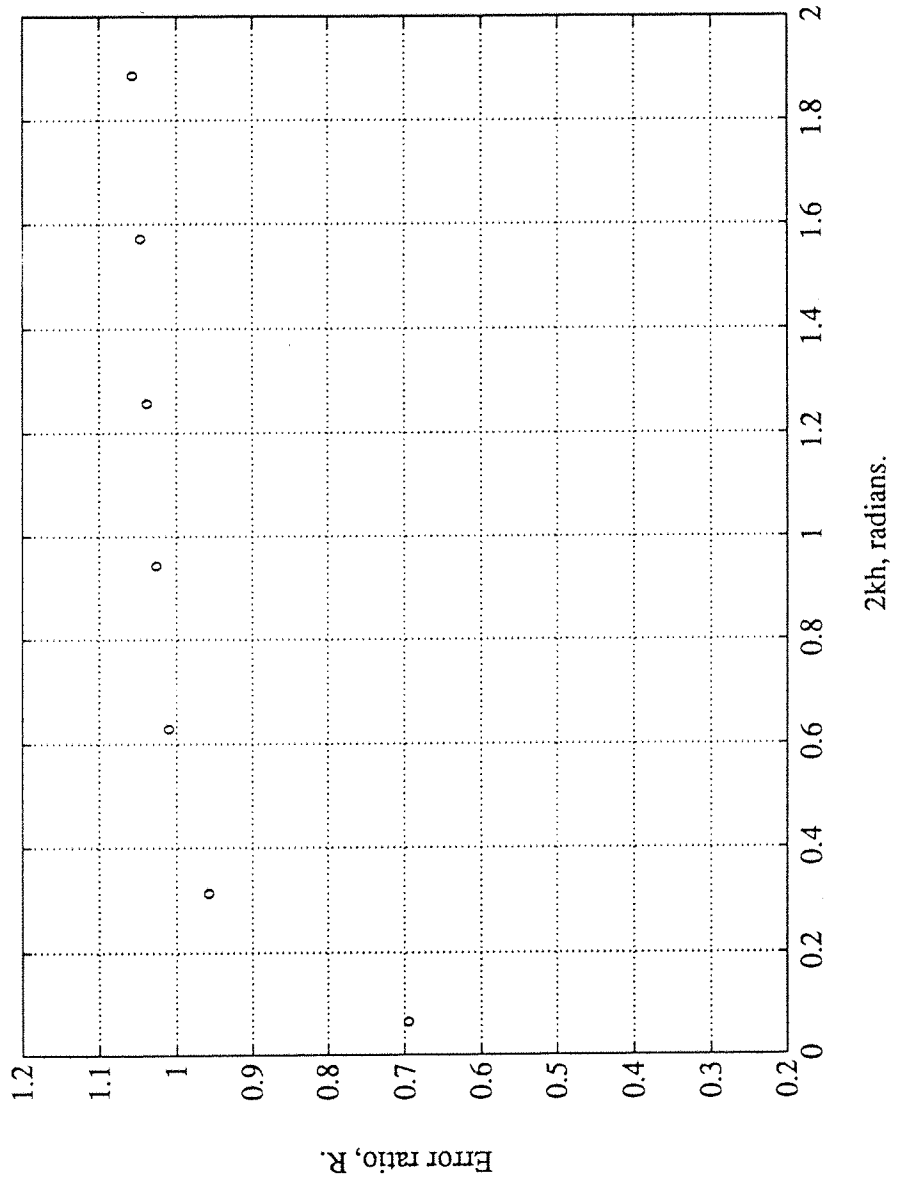

FIGURE 4.3 SHEAROGRAPHY: OPTICAL CONFIGURATION.

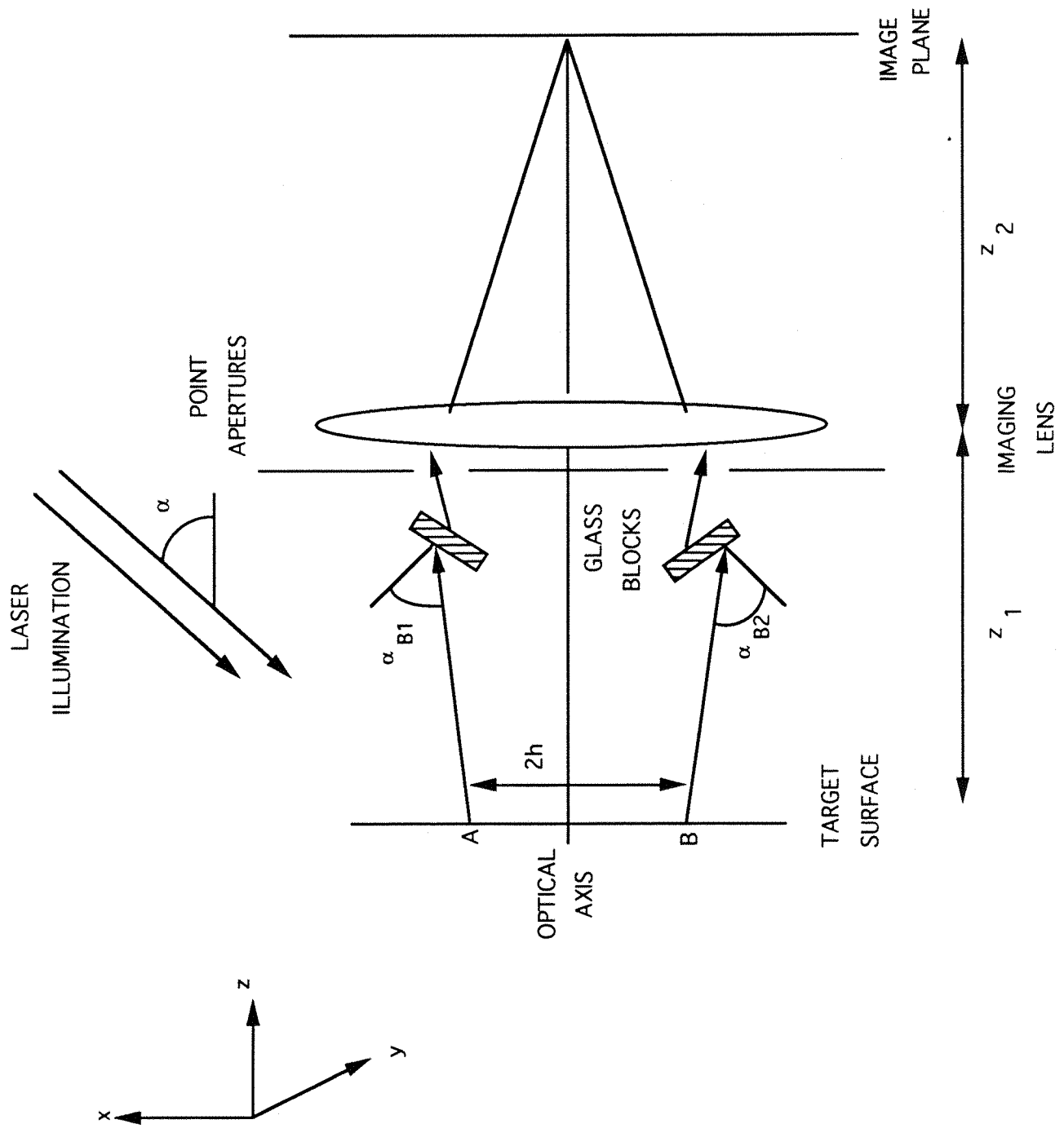

FIGURE 4.4 IMAGE SHEARING TECHNIQUE.

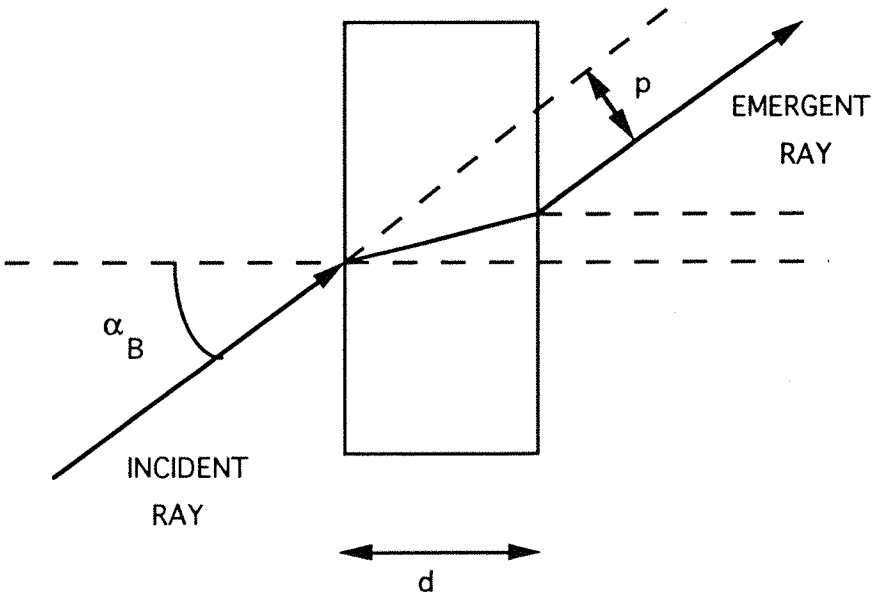

FIGURE 4.5 VELOCITY DIFFERENCE MEASUREMENT SCHEME.

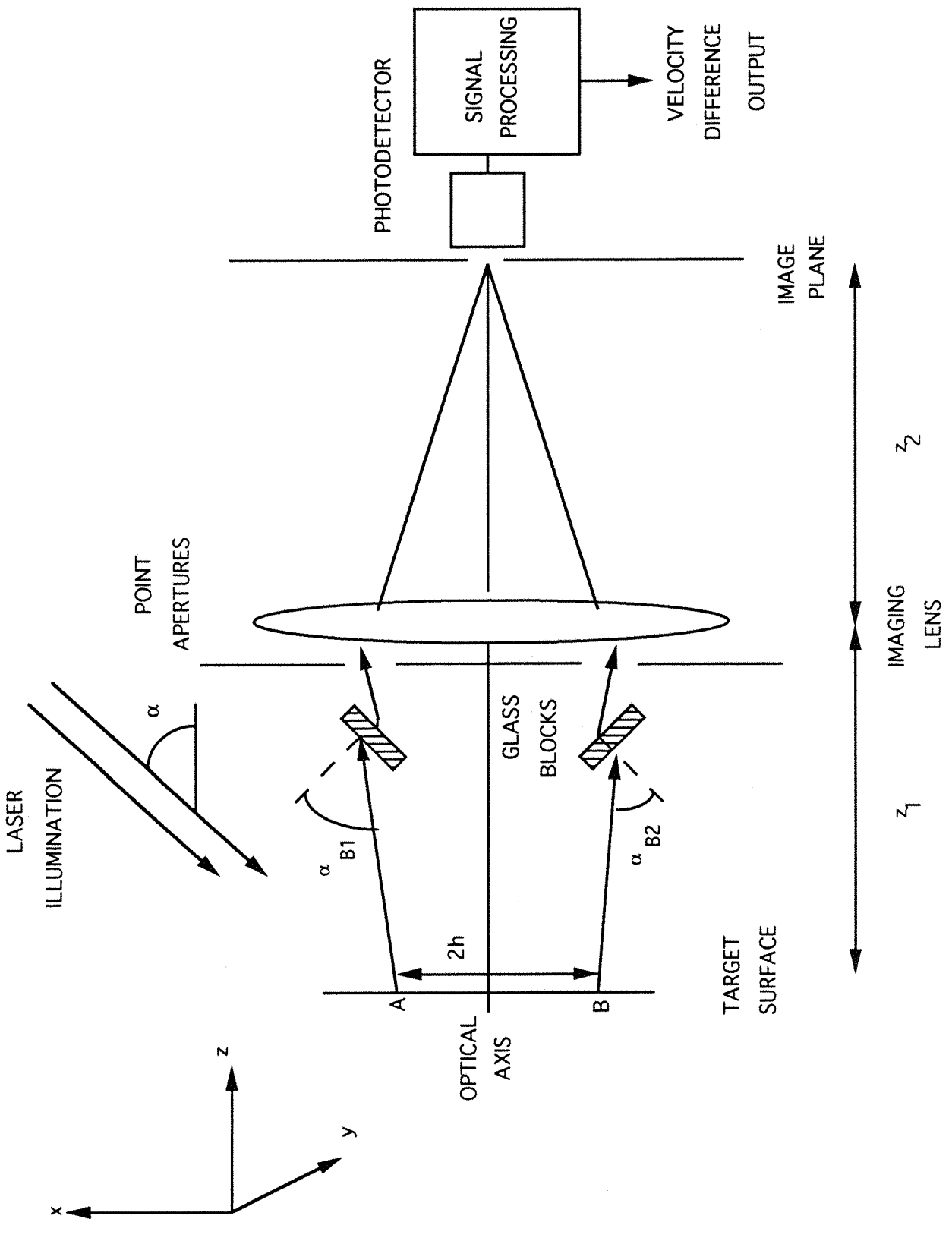

FIGURE 4.6 VELOCITY GRADIENT ANEMOMETER.

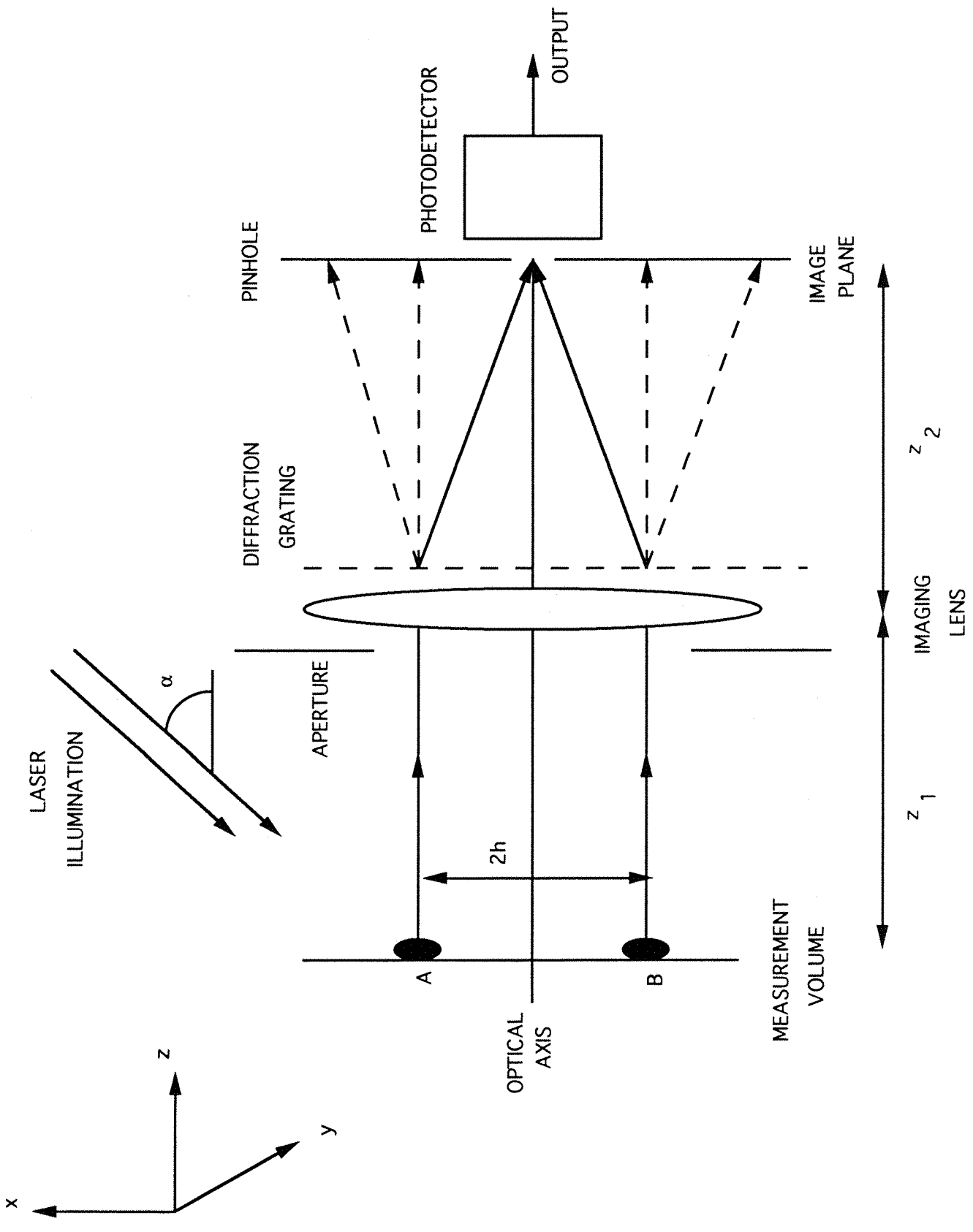

FIGURE 4.7 TORSIONAL VIBROMETER

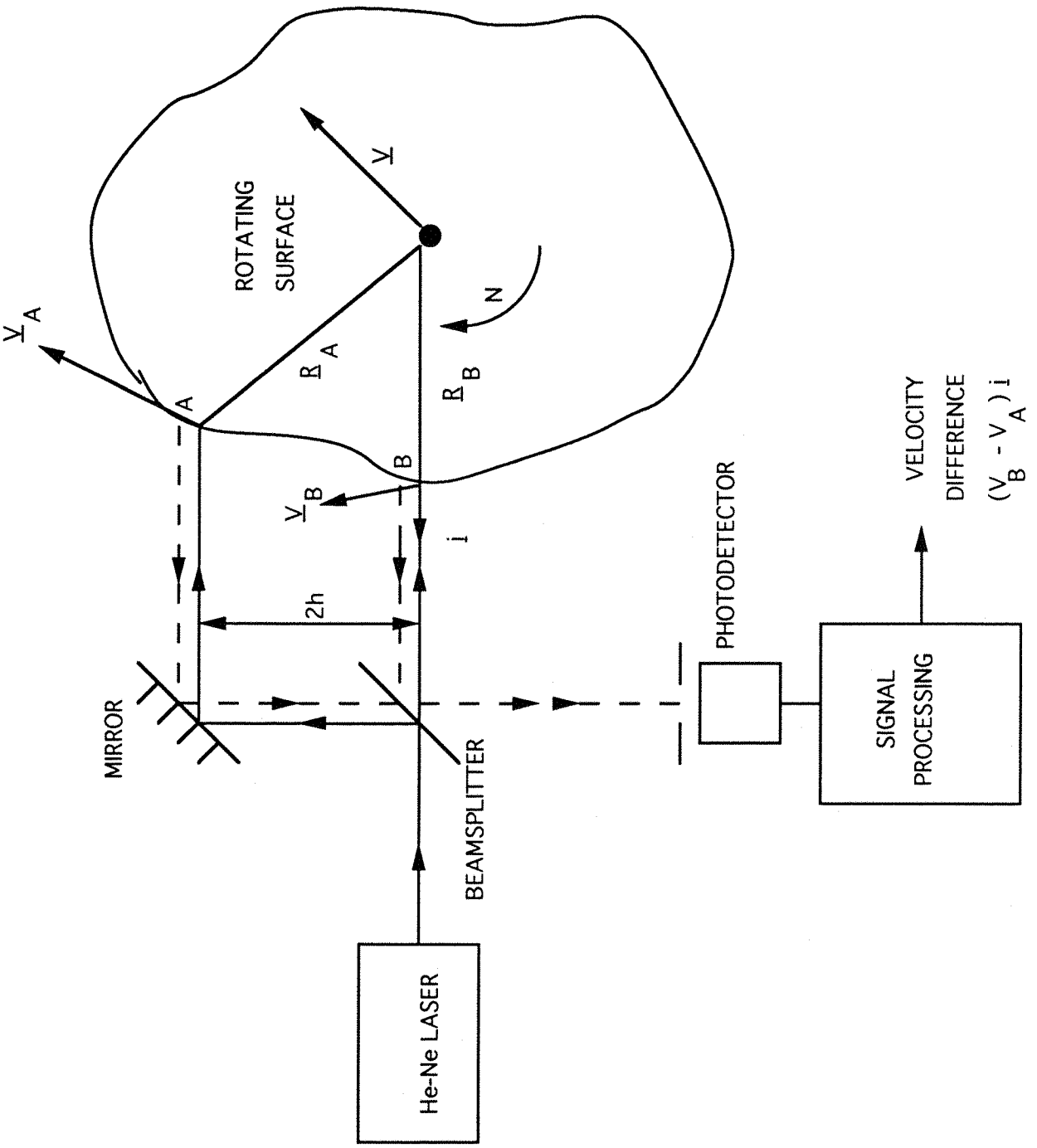

FIGURE 4.8 VELOCITY GRADIENT MEASUREMENT SCHEME.

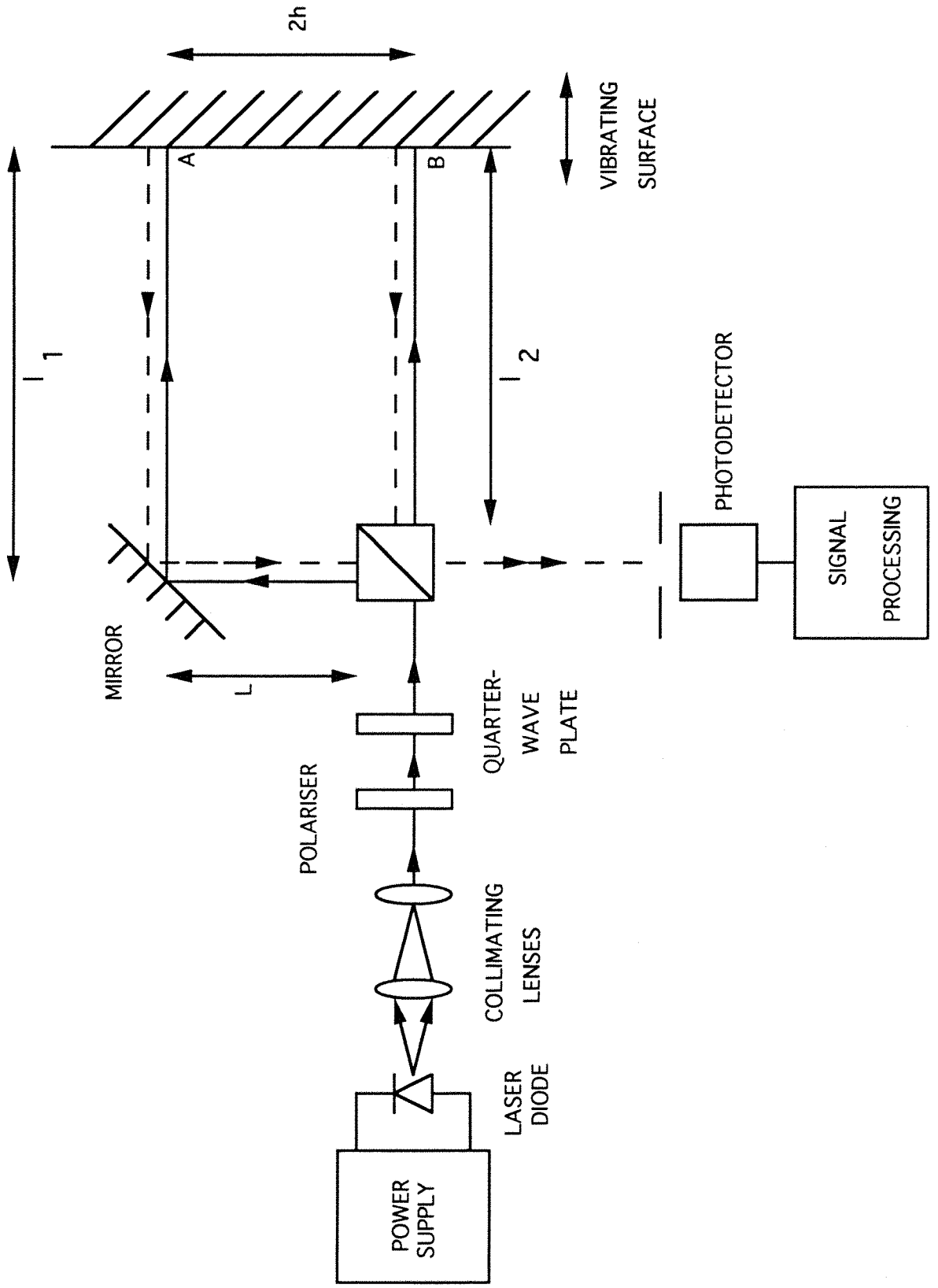

FIGURE 4.9 FIBRE VIBROMETER.

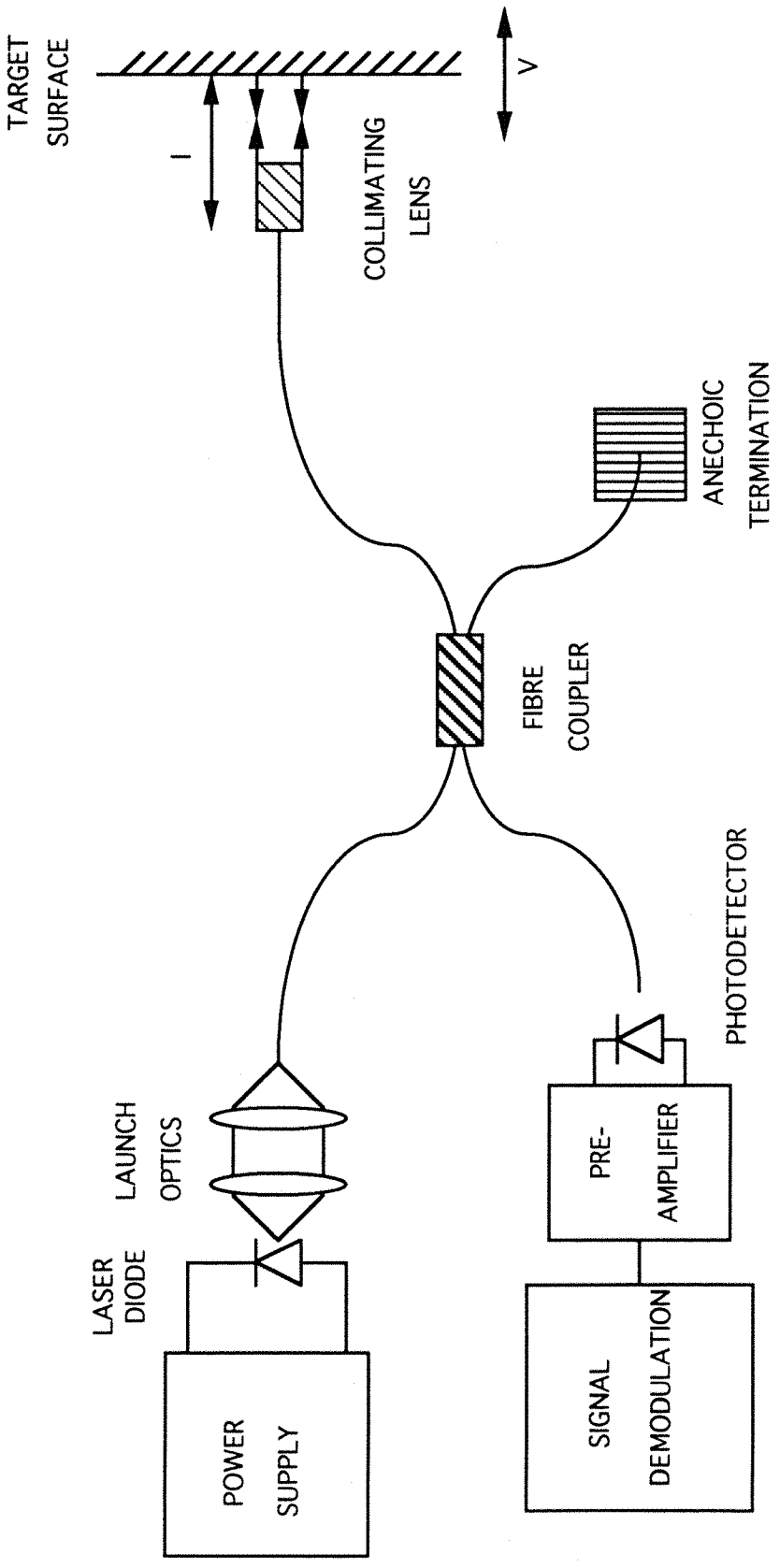

FIGURE 4.10 SIGNAL PROCESSING.

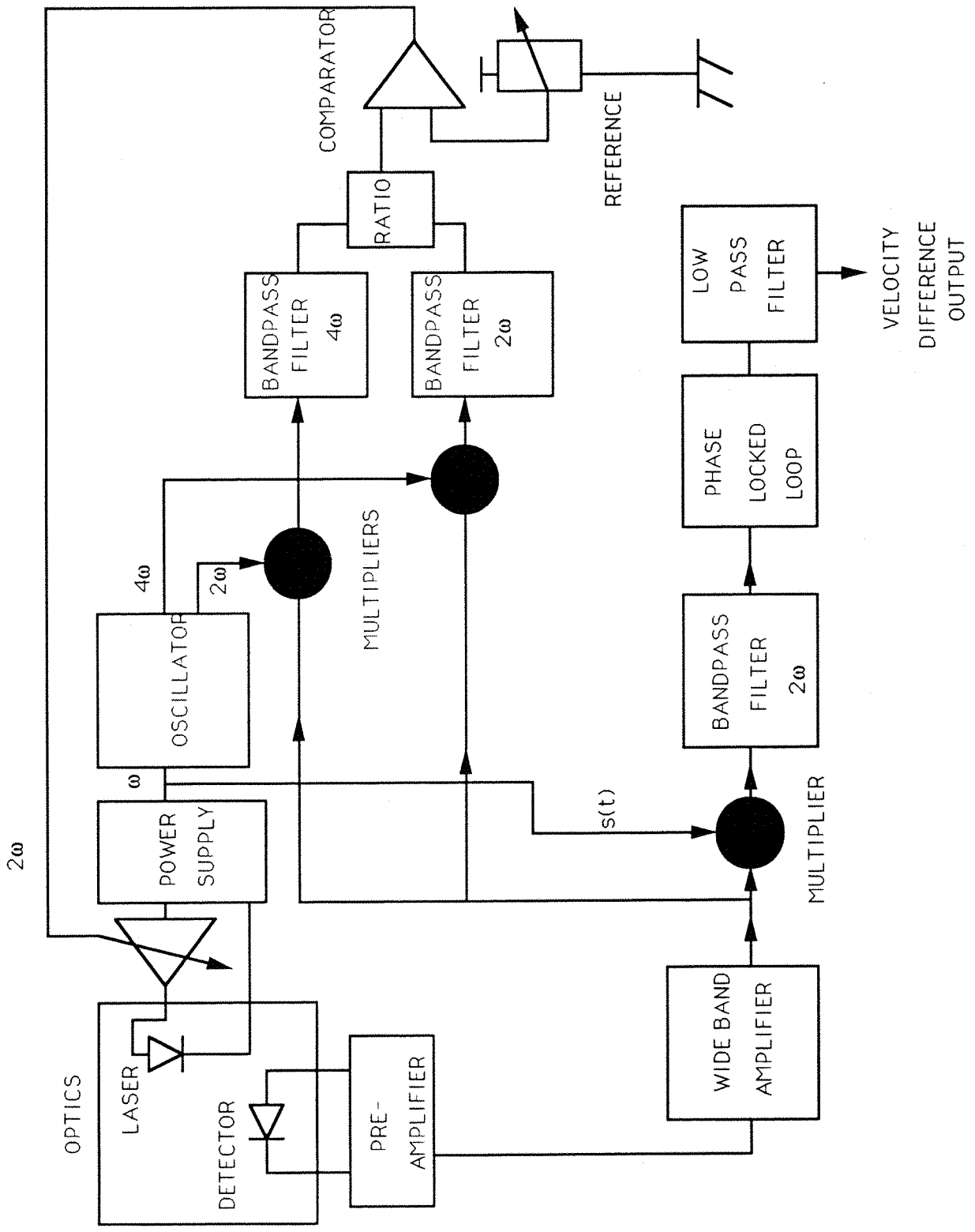

FIGURE 4.11 PHASE ERROR.

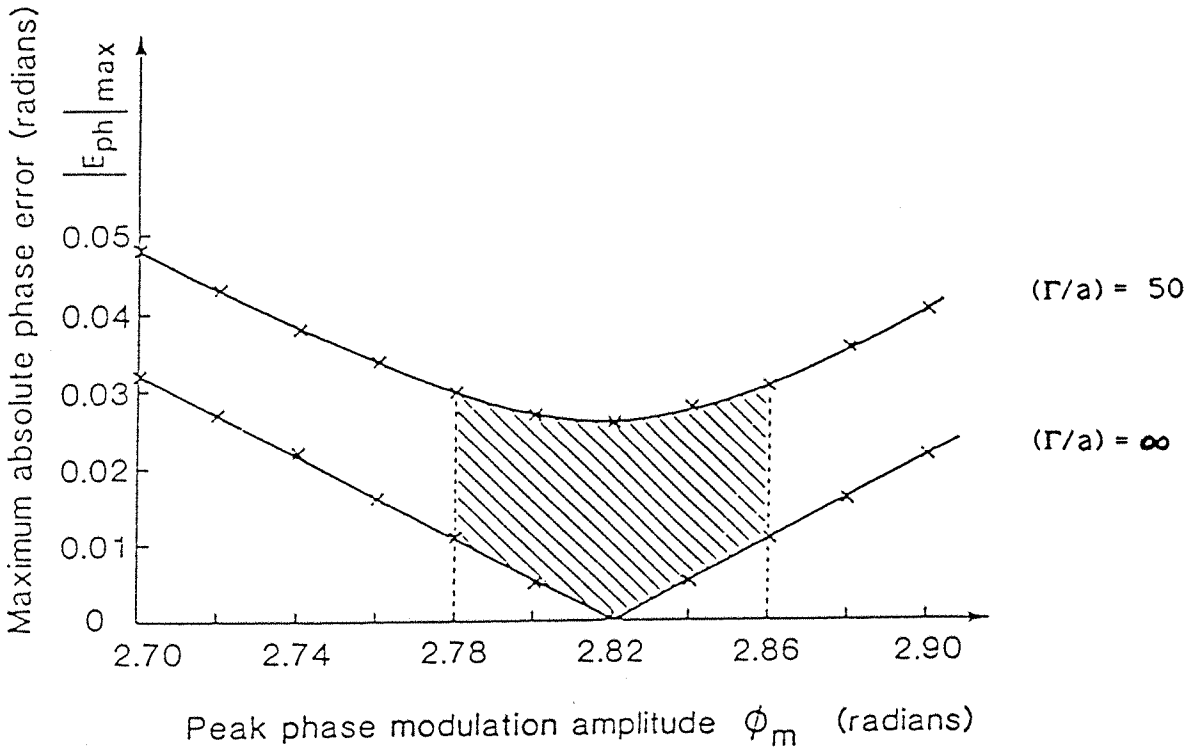

FIGURE 4.12 VIBRATION MEASUREMENT SCHEME.

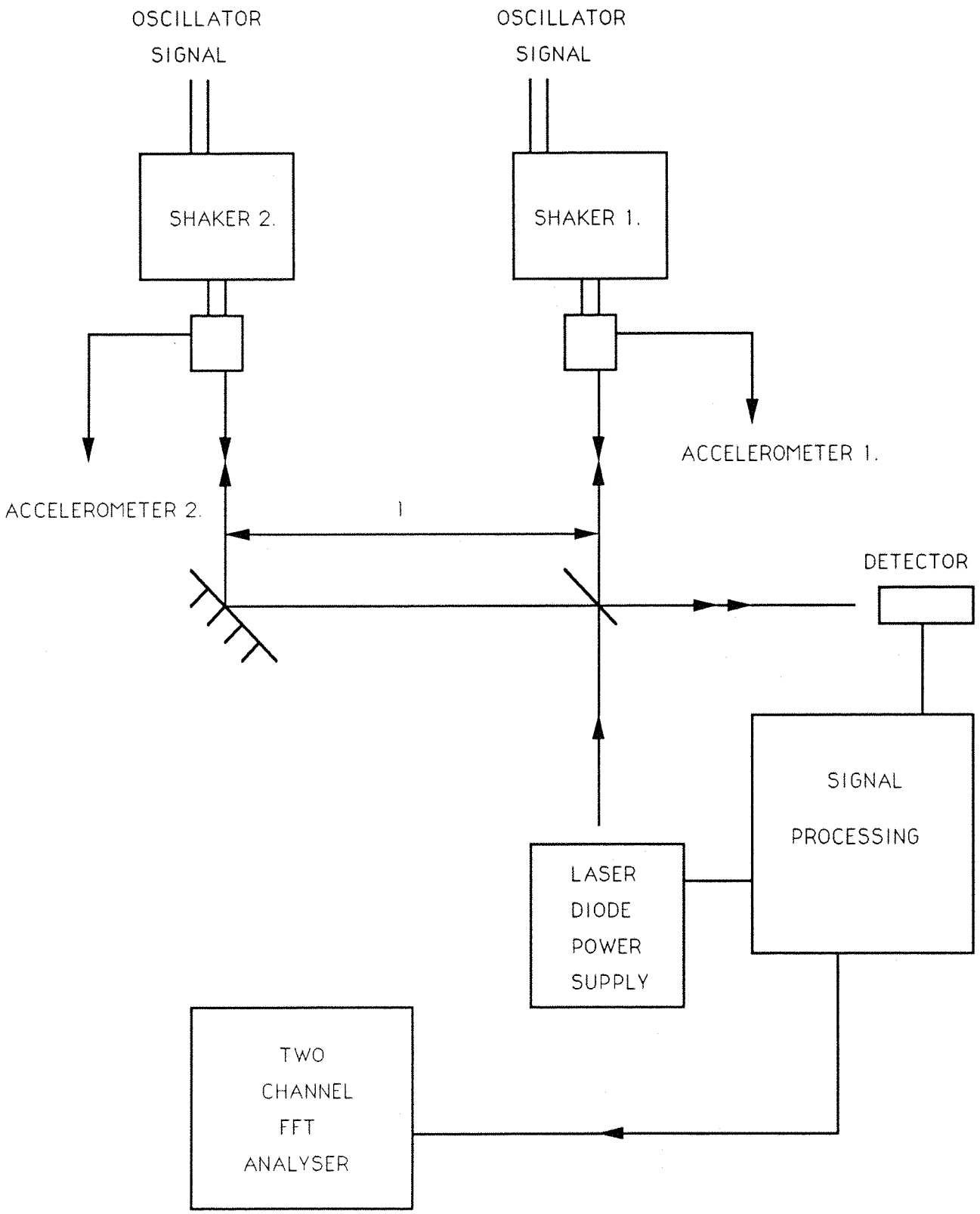

FIGURE 4.13 POINT VELOCITY MEASUREMENT

FIGURE 4.14 INTEGRATED ACCELEROMETER VIBRATION MEASUREMENT

FIGURE 4.15 VELOCITY DIFFERENCE MEASUREMENT

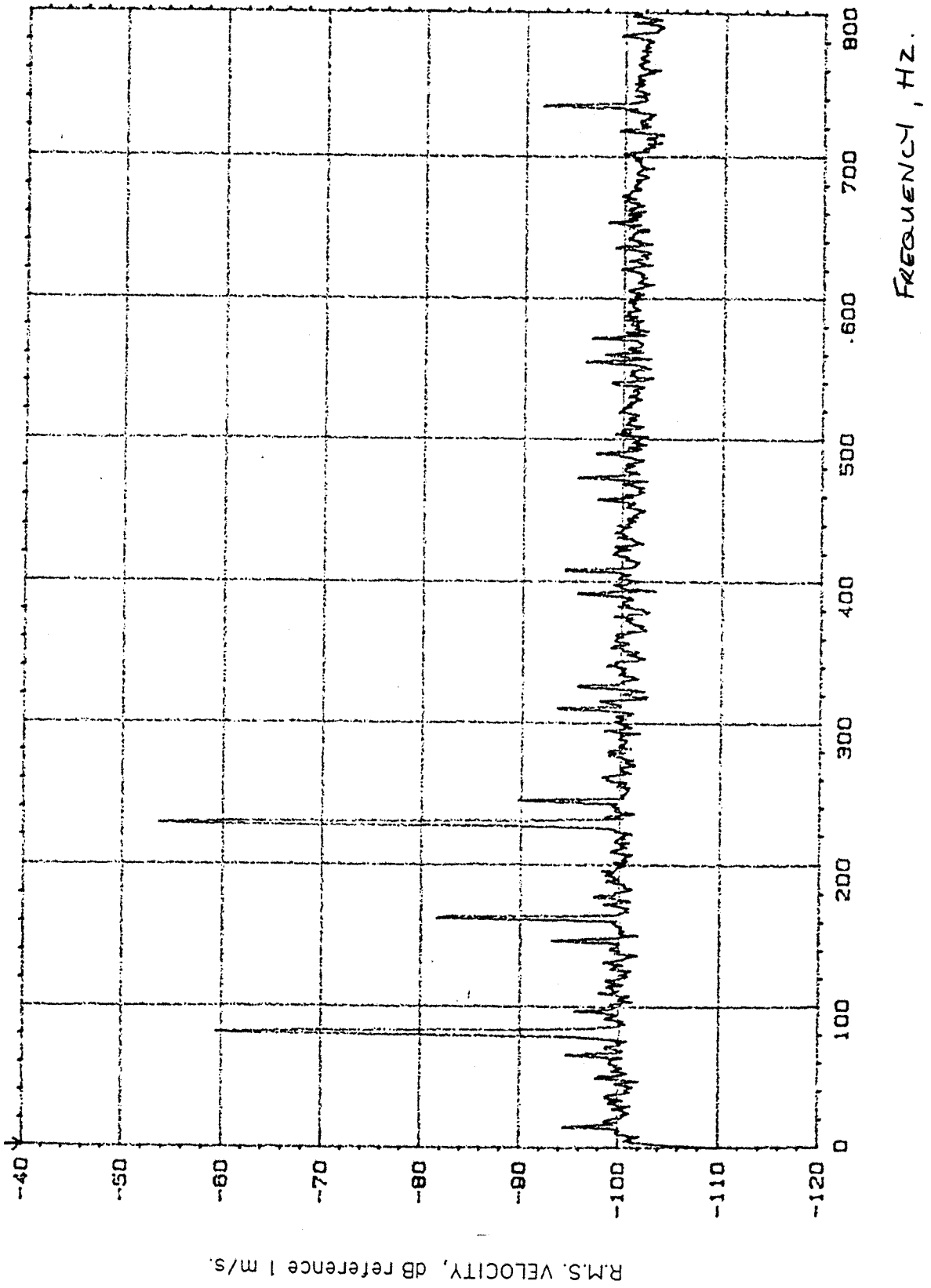

FIGURE 4.16 STRUCTURAL INTENSITY MEASUREMENT SCHEME.

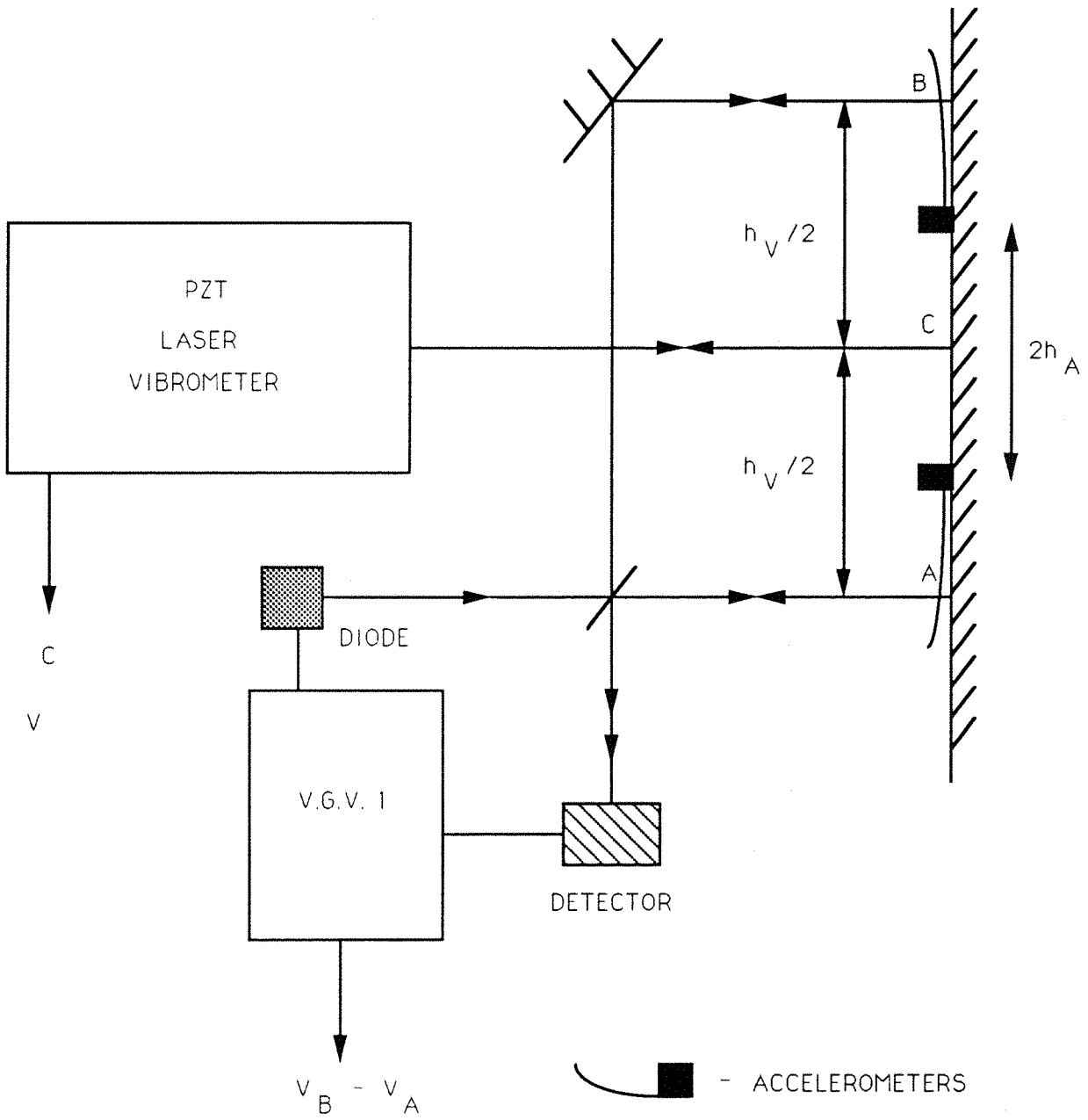

FIGURE 4.17 STRUCTURAL INTENSITY MEASUREMENTS.

| FREQUENCY Hz. | VELOCITY AMPLITUDE dB, ref. 1m/s | TWO ACCELEROMETER SCHEME, S.I. dB, ref. 1 Watt.* | V.G.V. SCHEME, S.I. dB, ref. 1 Watt.* | S.I. DIFFERENCE dB. |
|---|---|---|---|---|
| A) MID-RANGE VELOCITY AMPLITUDE EXCITATION. | | | | |
| 500 | -54.9 | -23.63 | -24.14 | - 0.51 |
| 750 | -54.2 | -23.06 | -23.72 | - 0.66 |
| 1000 | -55 | -25.98 | -26.43 | - 0.55 |
| 1250 | -54.6 | -26.2 | -26.89 | - 0.69 |
| 1500 | -59.3 | -24.46 | -24.7 | - 0.24 |
| 1750 | -55 | -26.76 | -27.37 | - 0.61 |
| 2000 | -54.6 | -26.02 | -26.46 | - 0.44 |
| 2250 | -54.5 | -27.41 | -27.55 | - 0.14 |
| B) LOW VELOCITY AMPLITUDE EXCITATION. | | | | |
| 500 | -75.7 | -44.98 | -45.6 | - 0.62 |
| 750 | -75.3 | -44.17 | -44.96 | - 0.79 |
| 1000 | -76 | -46.98 | -46.82 | 0.16 |
| 1250 | -74.1 | -46.35 | -46.5 | - 0.15 |
| 1500 | -75.3 | -44.2 | -44.62 | - 0.42 |
| 1750 | -75.4 | -46.91 | -46.56 | 0.35 |
| 2000 | -74.45 | -45.9 | -46.73 | - 0.83 |
| 2250 | -76.1 | -49.85 | -50.75 | - 0.9 |

* NO FINITE DIFFERENCE APPROXIMATION CORRECTION
3.2KHz FREQUENCY BANDWIDTH WITH 1Hz FREQUENCY RESOLUTION.
10 AVERAGES.

FIGURE 5.1 FORMATION OF OBJECTIVE LASER SPECKLE PATTERNS.

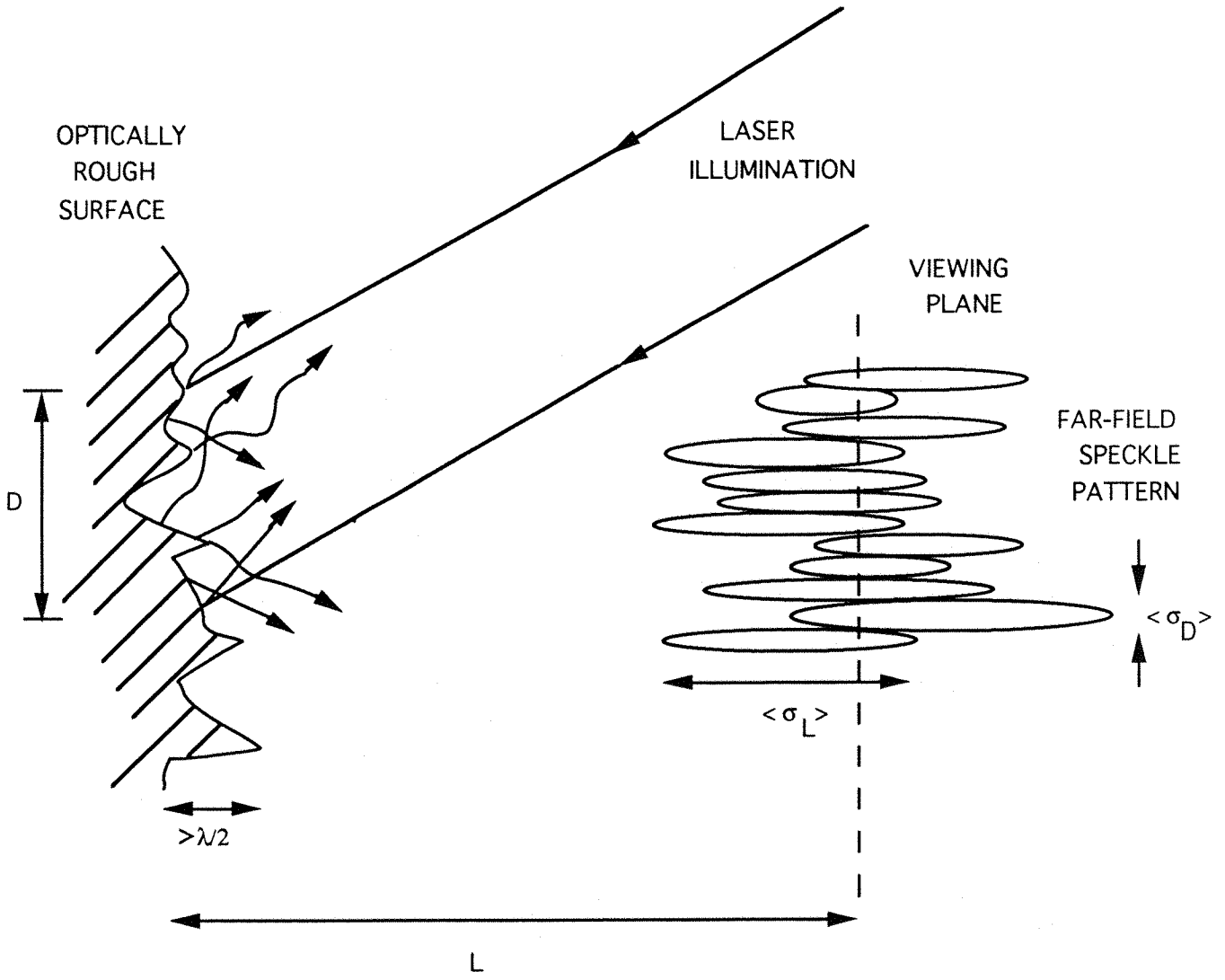

FIGURE 5.2 ROTATING DIFFRACTION GRATING LASER VIBROMETER.

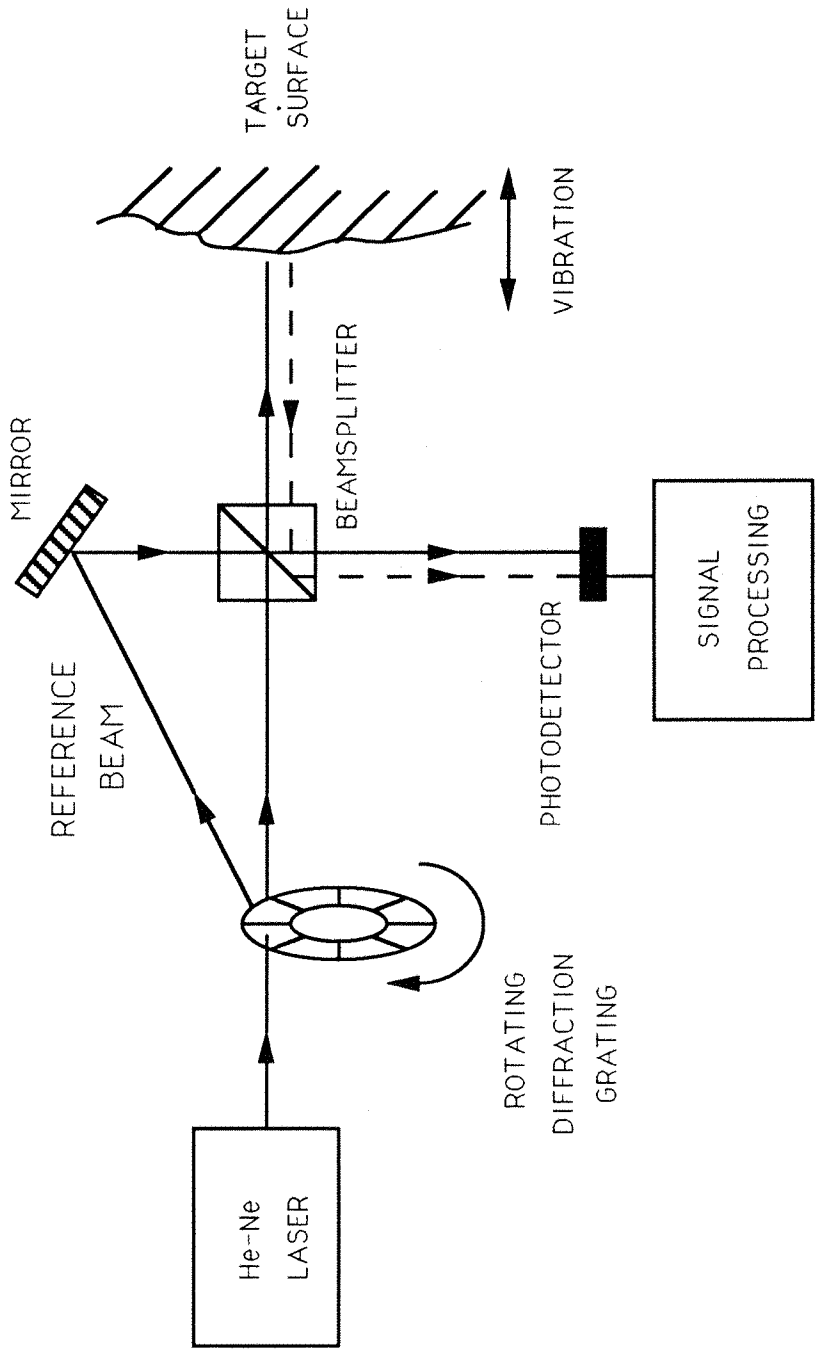

FIGURE 5.3 PERIODIC, DYNAMIC SPECKLE NOISE SIGNAL.

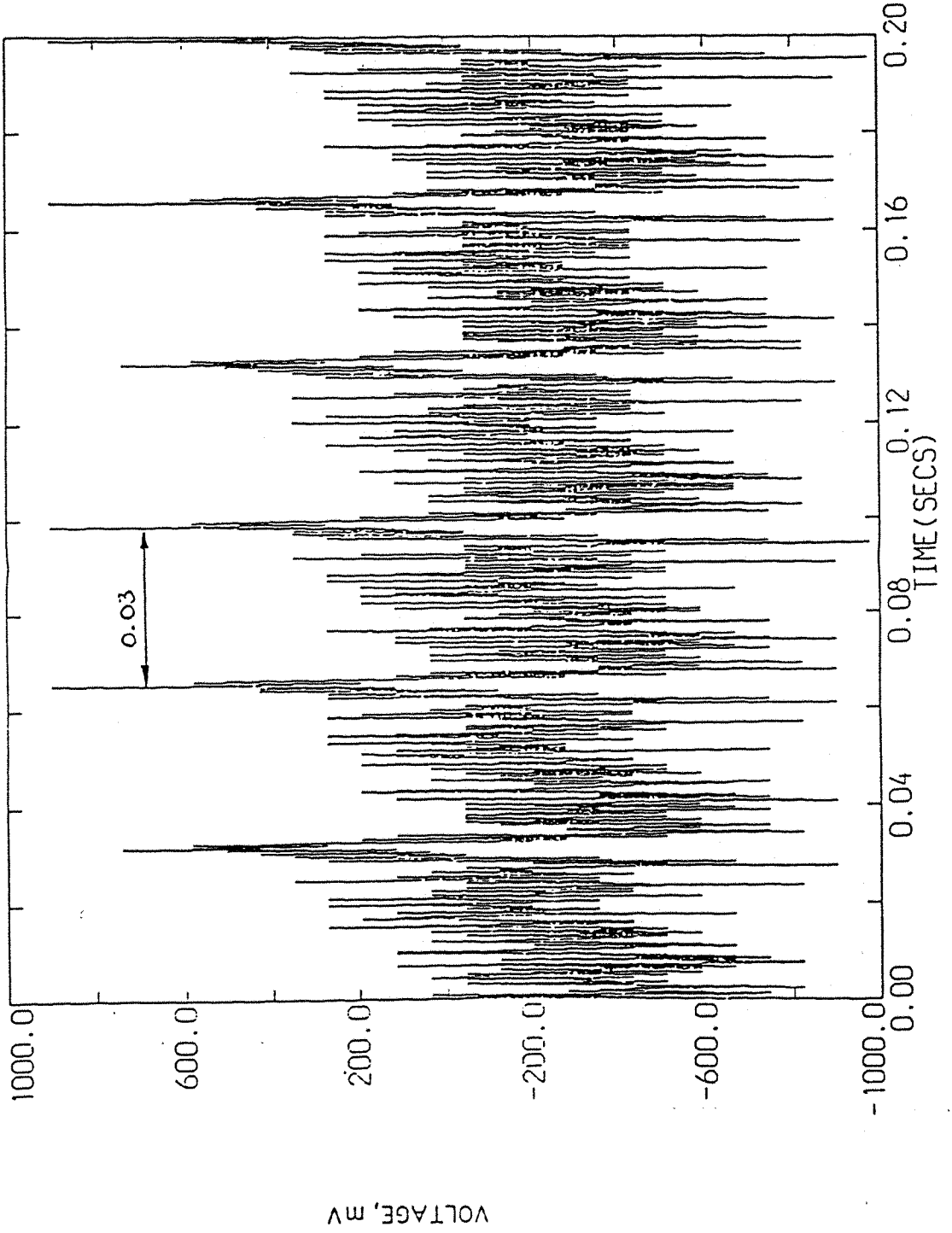

FIGURE 5.4 DYNAMIC SPECKLE SPECTRA MEASUREMENT SCHEME.

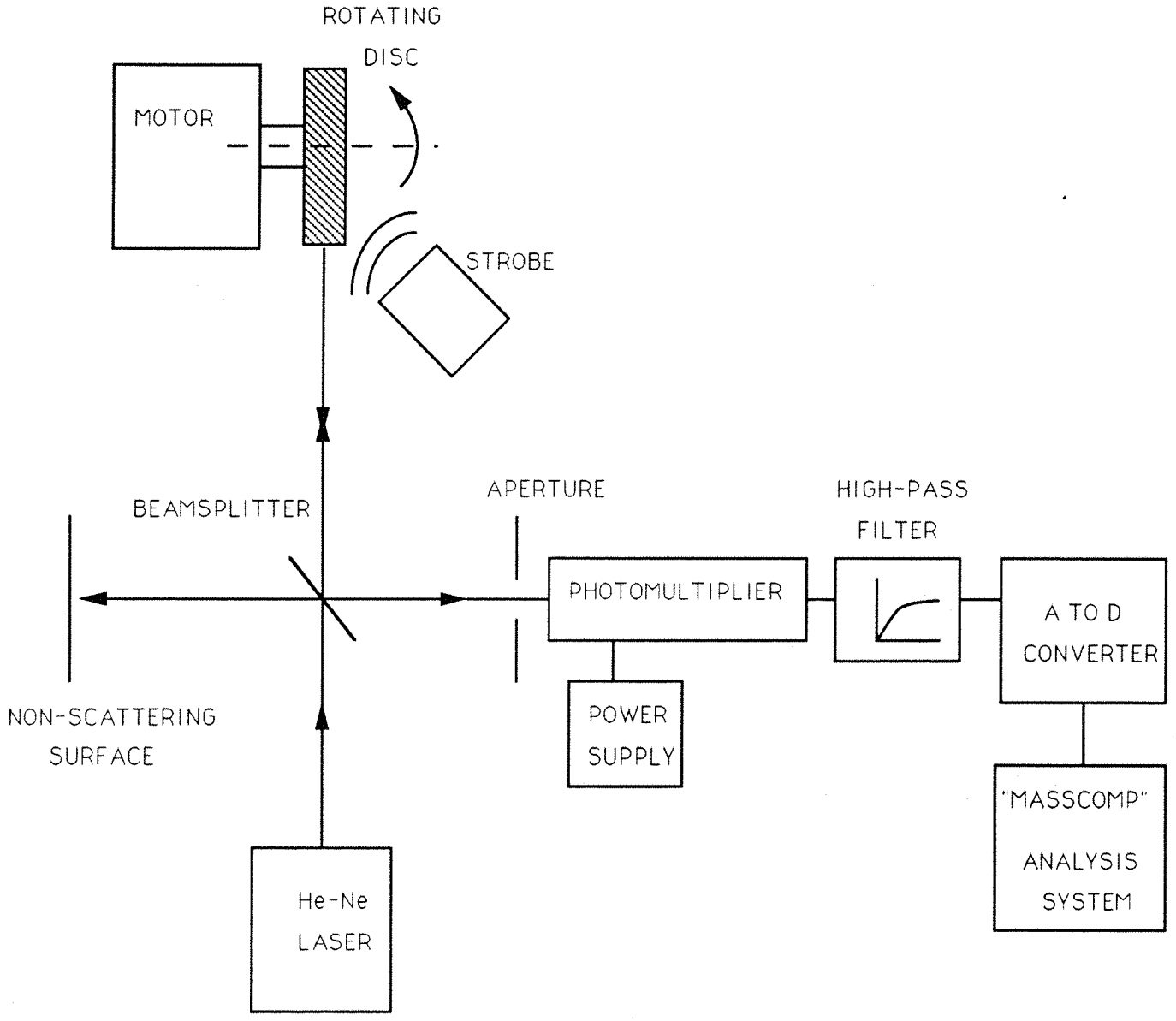

FIGURE 5.5 DYNAMIC SPECKLE NOISE SPECTRA:
MEASUREMENT PARAMETERS.

| TARGET-DETECTOR DISTANCE, cm | AVERAGE SPECKLE DIAMETER, $\langle\sigma\rangle$, m | AVERAGE SPECKLE AREA, A, $m^2$ | AVERAGE No. OF SPECKLES ON DETECTOR S/A |
|---|---|---|---|
| 26 | 2.007E-04 | 3.164E-08 | 24.8 |
| 36 | 2.779E-04 | 6.066E-08 | 12.9 |
| 46 | 3.551E-04 | 9.9E-08 | 7.9 |
| 56 | 4.323E-04 | 14.678E-08 | 5.3 |

DETECTOR APERTURE DIAMETER = 1mm

=> DETECTOR AREA, S = 7.854E-07$m^2$

FIGURE 5.6 DYNAMIC SPECKLE NOISE SPECTRA:
VARIATION IN SPECKLE VELOCITY.

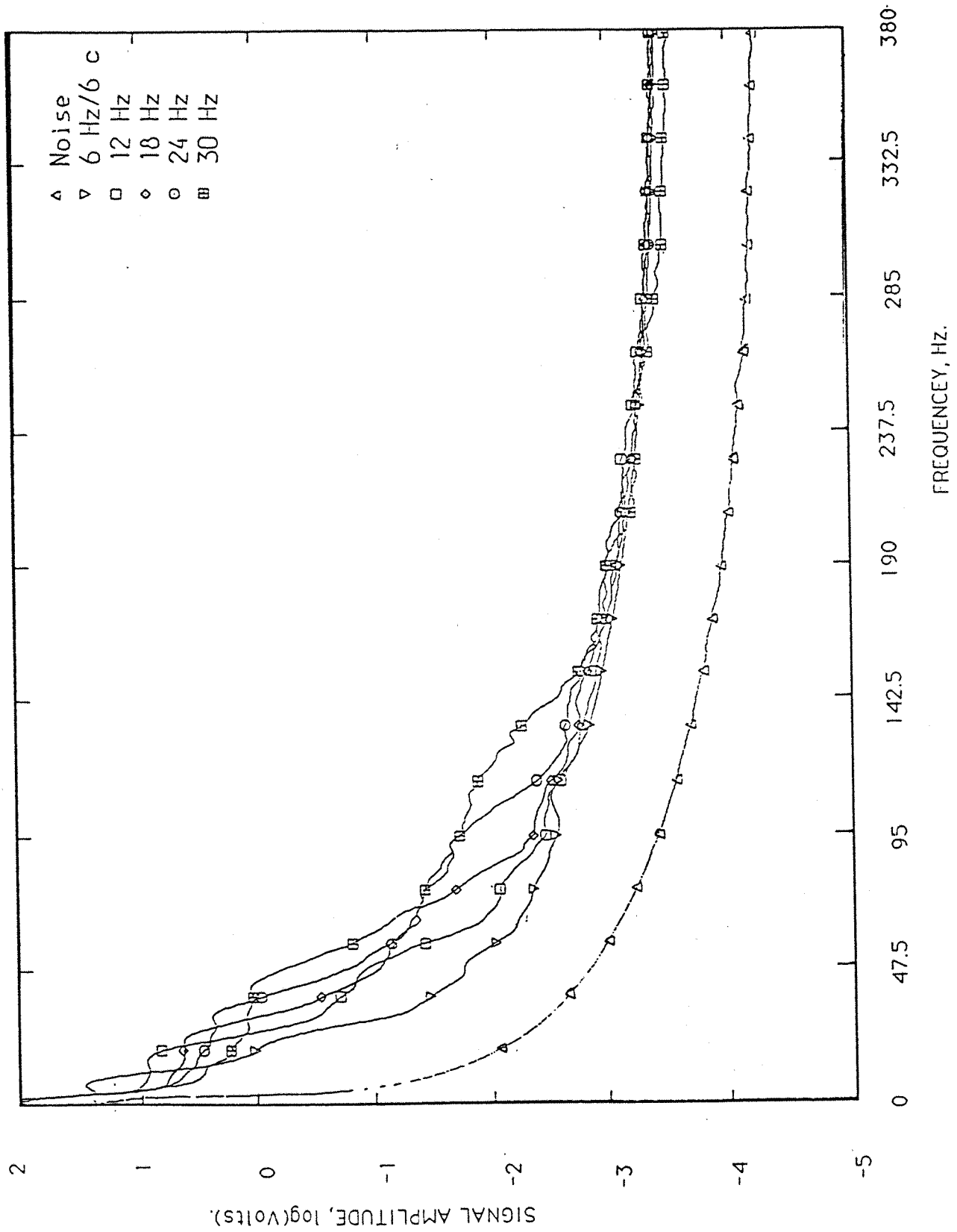

FIGURE 5.7 DYNAMIC SPECKLE NOISE SPECTRA:
VARIATION IN SPECKLE SIZE.

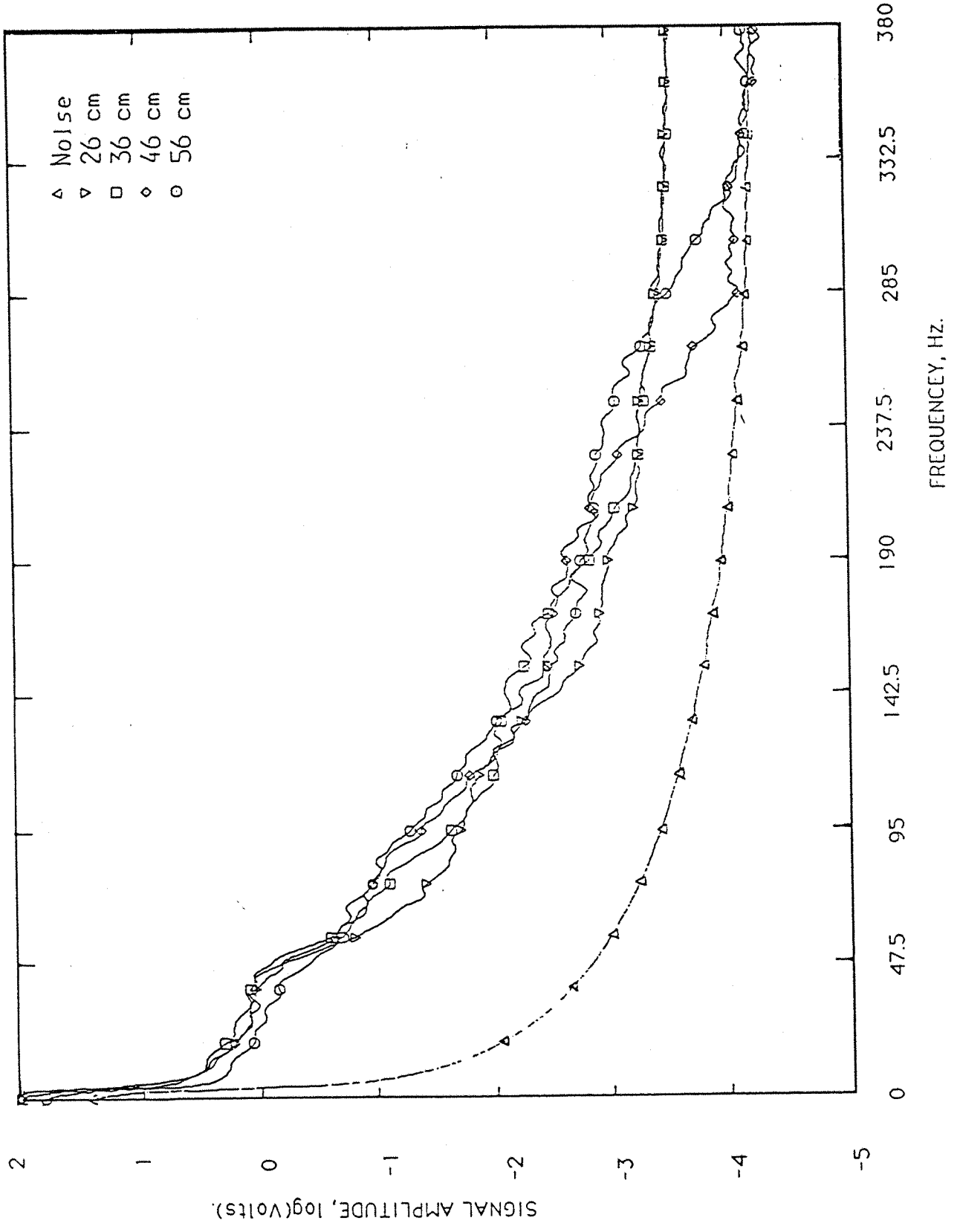

FIGURE 5.8 LASER VIBROMETER MEASUREMENT OF NORMAL-TO-SURFACE VIBRATION.

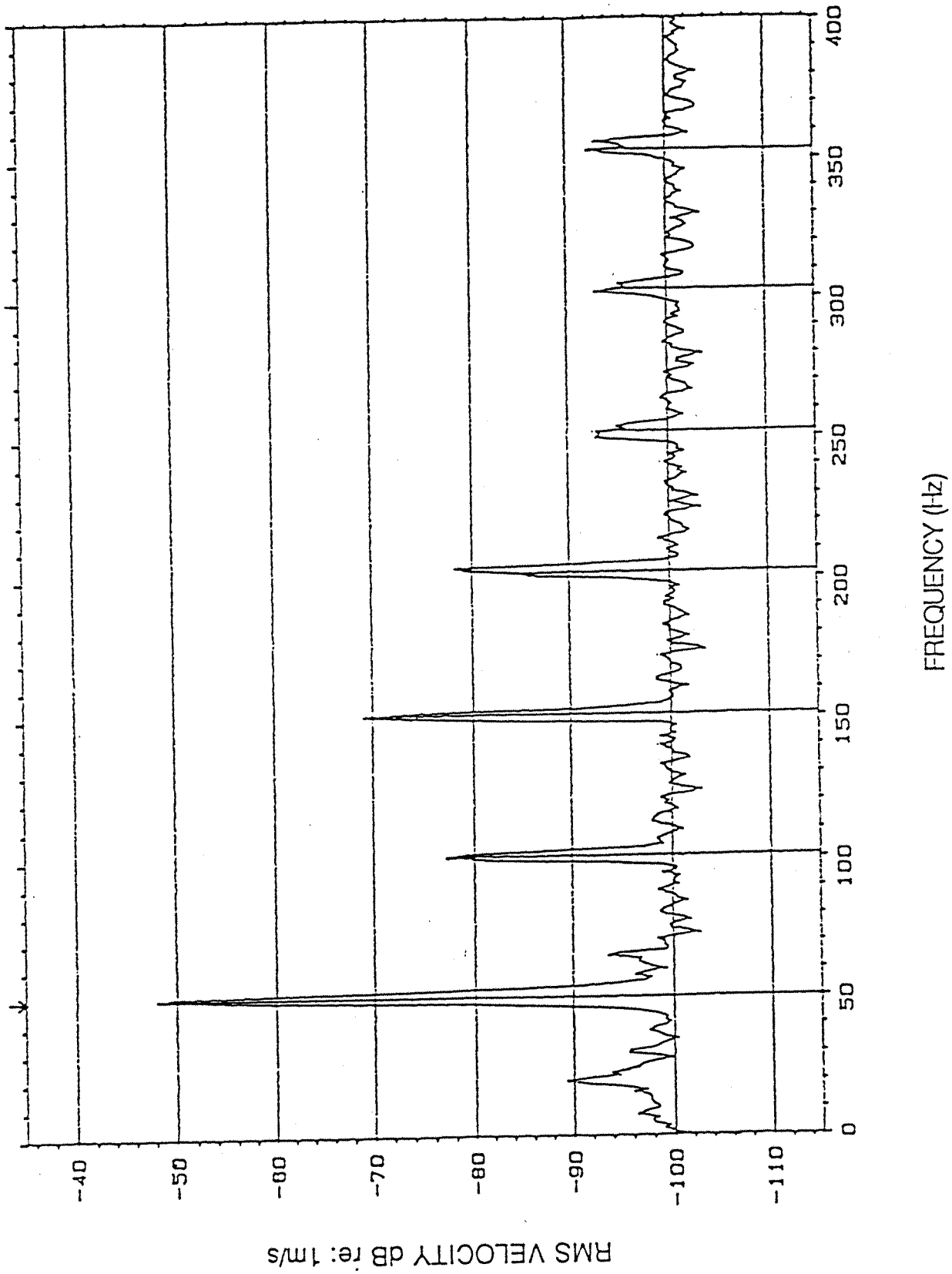

FIGURE 5.9 COMPARISON OF IN-PLANE PSEUDO-VIBRATION WITH TRUE, NORMAL-TO-SURFACE VIBRATION.

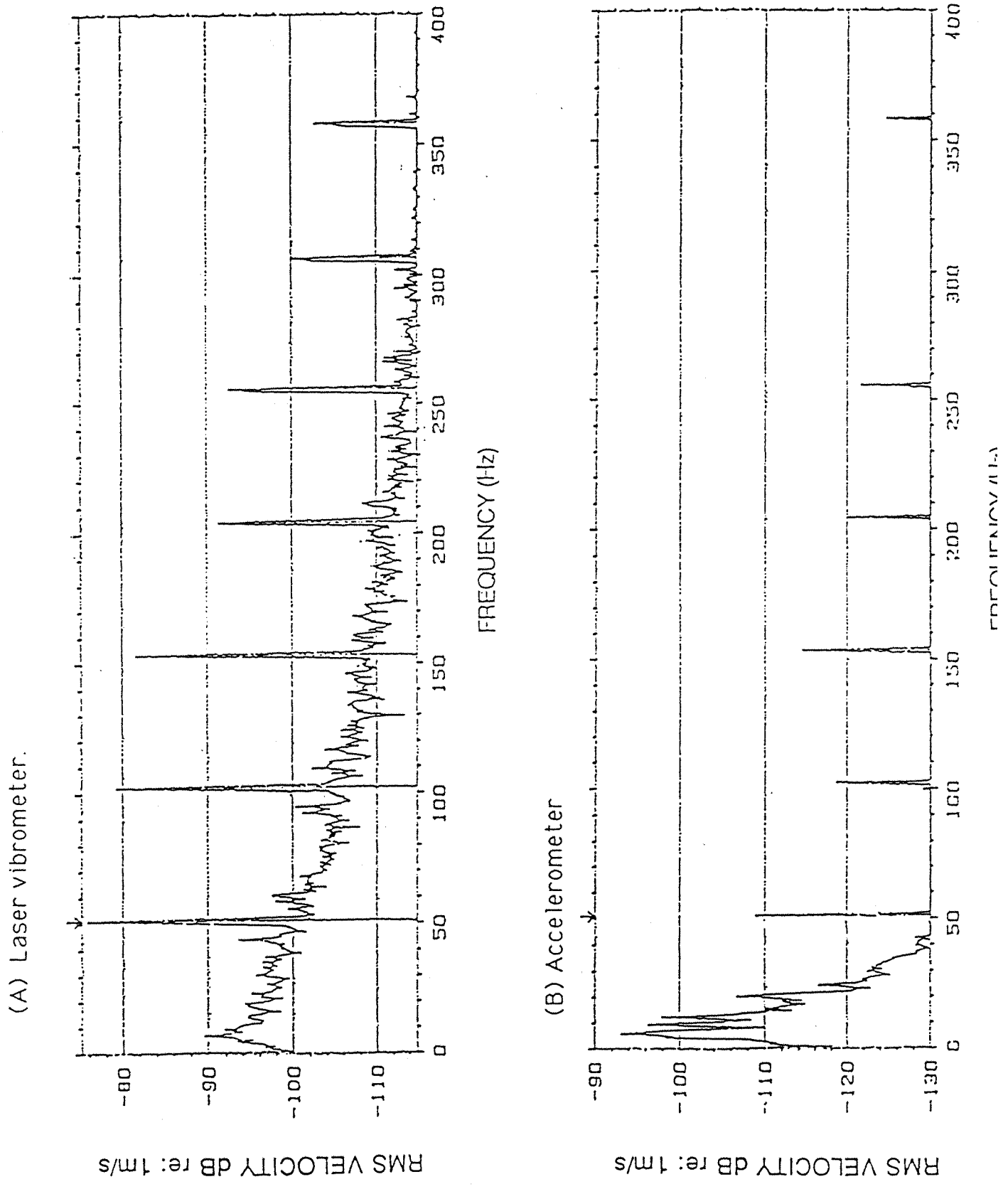

FIGURE 5.10 IN-PLANE VIBRATION MEASUREMENT SCHEME

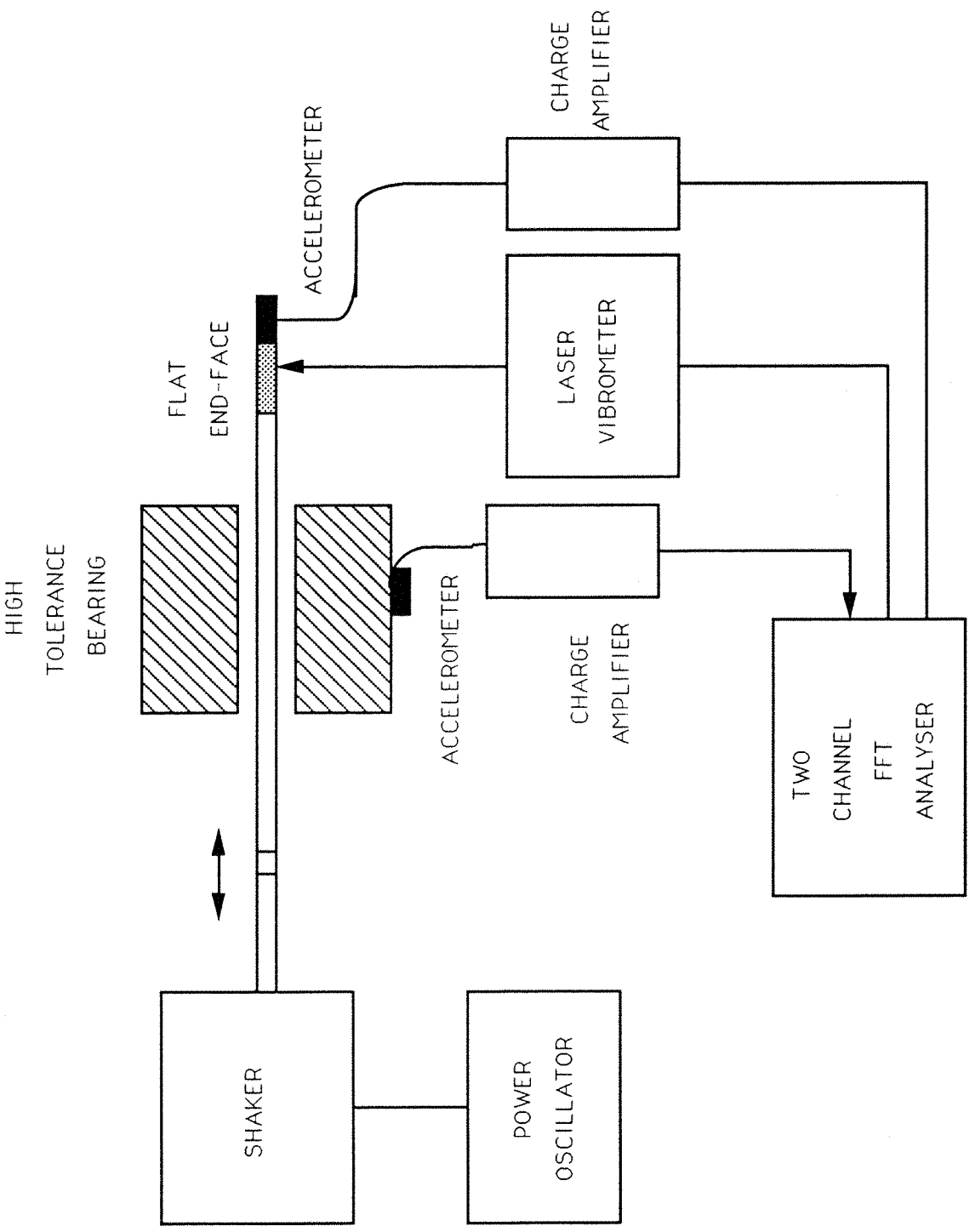

FIGURE 5.11 VIBROMETER OUTPUT FROM A TILTING SURFACE.

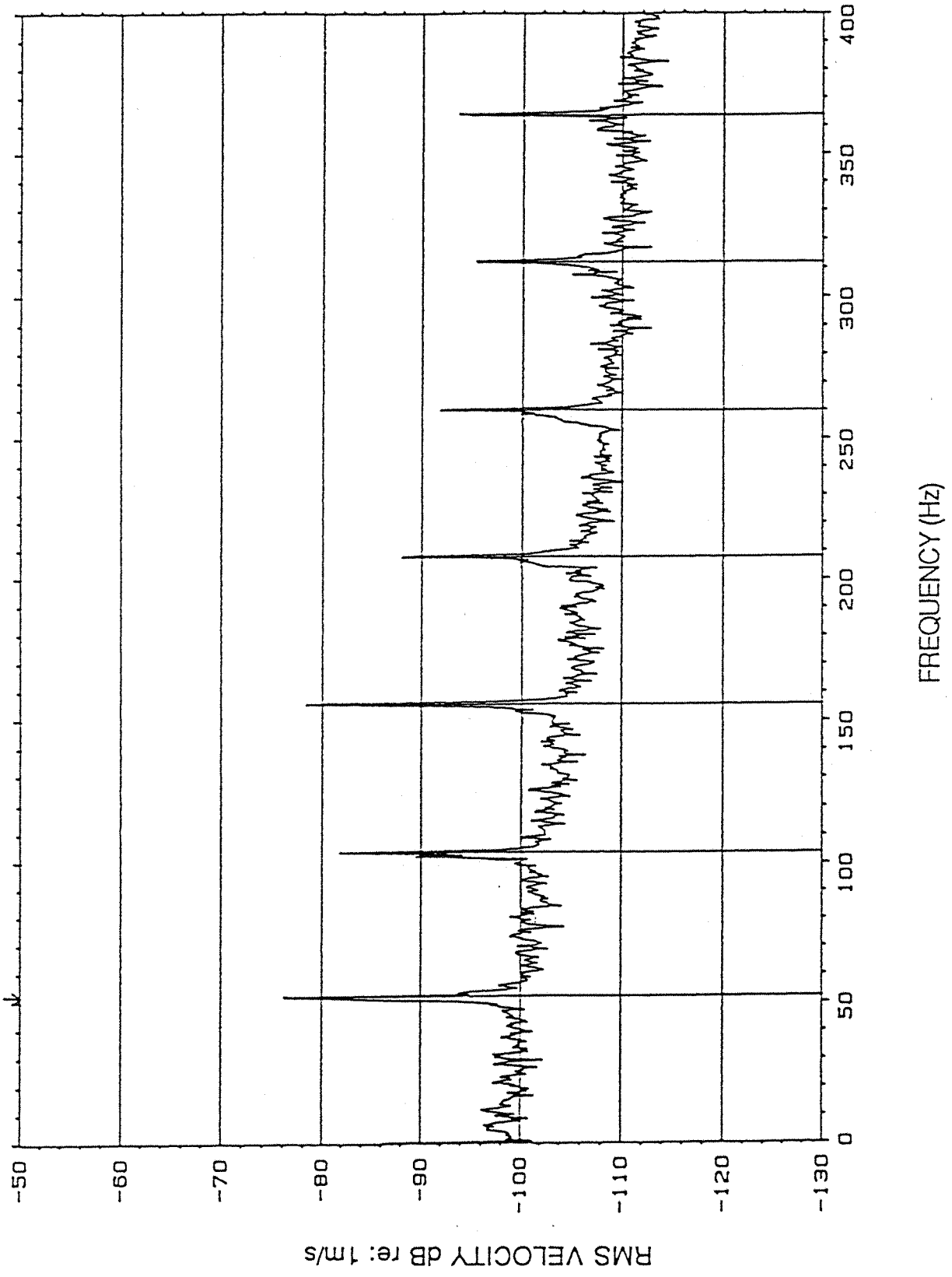

FIGURE 5.12 VIBROMETER OUTPUT FROM A ROATING SURFACE.

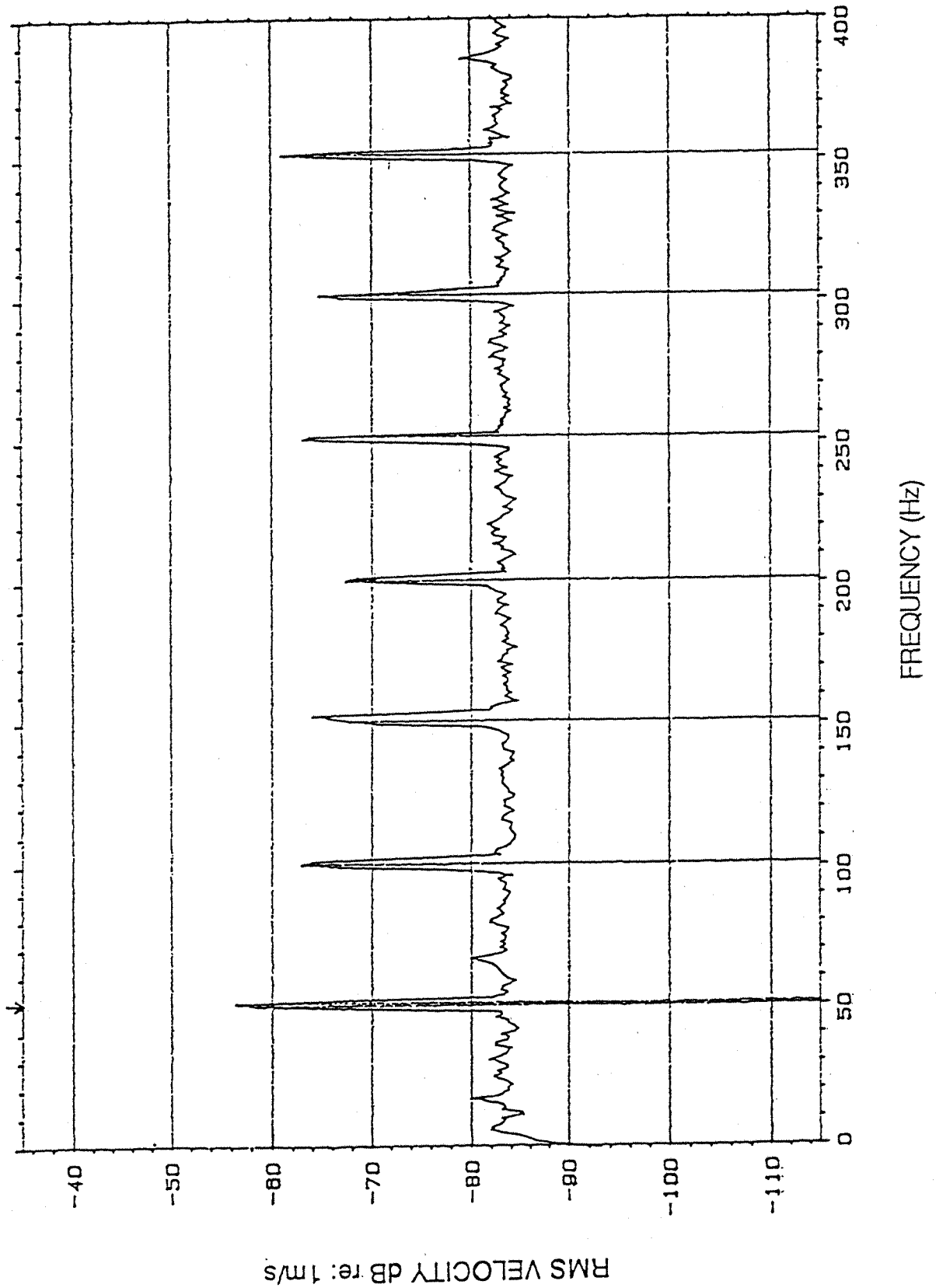

FIGURE 5.13 CONSTANT AMPLITUDE, IN-PLANE EXCITATION.

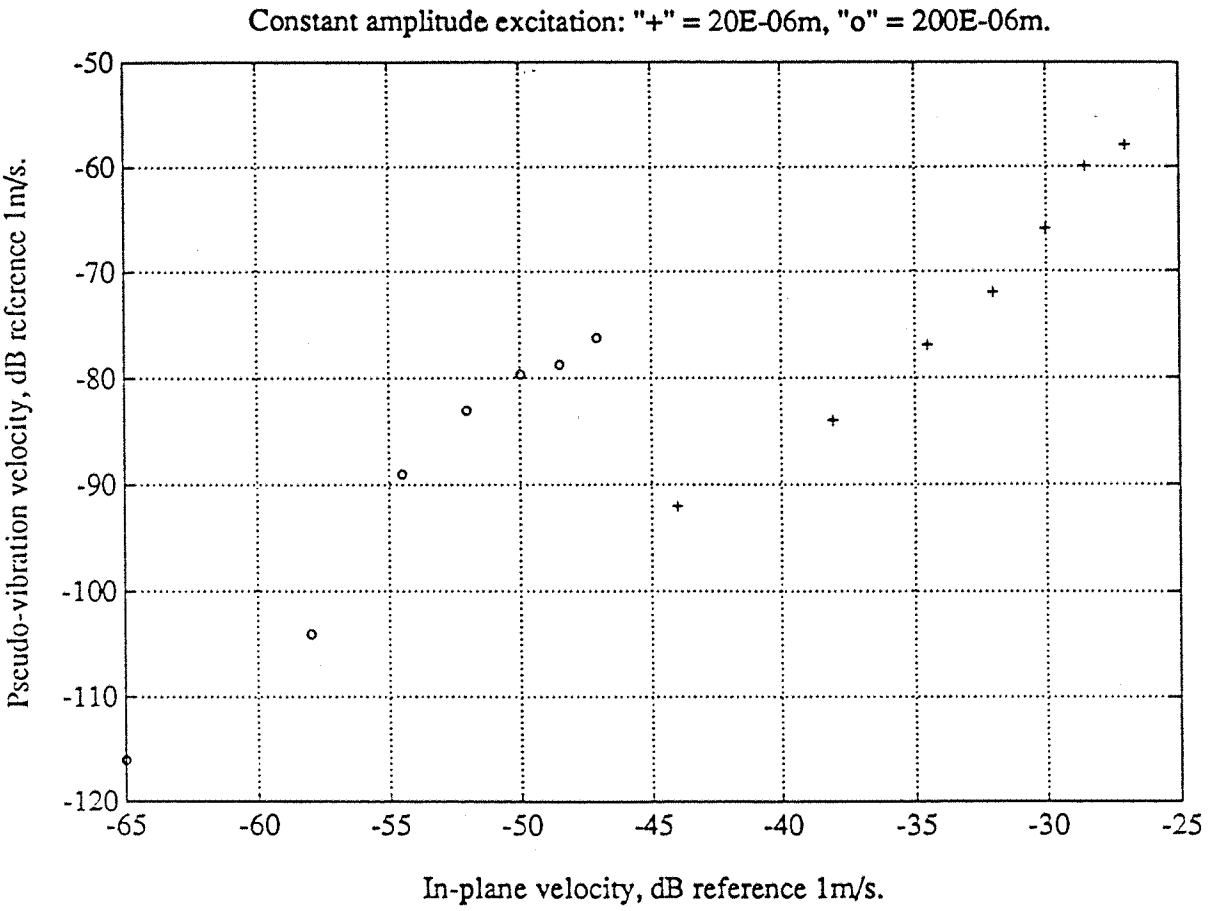

FIGURE 5.14 CONSTANT FREQUENCY, IN-PLANE EXCITATION.

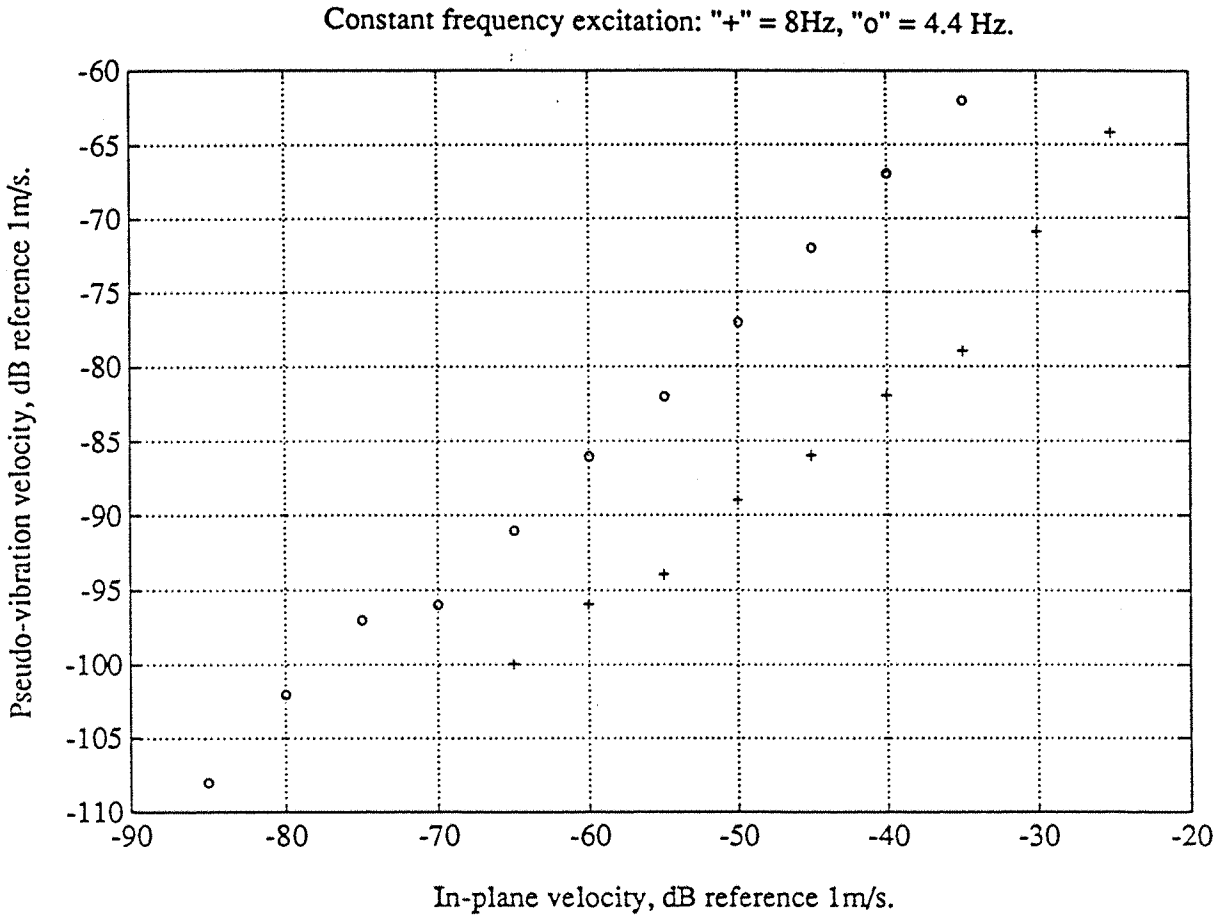

FIGURE 5.15 CONSTANT VELOCITY, IN-PLANE EXCITATION

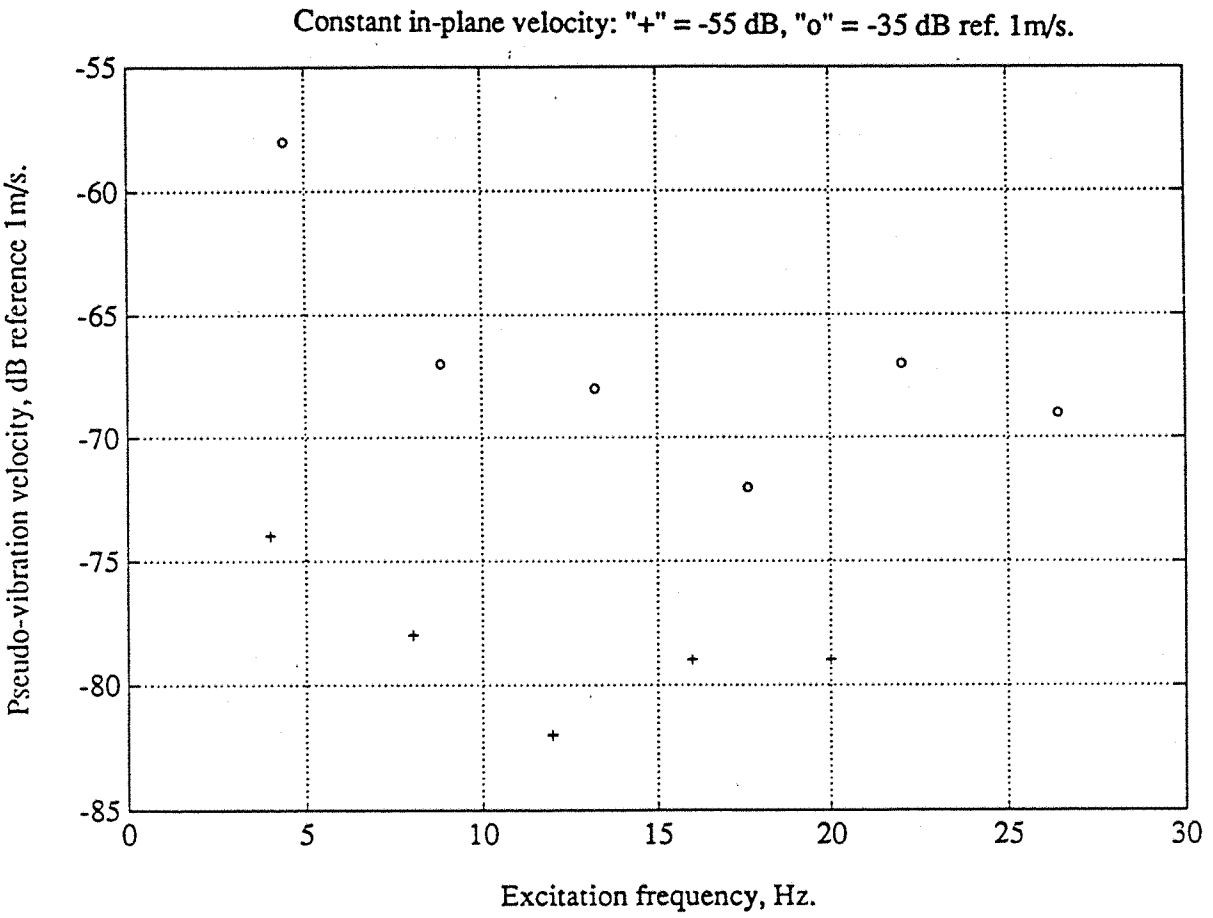

FIGURE 5.16 CONSTANT AMPLITUDE, TILT EXCITATION.

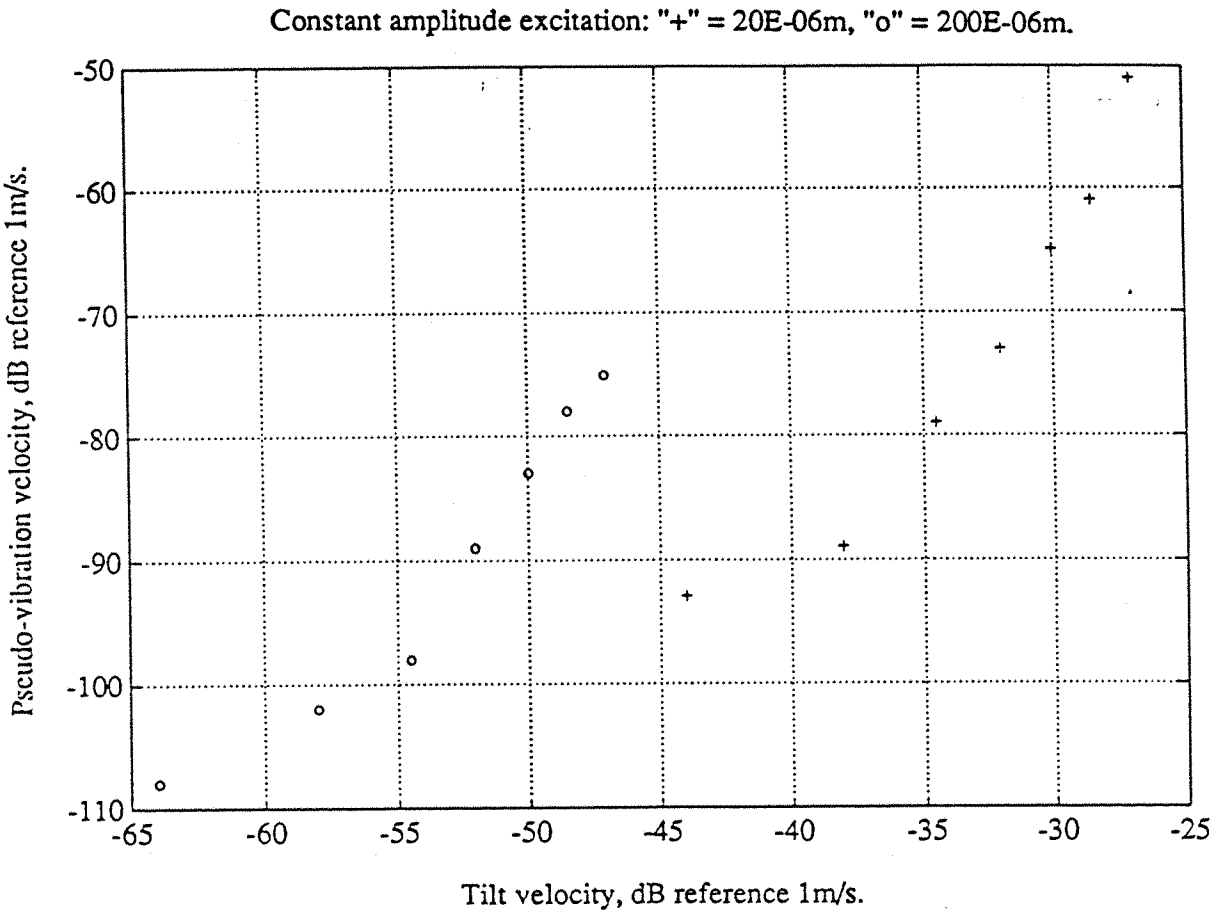

FIGURE 5.17 CONSTANT FREQUENCY, TILT EXCITATION.

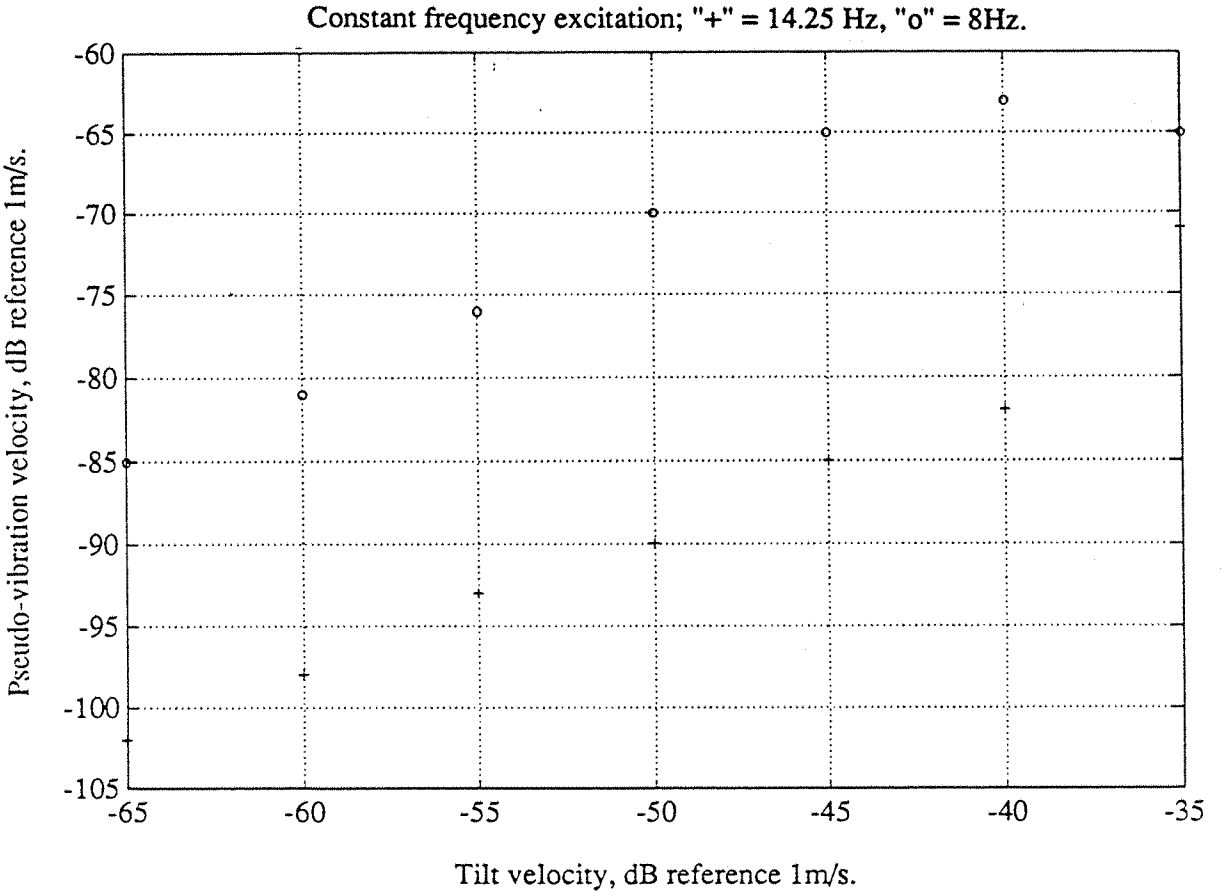

FIGURE 5.18 CONSTANT VELOCITY, TILT EXCITATION

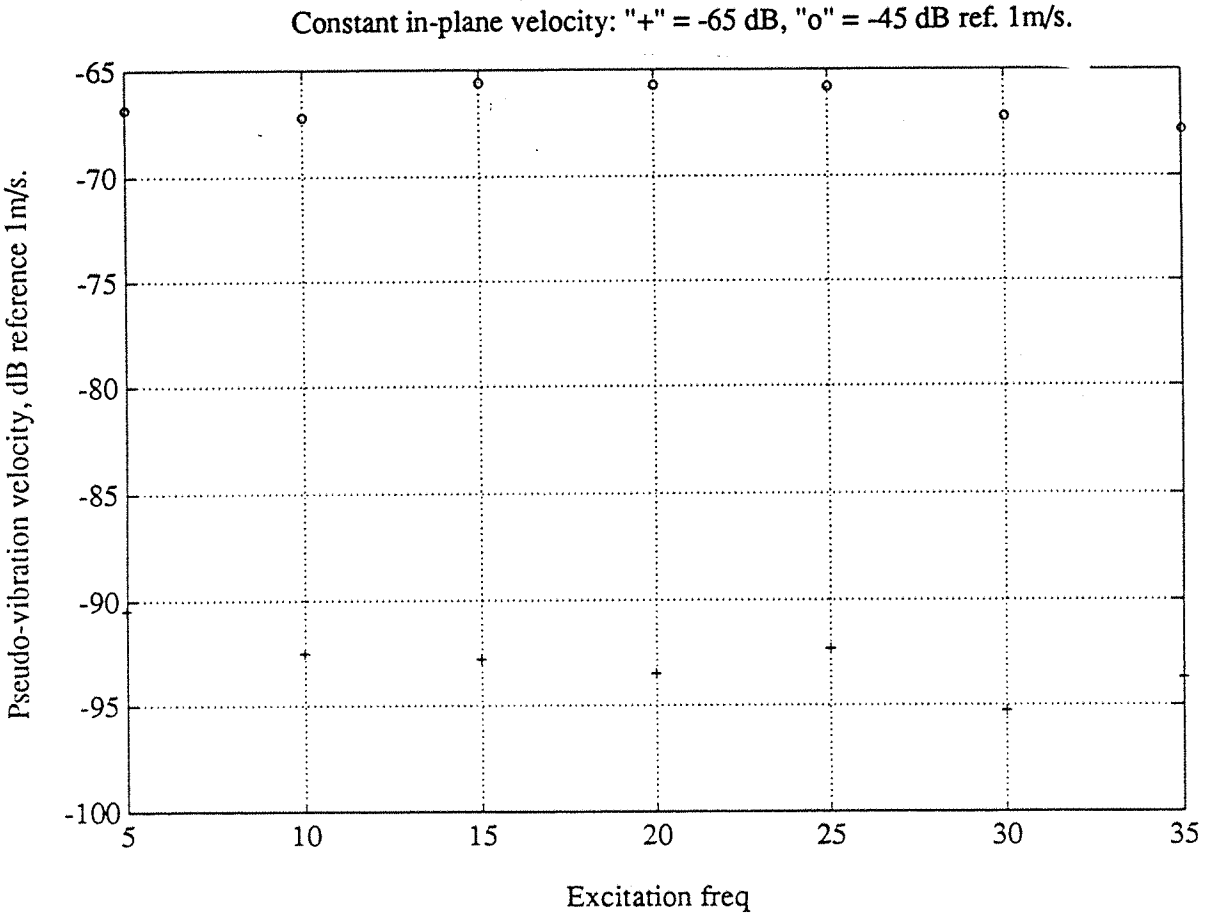

FIGURE 5.19 RESULTANT LIGHT AMPLITUDE VECTOR FOR P SPECKLES.